UNIVERSITY OF SOUTHAMPTON
FACULTY OF PHYSICAL AND APPLIED SCIENCES
Electronics and Computer Science

Fabrication and characterization of biomimetic antireflective surfaces with reduced glare

by

Petros Ioannis Stavroulakis

Thesis for the degree of Doctor of Philosophy

March 2012

UNIVERSITY OF SOUTHAMPTON

ABSTRACT

FACULTY OF PHYSICAL AND APPLIED SCIENCES
ELECTRONICS AND COMPUTER SCIENCE

Doctor of Philosophy

Fabrication and characterization of biomimetic antireflective surfaces with reduced glare

by Petros Ioannis Stavroulakis

Providing antireflection in the visible spectrum is useful for a number of applications. Solar cells, LCD screens, optical lenses and stealth surfaces are a few examples of applications that can benefit from antireflection. In this work, maximizing the performance of a biomimetic moth-eye metamaterial antireflection layer via optimization of its design parameters was investigated. Additionally, case studies of designing optimized antireflection solutions were carried out for some of the most demanding applications such in solar cells and stealth coatings.

More specifically, simulations of the moth-eye design parameters for feature period, height, density factor, shape and topology were carried out. For feature height, it was found that for a height larger than 400nm, the gains in providing antireflection for the visible spectrum are low, so it is not necessary to create features taller than this to achieve a good antireflection performance. For feature density factor an almost linear monotonic relationship was observed, so for this design parameter, maximization is necessary. For the feature period parameter, it was found that a simple rule could not be extracted and thus to optimize performance, a tailoring of the period for each application has to be done whilst taking into account the incident spectrum. An optimization of the feature period was carried out for monocrystalline silicon solar cells and the AM 1.5 solar spectrum and it was found that for this spectrum, the optimum period is 397nm. Feature topology was not found to provide a significant advantage to the antireflection behaviour of the metamaterial layer in terms of power, however it does provide a more diffuse scattering of the backscattering diffraction order which emanates from the structure at high angles of incidence, an attribute which is very useful for stealth applications.

To verify simulation results, fabrication of moth-eye antireflection structures were carried out via nano-imprint, electron-beam and nanosphere lithography. The nanosphere lithography technique presented was optimized specifically for the samples required in this thesis. Complete monolayer coverage of large areas (2x2cm^2) was accomplished and thus complex biomimetic feature topologies could be readily investigated. Optical experiments measuring specular reflectance and the backscattered diffraction orders were carried out both with readily available and custom built optical setups. The simulation trends were all verified successfully and a summary of suggested design parameters for a range of different applications has been suggested.

Contents

Declaration of authorship

I, **Petros Ioannis Stavroulakis**, declare that the thesis entitled:

Fabrication and characterization of biomimetic antireflective surfaces with reduced glare

and the work presented in the thesis are both my own, and have been generated by me as the result of my own original research. I confirm that:

- this work was done wholly or mainly while in candidature for a research degree at this University;
- where any part of this thesis has previously been submitted for a degree or any other qualification at this University or any other institution, this has been clearly stated;
- where I have consulted the published work of others, this is always clearly attributed;
- I have acknowledged all main sources of help;
- where the thesis is based on work done by myself jointly with others, I have made clear exactly what was done by others and what I have contributed myself;
- parts of this work have been published as:

P.I. Stavroulakis, S. Boden, and D. Bagnall, *A moth-eye bio-inspired approach to planar isotropic diffraction*, MRS Proceedings, 2010.

P.I. Stavroulakis, N. Christou, and D. Bagnall, *Improved deposition of large scale ordered nanosphere monolayers via liquid surface self-assembly*, Materials Science and Engineering: B, vol. 165, Sep. 2009, p. 186189.

Signed: ....

Dated: ....

Acknowledgements

There is not a huge difference in writing acknowledgements and award ceremony speeches except that for the most part acknowledgements are directed to a much smaller audience and don't usually start with "I would like to thank Jesus...". However, God probably did have something to do with it because considering the status of the clean room when I started my PhD and that it still is not fully operational, it seems like a miracle that I managed to finish on time. Taking into account the truly great time I have had at the University of Southampton and the many things that I am thankful for I could go on forever, but I will try to condense it.

First and foremost, I would like to thank my supervisor Prof. Darren Bagnall who has supported me all these years. I feel very fortunate to have been under his guidance for 5 years now, including his supervision of my undergraduate and masters projects. I believe I have learned a lot being his student and I think if there is one phrase that sums it all up is that there is never a dull moment when someone is around Darren either at University, or outside its walls.

Furthermore, I would like to thank Stuart Boden, for his help in manufacturing lots of the samples at NILT and INNOS, and all his help in proof-reading and contributing to conference papers and posters and training me on various equipment and experimental setups. I would also like to thank Tristan Temple for allowing me use his nanosphere lithography apparatus with which I created all the relevant samples shown here and Chien Fat Chau for his help and advice in carrying out the initial procedure. Finally, I would like to thank Dr Martin Charlton for his assistance in setting up and calibrating the experimental setup which was created to measure the diffraction from the samples created.

For their assistance not only to the technical, but all aspects of PhD life, I would like to thank Michael Pollard and Gregory Ayre with whom I started the PhD and have been my brothers-in-arms along this journey.

Even though I have been far from home for a long time, the feeling of home has not been far from me at all. I would like to thank my loving parents for always being there for me. I would like to personally thank my father for his advice and wise words and my mother for her everlasting patience and caring. Love you both. My three brothers were not out of the picture either, Stavros was here in Southampton with me most of the time, and the other two namely Vasilis and Stelios whom I have been away from for most of this time always made up for lost time with me when I visited home.

From here on out the list is endless. If I had to name a few, first of all it would be Mehdi for all the hours we spent talking and playing backgammon which will be missed deeply. I just hope we will be able to play again in some hotter 'climes' like in Persia or Greece. (Similar goes to Hamish). A special thanks to my office and coffee-mate Mario

for making the day to day working environment seem less monotonous. I will definitely take up your advice about the secrets of Mexico and come to visit someday.

Additionally and in no particular order, the following people come to mind: Vaggelis, Nikitas, Mitsos, Ilias, Giannis, Eduardo, David, Owain, Steffi, Ashwin, Akhtar, Sun Kai, The Persians, the technicians in various labs I worked with and especially our caring secretaries Glenys and Luch, thank you both for your support!

Finally, I would like to thank my internal and external examiners, Dr. Tracy Melvin and Dr. Duncan Allsopp for their very useful comments and for assisting greatly in shaping the final version of this thesis.

Goodbye Southampton!!! XXX

List of Abbreviations

$2D$ - Two-dimensional

Al_2O_3 - Aluminium Oxide

AM - Air Mass equivalent

AOI - Angle of incidence

ARC - Anti-reflective coating

CAD - Computer Aided Design

CdS - Cadmium Selenide

$CdTe$ - Cadmium Telluride

$CIGS$ - Copper Indium Gallium di-Selenide

CIS - Copper Indium Selenide

$CNRS$ - Centre National de la recherche scientifique

DC - Direct Current

DFT - Discrete Fourier Transform

DI - De-ionized

$DRIE$ - Deep Reactive Ion Etching

DUV - Deep Ultra Violet Photolithography

EMT - Effective medium theory

EUV - Extreme Ultra Violet Lithography

EVA - Ethylene-vinyl acetate

$FIBL$ - Focused Ion Beam Lithography

FiT - Feed in Tariff

H_3PO_4 - Phosphoric acid

HF - Hyrdofluoric acid

HNO_3 - Nitric acid

ICP - Inductive Coupled Plasma

$iLIA$ - Improved Liquid Interface Assembly

IR - Infra Red

KOH - Potassium Hydroxide

LED - Light Emitting Diode

MgF_2 - Magnesium Fluoride

$MOST$ - Multi-variable Optimizer and Scanner Tool

$NaOH$ - Sodium Hydroxide

NIL - Nano-Imprint Lithography

$NILT$ - Nano-Imprint Lithography Technologies

$NREL$ - National Renewable Energy Laboratory

NSL - Nano-Sphere Lithography

$PDMS$ - Polydimethylsiloxane

$PESC$ - Passivated emitter solar cell

$PMMA$ - Poly methyl methacrylate

PSi - Porous silicon

$PTFE$ - Polytetrafluoroethylene

PV - Photovoltaic

$RA.D.A.R$ - Radio Detection And Ranging

$RCWA$ - Rigorous Coupled Wave Analysis

RIE - Reactive Ion Etching

SEM - Scanning Electron Microscope

Si - Silicon

SiH - Hydrosilane

$SiO2$ - Silicon Dioxide

TE - Transverse Electric

TM - Transverse Magnetic

TMAH - TetraMethyl Ammonium Hydroxide

UNSW - University of New South Wales

UV - Ultra Violet

Y_2O_3 - Yttrium Oxide

Chapter 1

Introduction

Antireflection technologies are used in a variety of consumer applications such as optical correction lenses, camera lenses, car windows and television screens. The military also finds use of antireflective stealth technology for a myriad of applications including glare reduction from gun scope lenses and minimizing radar cross-sections of fighter jets to gain tactical advantage. However, one of the most challenging applications of antireflection, where every extra photon absorbed counts in improving the device efficiency, is in photovoltaics. Photovoltaics is one of the most challenging applications for designing optimal antireflection solutions because the whole range of angles of incidence are important (as the sun moves from sunrise to sunset) and the solar irradiation striking the surface of the earth contains a very broadband spectrum of electromagnetic radiation which varies with time of day, relative position on the globe and weather conditions. It is a very unpredictable and dynamic system which pushes the limits of what current nanoengineering is able to achieve.

1.1 Global Outlook on Photovoltaics

Solar cells are becoming an increasingly important field of research as they have the potential of satisfying all of the global electrical energy demand via clean and abundant means of production. The potential of supplying the world energy demand with use of photovoltaics is demonstrated by placing only 8% efficient solar cells in the areas with most sunlight on the global radiation map (Figure 1.1) which in total cover less than 0.001% of the global surface area (510,000 km^2). Using this simple calculation, it is possible to produce an average output of 18TWe [1] which corresponds to 13,567Mtoe [1] per year. In comparison, the global energy consumed in 2007 from all energy sources was 8,500Mtoe (Figure 1.2 (b)).

---

[1] toe = tonne of oil equivalent, a measure of energy which is around 42GigaJoules

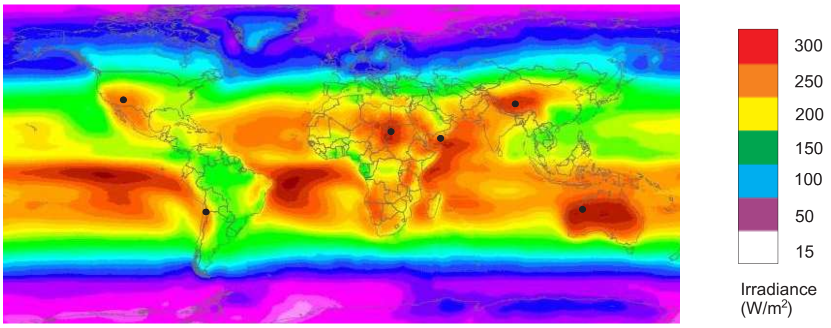

Figure 1.1: Averaged annual solar irradiance between years 1990-2004. The colour bar is presented on the right of the image. The regions of highest solar irradiance are represented by red regions on the map. The black dots represent the positions on the globe where 18TWe power stations could potentially be installed to cover global electricity demand. Source: Ecole des Mines de Paris / Armines / CNRS. [2]

The inherently limited fossil fuel resources that are currently used for the production of the majority of the world's energy needs are not self-sustainable. First of all, there is an inherit distant future risk (some analysts claim we only have around 40 years worth of petrol left based on the current consumption trends [3]) that an obvious future crisis will be created when all the oil reserves have been exhausted or reduced in supply. The cost of changing all fossil fuel dependent machinery/auto mobiles at that point will be immense, not to mention the socio-political impact of the situation. Hence, a phasing out of this energy source is inevitable and it would make much more sense to plan for it in advance rather than to wait for all the fossil fuel to be exhausted before action is taken. However, it is predicted that the more pressing and current issue of CO_2 greenhouse gas pollution will dominate before resource limitations become an problem. Environmental factors of current energy sources such as climate change and CO_2 emissions are already becoming an important concern in public opinion and is bound to influence energy policies for years to come.

In any case, sustainable levels of energy production and more importantly stable energy prices are not guaranteed with the current fossil fuel supply chain. A sudden unavailability of supply affects prices dramatically because there is a concurrent global exponential growth in demand of fossil fuel energy which creates a constant need to add new resources to the system. The political instability in many oil producing nations produces a real risk of short term supply unavailability, which forces price spikes when unpredictable circumstances take place in these places (e.g. armed conflicts, embargo e.t.c.). More importantly though, as tapped sources become drained and new sources are harder to find, a consistent reduction in capacity will be met with a sharp increase in price to reduce demand before new resources can become available to the system. If new resources cannot be found fast enough to keep up with demand, there will be a future consistent rise in price until all capacity is exhausted.

Solar energy on the other hand is a more than adequate and mostly untapped energy resource as previously discussed, that will not cease in the predictable future (our sun still has 5 billion years to go...) and philosophically speaking, life on our planet is directly related to the sun, so there is no point in talking about a future without it. The main advantage of renewable energy sources though is that they are clean means of producing energy, as far greenhouse emissions are concerned which is a major environmental and political gain over fossil fuels. The opinion that renewable energy is the optimum solution for energy is becoming popular with consumers. Solar energy is a ubiquitous and hence more stable supply of energy because the operational cost compared to that of buying and installing the solar panels is very small. So essentially, the total cost of producing solar energy throughout the panel's lifetime is essentially fixed at the time of installation.

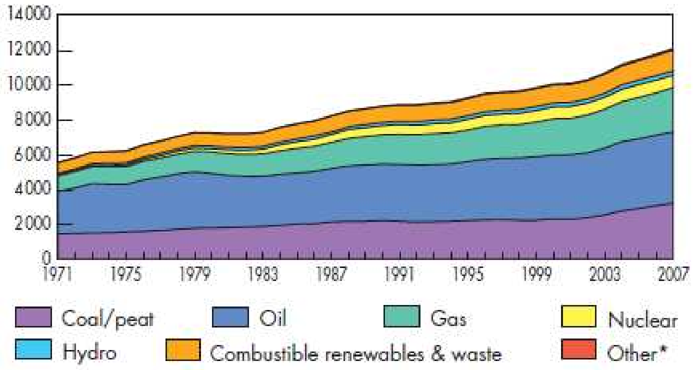

(a) Trend in global energy supply between 1971-2007 in Mtoe

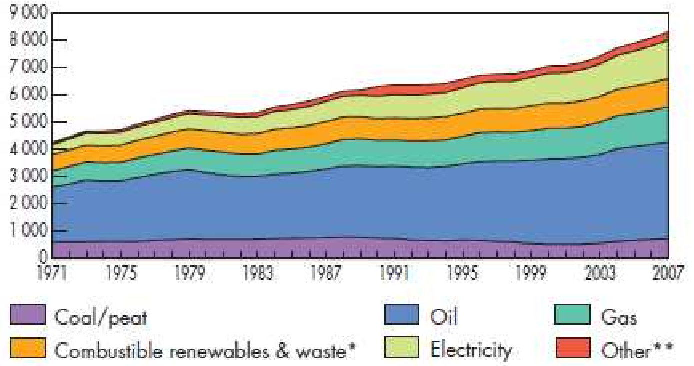

(b) Trend in global energy consumption between 1971-2007 in Mtoe

Figure 1.2: Global world statistics for sources of energy supply and consumption for Coal, Oil, Gas, Nuclear, Hydro Combustible renewables and waste, and Other sources. Both energy supply and consumption show a steady increase in demand for all sources of energy between 1971-2007 Source: IEA International Energy Agency Key World Statistics 2009 [4]

The largest disadvantage of solar cell technology is that the price of producing energy via solar cells is currently much higher than alternate sources, and this is the main barrier for widespread adaptation of the technology by the consumer and business markets as it still cannot compete with fossil fuels. There are two ongoing trends that might help reverse this situation in the near future. The first one is legislation in accordance to clean energy sources. If global warming and climate change continue to gain traction in the political arena and become translated into favourable legislation for promoting renewable energy sources in the major energy markets of US, China, and the EU, demand for renewable energy sources will increase substantially. The second trend, is that the cost of consuming electricity from the grid is increasing faster at some places of the globe than the price of consuming energy via solar cells, hence solar cell technology will become a viable alternative to grid electricity in areas of the world where sunshine is abundant enough to provide grid parity (i.e. when the cost of producing energy by the use of solar cells is equivalent to buying the energy from the grid). There are already some areas in the world today (California, Italy and Japan) where the price of purchasing electricity from the grid is becoming very close to the cost of solar technology and these places might be the first to achieve grid parity [5].

Currently, PV growth is mainly sustained by government incentives such as investment subsidies where the government contributes considerably in paying for the cost of installing the solar cells. Renewable Energy Certificates are another way of supporting green energy providers who can trade their 'green points' to companies that produce carbon over the limits set by legislation. This makes producing carbon more expensive for companies and also directly subsidizes green energy providers. However, the most successful scheme so far has been that of Feed-in-Tariffs (FiT) whereby the electricity utility buys electricity directly from grid-installed solar systems at a set rate as part of a multi-year contract. FiT's have proven to be extremely successful in Germany who has topped the leagues in Europe as far as installed capacity of photovoltaics is concerned, mainly because it was one of the first countries to employ a generous FiT scheme [6]. The growth of global installed solar cell capacity is shown in Figure 1.3.

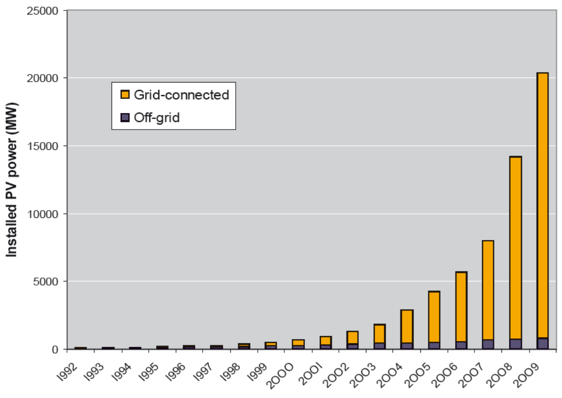

Cumulative installed PV power in the reporting countries

FIGURE 1.3: Growth of installed solar capacity in all countries monitored by the International Energy Agency. An exponential increase of installed systems has taken place between 1992-2009. It is noticed that the vast majority of installed photovoltaic systems are grid-connected which is represented by a yellow colour-bar whereas off-grid systems are represented by a blue colour-bar.(Source: IEA PV Power Update August 2010) [7]

In any case, although all of these government-backed schemes assist the widespread application of renewable energy sources, they do not allow efficient large scale deployment

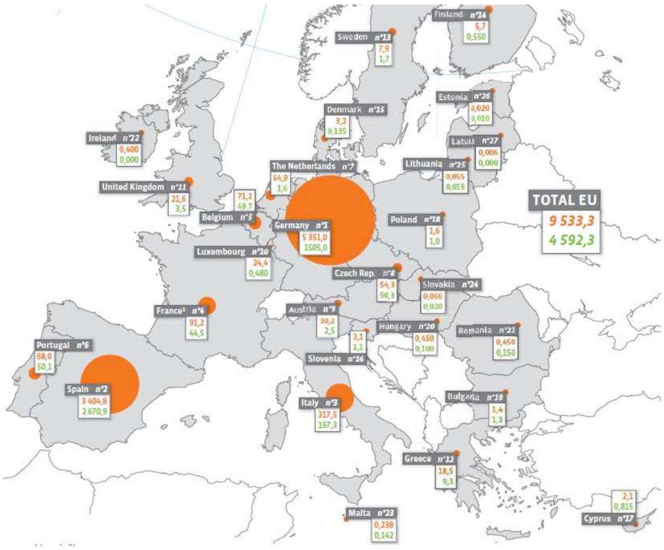

FIGURE 1.4: European installed photovoltaic capacity in MWp during 2008 per country (total installed capacity by end of 2008 on top, installed in 2008 on the bottom). The photovoltaic system capacity of each European country is represented by an orange circle, the larger the circle the larger the installed capacity of that country. It can be easily noticed that Germany, Spain and Italy are the European leaders in terms of installed photovoltaic capacity. Source: EurObserv'ER barometer 2009 [8]

of the technology and are mainly dependent on the size of the local economy and not their solar potential (Figure 1.4), because developed countries can afford to spend more on FiT's (e.g. Germany) than do nations where more solar potential is present (e.g. Greece).

The only way of making PV technology competitive enough for efficient large scale deployment is by increasing or at least sustaining panel efficiencies while using cheaper raw materials (which is by far the largest cost in the process) in order to substantially reduce the cost of the overall production processes. If this is done, the cost per watt produced via solar cells will become directly competitive to alternate sources of energy. This is the only sustainable way of perpetuating efficient growth of solar cell technology to its rightful place in the energy production market.

1.2 Review of photovoltaic technologies

1.2.1 First generation photovoltaics

There are various types of solar cells. However, the most basic and common type is the simple silicon semiconductor P-N diode. First generation solar cells are made out of these P-N diodes; a combination of P-doped and N-doped single crystal silicon with electrical contacts present at either side of the diode. This type of solar cell is the main production solar cell technology today, and is expected to be phased out by cheaper technologies that produce a better cost per watt ratio even if their efficiency and lifetime are poor compared to crystalline silicon (Figure 1.5).

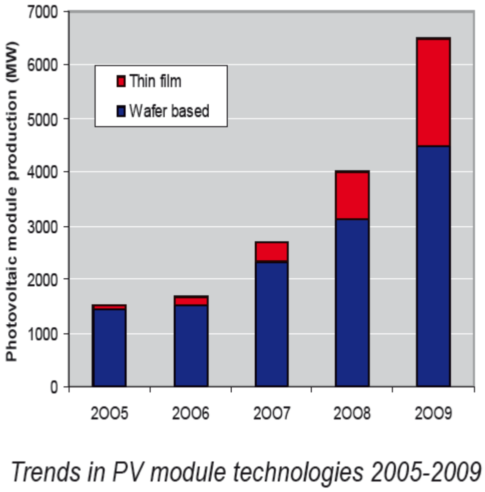

Figure 1.5: Trends in producing different photovoltaic module technologies between 2005-2009. It can be noticed that thin film systems represented by a red colour bar are rapidly gaining an ever-increasing share of the total modules produced compared to wafer based systems which are represented by a blue colour bar. Source: IEA - PVPS report 2009 [7]

This trend of course is based on the assumption that the price of silicon wafers are expensive compared to thin film technologies. With the recent economic crisis in place, the spot price of silicon wafers has plummeted from \$ 500 per kilogram in Feb of 2007 to under \$ 100 per kilogram in May of 2009 according to the silicon wafer price index (Figure 1.6). If this trend continues and production of wafers can keep up with demand, it might overturn the recent popularity of thin film solar cells.

Sunlight enters the solar cell in the form of photons (Figure 1.7). If the energy of the photon is higher or equal to the band gap energy between the valence and the conduction band of the semiconductor and the thickness of the cell is enough to allow significant absorption at that wavelength, it has a good chance of being absorbed by an electron in the silicon lattice. When a photon with enough energy is absorbed by an electron in the silicon lattice it is excited from the valence to the conduction band, and thus becomes unbound from the silicon atom and is free to move within the crystal lattice. The in-built inherit electrical field that exists in the space charge region accelerates the electron and allows it to drift across the PN junction. It then becomes a majority charge carrier in the N type region before being collected by the metal contacts. The opposite occurs for the 'hole particle' which is the positively charged particle that accounts for the absence of an electron from the lattice, it drifts across the PN junction and travels through the P type material to the metal contact. This effect produces current which, combined to the voltage created by the inherit field across the P-N junction provides

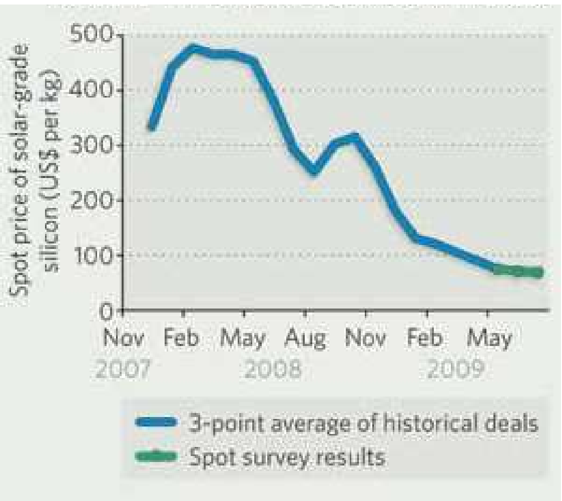

FIGURE 1.6: Trend of silicon wafer price index between 2007-2009. It can be noticed that the average price of a solar grade silicon wafer which contributes the most to the price of the solar cell has been plummeting due to a sharp reduction in demand during the recent economic recession. The blue line is a results of averaging complete market data whereas the green line is a result of spot surveys. (Source: Bloomberg New Energy Finance) [9]

electrical power. If the photon that enters the cell has energy which is smaller than the band gap of the material, then it is not absorbed by the device and passes through it.

The IV curve of a solar cell is a depiction of the 3rd quadrant in the diode relationship of current and voltage on these devices (Figure 1.8). The maximum power point on this curve is the point at which the IV product is maximum (Figure 1.9).

The external efficiency of the solar cell is defined as the maximum electrical power that is achieved in the IV curve over the power incident on the cell in the form of sunlight. The maximum efficiency that has been achieved for first generation solar cells in the lab is 25% [10], however maximum efficiency achieved by commercially available cells is around 22% (SunPower Corp).

The main sources of efficiency loss in all generations of solar cells are:

- Reflection of light from the surface (and back contact for thin film solar cells)
- Absorption losses within the material
- Thermal losses from high energy photons
- Carrier recombination and losses from the contacts

Reflection of light from the top surface of the cell causes losses in the efficiency of the device because a percentage of the incident photons with enough energy to create an electron hole pair in the solar cell are lost. Absorption losses within the material are due

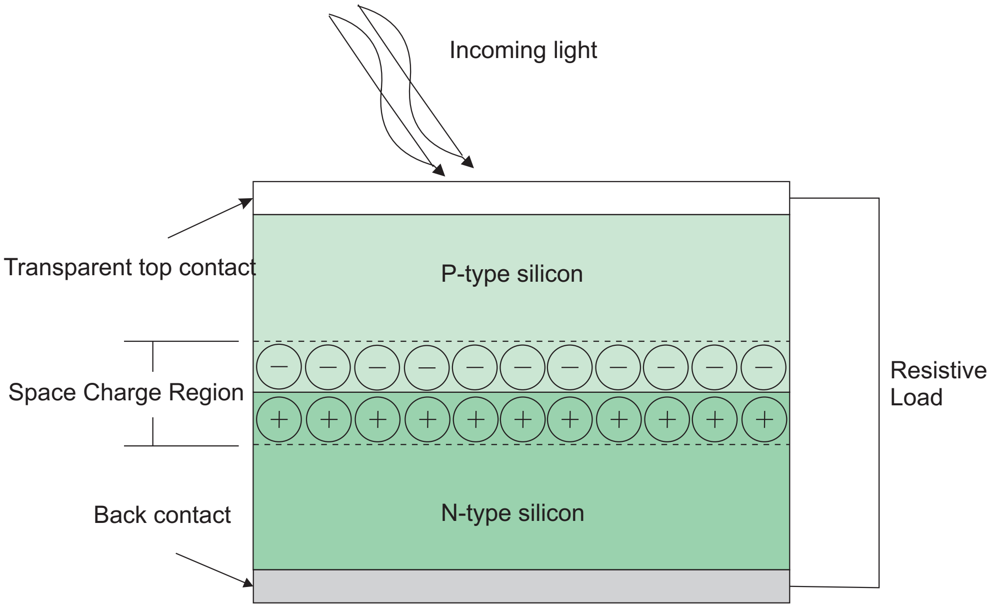

FIGURE 1.7: Schematic of operation of first-generation monocrystalline photovoltaic solar cell. Incoming light creates electron-hole carrier pairs in the space charge region which are separated due to the inbuilt electrical field that exists in this region. The charge carriers initially drift through the space charge region and and then travel through the bulk material towards the contacts. In the depicted configuration, the electrons drift downwards in the space charge region and then travel as majority carriers to the back contact. Inversely the holes get collected by the top transparent contact. When the two contacts are connected via a resistive load the extra carriers generated produce electrical current through the circuit.

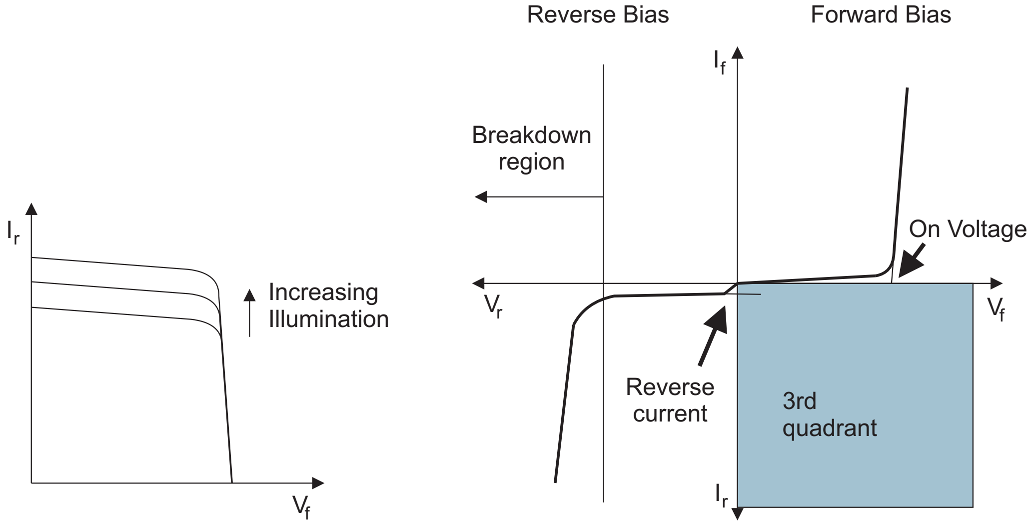

(a) The IV curve of a solar cell

(b) The current voltage graph of a normal PN diode or a solar cell without illumination

FIGURE 1.8: The IV curve of a solar cell is essentially the relationship between current and voltage in the third quadrant of a normal PN diode characteristic

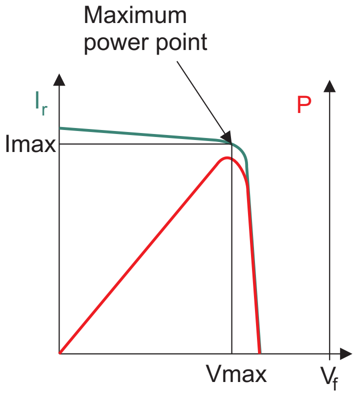

Figure 1.9: Maximum power that can be extracted from a solar cell for each illumination can be calculated from the IV curve

to the inability of the material to take advantage of the whole incident solar spectrum. This is due to the singular band gap properties of each material where photons with energy below the band gap do not interact with the material and hence are transmitted through it. Moreover, photons with energy above the band gap, which have more energy than required to create an electron-hole pair, waste their extra energy as heat. Finally, when a photon succeeds in creating an electron-hole pair, the charge carriers have to be efficiently extracted before it recombines in the crystal lattice.

1.2.2 Second generation photovoltaics

Second generation solar cells are based on thin film technology. Thin films are able to reduce the high costs involved in first generation solar cells by decreasing the amount of raw material used to produce the PN junction. The bulk single crystal silicon material in first generation cells is a major percentage of the total cost of the cell [11]. By making thinner solar cells grown on cheap substrates like glass, both the material and production costs are reduced.

Second generation photovoltaics can still be silicon-based PN junctions but they are not made from the standard thick single crystal silicon wafers used by the semiconductor industry. Rather, thin layers of silicon in amorphous and polycrystalline form are deposited on glass substrates at low temperatures and are made to cover larger areas with less cost. The basic material used is still silicon, but of inferior crystal quality (amorphous/polycrystalline), which means that the active layer possesses poorer electrical properties and increases carrier recombination losses. Poly-crystalline and especially amorphous cells also degrade faster than monocrystalline cells [12].

These devices suffer from similar energy loss mechanisms to those associated with first generation single crystal silicon solar cells during their operation because they are also single junction devices. However, in second generation solar cells there is an extra

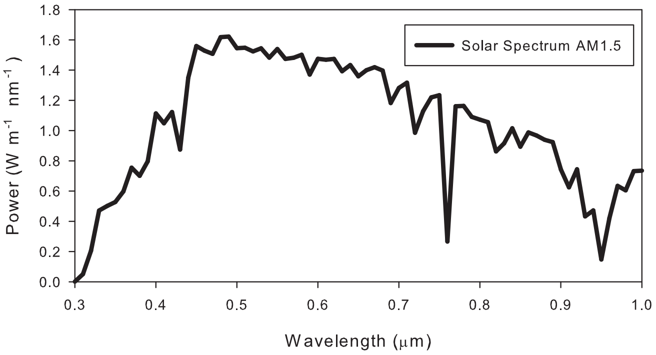

FIGURE 1.10: The Solar Power Spectrum for wavelengths between 300-1000nm after having passed through the atmosphere at a distance equivalent to 1.5 times the thickness of the atmosphere at the equator, also referred to the A.M. (Air Mass) 1.5 spectrum. [13]

issue arising from the fact that the thin films cannot absorb light efficiently due to the small thickness of the material (1-10μm). This however also depends on the absorption coefficient of the material used for the wavelength in question, which can be expressed via the Beer-Lambart law (Equation 1.1).

$$I = I_0 exp^{-\alpha L} \tag{1.1}$$

Where I is the intensity at a distance L within the absorption material, I_0 the incident intensity and α the absorption coefficient.

The short photon path that arises from the very small thickness of the active material affects the portion of photons that have energy closer to the band gap (i.e. longer wavelength) and do not remain in the cell for long enough for absorption to occur with one pass through the material. This is more important for materials like silicon which have an indirect band gap and not for other thin film materials that can be used such as CdTe which are direct band gap materials.

Thin film solar cells are thus also made of various other materials such as CIGS (Copper Indium Gallium di-Selenide), CIS (Copper Indium Selenide), CdS (Cadmium Selenide), CdTe (Cadmium Telluride). These materials are more suitable for creating thin film solar cells than silicon due to their larger absorption coefficients and thus can absorb light with very thin (1-10μ m) layers of material in a single PN junction design. Additionally their open circuit voltages are usually larger than silicon which allows them to achieve higher power conversion efficiencies with less photo-current so they do not need to absorb a wide wavelength spectrum. The band gaps for all these materials are of higher energy and absorb photons in the blue-green region near the the peak power of the solar spectrum (around 500nm, Figure 1.10).

For indirect band-gap materials such as silicon the situation can be improved by employing light trapping schemes. Light trapping schemes are used for converting more of the photons (normally not absorbed due to shallow active layer thickness of the thin film) to useful photocurrent by keeping them in the active material for as long as possible. The light is forced to travel further within the active material before it can escape, which increases its chances of absorption. Various light trapping schemes are based on increasing light scattering at the back or front contact, so that the photons are directed in oblique angles and guided by total internal reflection in the active material. Future light trapping schemes might employ plasmonics to scatter incoming radiation on the top contact, so that the photons enter the material at a high angle of incidence to and are again trapped by total internal reflection.

Despite the disadvantages of second generation devices, which don't allow them to reach similar efficiencies to first generation solar cells, their production cost is much cheaper and could possibly yield an overall improved power vs. cost ratio. It is therefore expected that the majority of the mass production solar cell industry will switch to second generation cells because of the overall benefit that is achieved in terms of the cost of the energy produced.

However, this does not mean that there will cease to be a market for single crystal solar cells, first generation devices will still be preferred where installation space needs to be minimized and a long cell lifetime is required such as in large scale power utility installations and residential rooftops. Additionally, the price of the panel depends heavily on the price of the silicon wafer as was previously noted, in recent years demand has decreased so the price of the wafers available has also decreased and the panel price of first generation solar cells is becoming very competitive with that of thin film technology.

1.2.3 3rd generation photovoltaics

Third generation solar cells also use PN junction devices for producing photo-current as in the two previous solar cell generations, but employ photon management techniques and use combinations of different materials to improve the efficiency of the device by making better use of the solar spectrum [11]. An important source of photon loss in the previous generations of solar cells is the fact that a single material cannot absorb the whole solar spectrum of light efficiently.

The most common method of mitigating the single material/band gap problem is by stacking multiple PN junctions made from different materials within the cell. These types of multi-band-gap cells are also called tandem cells and they are typically made so that the material with the largest band gap, which absorbs the photon with the shortest wavelength, is topmost on the cell, closer to the illuminated surface. The material PN junctions are stacked in such a way that their band gaps decrease in size the deeper one goes into the cell. This order is also preferred because the absorption depths required for higher energy photons is smaller than that of lower energy photons in any given material. Additionally materials with large band gaps are transparent to photons that are of lower energy. Hence, by stacking the band gaps in terms of decreasing energy, optimization of the energy absorption can take place reaching theoretical efficiencies of up to 60% [14]. The more band gaps incorporated in a single device the larger the spectrum of photons with different energies that can be efficiently absorbed. Hence, the total amount of electron hole pairs created will be higher than a single band gap material would allow. This concept is usually implemented in very high efficiency solar cells for space applications where cost is not as much of an issue as is efficiency and size/weight, and in concentrator cells where maximum power output is required when concentrating 200 suns of solar energy on a small cell area.

Another method of photon management is the creation of multiple electron-hole pairs per incident high-energy photon (whilst satisfying the conservation of energy) by either seeking to enhance the concept of impact ionization [15] or Raman luminescence [16].

Finally, it is also suggested to take advantage of hot carrier effects, where the sun's energy is converted to photo-excited carriers which are collected before they can loose energy by 'thermalising' (i.e. releasing their energy by colliding with the surrounding lattice [17]).

Third generation solar cells are always likely to be expensive to manufacture because they involve a large number of usually expensive materials such as Indium and Gallium. Another problem with this technology is its poor electrical performance because of the multiple PN junction device structure. Every layer has to be closely matched to the previous layer in terms of lattice structure so that any dangling bonds at the material interfaces are minimized because they operate as trap states for current flow through the active layer. Finally, when multiple PN junctions are stacked in series they need to be current matched to the incident spectrum, that is, the number of carriers created at each junction per unit time should be similar in order to avoid loss of current. This is easy to understand if we represent each PN junction as an equivalent current source and connect them all in series. The maximum current through the system is determined by the source with the lowest value. The fact that these cells need to be current matched to the incident spectrum does not allow them to reach their full potential when used in terrestrial applications because the solar spectrum on the surface of the earth is variable. However, an overall greater efficiency can be achieved with these devices, compared to that of single-junction solar cells.

1.2.4 Conclusions

Solar cell technology has the potential of providing the world with the ability to tap a very clean, abundant and independent source of energy. For this to happen, solar cell technology has to become directly competitive with existing energy production methods as far as the cost per watt of produced energy is concerned throughout the whole lifetime of the cell. One way of doing this is to increase the efficiency of the cell without significantly increasing the production cost. A substantial source for loss of efficiency in a solar cell is Fresnel reflection of the light on the top surface. In this thesis the reduction of Fresnel reflection from monocrystalline silicon is investigated by applying a biomimetic metamaterial layer.

Chapter 2

Literature review

A review of the anti-reflection technologies that are currently available for optical applications is presented in this chapter. The methods that are analysed can be divided into three main categories:

- Thin film anti-reflective layers
- Surface texturing and light trapping
- Sub-wavelength surface texturing

2.1 Thin film antireflection layers

At every optical interface where a change of refractive index exists the propagation of a electromagnetic wave is altered. In the case where there is a positive change in refractive index there is a reflected and a refracted beam (Figure 2.1). In the case where the difference in refractive index between the two media is negative, we again observe a reflected and refracted beam unless the angle of incidence is larger than that required for total internal reflection, in which case, the beam remains in the material of higher refractive index via reflection.

When considering reducing optical reflection in real world applications, the most common situation that is encountered is the shift from low to high refractive index (usually from air to another medium). In this case, according to the law of reflection (Equation 2.1) part of the incoming beam is reflected back at an angle similar to that of the angle of incidence and part of it is refracted in transmission according to Snell's law of refraction (Equation 2.2).

$$\theta_i = \theta r \tag{2.1}$$

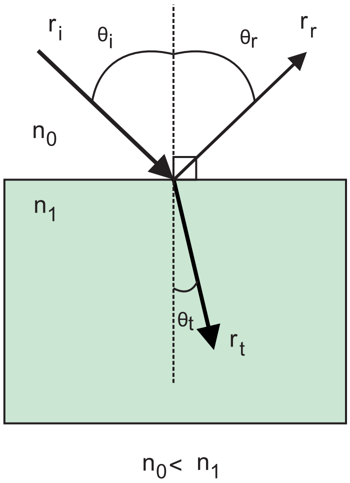

FIGURE 2.1: Law of reflection and refraction at an abrupt interface with light travelling from a material of low refractive index ($n_(0)$) to a material of high refractive index (n_1). The reflected angle (θ_r) is the same as the angle of incidence (θ_i) whereas the angle of transmission (or refraction) through the material (θ_t) is reduced compared to the angle of incidence (θ_i).

$$n_0 sin(\theta_i) = n_1 sin(\theta_t) \tag{2.2}$$

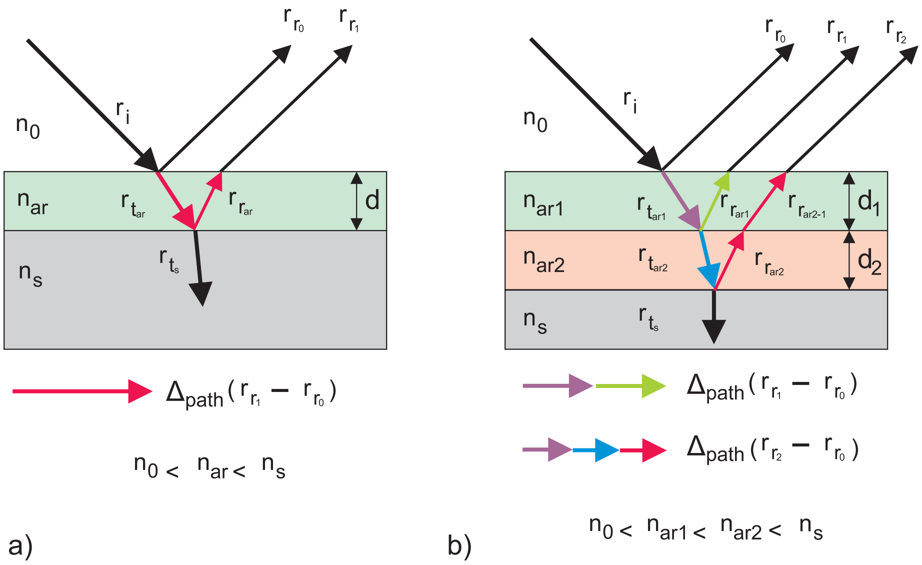

FIGURE 2.2: Destructive interference in single and double antireflection coatings showing the different path differences experienced by the various reflected beams. For the single antireflected layer, the path difference between reflected beams r_{r0} and r_{r1} is coloured in red whereas for a double antireflection layer the path differences between r_{r0}, r_{r1} and r_{r2} are coloured individually.

Single- and multiple-layer anti-reflective coating (ARC) technologies operate on the principle of destructive interference between two abrupt interfaces to reduce reflection. When two interfaces are very close to each other, such as in the two sides of a thin film on a substrate, the power of the reflected beam from the inner surface is enough to propagate back out of the cell without significant absorption (Figure 2.3). Following the laws of reflection and refraction all the way through for the second reflected beam r_{r_1}, it can be shown that the angle of refraction is identical to that of the initial reflected beam r_{r0}. Their superposition creates interference because of the path difference between the two rays (Figure 2.3 - red vectors).

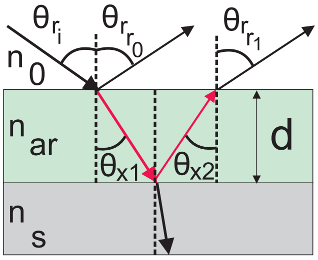

FIGURE 2.3: Comparison of reflection angles for rays with phase difference in thin layer ARC. To prove that the angle ($\theta_{r_{r1}}$) at which the second ray emanates from the thin film is identical to the angle ($\theta_{r_{r0}}$) of the reflected ray we trace the ray through the film applying Snell's law of refraction for the n_0 / n_{ar} interface and the law of reflection at the n_{ar} / n_s interface.

$$n_{air} sin\theta_{r_i} = n_{ar} sin\theta_{x_1} \tag{2.3}$$

$$\theta_{x_1} = \theta_{x_2} \tag{2.4}$$

$$n_{ar} sin\theta_{x_2} = n_{air} sin\theta_{r_{r_1}} \tag{2.5}$$

Combining equations 2.3 to 2.5:

$$\theta_{r_i} = \theta_{r_{r_1}} \tag{2.6}$$

The aim in single layer ARC technology is to coat the surface with a particular layer which has a specific refractive index (n_{ar}) and thickness (d) so that the optical path difference created between the two beams is $\lambda/2$, or at least an odd multiple of $\lambda/2$: $3\lambda/2$, $5\lambda/2$ etc. (Figure 2.2a). If this condition is satisfied, the superposition of the two reflected beams results in destructive interference for the desired wavelength. The explanation for this is that the path difference of an odd multiple of $\lambda/2$ between the two beams r_{r_0} and r_{r_1} will create an equivalent phase difference of π in their waveforms and hence their superposition will be destructive thus reducing the total reflection from the surface for this wavelength.

The wavelength for which the layer is tuned to is reduced in reflection the most. The effect also partially covers a band of nearby wavelengths. A typical wavelength dependence of the reflectance for such single films is shown in Figure 2.4. For visible spectrum applications, the wavelength that is usually reduced the most is in the middle of the visible spectrum around 550nm. Such applications can be found in optical lens systems such as cameras, telescopes and eyesight correction lenses. The material usually used to coat glass with a single thin film for visible spectrum antireflection is MgF_2 because of its cheap price and its good adhesion properties[18].

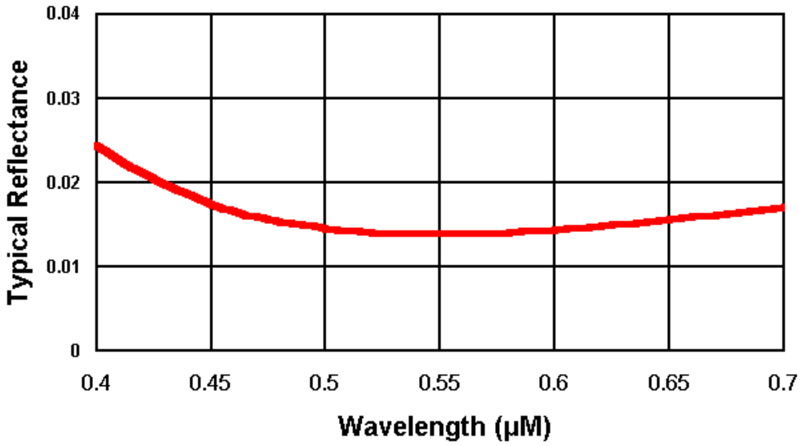

Figure 2.4: Reflection of a aingle layer MgF_2 antireflection coating on glass for the visible spectrum. (Central wavelength layer was designed for: 550nm, refractive index of $MgF_2 = 1.384$, Substrate: glass) [18]

ARC technology allows two or more layers to be developed in an attempt to reduce reflection of multiple frequencies of incoming light via adding more path/phase differences in the design and improving performance (Figure2.2b). A typical wavelength dependence of the reflectance of a bi-layer operating in the visible spectrum can be found in Figure 2.5. The materials usually used in multilayer thin films are a combination of MgF_2, SiO_2, Y_2O_3 and Al_2O_3 [19] [20]. In general, ARC benefits from easy deployment and cheap production whilst giving acceptable results for most commercial applications and can achieve low reflectance (<0.5%) for only a narrow bandwidth ($\sim$ 200nm).

One of the limitations of this technology is the difficulty in finding materials with refractive indices that are suitable for all applications. The material not only has to have the required refractive index but also needs to bond very well with the surface it is applied to and similarly bond well with the other anti-reflective layers in the case of a multi-layered structure. Hence, finding or creating materials that will possess these properties is generally difficult since such materials may not exist in nature, or their production may be complicated and expensive in a multi-layer system. In general it is difficult to find commercial ARC's with more than two layers and, considering that each

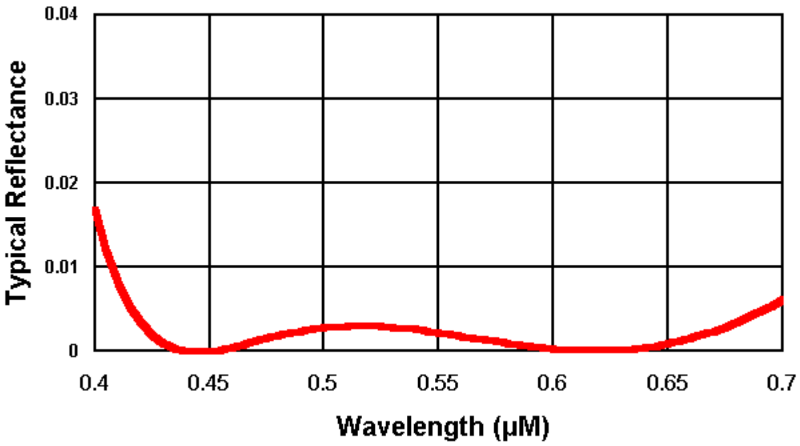

FIGURE 2.5: Reflectance of a double layer antireflection coating on glass for the visible spectrum (Central wavelength the two layers were designed for: 450nm and 600nm, Substrate: glass) showing improved performance and operating bandwidth compared a single antireflection layer solution designed for the same spectral range Figure 2.4 [18]

layer operates efficiently in a relatively narrow bandwidth, broadband applications are not efficiently facilitated using this kind of technology.

Nevertheless, ARC technology has come a long way in increasing efficiency and decreasing product cost which makes it a successful choice in many cheap commercial applications including solar cells. Optimization of the layers is necessary to achieve maximum performance for the desired application [21].

2.2 Supra-wavelength surface texturing used for antireflection

Supra-wavelength surface texturing refers to the process of texturing a surface on a scale large enough so that it is perceived by the incoming photon as a morphological structure. In supra-wavelength texturing there are two main techniques used to reduce reflection. The first is texturing the surface such as to direct the reflection from the surface so that it strikes the substrate multiple times. This increases the absorption in the substrate because with every successive reflection, the beam is reduced in power by an extra amount and depending on the number of reflections that take place, the beam reduced in power proportionally.

Another technique used in supra-wavelength surface texturing focuses on increasing the surface roughness to scatter the reflected and refracted beam into oblique angles. This second technique does not involve an equal increase of transmission but does reduce the specular reflection by redistributing the power into scattered reflected beams. This increases haze and provides an alternative stealth technology [22].

2.2.1 Top surface texturing

In the case of supra-wavelength texturing the top surface, the antireflection schemes used are based on geometric optical designs that give the incoming light beam more opportunities to be absorbed by the cell via multiple reflections. When this technique is applied to the front layer of photonic devices such as solar cells, the incoming beam gets weaker with every additional reflection on the surface and by the time it escapes away from the surface it has lost much more energy than if it had reflected on the surface only once (Figure 2.6). This increases absorption and reduces the reflection from the top surface. The first efficient approach of this type was the Comsat non-reflecting cell or 'black' solar cell (Figure 2.7b) which took advantage of the differing etch rates between the (100) and (111) silicon crystal planes to create a native pyramid structure in the active layer [23].

This concept was also employed in the record breaking PESC (passivated emitter solar cell) and more substantially in the PERL (passivated emitter, rear locally-diffused) solar cell design (Figure 2.7a) both created by researchers in the UNSW (University of New South Wales) where an inverse pyramid structure was employed to reach efficiencies of 24% for the first time [24].

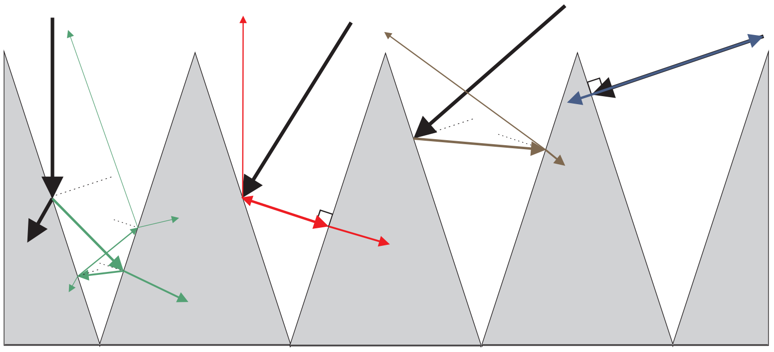

Figure 2.6: Cross-section of the corrugated inverted pyramid structure and the optical path for the reflected beam at different angles of incidence.

Top surface supra-wavelength roughening is also used by commercial glass manufacturers such as Asahi Glass which are developing very low reflectance glass superstrata for use in amorphous silicon solar cells [25].

2.2.2 Back surface texturing

In order to reduce manufacturing costs whilst retaining device efficiencies as high as possible, reducing the device thickness is highly desirable. This is especially important in solar cell production where the cost of the material accounts for most of the total cost of the solar panel. The main problem that is faced when the device thickness becomes so small that reflection from the back contact becomes significant (Figure 2.8a), especially when the thickness of the device is much smaller than the absorption length required.

In this case, back-surface diffuse reflectors are employed by utilizing geometrical concepts similar to those presented for top surface scattering of incident light. In the case of texturing the back contacts, the goal is to reflect the incident light at oblique angles so that it can be trapped in the active layer. The collection of techniques used to introduce roughening in order to favour oblique angle scattering (preferably into angles that create total internal reflection so that the photon gets trapped in the device for longer than usual) are known as "light trapping" techniques (Figure 2.8b).

Keeping the photons within the cell as long as possible results in an increase of absorption for the longer wavelengths of the incident spectrum which in turn increases the overall efficiency of the device. The main figure of merit in these cases is the path enhancement factor Z (i.e. the factor by which the effective width of the material has "increased"). This effective increase of the thickness of the material is a measure of the optical path length that the photon 'experiences' before escaping the cell. Thus, the higher the path enhancement factor, the better the performance of the system, since the chance of the photon being absorbed is increased. It is desirable to increase the path enhancement factor so that the typical path length that the lower energy photons have to travel in the device before escaping is equal to their average absorption length and hence have much higher chances of getting absorbed. There are multiple definitions for the optical path length enhancement factor but a more practical approach has been recently developed for silicon solar cells by Abenante [26].

The concept of reducing reflection by scattering the reflected light into oblique angles which are far from that of the zero order (or specular reflection) is also applied in 'stealth' applications where reducing total hemispherical reflectance from a surface is not as of much importance as reducing specular reflectance. For instance, stealth technology is widely used in the design of military aircraft such as the B-2, F-117 and F-22 [27]. Their fuselage is designed in such a way so that electromagnetic radiation from RA.D.A.R (Radio Detection And Ranging) tracking systems reflects at angles which are non-specular, so that the radar detector cannot trace them easily. This stealth design, in combination with the use of radar radiation absorbing material, creates a smaller radar cross-section (i.e. the magnitude of radar reflection vs angle of incidence on the aircraft [28]).

---

[1] http://benfoden.com/wp-content/uploads/2009/09/F-117_Nighthawk_Front.jpg

[2] http://www.howstuffworks.com/question69.htm

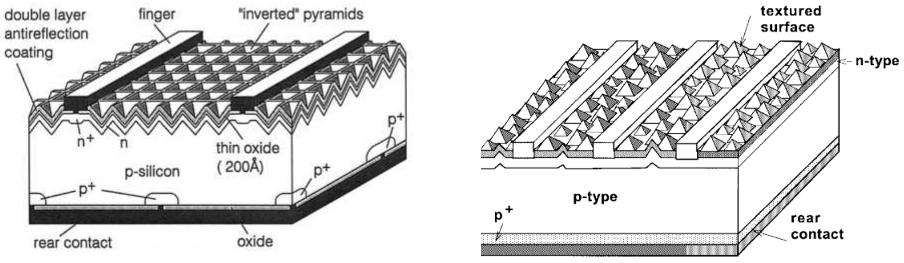

(a) (b)

FIGURE 2.7: (a) The record breaking PERL cell with an inverted pyramid light trapping structure on the top of the cell [10], and (b) the Comsat cell [24]

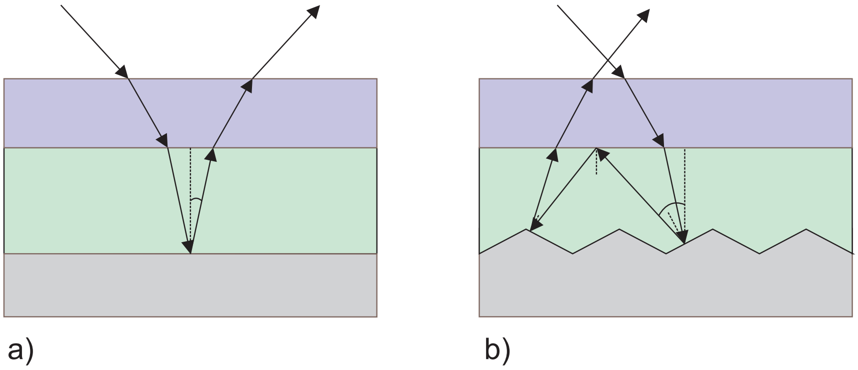

FIGURE 2.8: Difference of optical paths in (a) a normal planar multilayer and (b) with a light trapping back surface

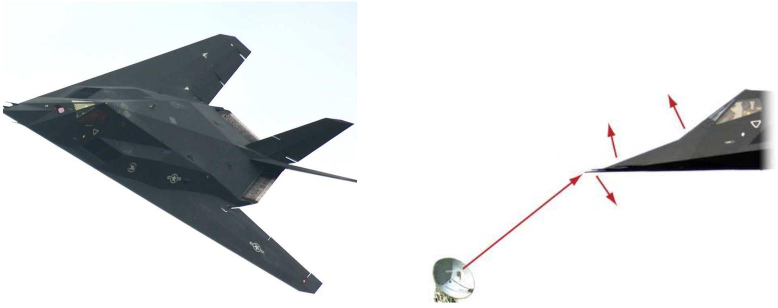

(a) (b)

FIGURE 2.9: (a) The F117 "Nighthawk" [1] and (b) a schematic of the way its stealth design deflects the reflection of the radar beam away from the direction of the radar to avoid detection[2]

2.3 Sub-wavelength surface texturing

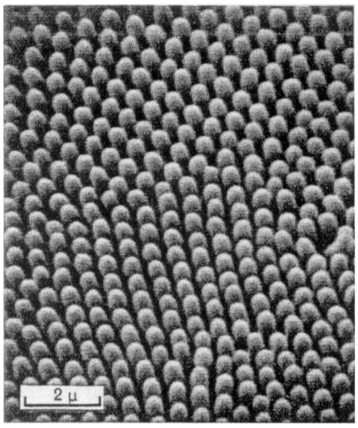

Figure 2.10: SEM Image of sub-wavelength protuberances on a moth's eye. The features on a moth-eye provide effective antireflection for a broad range of angles of incidence and a wide wavelength spectrum. For the moth eye shown, the period and height of these features are around 220nm and are optimized to provide antireflection for a wavelength range of 440-550nm. [29]

.

The so called "moth-eye" antireflection principle is a type of metamaterial layer that provides anti-reflection by sub-wavelength surface texturing. The textured surface is made up of features that are sub-wavelength in size to that of the wavelength of the incident light. This type of layer is referred to as a "moth-eye" anti-reflection surface in recognition of their discovery on the cornea of a moth's eye (Figure 2.10) by Bernhard [29]. The design rules for engineering a 'moth-eye' surface to a given wavelength spectrum were first outlined in the work of Caplam and Hutley [30].

Sub-wavelength texturing of materials is a more subtle and biomimetic approach to creating antireflection than long range surface texturing. The principle used is similar to that of anechoic chambers for microwaves and acoustics. Applying texturing on a small enough scale to achieve sub-wavelength antireflection for the visible spectrum is now possible due to the availability of advanced nanoengineering processes like e-beam lithography. The wavelengths of the visible spectrum (400-700nm) are an order larger than the features that can be produced by e-beam lithography ($\sim$ 20nm), a crucial requirement in creating sub-wavelength textures.

The ability to texture a material on a scale that is smaller than the wavelength of incident light enables greater control of the optical properties of the interface, by effectively inserting a metamaterial layer between two media. When the features of the structure are smaller than the wavelength of the incident light, they can be perceived as an effective medium which has a refractive index between that of the air and silicon. Depending on the period and size of the feature, a layer with an effective refractive index can be created. The value of the effective refractive index can be any value between that of the two media [22].

‘Effective multi-layer’ and ‘effective gradient index’ regions can also be formed by controlling the shape and profile of the sub-wavelength features. Almost any gradient can be provided by controlling the profile of the features. For instance, a linear gradient can be produced via a conical profile (Figure 2.11)

One of the main advantages of sub-wavelength texturing is that the ’effective’ refractive index of the interface can be essentially tuned to any intermediate singular value between that of the two media at the interface by changing the spacing period, depth and profile of the nanostructures. Hence the structure of the interface can be chosen in such a way as to optimize the optical response of the layer for any given application [31].

Another crucial advantage of sub-wavelength texturing compared to the other two methods described (thin film layer anti-reflectance and macroscale texturing) is that sub-wavelength surfaces can work for a broader spectrum and wider angle of incidence.

Studies on creating an optimum refractive index gradient and the corresponding surface relief feature profile required to produce a broadband ’moth-eye’ antireflection layer have been carried out by Southwell [32] [33]. It was shown that a near-optimum antireflective performance can be achieved in the visible spectrum between two dielectric media when the refractive index varies according to a quintic polynomial as depth is increased [32].

The quintic equation makes the refractive index and its second derivative continuous [32]. The quintic change in refractive index through the layer is defined by equation 2.7. It has shown to improve performance of the antireflection layer compared to a linear graded index (Equation 2.8).

$$n_{eq} = n_i + (n_s - n_i)(10t^3 - 15t^4 + 6t^5) \tag{2.7}$$

$$n_{eq} = n_i + (n_s - n_i)t \tag{2.8}$$

Where n_{eq} is the effective refractive index, t is the depth of the antireflection layer, n_i the refractive index in air, n_s the refractive index in silicon.

Texturing a large surface, such as a whole silicon wafer, with nano-scale sub-wavelength features via e-beam lithography is tremendously time consuming and expensive. However, there are some new scalable technologies which are based on e-beam technology such as nano-imprinting which are promising and have the capability of accelerating the texturing process and bringing down the cost but these also have limitations which will be discussed in following chapters.

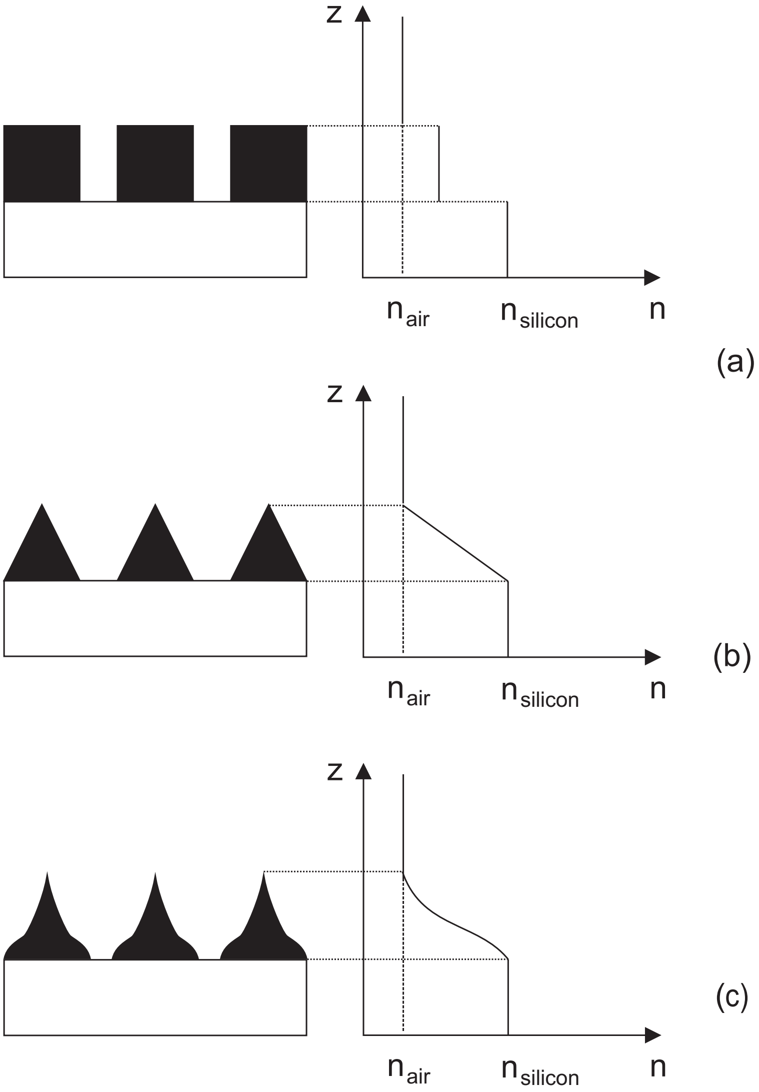

FIGURE 2.11: Effect of moth eye shape on refractive index gradient (a) a zero step gradient is equivalent to placing a material with the same thickness and an intermediate refractive index between the two media (b) linear gradient is equivalent to placing a layer with a linearly graded refractive index which starts from the refractive index of air and ends up to the refractive index of silicon (c) a quintic gradient has a similar effect to (b) with the exception that the refractive index gradient is not linear between the two media

Some studies on optimizing the period for these structures have been carried out by Boden et. al. [31]. In this work, sub-wavelength texturing will be employed to create features that are antireflective and optimized to a maximally broadband spectrum and angle of incidence. A case study of applying and optimizing these layers to solar cell applications has also been carried out.

2.4 Methods of manufacturing nanostructures for supra- and sub-wavelength texturing on silicon

In this section nano-manufacturing methods described in the literature for texturing silicon for antireflection purposes will be examined. Although the substrate most commonly considered is silicon, similar concepts are applicable to all kinds of substrates. There is a variety of information in the literature on etching silicon and texturing surfaces, the main procedures available will be outlined in the following sections.

2.4.1 Anisotropic alkali etching

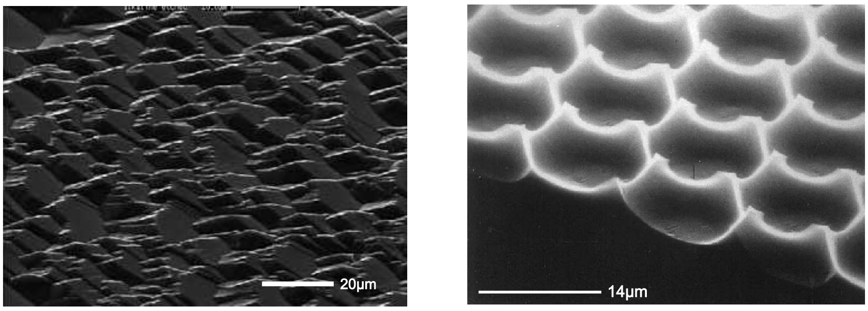

(a) From [34]

(b) From [35]. Hemispherical 'wells' are 14μm apart.

Figure 2.12: Examples of alkali etched silicon surfaces etched with an (a) unmasked and (b) masked procedure. It is noticed that the unmasked procedure does not achieve texturing of the surface rather a very flat polished surface is achieved on multicrystalline silicon. The masked procedure can provide texturing of multicrystalline silicon and the resultant pattern is a 'honeycomb' lattice.

Anisotropic alkali etching (NaOH, KOH etc) has been very successful in creating textured surfaces for light trapping and antireflection on the top and bottom surfaces of device layers. The first such antireflection scheme used for solar cells (the 'COMSAT' cell [24]) used alkali etching to create the morphological structure required to enhance antireflection of silicon substrates. Furthermore, structures such as the 'honeycomb' lattice [35] and the commonly used inverted pyramids with organized [23],[24] or random [36],[37],[34] topologies have been demonstrated.

Another technique using alkali etching is the porous-silicon (PSi) process. A thick alkali-etched silicon substrate is formed as a template for thin film crystalline silicon growth. The technique has demonstrated the ability to address the structural problems in using alkali texturing for very thin devices. In this process, silicon is epitaxially grown on a porous substrate which resides on a master silicon substrate previously textured with inverted pyramids via alkali etching. The porous silicon is then removed and the textured layer is bonded to a super-strate creating a material with a thin corrugated top and bottom layer. The topology of the inverted pyramids can be both in regular [38] and random arrangements [39]. The efficiency of a 15.5μm thick device is around 12.2% for the random textured method [39]. However the silicon epitaxial growth step required in this procedure makes manufacturing very expensive.

The change in optical behavior from the supra-wavelength to the sub-wavelength region is demonstrated by using the same alkali process described previously at a different length scale. Sub-wavelength features can also be created via alkali etching. Sun et al. [40] report that scaling down the classic supra-wavelength 'inverted pyramid' structures (Figure 2.6) to the sub-wavelength optical scale (Figure 2.13), results in altering the behavior of the interface from a rough morphological surface to an equivalent graded-index antireflection layer.

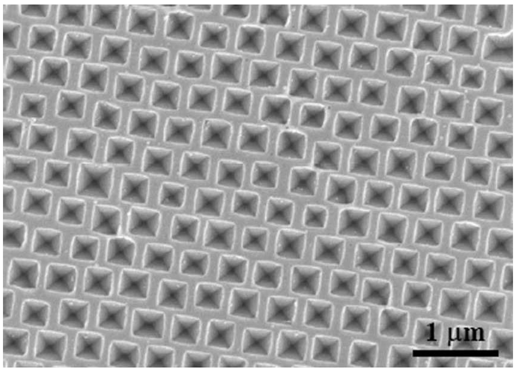

FIGURE 2.13: Inverted pyramids in the sub-wavelength 1μm region. 360nm-deep pyramids spaced 320nm apart were etched via KOH (mixture temperature: 60^o,time: 210seconds) through a chromium mask on a silicon substrate. The chromium mask was patterned by nanosphere lithography of 320nm silica spheres which were spin coated on the wafer. From [40].

The main disadvantage of using alkali etchants is that they contaminate the silicon layer after the process is finished. An anisotropic silicon-wafer-friendly process was recently shown by Papet et al [41] containing TMAH (TetraMethyl Ammonium Hydroxide) instead of classic alkali etchants. TMAH does not pollute the silicon wafer with contaminants after the process and a measured reflectance reduction (compared to an untextured flat silicon substrate) of 13% was achieved [41]. Figure 2.14 summarizes the reflectance results achieved by the work described in this section.

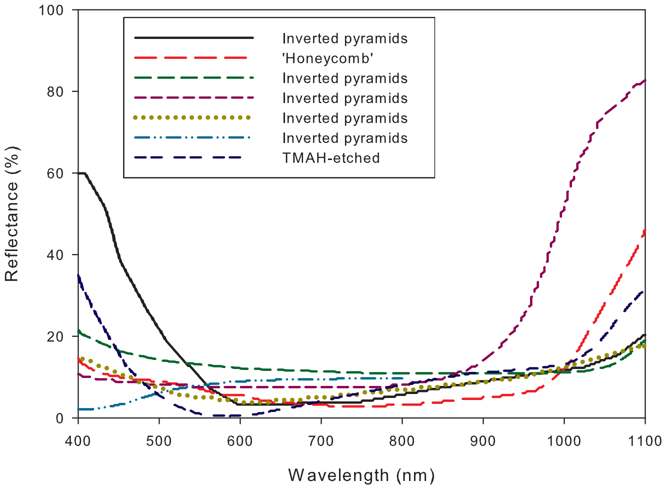

Figure 2.14: Comparison of the performance of antireflective structures created by alkali etching in the literature presented by MacDonald [34] (Inverted Pyramids, black line, SEM Image of structure shown in Figure 2.12a), Zhao [35] ('Honeycomb',SEM Image of structure shown in Figure 2.12b), King [36] (Inverted Pyramids, green dotted line on graph, created by dipping wafers in a mixture which was heated at 70^{o}C for 30 minutes with 1.5% KOH, 3.8% IPA), Brendel [38] (Inverted Pyramids, purple dotted line, was patterned with photolithography to a square pattern with a 13μm period followed by a KOH to create inverted pyramids on the substrate), Brendel[39] (Inverted Pyramids, olive dotted line, a random inverted pyramids were created on a silicon substrate using a KOH etch), Sun [40] (Inverted Pyramids, light blue dotted line, Shown in Figure 2.13) and Papet [41] (TMAH etched, dark blue dotted line, (2% TMAH, 8% IPA, 80^{o}C for 30 min))

2.4.2 Acidic etching

Acidic etching of silicon usually consists of the use of HF/HNO_3 in combination with a substance used to buffer the reaction, usually H_3PO_4. Phosphoric acid acts as a buffer to prevent overheating the mixture. There are two steps in the process, firstly silicon is oxidized by HNO_3 followed by the dissolution of the oxidized Si layer by HF.

The overall reaction of the HF-HNO_3 system is as follows [42]:

$$3Si + 4HNO_3 + 18HF = 3H_2SiF_6 + 4NO + 8H_2O \tag{2.9}$$

Stocks et al [43] have used this process to manufacture light trapping structures such as hemispherical 'tubs' created by initially pre-patterning the surface via photolithography with an array of holes 4μm in diameter, 10μm apart followed by a subsequent isotropic acid etch $(HF/HNO_3/H_3PO_4)$.

Nishimoto et al [44] have demonstrated top surface antireflection schemes used in multicrystalline solar cells by a similar acid etch method. Acidic etching was used instead of alkali mixtures because in multicrystalline silicon various orientations of the lattice exist on the surface, each of which have a different sensitivity to the alkali etch. If an alkali etchant was to be used, its anisotropic nature would etch some surface orientations faster than others, creating an inhomogeneous etch which would not be useful for the device design.

Tsujino et al [45] have used silver and platinum particles in an acidic etch environment to create a microporous layer on the silicon substrate. Their method yielded a reflectance 10% lower than the NaOH alkaline method they compared it to.

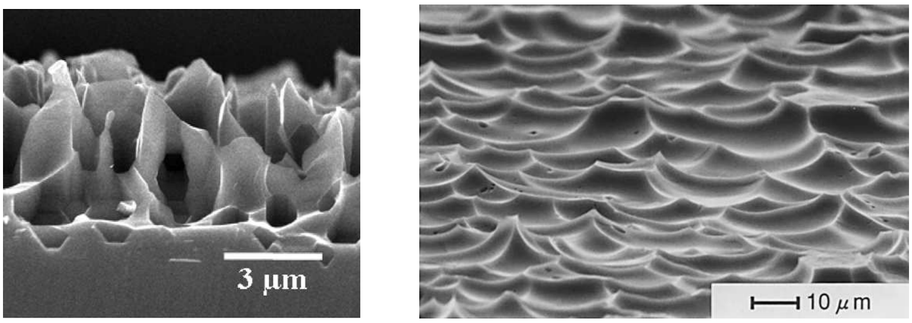

(a) From [45] (b) From [44]

Figure 2.15: Random acid surface texturization used in (a) light trapping (Substrate was a (100)-orientation monocrystalline silicon wafer and silver nanoparticles were used as a catalyst for the reaction. (Silver nanoparticles were loaded by immersing the wafer in 10^{-4}M $AgClO_4$ and 10^{-3}M NaOH for 20 min, the acidic etching process was accomplished by placing the silicon wafer for in 10% HF: 30% H_2O_2 (10:1) for 5minutes). and (b) antireflection schemes respectively (The substrate was a multicrystalline silicon wafer, no metallic catalysts were used, the multicrystalline wafers were dipped in a 46% HF : 69 % HNO_3 (12:1) solution)

Koynov et al [46] have successfully used a metal gold mask along with an subsequent acid etch (HF:H_2O_2:H_2O)to texture single crystal, multicrystalline and amorphous substrates with a random topography of sub-wavelength pillars 200-300 nm in height and 50-100nm in diameter. The gold clusters have a catalytic effect to the process which normally etches the silicon at a rate of 1nm/min. In the presence of the gold particles, random pillars of up to 167nm in height were observed in the same time. Figure 2.16 summarizes the reflectance results achieved by the work described in this section.

2.4.3 Mechanical and laser grooving

Mechanical and laser texturing methods are also useful for texturing multicrystalline solar cells and replace chemical techniques such as alkali etching, which produces considerable damage and deepens the grain boundaries present on the surface. By deepening the grain boundaries, more dangling surface bonds are present in the system. These free bonds act as trap states for the propagation of charge carriers through the device and reduce the carrier mobilities and device efficiency.

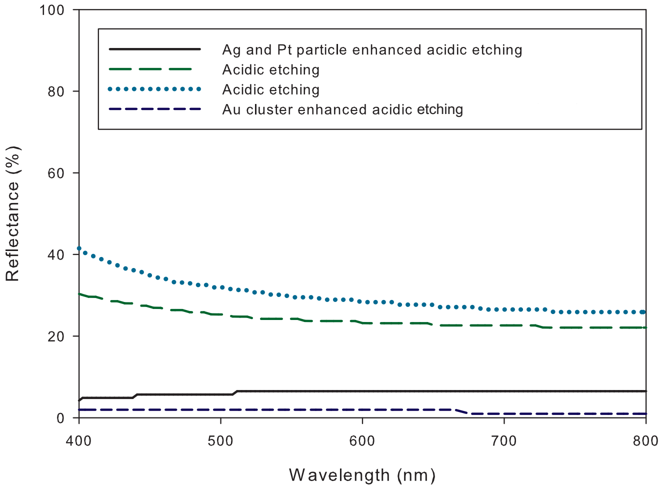

Figure 2.16: Comparison of the performance of antireflective structures presented in the literature by Tsujino [45] (Created via Ag and Pt particle enhanced acidic etching, sample of Figure 2.15a), Nishimoto [44] (Created via Acidic Etching, green dotted line,sample of Figure 2.15b), An [42] (Created via Acidic etching, light blue dotted line, etch used was a HF/HNO_3/H_2O) and Konyov [46] (Created via Au cluster enhanced acidic etching,HF(50%) : H_2O_2(30%):H_2O=1:5:10) all created via acidic etching.

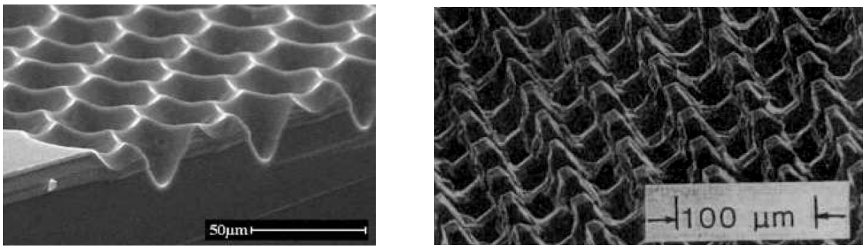

(a) From [47]

(b) From [48]

Figure 2.17: (a) Inverse pyramid structure. To create the 40μm-period close-packed holes structure a Q-switched, Nd:YAG laser at a wavelength of 1064 nm was used, followed by a damage removal etch (NaOH (25%): deionized water (75%) for 3 min at 40^{o}C) and an isotropic etch (Nitric acid (70%): Acetic Acid (99%): HF (49%) 30:10:4 for 3 min with constant manual agitation) to remove ablation damage and (b) normal pyramid structure created by laser grooving (A 40μm-wide cross-hatched laser beam on a 70μm pitch was grooved in a monocrystalline silicon wafer, followed by a 15 minute etch in 12% KOH at 52C and a 15-second etch in 1:20, HF:HNO_3.)

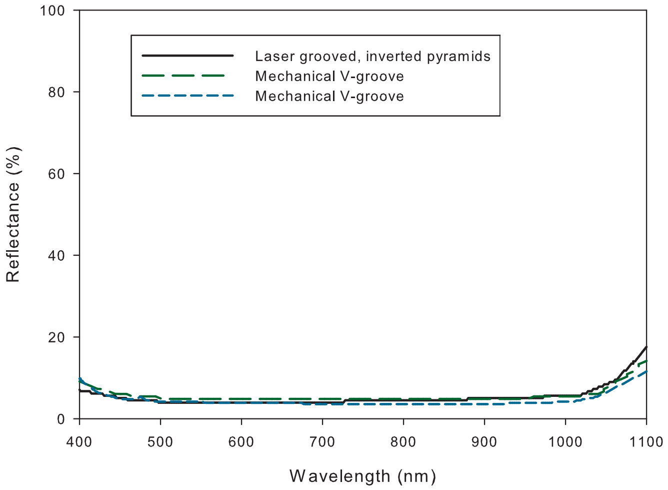

FIGURE 2.18: Comparison of the performance of antireflective structures presented in the literature by Abbott [47] (Shown in Figure 2.17a), Bender [49] (The grooves were 80μm in depth and they were applied on a 120μm pitch, the saw damage was subsequently removed with a 20 minute HF(50%) : HNO_3 (65%) :CH_3COOH(96%), and Nakaya [50] (The grooves were 70μm in depth and they were on a 70μm pitch, the saw damage was removed with a 5 minute 3% NaOH etch.) all created via mechanical and laser grooving.

Mechanical and laser grooving use a mechanical saw or a laser respectively to create supra-wavelength surface features which are corrugated and provide antireflection. Laser grooving has been shown to produce ordered pyramid structures [48] as well as inverted pyramids [47] whilst mechanical grooving has produced one dimensional V-groove shapes [49] [50] Figure 2.18 summarizes the reflectance results achieved by the work described in this section.

2.4.4 Reactive Ion Etching (RIE)

The RIE procedure uses a combination of fluorine containing gases (SF_6, CHF_3) to etch silicon substrates in an isotropic manner. RIE texturing is usually more useful when applied to multicrystalline silicon substrates because it is independent of silicon orientation and thus affects the whole surface in the same way. Ruby et al have developed a maskless RIE texturing procedure for multicrystalline solar cells which creates a randomized relief texture on the surface [51]. Nositscha et al [52] later demonstrated a silica nanosphere template RIE etching procedure which allowed the controlled etch of the substrate to form pillars of set height and width. They report an increased internal quantum efficiency (IQE) as the chemical etch progresses, as well as significantly increased antireflection properties compared to untextured silicon passivated with a SiN antireflection layer.

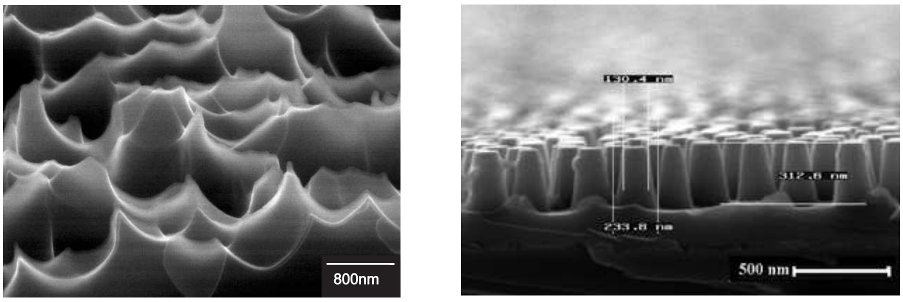

(a) From [51]

(b) From [52]

Figure 2.19: (a)Maskless moncrystalline RIE silicon surface texturing using SF_6/O_2 gas mix and (b)masked monocrystalline RIE silicon surface texturing using a SF_6/O_2 gas mix and 250nm SiO_2 colloid particles

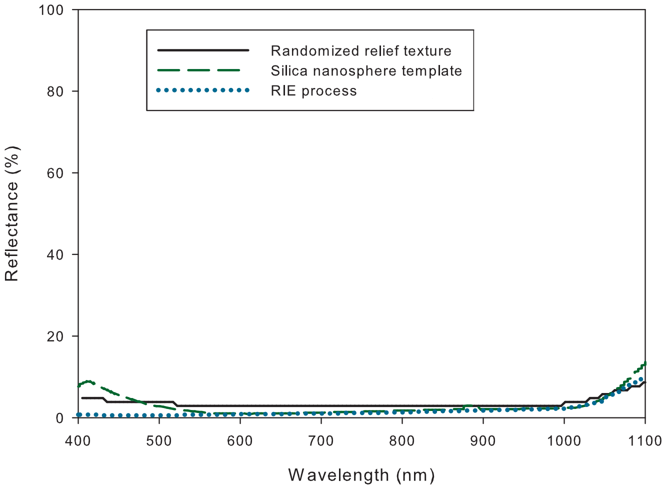

Figure 2.20: Comparison of the performance of antireflective structures presented in the literature by Ruby [51] (Shown in Figure 2.19a), Nositschka [52] (Shown in Figure 2.19b) and Inomata [53] all created via RIE etching

Inomata et al have shown reactive ion etching procedures that reduce the reflection of multicrystalline solar cells and have produced devices with conversion efficiencies up to 17.1% [53]. However, RIE texturization creates RIE-induced damage in the top layers of the surface and lowers the device's open circuit voltage. This is usually removed by a subsequent acid etch [52]. Also, RIE is not compatible with high throughput manufacturing because it requires a high vacuum environment to operate. Figure 2.20 summarizes the reflectance results achieved by the work described in this section.

2.5 Novel antireflection concepts beyond destructive interference and surface texturing

Previous antireflection techniques relied on varying the refractive index or the morphological structure of the surface to create antireflection. Some more ‘exotic’ and new methods that have been discussed in the literature will be briefly described here.

One of the most well known techniques is that of using ’negative’ refraction. Negative refraction dates back to the days when Veselago [54] predicted that materials in which the vectors of a plane wave form a left-handed (LH) rather than right-handed (RH) set would exhibit unique optical properties.

The first practical design of such media was suggested by Pendry et al [55],[56] who also made the prediction that they can act as a perfect lens. Smith et al [57] were the first to implement these ideas and show the existence of a medium with simultaneously negative permeability and permittivity.

The work of Shelby et al [58] first demonstrated negative refractive index in these left handed materials. Since then the concept of ’complementary media’ by putting together slabs of one material made by RH and the other by LH materials that cancel each other’s optical properties was put forward by Pendry in order to create the ’perfect lens’ [59] and the ’perfect spherical lens’ [60] (i.e. one with a subwavelength focusing property). This concept has been used by Monzon et al [61] to show the first feasible implementation of building the inverse of a inverse matrix which in his view could lead to perfect antireflection via negative refraction in all wavelengths and angles of incidence.

Another candidate method which has been proposed to gain perfect antireflection for materials in air, in a wide range of angles of incidence but narrow bandwidth, is via the use of Reststrahlen materials. Reststrahlen materials exhibit a refractive index for a band of wavelengths that is close to unity [62]. This concept is based on the fact that for an antireflective coating to be operational over wide angles of incidence the coating must be thick, have a refractive index that is very close to that of the incidence medium and an extinction coefficient which is small over the entire range of wavelengths that it is used for [63],[64].

2.6 Conclusions

Out of all the antireflection methods described in this section, the one that is expected to be effective for a multitude of various spectra and angles of incidence, whilst still has the potential to be manufactured on a large scale, is that of sub-wavelength surface texturing.

Possible applications of sub-wavelength textured surfaces are numerous. Military infantry use lasers to guide smart missiles to sensitive targets. These targets could employ sub-wavelength antireflection as a stealth technology because they would operate in a wide angle of incidence and bandwidth and thus neutralize the hostile's laser targeting advantage [65].

Sub-wavelength texturing could also be very useful for other commercial applications other than solar cells, such as reducing the reflection of optical LCD displays whose contrast reduces dramatically when they are used in bright light. Cheap and effective anti-glare surfaces for automotive displays such as dashboards and windscreens are also possible applications. Hence, developing a cheap nanotexturing methodology that would work reasonably well for the visible and infra-red spectrum is commercially very appealing.

Solar cells would potentially be the most applicable and potentially widespread use of sub-wavelength texturing antireflective technology because is critical to minimize losses throughout the day in order to harvest a maximum of solar energy.

Thin-film antireflection layers are commonly used today for passivation and antireflection layers on silicon (usually SiN or SiO_2). They are cheap and are compatible with mass manufacturing techniques already in use today. Intricate double layer coatings have also been designed to maximize the antireflection bandwidth available by this technology. Using single or double layer antireflection schemes for solar cell applications is not optimum due to the great variance of the incident solar spectrum during the course of the day and the concurrent variance of the angle of incidence of the sun both during the course of one day and throughout different seasons of the year.

Increasing efficiency of solar cells by reducing reflection without significantly increasing their price allows for a lower cost per watt of energy produced and hence makes solar energy more affordable and more competitive with other forms of energy production. Solar tracking systems are the current popular method used for mitigating reflection losses due to the variability of the angle of incidence of the sun. When applying these systems to solar panel arrays, the panels change their tilt during the course of the day in such a fashion so that the angle of incidence of the sun is always perpendicular to the panel. However, solar tracking systems require energy to move the panels and the total surface area that is required to install tracking systems is much larger than that of the actual panel because firstly, the panel needs room to rotate and secondly, it has to avoid shading from nearby panels during sunrise and sunset. The power/space that is lost could otherwise be gained by using more efficient antireflection schemes such as sub-wavelength texturing.

A sub-wavelength antireflection scheme that works in a broadband spectrum and at wide angles of incidence is thus highly desirable in solar cell applications [21]. A study by Boden et al [66] comparing double layer antireflection coatings to moth-eye antireflection layers for the same spectrum over the course of a whole day has shown that moth-eye layers create a higher photo-current because they are more efficient for broadband spectra and variable angles of incidence.

It is therefore predicted that sub-wavelength antireflection should be the technology of choice for applications which require broad-bandwidth and variable angles of incidence. The only barrier to their implementation in commercial applications is their high price of manufacture on a large scale.

In this work, sub-wavelength antireflection surfaces are going to be constructed using e-beam, Nano-Imprint and nanosphere lithography. Nanosphere lithography (NSL) will be researched as a possible candidate for cheap and large area production of these surfaces. Additionally, the possible use of subwavelength antireflective surfaces in stealth and anti-glare applications will be investigated.

Chapter 3

Simulation of ‘moth-eye’ layer optical properties

3.1 Zero order reflectance simulations

Rigorous electromagnetic computational methods started to be developed in the 1960’s [67], [68]. The goal to their development was to allow for numerical solutions of Maxwell’s equations without approximation. All these techniques, project a differential or integral form of Maxwell’s equations onto a set of functions. After simplification, and in order to avoid singularities and instabilities, a linear set of algebraic equations is formed [69]. The limits of computational accuracy/time tradeoff are still however hardware and design dependent as with most numerical simulations.

3.1.1 The Rigorous Coupled Wave Analysis (RCWA) Technique

The RCWA procedure represents the electromagnetic fields as a sum over coupled waves. Fourier harmonics are used in the x and y direction to depict a periodic permittivity function. Each coupled wave is related to a Fourier harmonic, allowing Maxwells equations to be solved in the full vectorial form in the Fourier domain. The diffraction efficiencies are then calculated at the end of simulation via transfer matrix theory. The spatial field distributions are derived from the Fourier harmonics. A detailed study of the RCWA technique can be found in [70].

Simulations of ordered hexagonal lattices have been performed using the RCWA technique implemented by a software called RSoft DiffractMOD. This software uses the differential form of Maxwell’s equations[71].

Hence, for the magnetic field:

$$\frac{\delta E_z}{\delta y} - \frac{\delta E_y}{\delta z} = i\omega\mu H_x \tag{3.1}$$

$$\frac{\delta E_x}{\delta z} - \frac{\delta E_z}{\delta z} = i\omega\mu H_y \tag{3.2}$$

$$\frac{\delta E_y}{\delta x} - \frac{\delta E_x}{\delta z} = i\omega\mu H_z \tag{3.3}$$

and the electric field:

$$\frac{\delta H_z}{\delta y} - \frac{\delta H_y}{\delta z} = -i\omega\epsilon_0\epsilon_{r,x} E_x \tag{3.4}$$

$$\frac{\delta H_x}{\delta z} - \frac{\delta H_z}{\delta z} = -i\omega\epsilon_0\epsilon_{r,y} E_y \tag{3.5}$$

$$\frac{\delta H_y}{\delta x} - \frac{\delta H_x}{\delta z} = -i\omega\epsilon_0\epsilon_{r,z} E_z \tag{3.6}$$

Where $\epsilon_{r,x}, \epsilon_{r,y}, \epsilon_{r,z}$ the principal axes diagonal elements. The transverse format is then derived by substituting equations 3.3, 3.6 into equations 3.1, 3.2, 3.4, 3.5 and hence:

$$\frac{\delta E_x}{\delta z} = \frac{-i}{\omega\epsilon_0}\frac{\delta}{\delta x}\frac{1}{\epsilon_{r,z}}\frac{\delta}{\delta y} H_x + (\frac{i}{\omega\epsilon_0}\frac{\delta}{\delta x}\frac{1}{\epsilon_{r,z}}\frac{\delta}{\delta x} + i\omega\mu) H_y \tag{3.7}$$

$$\frac{\delta E_y}{\delta z} = (\frac{-i}{\omega\epsilon_0}\frac{\delta}{\delta y}\frac{1}{\epsilon_{r,z}}\frac{\delta}{\delta y} - i\omega\mu) H_x + \frac{i}{\omega\epsilon_0}\frac{\delta}{\delta y}\frac{1}{\epsilon_{r,z}}\frac{\delta}{\delta x} H_y \tag{3.8}$$

$$\frac{\delta H_x}{\delta z} = \frac{i}{\omega\mu}\frac{\delta}{\delta x}\frac{\delta}{\delta y} E_x + (\frac{-i}{\omega\mu}\frac{\delta}{\delta x}\frac{\delta}{\delta x} - i\omega\epsilon_0\epsilon_{r,y}) E_y \tag{3.9}$$

$$\frac{\delta H_y}{\delta z} = (\frac{i}{\omega\mu}\frac{\delta}{\delta y}\frac{\delta}{\delta y} + i\omega\epsilon_0\epsilon_{r,x}) E_x + \frac{-i}{\omega\mu}\frac{\delta}{\delta y}\frac{\delta}{\delta x} E_y \tag{3.10}$$

The Bloch Theorem is then used to simplify the solution of equations 3.7 - 3.10 for a periodic pattern by substituting the electric and magnetic fields in the following way:

$$E_x = e^{i(k_{x,0}x + k_{y,0}y)} \sum_p \sum_q e^{i(\frac{2\pi}{\Lambda_x}px + \frac{2\pi}{\Lambda_y}qy)} \sum_m a_{x,m,p,q}(f_m e^{i\kappa_m z} + g_m e^{-i\kappa_m z}) \tag{3.11}$$

$$E_y = e^{i(k_{x,0}x+k_{y,0}y)} \sum_p \sum_q e^{i(\frac{2\pi}{\Lambda_x}px+\frac{2\pi}{\Lambda_y}qy)} \sum_m a_{y,m,p,q}(f_m e^{i\kappa_m z} + g_m e^{-i\kappa_m z}) \tag{3.12}$$

$$H_x = e^{i(k_{x,0}x+k_{y,0}y)} \sum_p \sum_q e^{i(\frac{2\pi}{\Lambda_x}px+\frac{2\pi}{\Lambda_y}qy)} \sum_m b_{x,m,p,q}(f_m e^{i\kappa_m z} + g_m e^{-i\kappa_m z}) \tag{3.13}$$

$$H_y = e^{i(k_{x,0}x+k_{y,0}y)} \sum_p \sum_q e^{i(\frac{2\pi}{\Lambda_x}px+\frac{2\pi}{\Lambda_y}qy)} \sum_m b_{y,m,p,q}(f_m e^{i\kappa_m z} + g_m e^{-i\kappa_m z}) \tag{3.14}$$

Where $\Lambda_{x,y}$ the periodicity of the structure in the transverse directions, p,q are the reciprocal lattice vectors, m is the layer number, a, b the coefficients which are found from the eigenvalues that will be calculated, κ_m is the Bloch wave number, k the wave number of the electromagnetic wave and f_m and g_m arbitrary equations with the same periodicity of that of the structure.

Substituting equations 3.15-3.14 into equations 3.7-3.10 creates an eigenvalue problem of the form:

$$AX = \lambda x \tag{3.15}$$

Where λ is the eigenvalue to be calculated.

The boundary conditions that result are solved by treatment-line methods [71]. Namely, the tangential electric and magnetic fields have to match at each boundary. For example, for an electromagnetic field where the vector of the electric field is TE polarized, for each boundary between the diffraction grating relief layers the electric and magnetic field should be continuous across the boundary:

$$Ex_n \mid_{y=0^+} = Ex_{n+1} \mid_{y=0^-}, \tag{3.16}$$

$$Hz_n \mid_{y=0^+} = Hz_{n+1} \mid_{y=0^-} \tag{3.17}$$

Where y=0 is the boundary between two successive layers n and n+1.

The assumptions that are made to extract the previous equations for the diffraction efficiency in RCWA are that the material is homogeneous, linear and isotropic, the grating is arbitrary shaped and the light is linearly polarized of arbitrary polarization.

A major limitation of the RCWA method is that when the grating is too thick and the dielectric modulation is too large the solution becomes unstable and inaccurate. The method gives rise to exponential arguments and when the eigenvalues are solved to compute the response of the whole system these very large and very small exponential arguments cause the solution to be inaccurate.

This issue has been tackled by Moharam et al. [72] [73] by formulating Maxwell's equations into a second order matrix state variable form. Then the exponentially large and small variables get summed together into the same element and hence the sources of instability are removed from the calculation.

3.1.2 Specification of the close-packed moth-eye pattern design

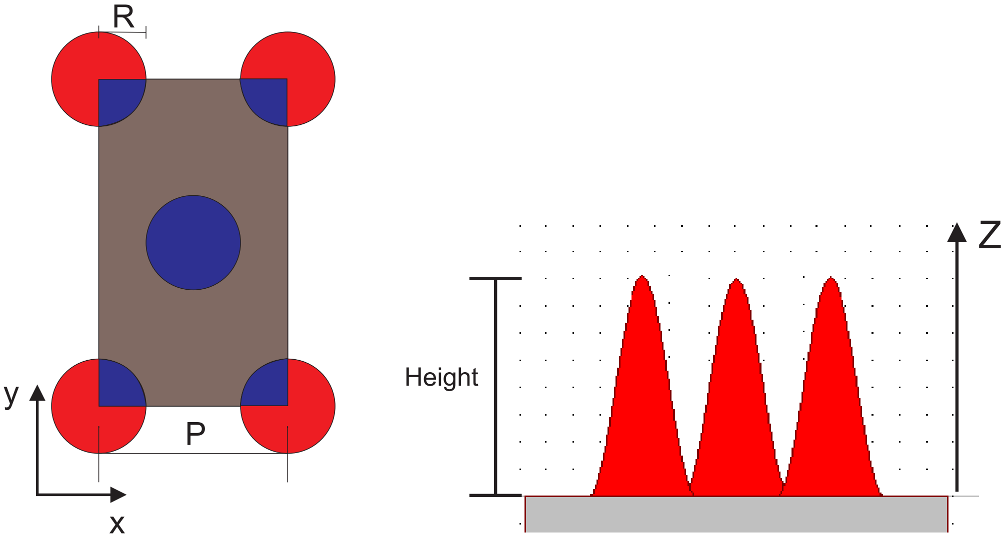

(a) Top view of moth-eye computer design

(b) Profile view of moth-eye layer

FIGURE 3.1: Specification of the 3D simulation model of a moth-eye pattern unit cell with a close packed orientation in the Diffract MOD software package

RSoft's DiffractMOD software initially requires a 3D surface relief CAD design to be created. A simulation grid is then set in order to evaluate the grating with respect to its diffraction efficiency in each of the reflected or transmitted orders.

Nearly all variables related to the morphological and topographical specification of moth eye features affect the reflectance of the metamaterial layer (i.e. material height, shape, density factor, period).

To compare the effect of each of the basic design parameters, (i.e. height, density factor and period) the shape of the pillars needed to kept consistent in the first batch of simulations (Section 3.1.5.1) and hence a sinusoidal pattern was selected. The sinusoidal pattern was used because it was considered to closely approximate the features found on the real moth-eye (depicted in Figure 3.1b).

The parameter scan ranges were chosen to be close to the values which are required for antireflection in the visible spectrum. These features as explained by Caplam [30], have to be specified with a period smaller than half that of the smallest wavelength ($\lambda_{min} =$ 400nm) and taller than half the longest wavelength ($\lambda_{max} =$ 700nm) . In our case, this translates to a pattern period smaller than 200nm and a height larger than 350nm.

The basic design parameters of pillar height, pattern period and fill factor were then scanned to investigate the effect each one had on the reflectance of the moth-eye pattern for the incident wavelength spectrum that was used(300-1000nm). In the second batch of simulation results, the basic design parameters were fixed and the shape of the pillars was altered (Section 3.1.5.3). All simulations were carried out for a single-crystal silicon substrate.

The parameters that were systematically investigated were:

- the period of the pillars (P)
- the height of the pillars (H)
- density factor (DF)

A schematic of the pillar design parameters is depicted in Figure 3.1a. The density factor is defined as the factor of the pillar diameter over the period, as depicted in Equation 3.18.

$$\text{Density Factor} = \frac{\text{Diameter}}{\text{Period}} = \frac{2 * R}{P} \tag{3.18}$$

Where: R = Pillar Radius and P = Pattern Period.

3.1.3 Simulation validation

The validation of the RSoft simulation procedure was done by comparing the results with an analytical method of calculating the reflectance of a single thin film, called the transfer matrix method.

In the specific example, the reflectance of a 400nm thick silicon dioxide layer on silicon was simulated and the results were compared for both methods (Figure 3.2). The results are identical as expected and hence, the validation of the model was accomplished.

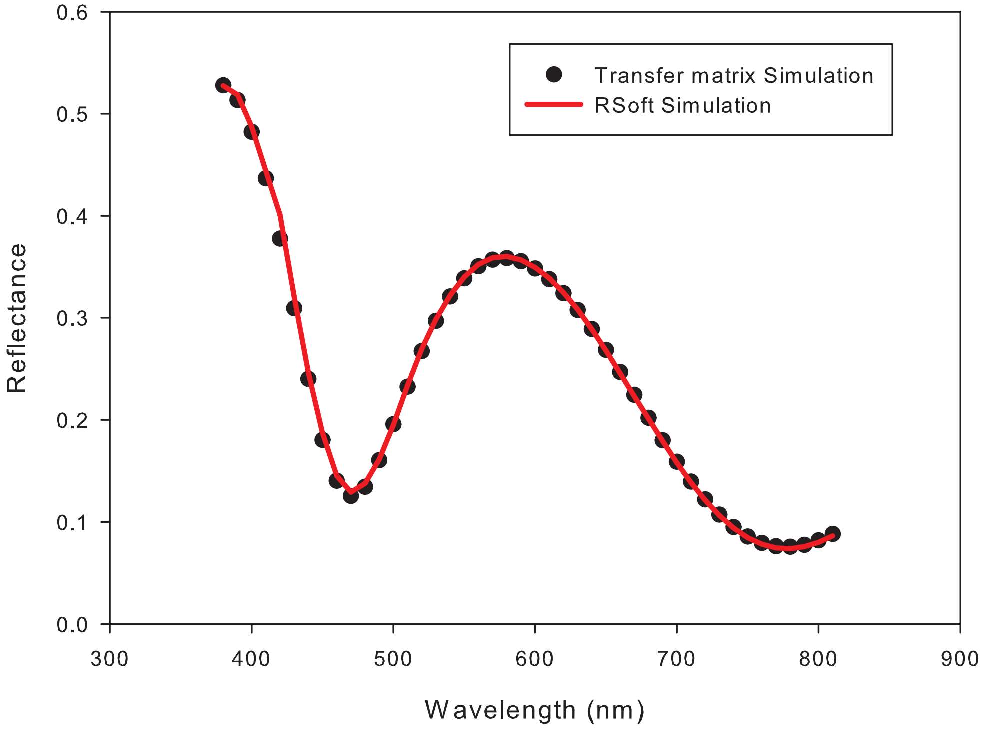

Figure 3.2: Validation of RSoft simulation by comparing the results to an effective medium theory simulation of a 400nm thin-film SiO2 layer on Si.

3.1.4 Convergence tests

The moth eye features that need to be simulated are more complicated than thin film layers and hence an appropriate simulation grid needs to be created so that they can be accurately represented with the minimum amount of simulation blocks and calculated in the fastest possible time.

For this to be done, convergence tests need to be carried out for the parameters that affect the grid to progressively converge the simulation results to the accuracy that is required. The parameters that affect the density of the simulation grid in this case are: the number of harmonics used in the x and y directions, the height step in the Z direction, and the number of reflectance orders. The spatial axis set-up that was used by the software is depicted in Figure 3.3.

It was found that the precision specified in the simulation software started giving diminishing returns in accuracy when the simulation grid was defined with more than 5

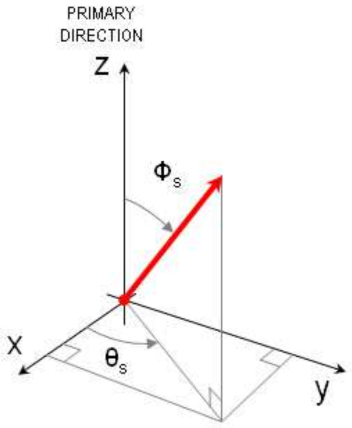

Figure 3.3: Dimension variables in RSoft software, Z is the direction of propagation and x,y is the grating plane. The primary direction refers to the direction of propagation of the electromagnetic beam if the angle of incidence was zero. Φ_S and θ_s refer to the angle of incidence and the azimuth angle respectively. The red arrow signifies the direction of propagation of an electromagnetic beam within the material with respect to the x-y antireflection surface plane.

harmonics in the x and y directions (Figure 3.4a), when more reflection orders than just the specular order were considered (Figure 3.4b) and a step size which was smaller than 50nm in the Z direction(Figure 3.4c). Hence, these simulation grid parameters were set to the values stated and hence the simulation of the structures could be carried out with the confidence that the simulation environment has been properly set up to closely match the structure that needs to be simulated.

3.1.5 Design parameter scans of the close-packed ‘moth-eye’ pillar structure

3.1.5.1 Basic design parameter scans for ‘moth-eye’ pillar structure period, fill factor and height

In order optimize the pattern for any of the basic design parameters (i.e. height, period, packing density), an initial rough scan of the variable in question is always necessary. The scan will show how the parameter generally affects the reflectance in the region that is investigated. If there is an optimum value in the region that is scanned, it can be subsequently calculated to the required accuracy in the MOST (Multi Variable Optimizer Scanner Tool) application. This is the integrated optimization tool of the RSoft Software Package which identifies the exact root value to the accuracy that is required.

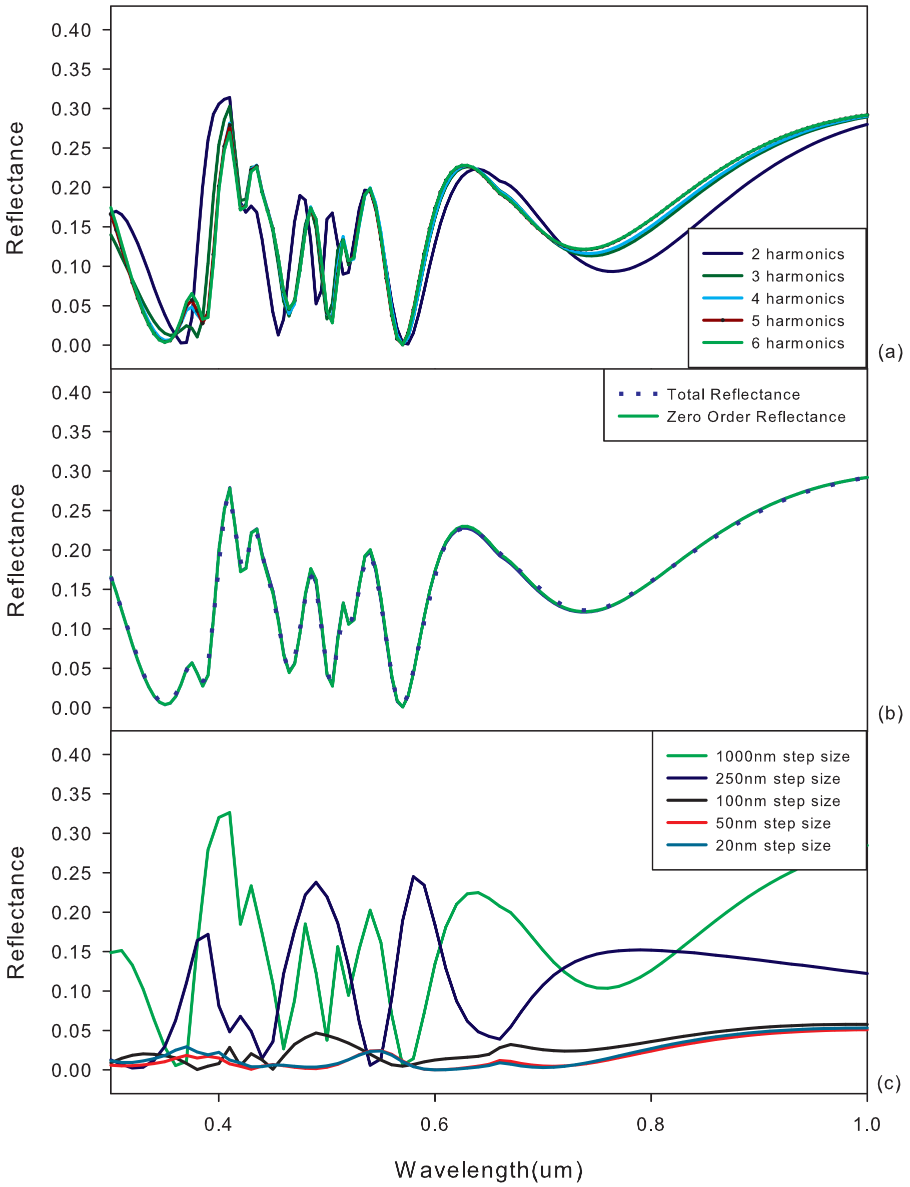

FIGURE 3.4: Example of a set of simulated reflectance plots used to determine the convergence values for the simulation parameters in terms of harmonics, reflectance order, and step size in the z axis of a sub-wavelength pillar structure with a period of 200nm a pillar height of 400nm and a pillar diameter of 100nm. Namely plots of a) harmonics convergence, showing that the reflectance graph stops changing significantly after considering more than 5 harmonics in the axes which form the substrate plane, b) reflectance order convergence, showing that considering all reflective orders creates a similar result to the reflectance of the zero order so higher orders do not contribute enough to be required to be included in the calculation and, c) z step size convergence, showing that the size of the steps considered in simulation grid in the axis which is vertical to the substrate plane can be sufficiently set to 50nm because considering anything smaller does not significantly change the simulated result.

Scans of the parameter space selected (period, density factor, height) for moth-eye antireflection pillars were are carried out whilst monitoring the reflectance in the visible/IR spectrum 300-1000nm (Figures 3.5a, 3.6a, 3.7a).

In order to distinguish the effect of a certain parameter on the total reflectance of the spectrum systematically, the reflectance value for all the wavelengths was integrated to a single value and plotted with respect to the parameter that was varied. This value (coined integrated reflectance) maps the effect of each variable to the total reflectance of the spectrum considered, and is shown in Figures 3.5b, 3.6b, 3.7b.

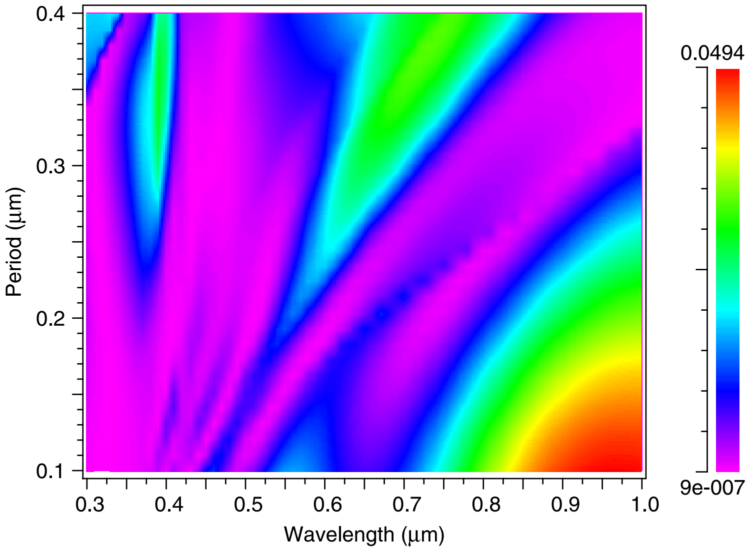

(a) Total Reflectance v Wavelength as the period of the protuberances increases from 0.1-0.4μm

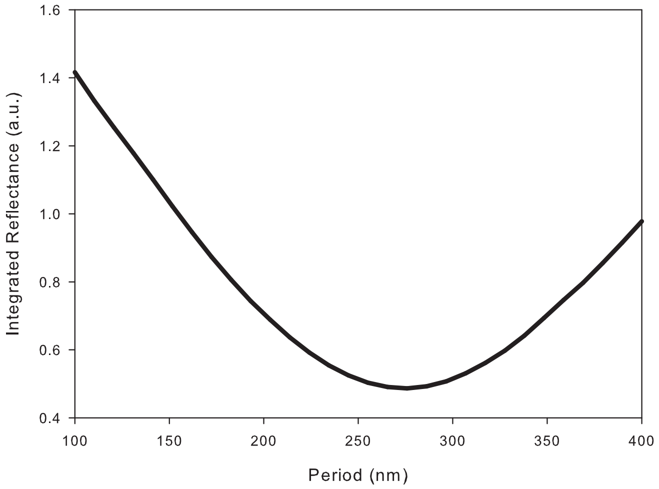

(b) Integrated total reflectance for all wavelengths as period varies from 0.1-0.4μm

FIGURE 3.5: Reflectance value trends at normal incidence when varying the period of sinusoidal profile pillars

In Figure 3.5(a) the effect of varying the pattern period from 100-400nm whilst keeping a density factor of 1 and a height of 400nm was mapped. The general trend shown in these results is that as the period is increased, the region of minimum reflectance splits up into multiple regions and shifts towards higher wavelengths. In Figure 3.5(b) the effect of period variation effect on the integrated reflectance in the wavelength range 300-1000nm is shown. A non-monotonic decrease is observed which means that for this device parameter there is not a clear trend and optimization of the period would benefit the application at hand because of a clear observable minimum value in the trend which in this case is around 275nm.

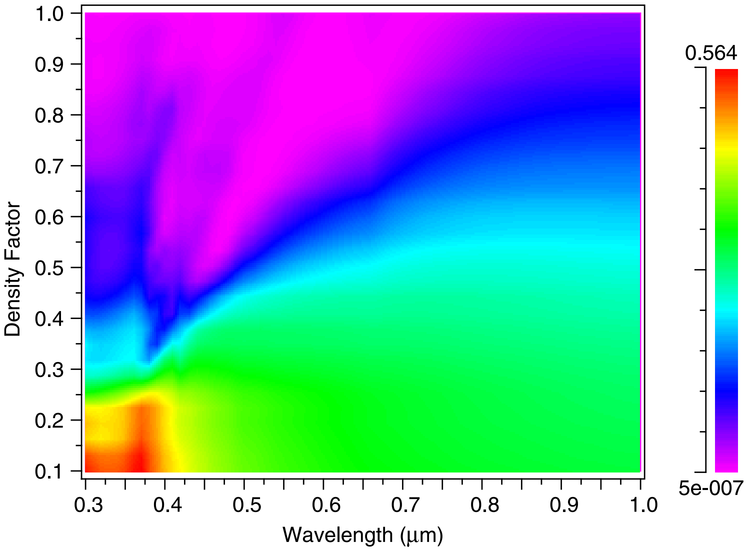

(a) Total Reflectance v Wavelength as the density factor of the protuberances increases from 0.1-1

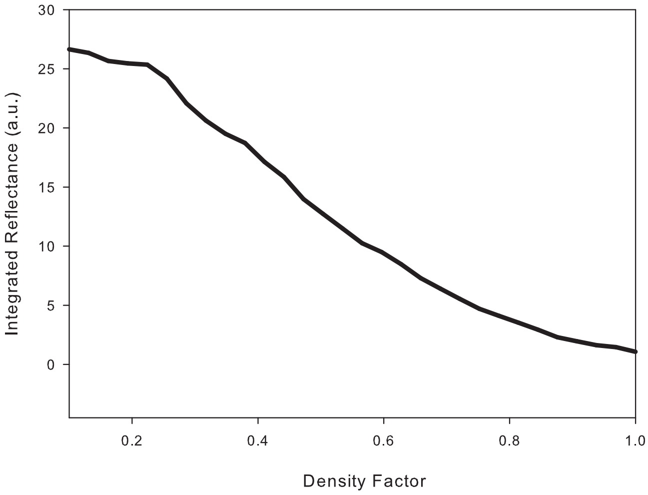

(b) Integrated total reflectance for all wavelengths as density factor varies from 0.1-1

Figure 3.6: Reflectance value trends at normal incidence with varying the density factor of sinusoidal profile pillars

In Figure 3.6(a) the effect of varying the density factor between 0.1-1 for a period of 400nm and a height of 400nm is shown. As the density factor increases, the space between the pillars decreases so the effective refractive index transition is smoother.

The trend shows that as the pillars become denser, the total reflectance is reduced in the whole region considered. In Figure 3.6(b) the total effect on integrated reflectance in the wavelength range 300-1000nm is shown. A mostly monotonic decrease is observed which means that for this device parameter the higher the value of the density factor, the higher the reduction of reflectance in the 300-1000nm wavelength range.

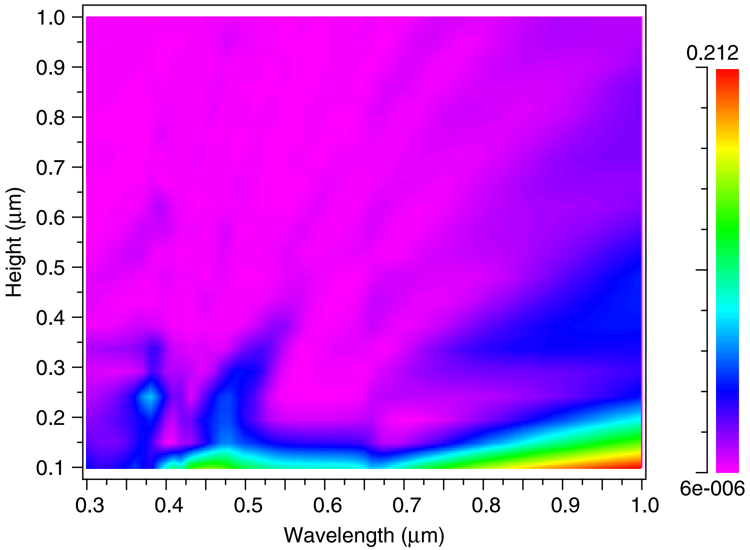

(a) Total Reflectance v Wavelength as the height of the protuberances increases from 0.1-1μm

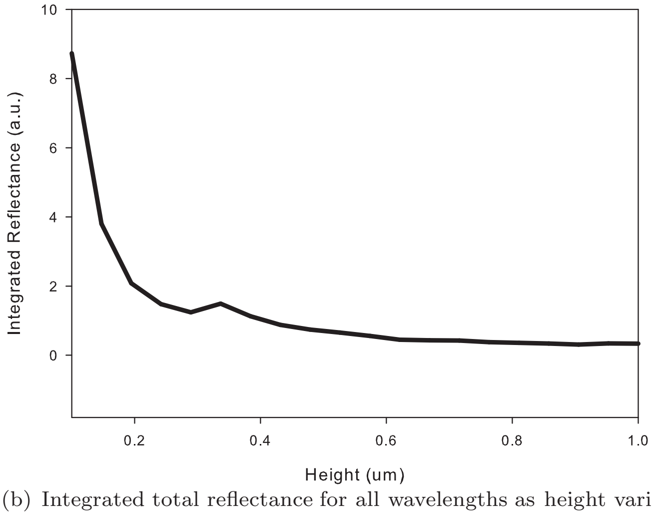

(b) Integrated total reflectance for all wavelengths as height varies from 0.1-1μm

Figure 3.7: Reflectance value trends at normal incidence with varying the height of sinusoidal profile pillars

Figure 3.7(a) shows the effect of varying the height of the pillars between 100-1000μm whilst sustaining a pattern period of 400nm and a density factor of 1. The trend shows that as the pillars get taller the reflectance is reduced for the whole spectrum. In Figure 3.7(b) the effect of increasing the height on the integrated reflectance in the wavelength range 300-1000nm is shown. A mostly monotonic decrease is observed which means that the higher the height of the pillars, the higher the reduction of reflectance in the

300-1000nm wavelength range. However, we can see that after in creasing the height more than 300-400nm, the decrease is almost flat. From this we can conclude that a 300-400nm height could be enough to provide good antireflection in most cases. This optimization is important because, using the minimum height of the pillars that provide adequate antireflection, can increase production speed and improve electrical device characteristics because a smaller height means the total interface area is smaller and hence the probability of having dangling bonds on the surface is reduced.

3.1.5.2 Optimization of close-packed moth-eye structure period for a specific spectrum at normal incidence

It has been shown in the previous section that the height and density factor have a 'monotonic' relationship with broadband reflectance at normal incidence. For optimum antireflection these values need to be maximized and thus, depend on the limitations of the manufacturing procedure. However, the effect of changing the period of the moth-eye structure is not as straightforward as the effect of the other two design parameters (height and density factor), so in general it can be seen that an optimization scan is required to evaluate the exact design period that would provide maximum antireflection.

In this section the period of the antireflective structure will be optimized for the part of the solar spectrum which is of particular interest to silicon photovoltaics (300-1000nm). Figure 3.8 shows the absorption coefficient of polished silicon in the wavelength range 300-1300nm.

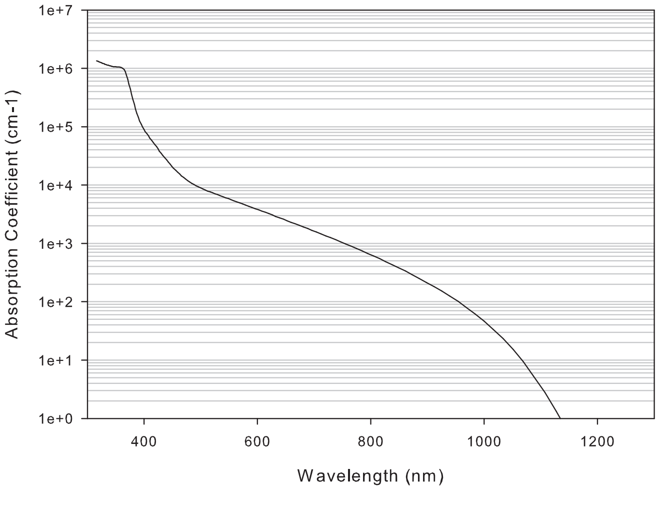

FIGURE 3.8: Absorption coefficient of silicon for the wavelegnth range 350-1100nm [74]

Before this optimization can be carried out we have to set values for the height and fill factor of the pillars. To make the scenario realistic we have to consider that all methods available for creating moth-eye arrays on the nano-scale have limitations with respect to the profile, height, density factor and period of patterns they can produce. Hence, even though simulations point towards the optimum properties that allow maximum antireflection for the 'moth-eye' surface as far as the height and fill factor of the pillars is concerned, the realization of these specifications is not always possible when dealing with real systems.

To emulate such a practical manufacturing shortcoming, some limits were imposed on the density factor (0.5), profile (sinusoidal) and height of the pillars (400nm). Using these parameters, the period was optimized for minimum reflectance. The AM 1.5 solar spectrum was selected as it is the most widespread spectrum used for solar cell device comparisons in the literature. The data for this spectrum was taken from the NREL SPCTRAL2 data application (Figure 1.10) [13]. By setting the specifications for the pillars to the specific values described above, a scan of reflectance in the wavelength range 300-1000nm was carried out by varying the design periodicity between 100-700nm. The reflectance data for this scan is shown in Figure 3.9(a).

For each period, the solar spectrum in the wavelength range considered (300-1000nm) was multiplied with the reflectance of the structure at this wavelength and integrated to a single value. Hence, a figure of merit for total reflectance can be assigned for each design period as shown in the previous section. As the parameter scan in Figure 3.9(b) depicts, there is a minimum reflectance region bracket for a range of pillar periods between 300-450nm.

We can carry out a further investigation in order to evaluate which period produces the minimum reflectance in this region by using the integrated RSoft Multi-variable Optimizer and Scanner Tool (MOST). MOST has five optimization algorithm options two one-dimentional options and three multi-variable options. Of the two one-dimentional options one is for root-finding and one for minimization, and they both use Brent's Method. Of the three multi-variable options, two are for local minima, (one using the downhill-Simplex method and the other using Powell's direction set method) and one for global minima which utilizes a genetic algorithm.

Each algorithm perform's better in different genres of problems and data sets. For example genetic algorithms perform better than the other algorithms suggested when a large number of parameters with a complicated parameter space is at hand. In our case, we are trying to find the optimum value of a single parameter within a specific range (e.g. silicon pillar period, height). By optimum, we define the value of the parameter varied which minimizes the Integrated Spectrum Reflectance. The most suitable algorithm in this case from the ones available in MOST is Brent's one dimensional minimization algorithm which was used to produce the results shown herein.

By using the MOST optimization tool it was found that the optimum design period for attaining minimum reflectance from a silicon substrate was 397.6nm calculated to an accuracy of 0.1 nm. For this optimization the incident spectrum considered was the

AM1.5 solar spectrum and the moth-eye antireflection pattern had an sinusoidal profile, a density factor of 0.5 and a pillar height of 400nm.

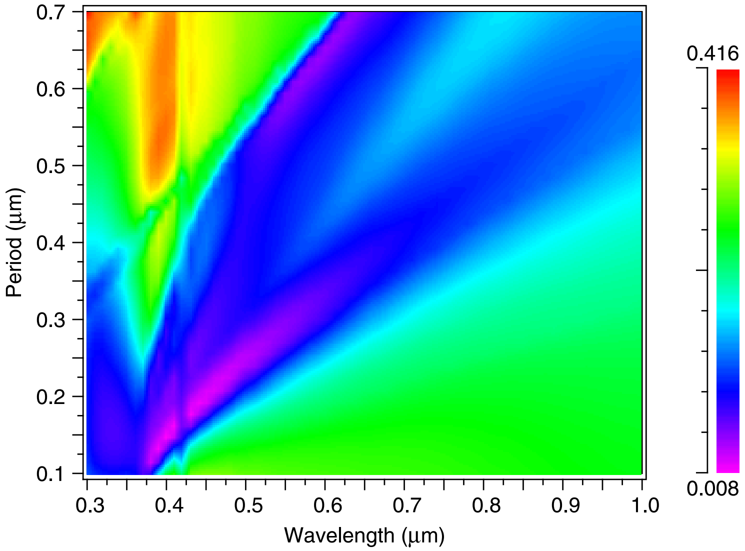

(a) Total Reflectance scan for 400nm period, 400nm height 0.5 density factor hexagonally packed moth-eye surface with a sinusoidal profile

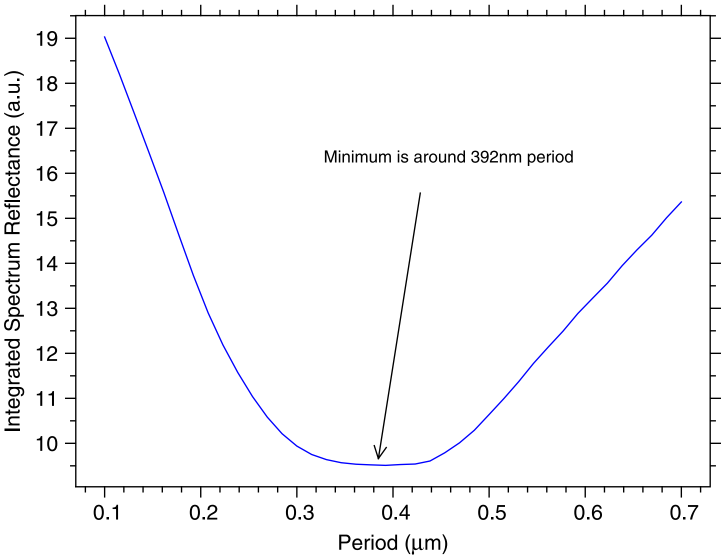

(b) Integrated total reflectance scan of solar spectrum reflectance whilst changing the period from 100-700nm for sinusoidal-profile hexagonally-packed pillars

FIGURE 3.9: (a) Total reflectance whilst varying pattern period (100-700nm) for the wavelength spectrum 300-1000nm and (b) the integrated solar reflectance scans for the same period range for a close packed pattern with a sinusoidal pillar profile

This type of optimization can be carried out for any spectrum, here the AM 1.5 solar spectrum was used as an example. This optimization is especially useful when designing "moth-eye" antireflection layers for solar cells because the average solar irradiance spectrum is not identical at different parts of the globe. Hence, if there is going to be a large power plant installation in Germany for example, the utility company could gain by selecting a customized antireflection solution for the solar irradiance at their installation location. Thus, the maximum performance of the antireflection layer can be achieved for each client specifically, by creating bespoke solutions according to their typical local solar spectrum.

The solar spectrum however, changes with time of day as well as location. Hence if the cells are at a certain fixed location (roof, wall mount) a customized antireflection solution could also be of interest when factoring in the time of day that these solar cells receive maximum energy (sunrise, mid-day, sunset etc) to optimize the antireflection solution.

Other applications might require maximum antireflection for one wavelength (laser beam antireflection) and for this reason the period could be customized to deliver maximum antireflection for a specific range of wavelengths only.

3.1.5.3 Variation of profile for close-packed moth eye patterns

Showing the effect of the profile in a systematic way is very tricky since 'morphing' the profile of the pillar from vertical to an arbitrary profile cannot be systematically specified in the simulation software available. For a trigonal profile however, an achievable variation does exist. By changing the radius of the top pillar, the profile can slowly be 'morphed' from a vertical profile to a trigonal one. Thus it was possible to simulate such a profile change. In figure 3.10(a) the effect of varying the profile from trigonal to square is shown. In Figure 3.10(b) the equivalent change in the shape along the y axis is depicted. The tip diameter was changed from 0-200nm for pillars with a pillar diameter of 200nm, a pillar period of 400nm and a height of 400nm.

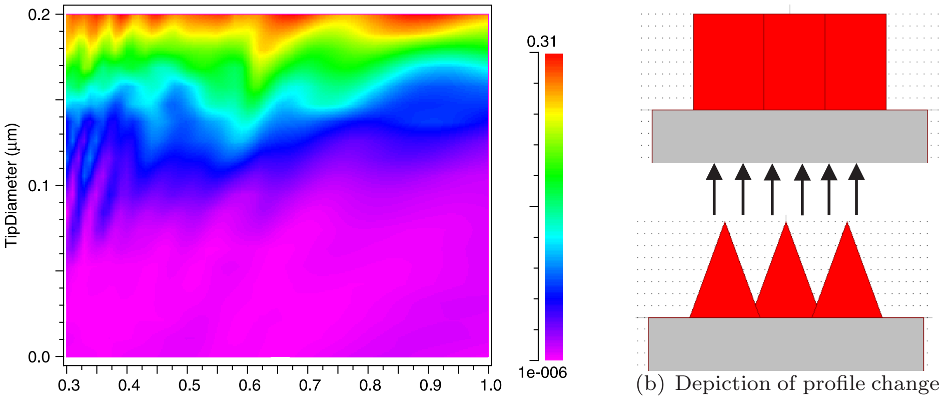

(a) Total Reflectance v Wavelength as the tip diameter of the protuberances increases from 0-0.2μ

(b) Depiction of profile change from trigonal to vertical (tip diameter 0 - 200nm)

FIGURE 3.10: Simulation of a range of pillar profiles between vertical and trigonal with a height of 400nm, a period of 400nm and a pillar base diameter of 200nm

3.1.5.4 Optimization of normal reflectance for moth eye patterns with different profiles

It has been investigated by Southwell [33] that the optimum antireflection profile for a subwavelength structure is one that produces an effective quintic variation in refractive index. For a material with refractive index of 3.42 this structure is shown in Figure 3.11.

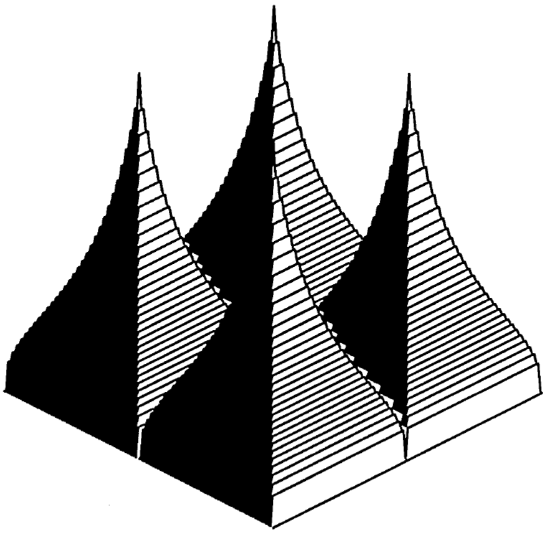

FIGURE 3.11: Surface relief that would produce effective quintic variation in refractive index for a material with refractive index of 3.42 [33]

Silicon has a widely variable refractive index between 0.3 - 1μm [74] so optimizing the relief for all wavelengths in the broadband spectrum is not possible. However, a quintic variation of the relief profile (Figure 3.14) was calculated and imported into the software to test the results by comparing this profile to a vertical (Figure 3.12), trigonal (Figure 3.13) and sinusoidal (Figure 3.9) variation of profile with depth.

A similar technique shown previously was used to scan the reflectance for various pillar profiles across the same region of design periods so that a comparison of the effect pillar profile has to the optimum design period for the AM 1.5 solar spectrum (Figure 1.10). Again, a 'solar product' was created for each profile and this figure of merit was used to compare minimum reflectance for each pillar profile design. The 'solar product' was calculated by multiplying the reflectance of the structure with the incident spectrum and integrating the result over all wavelengths at the optimum period for which each design produces minimum reflectance.

Table 3.1 collects the results comparing the 'optimum period' across all pillar profiles for the solar spectrum between 300-1000nm. It was found that the quintic profile, even though not optimized to create a quintic variation of refractive index for all wavelengths,

Profile	Number of minima in the 100-700nm period region	Optimum Period (nm)	Solar Product (a.u.)
Vertical	2	295	10.465
Sinusoidal	1	397	9.512
Linear	1	346	7.123
Quintic(Local min)	1	344	0.867
Quintic(Abs min)	1	104	0.204

Table 3.1: Size score lookup table

produces extremely low reflectance compared to the other profiles that were considered (Figure 3.14).

3.1.5.5 Conclusions

Evaluating the basic parameter scans shown, it can be summarized that to attain minimal broadband reflectance over the whole spectrum considered (300-1000nm), the density factor and height of the pillars need to be as large as possible because they provide a monotonic, albeit not linear, relationship to the total reflectance of the sample. However, changing the period of the structure does not have a monotonic effect on the reflectance because, as period increases, a minimum reflectance point is formed in the integrated reflectance plot. Hence, if minimum reflectance is required, the period of the structure needs to be optimized to the spectrum that is considered in each application. The second batch of simulations showed that when changing the shape of the features both by linear morphing and by trying various shapes, even small changes cause dramatic changes in reflectance. It was verified that a morphology which provides a quintic variation in refractive index as proposed by Southwell [33], was the most effective shape in providing broadband antireflection. It is concluded therefore that the feature shape is one of the most critical variables that need to be considered when broadband antireflection is required.

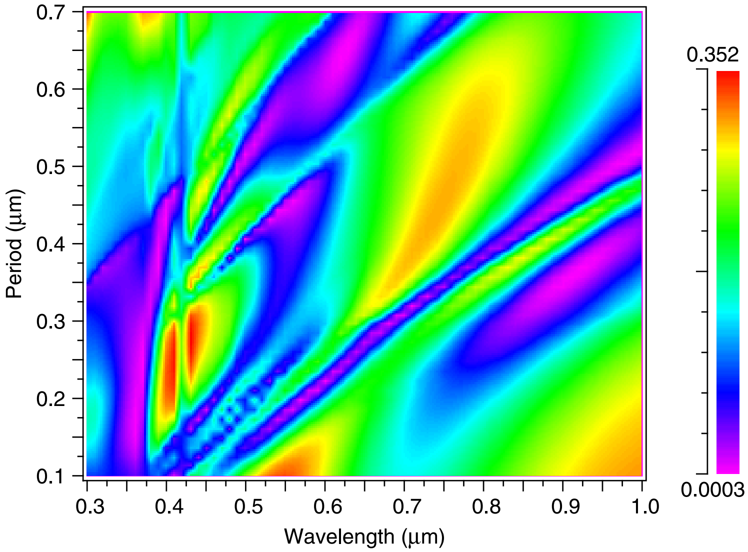

(a) Total Reflectance scan for 400nm height, 0.5 density factor, hexagonally packed moth-eye surface with a vertical profile

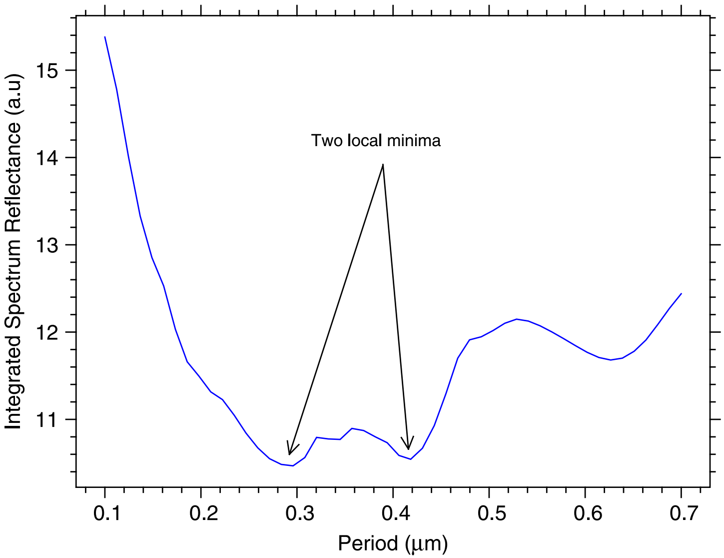

(b) Integrated total reflectance scan of solar spectrum reflectance whilst changing the period from 100-700nm for vertical-profile hexagonally-packed pillars

FIGURE 3.12: (a)Total reflectance of varying pattern period (100-700nm) for the wavelength spectrum 300-1000nm and (b) the integrated solar reflectance scans for the same period range for a vertical pillar profile

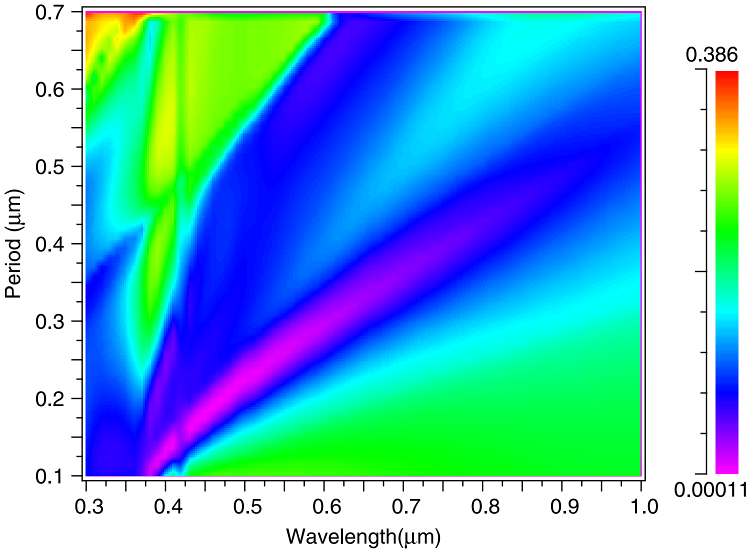

(a) Total Reflectance scan for 400nm height, 0.5 density factor, hexagonally packed moth-eye surface with a trigonal profile

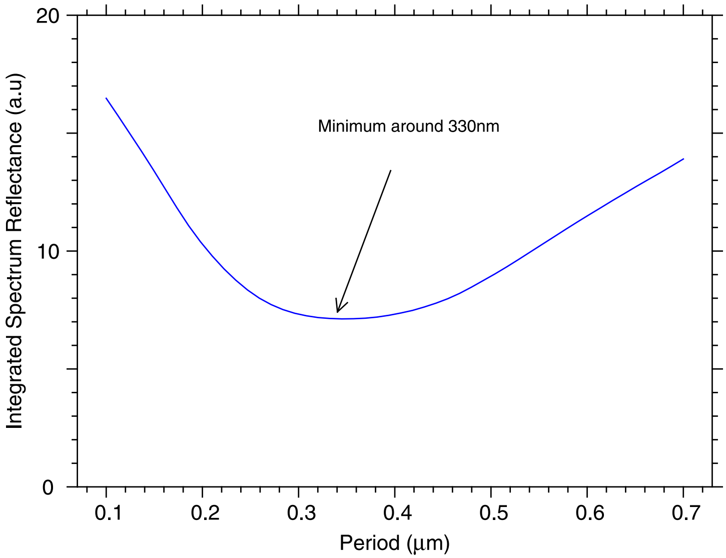

(b) Integrated total reflectance scan of solar spectrum reflectance whilst changing the period from 100-700nm for trigonal-profile hexagonally-packed pillars

FIGURE 3.13: (a) Total reflectance of varying pattern period (100-700nm) for the wavelength spectrum 300-1000nm and (b) the integrated solar reflectance scans for the same period range for a close-packed sample with a trigonal pillar profile

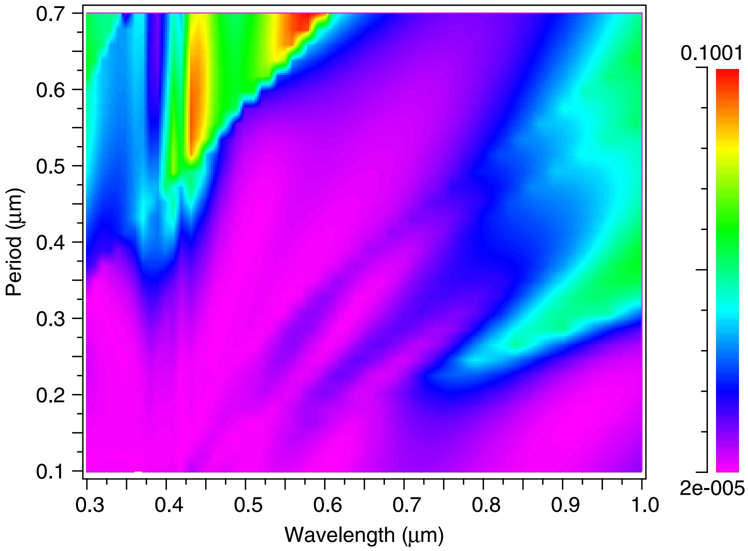

(a) Total Reflectance scan for 400nm height, 0.5 density factor, hexagonally packed moth-eye surface with a quintic profile

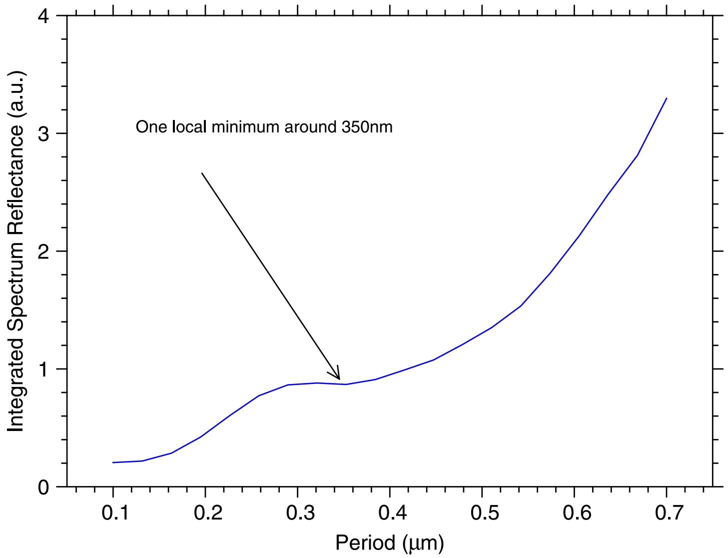

(b) Integrated total reflectance scan of solar spectrum reflectance whilst changing the period from 100-700nm for quintic-profile hexagonally-packed pillars

FIGURE 3.14: (a) Total reflectance of varying pattern period (100-700nm) for the wavelength spectrum 300-1000nm and (b) the integrated solar reflectance scans for the same period range for a quintic pillar profile

3.2 Moth-eye layer diffraction properties

The transition between the scale of features at which sub-wavelength (moth-eye), par-wavelength (2D diffraction grating) and supra-wavelength (rough surface) behaviour is noticed is quite vague. The general rule of thumb is that when the spacing of the features is an order of magnitude lower than the photon wavelength, sub-wavelength behaviour is noticed, whereas if the texturing is an order of magnitude larger, supra-wavelength behaviour is noticed. Additionally, when the spacing of features is of the order of the wavelength diffraction occurs. The transition in between these three modes of photon behaviour is not well defined.

The operation of a diffraction grating however is very well established. Diffraction is observed in reflection when the scale of features is the same order as the wavelength and there is an inherit periodicity or a consistent average spacing in the design. The characterization of the diffraction in terms of angles of elevation for the different diffraction orders is fully predicted by the diffraction equation (Equation 3.19) [75].

$$d(sin\theta_m + sin\theta_i) = m\lambda \tag{3.19}$$

Where d is the spacing between the diffracting elements, θ_i the incident angle, θ_m the angle of diffraction of order m, and λ the wavelength of light in the incident medium. In this case the incident medium is air, so the wavelength can be approximated to be equal to the free space wavelength.

In the case of moth-eye nanostructured surfaces, when considering a single wavelength, a low reflectance is expected if the spacing between the features is smaller than the wavelength and the height is taller than half the wavelength [22]. For broadband applications on the other hand, it is required that the period of the features in a nanoengineered structure be as small as possible and the depth as great as possible, in order to provide antireflection for the widest possible bandwidth [22].

On the actual eyes of a moth, the size of the protuberances are around 200nm and their period is also around 200nm [29]. The light that is most effectively absorbed by this structure is in wavelengths between 440-550nm, which provides the moth with the stealth property required when flying at dusk [22].

The minimum requirements that are therefore necessary in order to attain low reflection for a certain wavelength spectrum at all angles of incidence for subwavelength structures are [22]:

- the height of the protuberances be larger than half the largest wavelength in the spectrum

- the spacing between features be smaller than half the smallest wavelength in the spectrum

Following these rules we can deduce that in order to absorb the whole range of wavelengths in the visible spectrum (400-700nm) the pillar pattern design parameters need to have a period smaller than 200nm and a height larger than 350nm.

This scale of sub-wavelength texturing however, is not always possible or compatible with cheap mass manufacturing procedures. Photolithography procedures for example usually have a limit of 800nm for feature size and 800nm for minimum feature spacing, which translates to a 1.6μm period for 800nm pillar diameters. (Source: Compugraphics: OM Group Ltd). In such cases, a study of the diffraction orders emanating from the surface also has to take place.

3.2.1 Case study: reducing reflection for the visible spectrum on a structure with manufacturing constraints via analysis of the first diffraction order

By relaxing the manufacturing limitations of the 'moth-eye' structure in terms of the spacing between features by increasing the design period of the structure from sub-wavelength to par-wavelength, one can make the manufacturing of moth eye layers cheaper by using manufacturing procedures that have lower resolution and cannot create fully sub-wavelength features. The disadvantage of this approach is that diffraction orders start emerging for these wavelengths in reflection. If the amount of light lost in reflection from the diffraction orders is critical to the application (e.g. such as in solar cells, where maximum efficiency is sought), there can be a way to manage the light lost by trapping it in the intermediate layer.

An example of how diffraction analysis could aid in designing an antireflection layer which is not entirely subwavelength to the incident spectrum and yet retain most of the properties of an entirely subwavelength structure will be explained. Specifically, an example of designing such an antireflective structure so that the period increases to a scale slightly larger than the sub-wavelength regime and allows one diffraction order to emerge from the sample in reflection is studied.

The incident wavelength range that will be assumed in this example is the visible spectrum 400-700nm, the angle of incidence will be normal to the device and the capping layer will be made of a standard polymer used in photovoltaics called EVA (Ethylene-vinyl acetate) (n$\sim$1.56). We will assume a very thin layer of EVA and thus assume no absorption in the layer.

The critical angle for total internal reflection for diffracted light within the device for the air-EVA interface is calculated from Snell's law of refraction:

$$n_1 sin\theta_1 = n_2 sin\theta_2 \tag{3.20}$$

Where medium 1 is air and medium 2 is EVA.

The refractive index of EVA can be calculated from equation 3.21 (Nagel et al.[76]):

$$n(\lambda) = 1.56 - 5.75 * 10^{-5}\lambda \tag{3.21}$$

However, for practical purposes and since there is hardly any change to the refractive index in the visible spectrum we will assume a value of 1.56 for the refractive index for all the wavelengths in consideration (400-700nm).

Hence replacing $n_1 = 1$, $n_2 = 1.56$, the equation for total internal reflection at the eva-air interface becomes:

$$1 * sin90 = 1.56 sin(\theta_{TIR}) \tag{3.22}$$

Which can be rearranged as:

$$\theta_{TIR} = sin^{-1}(1/1.56) = 39.86 degrees \tag{3.23}$$

Thus any diffracted light from the device incident on the EVA-air surface at an angle of incidence that is larger than 40 degrees will be internally reflected (Figure 3.15). This means that light can be diffracted from the eva-silicon surface at angles between 40 and 90 degrees (measured from the surface normal) and still be trapped between the cell and the top layer.

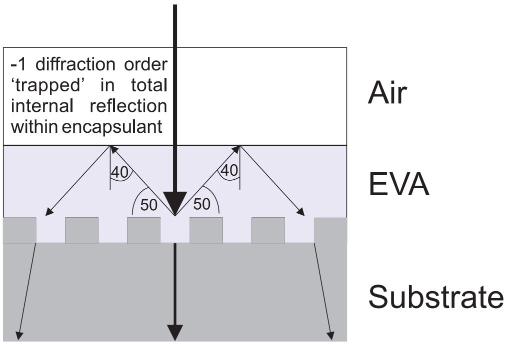

Figure 3.15: Design of relaxed specification antireflection layer which takes into account TIR between air - encapsulation layer to preserve antireflection properties.

To calculate what this means in terms of period ’relaxation’ we consider the following.

Light diffracted from the surface at an angle greater than 40 degrees (measured from the surface normal) will be totally internally reflected when striking the EVA-air interface. The wavelength that will diffract at this angle will have to be the lowest one in the spectrum (in our case 400nm) so that all the other wavelengths in the spectrum are also trapped in the substrate. In order for a wavelength of 400nm to diffract at 40 degrees we replace all the values required in the diffraction equation:

$$d = \frac{m\lambda}{(sin\theta_m + sin\theta_i)} \tag{3.24}$$

Where m = -1 (-1 diffraction order) , θ_m = 40deg, θ_i = 0deg , $\lambda = \lambda_{eva}$ = 256nm (equivalent to λ_{air} = 400nm). This gives a required period between diffracting features of: d = 398nm.

Hence, one can almost double the initial requirement of the subwavelength period being smaller than 200nm and still trap all light incident on the sample at normal incidence.

Therefore, it is shown that it is possible for one to mitigate somewhat the diffraction effects arising when using non-subwavelength manufacturing by designing the capping layer so that the angle of incidence with the superstrate in reflection is larger than the angle of total internal reflection between the substrate and the capping layer (Figure 3.15). Thus loss of efficiency from diffraction effects can be retained with clever design methods in order to make large scale deployment of subwavelength layers easier.

In any case, a full study of the diffraction properties of such surfaces is useful and will be carried out in the next sections.

3.2.2 Angle of elevation calculations: analysis of first diffraction order via use of the diffraction equation

The elevation angle for the first diffraction order will be studied in this section. The elevation angle is the angle defined between the surface vector of the interface and the diffraction direction as shown in Figure 3.16. The value of the diffraction elevation angle for various wavelengths will be measured as the period of the structure varies. Additionally the angle of elevation will be studied for various angles of incidence. Both these investigations can be facilitated by use of the diffraction equation.

The primary diffraction order elevation angle varies for each wavelength in a continuous fashion. Hence, when the incident light is not of single wavelength but a continuous spectrum, one can resolve it into its constituent wavelengths via diffraction. This concept is the principle of operation of modern spectrometers.

A graph of wavelength versus elevation angle for different grating periods can be calculated by rearranging the diffraction equation:

$$\lambda = \frac{d(sin(\theta_m) + sin(0^o))}{m} \tag{3.25}$$

Hence, via use of Equation 3.25, the wavelength dependence of the elevation angle can be plotted at normal incidence for varying diffraction grating periods between 450-600nm. (Figure 3.17).

A graph of wavelength vs elevation angle for different angles of incidence can also be carried out for a grating with a 800nm period:

$$\lambda = \frac{800nm * (sin(\theta_i) + sin(\theta_m))}{m} \tag{3.26}$$

Hence via use of equation 3.26 the wavelength dependence of the elevation angle is plotted in Figure 3.18 for varying angles of incidence (0-60 degrees) and a grating with period of 800nm.

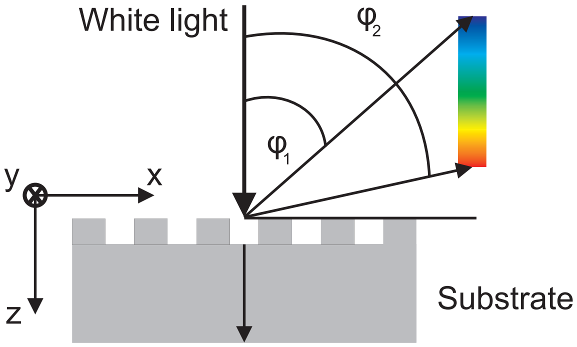

FIGURE 3.16: Elevation angles $\theta_1 < \theta < \theta_2$ for diffraction of different wavelengths from a sample interrogated with a white light beam at normal incidence

3.2.3 Angle of azimuth calculations: Primary diffraction order symmetry analysis via 2D Fourier transform

The inverse Fourier transform is a very useful tool used in physics, chemistry and in crystallography to characterize a crystal structure when knowing its diffraction pattern. In crystallography the structure of the crystal is inferred by the projection of the 3D diffraction pattern on a surface [77]. The opposite procedure will be carried out here via use of the normal Fourier transform. The structure is designed and the diffraction pattern is predicted from its Fourier pattern. The Fourier transform is hence a very useful tool in characterizing the azimuthal distribution of the diffraction pattern of a pillar topology in qualitative terms (Figure 3.19). Hence, with use of the diffraction equation described earlier the angles of elevation for different wavelengths can be predicted and by taking the Fourier transform of the pattern image the azimuthal distribution of the diffraction pattern can be inferred.

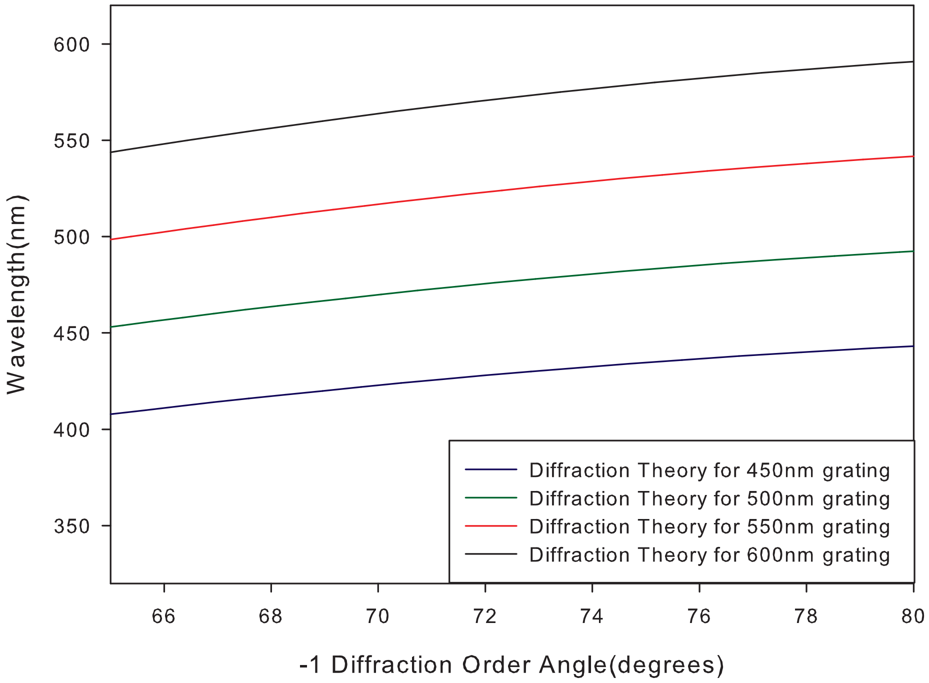

FIGURE 3.17: Diffraction order wavelength v elevation angle for gratings of different periods

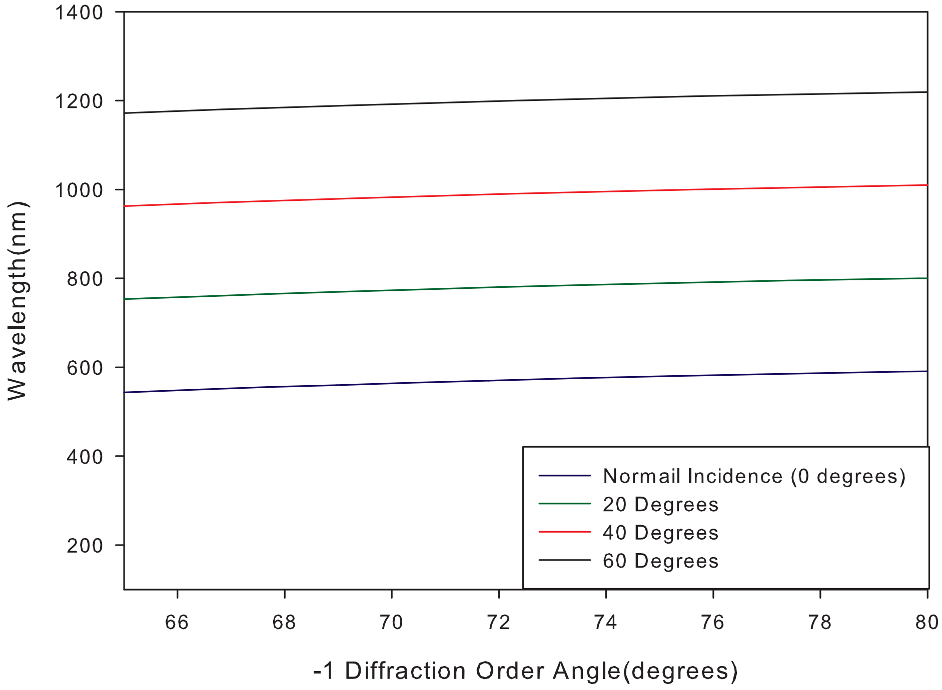

FIGURE 3.18: Diffraction order wavelength v elevation angle for different angles of incidence

The Fourier transform cannot however give information on the absolute power of each diffraction order. 'Rigorous' numerical techniques are required for such analysis. However, the RCWA simulation tools available did not allow such an analysis because they were only useful for simulating periodic patterns which can be defined by a unit cell.

The Fourier transform is a very flexible tool as it can be performed on any image whether it is a design file picture or a scanning electron microscope (SEM) image of a manufactured pattern. Hence, it works on samples that can be designed on a PC (i.e. hexagonal pattern, sunflower pattern) and self-assembled patterns that cannot be predicted but can be imaged by a SEM (i.e. tessellated biomimetic patterns). Both types of samples will be investigated and thus the Fourier transform can be used to aid in the characterization of these samples.

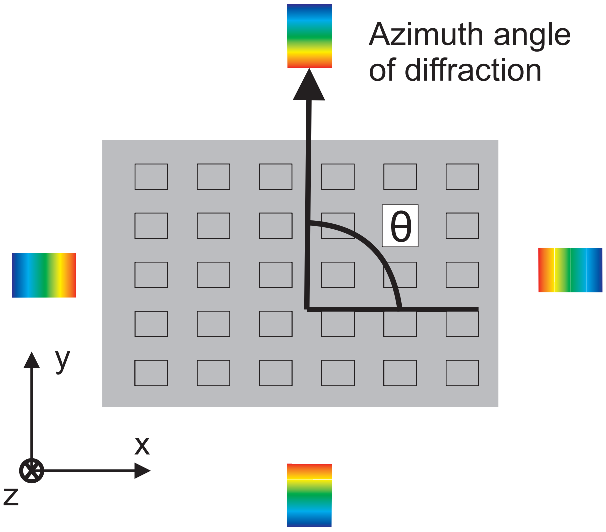

FIGURE 3.19: The azimuth diffraction angle for all wavelengths is identical, the number of diffraction spectra at different azimuth angles depend on the pattern symmetry

When the Fourier transform of the image of a moth-eye metamaterial layer is performed, each vertical pillar in the relief pattern is represented as a Dirac delta function with an associated unit mass. The "density function" is then characterized as the sum of all the points [77]:

$$\rho(x) = \sum_{y \in \Lambda} \delta(x - y) \tag{3.27}$$

$$J(s) = \left| \sum_{y \in \Lambda} exp(-2\pi i \mathbf{y} \cdot \mathbf{s}) \right|^2 \tag{3.28}$$

The Fourier transform computes the $\sqrt{J(s)}$. An analytical explanation for this derivation is presented in [78]. This value is not however an absolute measure of diffracted power.

3.2.4 Analytical explanation of information extraction from 2D image Fourier transforms

The Fourier transform of an image is a 2D Discrete Fourier Transform because a digital image is a collection of discrete entities (pixels). Hence, it does not contain all possible frequencies available in the original image, just those that are needed to sufficiently describe the image in digital form. The maximum frequency represented in any digital image is $fmax = 1/(2pixels) = 0.5pixels^{-1}$.

The DFT operation is defined as a linear operation. In order to calculate the Fourier transform of a digital image using the DFT we operate on each row of the image separately to create an intermediate DFT image. Then the operation is performed for each column of this intermediate image to create the 2D DFT image. The final result of these operations is known as the rectangular form of the real and imaginary components of the Fourier transform (Figure 3.20b). However, the most common form of presenting the real and imaginary components is in polar form (Figure 3.20c). These polar graphs relate to the magnitude and the phase of the Fourier components of the original image. The plot that will be of use to us in this section is the polar magnitude plot because it gives information about the symmetry and orientation of the axes of symmetry in the image. However, the polar magnitude plot of the normal 2D DFT is set up to arrange the high frequencies toward the middle of the image and the DC component toward the edge (Figure 3.20c). To interpret the results more intuitively, the magnitude plot is usually rearranged so that the DC component is in the middle of the image and the high frequency components are placed around the edges (Figure 3.20d). This form of the 2D DFT is the one which is most commonly presented in the literature when investigating axes of symmetry of an image or studying its Fourier transform. The image processing software that was used to carry out the 2D DFT Fourier transformations in this work was called ImageJ [79].

The further away the point is from the centre of the polar magnitude plot, the higher its frequency and consequently the smaller the wavelength associated with that feature. The highest frequency in any image is $f_{max} = 1/2$ pixels since the discrete pixel is the smallest feature in the image. This highest frequency is projected at the edges of the polar plot and the frequency closest to the centre projects the larger features in the image. In the centre of the image we have the DC component of the image which corresponds to the average magnitude of brightness of the image. We can ignore all other frequencies that are not related to the features we are interested in on the DFT image if the size of the feature (in pixels) is known.

In our case it is easy to extract the data that relate to the features we are investigating from the DFT of the image since they are the largest repeating features of the image and their 'frequency' is represented with the smallest amount of cycles on the Fourier

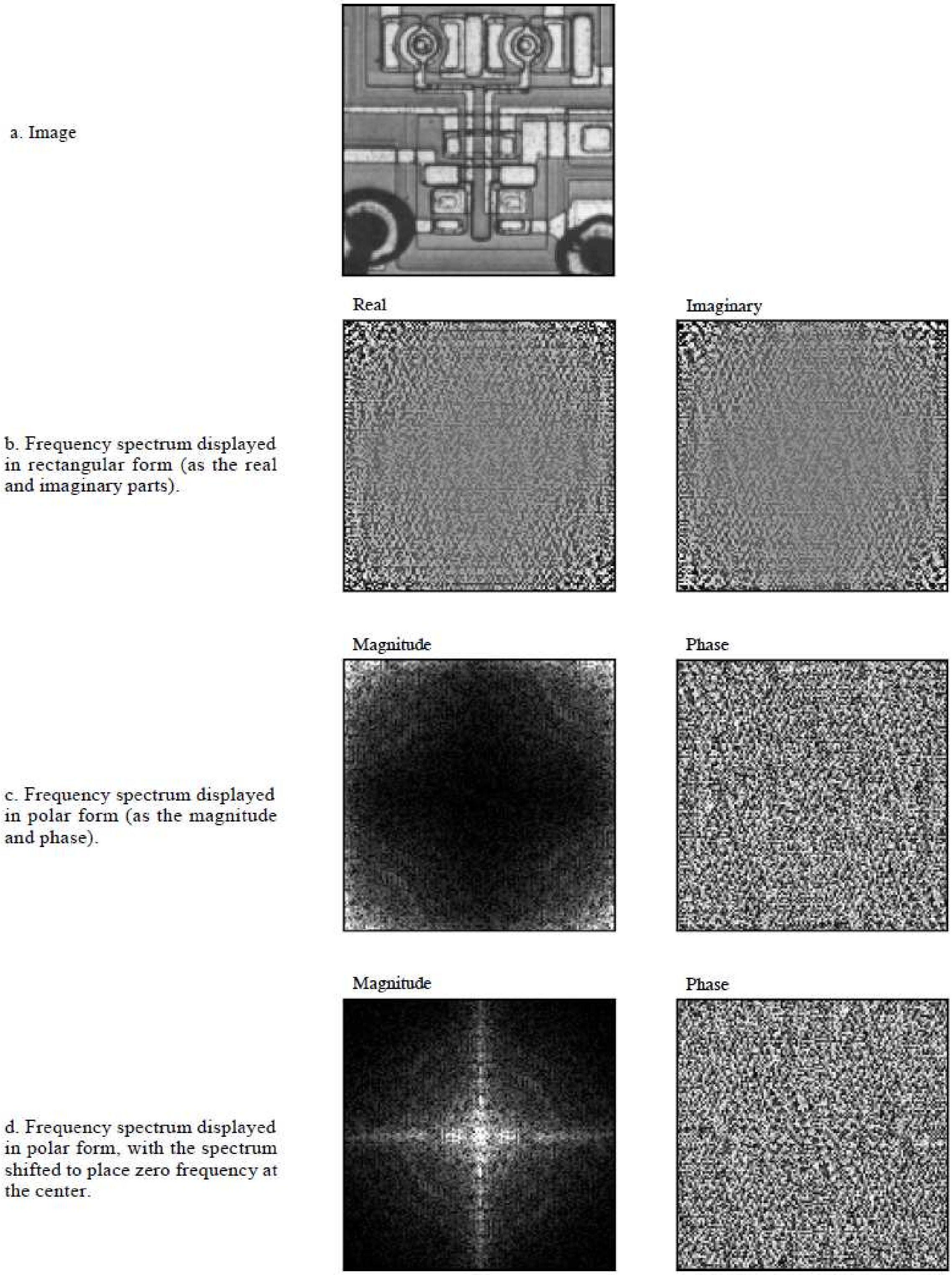

Figure 3.20: a) Original Image, b)Real and imaginary parts of image 2D DFT in rectangular form c) Polar equivalents of real and imaginary parts d) rearranged polar plots to depict DC in the middle of the image. [80]

plot, hence their frequency can be identified as the peak that is radially closest to the DC component in the 2D Fourier Transform.

However, when the feature periodicity is not aligned to the image pixel directions, we get extra features introduced to the image Fourier transform. The reason for this is that features that do not follow the two main axes of the pixels have to be stripe approximated which is required to represent curves in digital shapes and this effect adds extra high frequency components to the Fourier transform. In order to concentrate on the features of the Fourier transform that are relevant to the pattern characteristics we are interested in, we need to analyse the feature's digital shape. After analysis the Fourier transform can be cropped in order to provide the information which is relevant only to the features we are interested in. This was done for all the Fourier transforms depicted in this thesis.

Due to curve approximation in digital images, features can only be stripe approximated, since they will consist of a number of square pixels. To find the associated frequency of the feature we are interested in, the actual feature has to be analyzed first. The examples of two circular features which were approximated by the PC in pixelated form are shown in Figure 3.21.

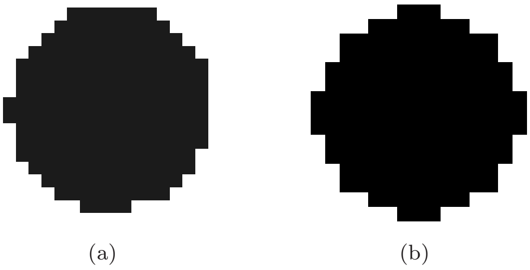
(a) (b)

Figure 3.21: PC rendering of circular features taken from two different images (a) with a close-packed pattern topology and (b) with a sunflower pattern topology

The average period of our feature in each direction will be the average of the length of all the rows of pixels that make up that feature in the x and y dimensions.

For example, the circular feature in Figure 3.21a consists of 15 rows of pixels with a number of pixels each (7, 9, 11, 13, 15, 15, 15, 16, 16, 15, 15, 14, 13, 11, 9). These are the sizes of the rows of pixels that make up the pc image of the circular feature. The average number of pixels per row is $12.93 pixels$. Hence the frequency of this feature when an 0.5 packing density is used is $1/(2 * 12.93) = 0.0386 pixels^{-1}$

If we want to find the frequency position that this average size corresponds to on the Fourier Transform image (again in pixels and counting from the center of the Fourier Transform) we have to invert this number and multiply this frequency by the half size of the Fourier image in pixels. $1024 * 0.0386 = 39.5 pixels$. Pixels are integer numbers and so the PC will round this figure up to 40. This means that the intensity of the frequency that corresponds to the feature we are repeating is located 40 pixels away from the center of the Fourier Transform.

Knowing this, we can plot the variation of relative intensity in frequency for this feature over all directions in the image if we take the intensities of all the pixels that lie at a radius of 40 pixels to the center. This pixel radius value of course is only for this particular feature shown in Figure 3.21a and varies according to the actual feature shape. The variation of the Fourier transform intensity vs azimuth angle for the close-packed and the sunflower patterns has been plotted in Figures 3.22b and 3.23b respectively.

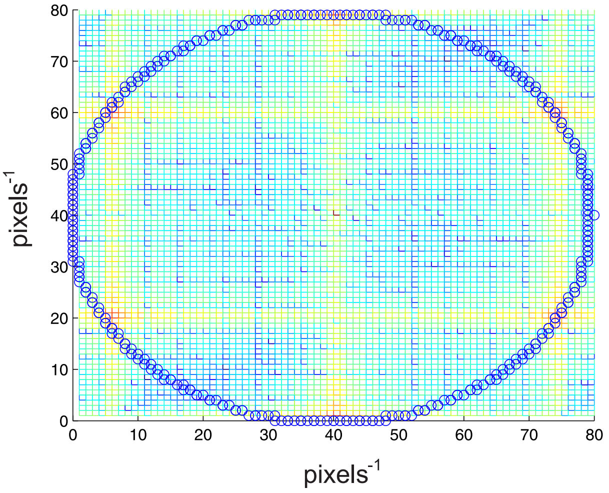

(a) Points selected from sunflower structure

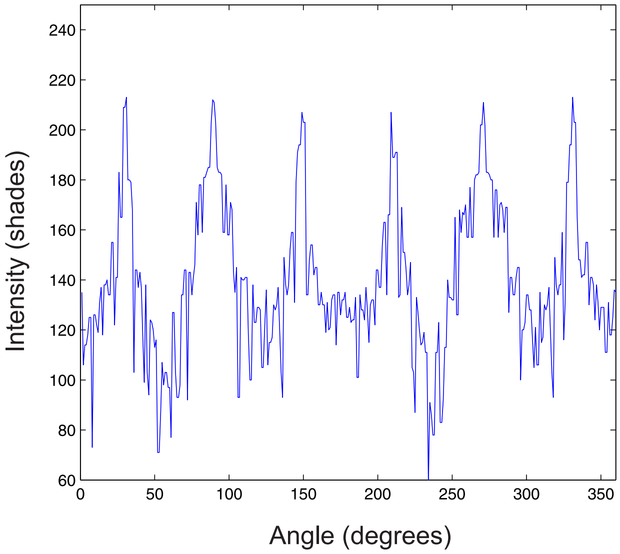

(b) Symmetry peaks extracted from FFT data and plotted from 0-360 degrees

FIGURE 3.22: Fourier data extraction.

In the sunflower pattern, which will be analysed further in Section 3.2.5.3, points are arranged around a central feature in counter rotating spirals. The number of spirals counted in each direction follows the Fibonacci series as one progresses from the centre of the pattern outwards. The distance between features follows a statistical distribution and hence predicting the feature 'frequency' in the Fourier transform is not straightforward. Hence, a simple averaging of the pixels in each row of the feature will not suffice. However, by using the previous technique, we can estimate a preliminary value for the 'frequency' of the radial value and from there we can find the closest frequency peak.

As for the close packed pattern, the number of pixels that approximate the circle in the image are calculated and averaged. For the sunflower the PC has approximated a feature shown in Figure3.21b. The average pixel length is $10.733 pixels$. This refers to a frequency of $1/10.733 = 0.0931 pixels^{-1}$. The point this refers to on the Fourier transform (from the center) is $512 * 0.0931 = 47.7$ which we approximate to 48 pixels.

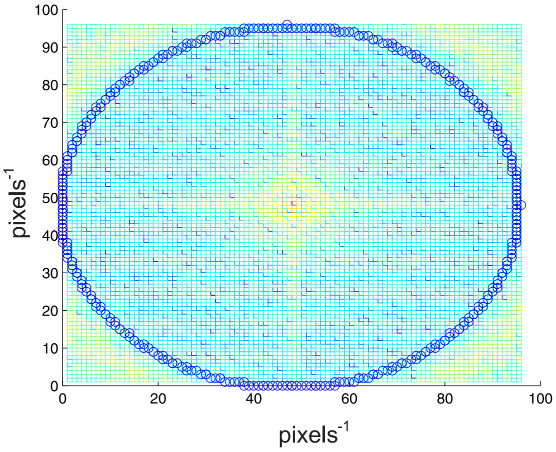

(a) Points selected from FFT that relate to the size of features

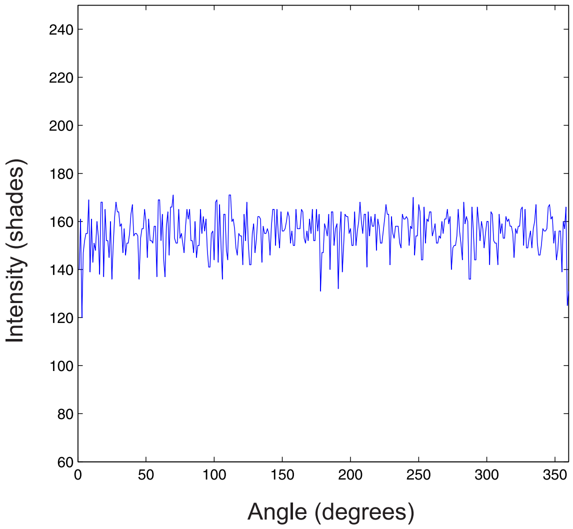

(b) FFT data for features plotted from 0-360 degrees

FIGURE 3.23: Fourier data extraction with the same method to hexagonal.

3.2.5 Analysing isotropic azimuthal diffraction gratings via Fourier Transforms

Ordered two dimensional crystals can possess up to six-fold optical rotational symmetry. This is the maximum that is allowed by the crystallographic restriction theorem as shown by the work of Rene-Just Hauy in 1822 [81]. In order to achieve higher orders of symmetry it is required to move to non-periodic quasi-crystals or quasi-periodic lattices. Thus to create an isotropic diffraction pattern, these concepts have to be applied to the design of the feature position.

The most common pattern topology used in the literature to construct ‘moth-eye’ antireflection layer is that of the ordered close-packed pattern which has six fold symmetry. Periodic patterns such as the close-packed pattern can be manufactured in large areas using conventional nanomanufacturing tools such as e-Beam and Nano-Imprint lithography since they can be described by a repeating unit cell. This feature is required to use the step-and-repeat method which can tile the nano-scale pattern without exceeding the machine memory limitations, by moving the stage under the pattern and stitching the same pattern next to the area already written. This way the pattern can be written over ’large’ areas (1x1cm) which is necessary for their full optical characterization. For example a typical laser beam spot size (∼1mm) becomes elliptical and considerably larger at high angles of incidence (5.7mm at 80 degrees).

The close packed arrangement can also be made in small areas ($\sim 10\mu\mathrm{m}^2$) using self-assembly methods such as Nanosphere Lithography (NSL) very easily because its linked to the minimum energy state of the particle ensemble. Self-assembly procedures operate by biasing the conditions of deposition so that the particle ensemble reaches its steady state of minimum energy and the close-packed arrangement happens to be the lowest energy state a group of particles can achieve on a flat surface [82].

There has been not much practical work done in investigating the effect of using higher rotational symmetry patterns to the moth-eye design. This can be partly due to the fact that most reports of antireflective measurements from moth-eye structures are interested only in comparing specular reflectance without taking into account the diffraction orders that emanate form the substrate at oblique angles of incidence [83], [84], [85].

Diffraction orders do not occur when the period of the packing is at the same scale as the wavelength of the incident light, but this is not the case at larger angles of incidence. For example, for a 250nm-period diffraction grating and a wavelength of 400nm, the first reflective diffraction order will start emanating from the sample at a very oblique angle of 89 degrees when the an angle of incidence increases beyond 36^o.

This can be calculated by rearranging the diffraction equation (Equation 3.19):

$$\theta_i = sin^{-1}(\frac{m\lambda}{d} - sin\theta_m) \tag{3.29}$$

Where d = 250nm , λ = 400nm, $\theta_m = 89^o$ and m = -1 (-1 diffraction order)

$$\theta_i = 36^o \tag{3.30}$$

Another possible reason for which the diffraction properties of non-periodic antireflection patterns have not been thoroughly studied is because of the numerous issues that arise when trying to simulate them. Most diffraction simulation packages such as GDCalc[1] and RSoft Diffract MOD[2]can easily accommodate periodic patterns because they only need to calculate the properties of the unit cell to describe the properties of the whole periodic pattern.

Diffract MOD is more flexible in defining the unit cell to be repeated which can be built without any inherit periodicity or limits imposed. GD Calc cannot operate with an arbitrary defined unit cell, because it operates by defining the design in regular stripes which creates various limitations in simulating random and regular pillar arrangements. In both cases however, the boundary conditions that are imposed are such that assume that this pattern is tiled over the whole surface.

In order to be able to simulate non-periodic patterns, all the points in the pattern have to be individually specified. There is no way of predicting the response of the whole cell by repeating the properties of a unit cell because by definition, a non-periodic pattern cannot be defined by a unit cell.

Concluding, even though the investigation of moth-eye arrays using the close-packed pattern is commonplace and relatively straightforward to simulate and manufacture, it is not optimum for studying the effect of increasing the isotropy of azimuthal 3D diffraction in biomimetic topologies. In order to improve matters in terms of isotropic diffraction, one has to move to quasi-crystal and quasi-periodic patterns whose manufacturing and simulation is much more ‘tricky’. The numerous issues noted here with simulating and manufacturing these patterns are tackled in various ways in the following chapters. The close-packed pattern will be revisited and used as the control example to which all other investigations are compared to.

---

[1] http://software.kjinnovation.com/GD-Calc.html

[2] http://www.rsoftdesign.com/

3.2.5.1 The close-packed pattern

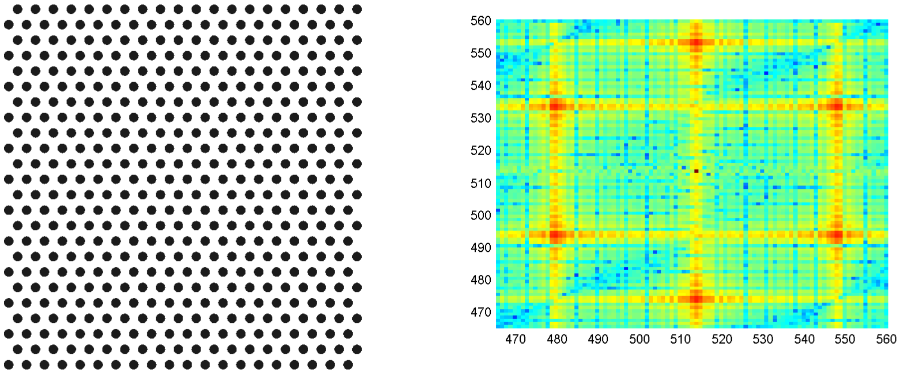

(a) Close-packed pattern design. (b) Fourier transform of the close-packed pattern.

Figure 3.24: The close-packed pattern design and its FFT.

The six-fold rotational symmetry of the close packed pattern can be depicted in its 2D Fourier Transform which shows six peaks associated with the protuberance features (Figure 3.24).

The six high-intensity peaks shown in the Fourier plot reveal the directions in which high periodicity is detected. In this case six such directions are recognized in the whole azimuth of the sample, depicting the six fold symmetry for the pillars in the close-packed pattern.

The image of the Fourier transform shown in Figure 3.24(b) illustrates the lowest spacial frequencies of the DFT image which are the ones closest to the centre of the image (DC peak). The lowest frequencies relate to the largest features of the image which are the design pillars. The exact method used to confirm the radial frequency of the features in the DFT image has explicitly been analysed in the previous section (Section 3.2.3).

3.2.5.2 Quasi-crystal Disorder

In order to create isotropic diffraction from a moth eye grating, more complex non-periodic patterns have to be employed. One such genre of non-periodic patterns are referred to as quasi-crystals. Quasi-crystals are a type of non-periodic crystals that possess a higher symmetry of Bragg diffraction. They were first reported in 1984 by Dan Shechtman et al. who described "the existence of a metallic solid that diffracts electrons like a single crystal which is inconsistent with lattice translations" [86].

Quasi-crystals provided the first proof-of-concept that non-periodic lattices exist in nature and verified their ability to produce rotationally symmetric diffraction patterns which were not limited to the classical periodic symmetry attained from the four crystal systems and 5 Bravais lattices of the plane [87]. Up until then, the diffraction patterns

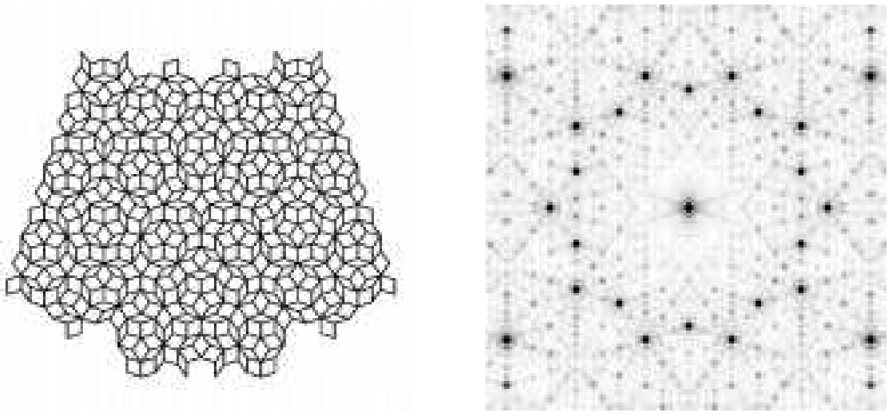

(a) Penrose tiling (b) Fourier transform

FIGURE 3.25: The penrose tiling pattern design and the Fourier transform of the points placed at the verices of the tiling. [77]

were limited to those produced by regular periodic patterns that can tile the plane in a step-and-repeat fashion which can only produce two- three- four- and six-fold rotational symmetric diffraction patterns [77].

In general, quasi-crystals are an example of the existence of aperiodic tilings in nature. The mathematical construct of aperiodic tiles was first conjectured by Hao Wang in 1961 [88] and later developed by his student Berger in 1966 [89]. Their work found application to the physical field of quasi-crystal research years later when their discovery created the paradigm shift that non-periodic symmetric crystals can produce Bragg diffraction similar to that noticed in regular periodic crystals.

Moth-eye antireflection surfaces are essentially a two dimensional packing of pillars which can be defined via lattice rules. Hence, a quasi-crystal tiling scheme can be applied to distribute the pillars on the substrate in a non-periodic symmetric fashion. Work in applying quasi-crystal concepts to photonic crystal design has recently been by Pollard [90].

An example of a quasi-crystal structure with 6-fold symmetry is the sphinx tiling [77]. Senechal et al [77] also show 10 fold-symmetric structures for chiral, the Penrose, and binary tiled structures. Examples of quasi-crystal lattices based on a square-triangle tiling system have been reported to obtain 12-fold symmetry [91]. The pin-wheel tiling has an apparent infinite symmetry due to the fact that the tiles occur in infinitely many orientations but practically, the symmetry obtained by this structure in real samples is reduced to 8-fold [92]. Hence, even when using aperiodic tiling rules to induce disorder in the protuberance pattern and increase diffraction symmetry one is not capable of achieving full azimuth diffraction isotropy.

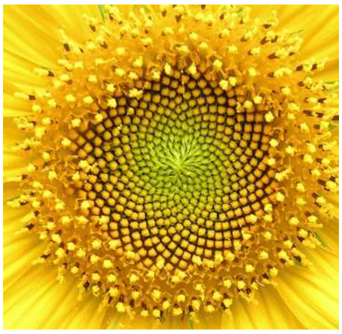

FIGURE 3.26: Pattern of seeds in actual sunflower

3.2.5.3 Fibonacci spiral biomimetic disorder: sunflower pattern

The sunflower pattern can achieve a complete ring in the Fourier transform which suggests complete isotropy for this design's diffraction pattern [93]. Photonic bandgap measurements have shown complete isotropy for a 2D planar photonic crystal [90] This pattern is not quasi-crystalline in nature, in the sense that it is not tiled across the surface using prototiles (a set of shapes which are non-congruent) or any other tiling rule. It is nonetheless non-periodic and completely rotationally symmetric around its centre. It is named the sunflower pattern because it resembles the positioning of the seeds in the head of the sunflower.

The sunflower pattern design consists of counter rotating spirals, the number of which follow the Fibonacci sequence. The position of each point in the sunflower can be expressed in polar coordinates by:

$$r = c\sqrt{n} \tag{3.31}$$

$$\theta = n\phi \tag{3.32}$$

Where $\phi \approx 137.51^o$, the golden angle, c, the scaling factor, and n the index number of each point (starting from the center and going radially outwards).

The method shown for the construction of the sunflower pattern mathematically, was suggested by Vogel in 1979 [94] and used to design the sunflower pattern in Matlab shown in Figure 3.27a.

The nearest neighbor distances in the sunflower pattern vary but do follow a relatively tight distribution. A histogram of inter-particle spacings for the sunflower pattern calculated by Delaunay Triangulation (Figure 3.27b) is shown in Figure 3.27c.

The 2D Fourier Transform analysis of the sunflower pattern image in Figure 3.27d produces a very dense circular distribution of peaks which is associated to the modal value of distances between the points in the pattern (calculated to be 1.675 for a scaling factor of c=1). The results of the DFT show that the pattern is symmetric in an uncountable amount of directions on the surface and hence can be characterized as fully isotropic.

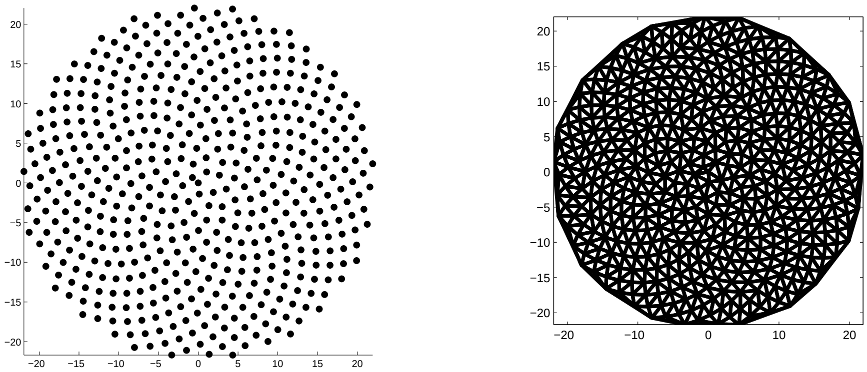

(a) 500 point Sunflower pattern

(b) Delaunay Triangulation of nearest neighbors

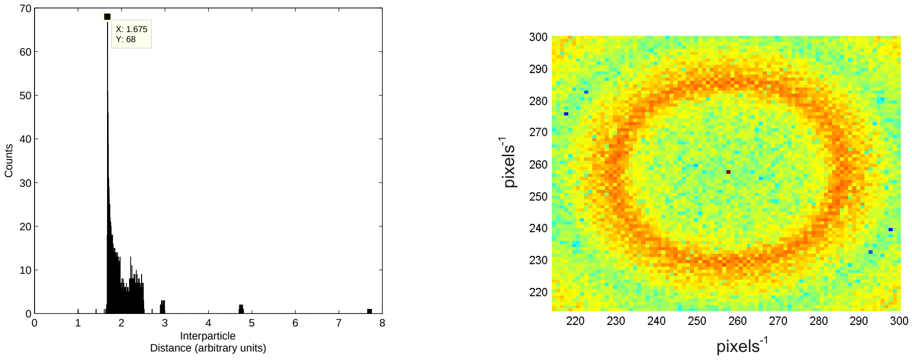

(c) Nearest neighbor distance histogram (Scaling factor: c = 1)

(d) Fourier transform of sunflower pattern.

Figure 3.27: Sunflower pattern inter-particle distance analysed in Matlab via Delaunay Triangulation and sunflower FFT pattern.

3.2.5.4 Biomimetic Moth-eye 'Domain Type' Disorder

By re-investigating the arrangement of the protuberances on the real moth-eye which originally inspired the use of subwavelength structures for antireflection purposes [29], one can notice that the protuberances are not strictly ordered but contain a certain 'biological'-type disorder. On a real moth's eye, small pockets of ordered lattices are organized on the surface within domains. The orientation of the ordered pattern varies between domains to create a 'patched' surface. This kind of disorder will be called 'tessellated close-packed' disorder and refers to the bio-inspired packing of protuberances in domains on the corneal surface of a moth's eye.

It is not obvious that the reason behind this disorder is evolutionary, since it is also noticed in a myriad of other naturally-occurring processes which have no reason to be optimized for antireflection such as the growth of polycrystalline lattices (Figure 3.28b). It could be that the disordered architecture is the only mechanism that is available in nature to create these moth-eye surfaces in the first place, but whatever the reason, moth species that have this type of tessellated pattern possess a stealth advantage over their predators which assists in their survival.

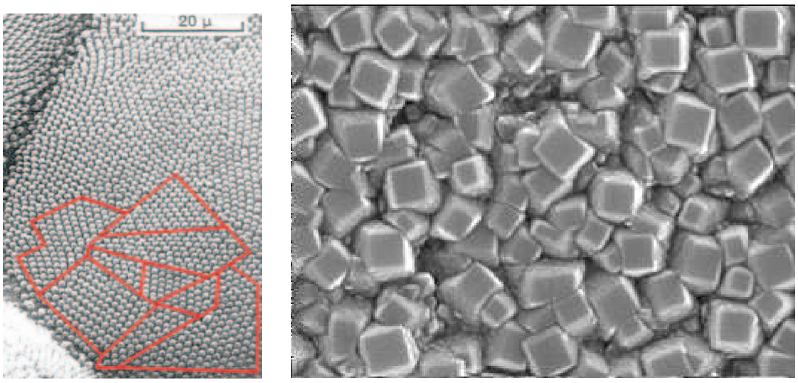

(a) SEM of a moth-eye showing natural forming domains

(b) Polycrystalline domains [95]

Figure 3.28: Examples of bio-inspired disorder

To show that this is the case, we start from the most simple disordered square domain pattern we can imagine, which includes two orientations of the close packed pattern (Figure 3.29a,c). We can immediately see that compared to a mono-orientational close-packed pattern (Figure 3.29 a), its 2D Fourier Transform (Figure 3.30 b) differs to that of the mono-orientational sample (Figure 3.30 a) in terms of rotational symmetry. Twelve peaks are present instead of six that would normally be expected for the close packed pattern. Continuing this trend, it was observed that the more orientations that were considered in the tiling (1-4) Figure 3.29 (a-d), the more peaks were shown in the Fourier transform (6-24) as shown in Figures 3.30 (a-d) but when two orientations which have an angular offset equal to the repeating symmetry of the underlying pattern were used, no increase of symmetry was observed 3.30(f)).

Hence, it was suggested from the Fourier transform of these patterns, that as the number of independent orientations included in the design is increased, so does the symmetry of the diffraction pattern. It can therefore be postulated that by having a large amount of random orientations, as in the case of the real moth-eye pattern, nature has found an 'easy' way to create an efficient stealth/antireflection pattern which scatters light in isotropic directions. It also seems that biological evolution has indeed produced an advanced optical design to allow night flying moths to avoid detection by predators by reducing optical reflection and additional diffraction orders from their corneas in a very efficient manner.

Being non-periodic, the study of the diffraction behaviour of the tessellated close-packed pattern with 'rigorous' simulation methods cannot be done via the software package that was available (RSoft Diffract MOD). Even if this was possible, a large amount of domains would require a very large design pattern which would be impractical and would require very large processing time to complete. Hence, it was decided that finding a way to manufacture this sample and testing its diffraction properties would be much more useful (and quick) than attempting to simulate it.

In conclusion, it was found via Fourier analysis that a pattern with high rotational optical symmetry can be acquired by positioning a large amount of independent orientations of the close packed pattern on a surface. Hence, one can perceive that a domain structure that would produce isotropic diffraction is one that has infinite orientations of the close packed pattern applied uniformly on a surface. Thus, finding a method to produce such a pattern with a very high number of independent orientations, would result in similar behaviour to that of an isotropic diffraction grating which possesses a ring in its Fourier transform, just like the sunflower. However, contrary to the sunflower, the points don’t have to be organized in a complex mathematical pattern.

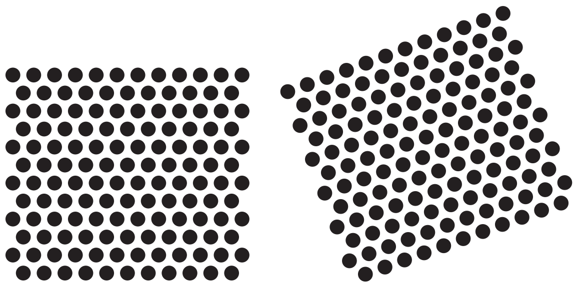

(a) Initial orientation (b) 15 degrees offset

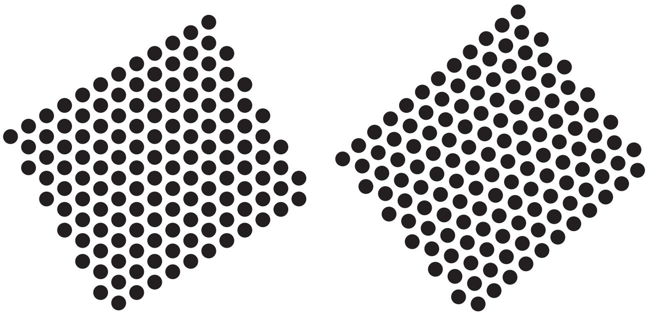

(c) 30 degrees offset (d) 45 degrees offset

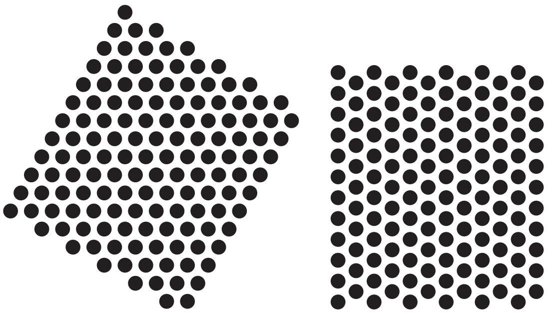

(e) 60 degrees offset (f) 90 degrees offset

Figure 3.29: Hex pattern orientations

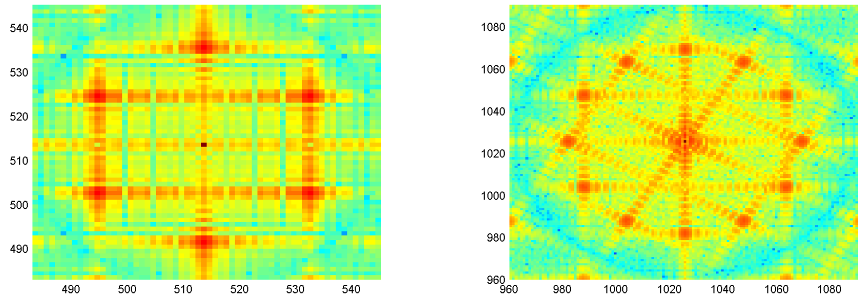

(a) FFT of orientation shown in Figure 3.29(a)

(b) FFT of pattern with orientations shown in Figures 3.29(a),(c)

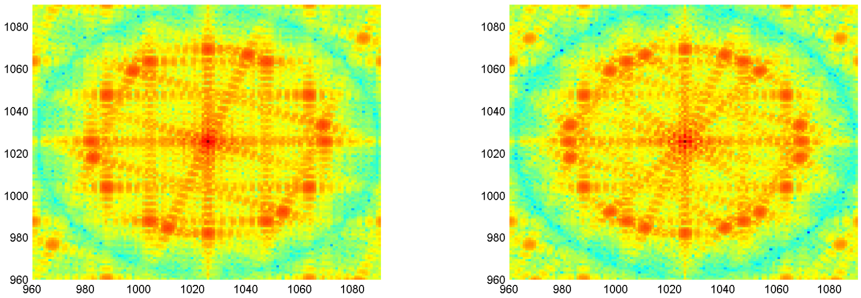

(c) FFT of pattern with orientations shown in Figures 3.29(a),(b),(c)

(d) FFT of pattern with orientations shown in Figures 3.29(a),(b),(c),(d)

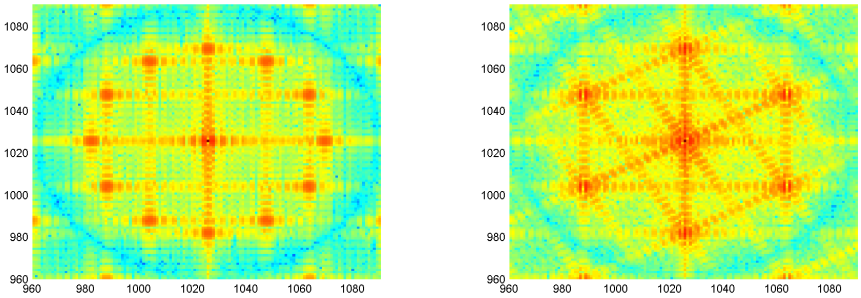

(e) FFT of pattern with of orientations shown in Figures 3.29(a),(f)

(f) FFT of pattern with of orientations shown in Figures 3.29(a),(e)

FIGURE 3.30: Fourier transform of various orientation combinations of patterns shown in Figure 3.29

3.2.6 Conclusions

Diffraction analysis of subwavelength feature antireflection layers can provide us with information on the elevation and azimuthal orientation of the diffraction orders that could emerge from the substrate for some wavelengths in the spectrum considered which are not completely subwavelength to the period of the features and/or strike the substrate at a high angle of incidence. Elevation analysis of the diffraction order can be carried out using the standard diffraction equation. This information could allow relaxation of the optical design by making the period of the features larger on purpose and trapping the diffraction orders via total internal reflection with an intermediate layer.

Azimuthal diffraction analysis is carried out by taking the Fourier transform of a top view image of the feature topology. The Fourier transform shows the directions of symmetry of the pattern or equivalently, the azimuthal directions that diffraction orders will appear at. The Fourier transform is a useful tool in characterizing antireflection layers in terms of their diffraction order azimuthal isotropy. A straightforward method of designing a more isotropic pattern is by increasing the design complexity in terms of the rotational symmetry of the pattern. By revisiting biomimetic tessellated patterns, it was found that isotropic diffraction could be achieved by increasing the number of orientations of a low symmetry topology in a biomimetic manner. Methods of realizing these biomimetic tessellated surfaces will be investigated in later chapters.

Chapter 4

Nano-Manufacturing moth-eye anti-reflection layers

The procedures that were used to create the samples which were characterized in this thesis will be presented in this chapter. An extensive analysis of the nanosphere lithography method that was used for the purposes of this thesis, will be presented separately in Chapter 5. In this chapter the other nanomanufacturing methods that were used will be described. Some of the samples which were created with the methods described in this chapter were made at Nano-Imprint Lithography Technologies (NILT , Diplomvej 381, DK-2800 Kongens Lyngby, Denmark) and others were made at the University of Southampton by INNOS (University Road, Southampton, United Kingdom, SO17 1BJ). Before explaining the specific techniques that were used for manufacturing the moth-eye structures in detail, a general review of current nanomanufacturing methods will be carried out.

4.1 Nano-Pattern engineering

4.1.1 ’Top-down’ pattern design methods

Methods that require a predetermined design are called ‘top-down’ techniques because the pattern is made on the large scale (i.e. on a CAD program) and then scaled down to the required size. In a top-down procedure, the pattern design and its position on the substrate are set from the beginning. The pattern is inscribed by exposing a resist in specific areas to a form of energy which changes its internal chemistry such as an electron beam, or light of a specific wavelength. Examples of such ‘top-down’ nanoengineering techniques are Photolithography, Electron-Beam lithography (e-beam), Nano-Imprint Lithography (NIL), Focused Ion Beam Lithography (FIBL) and Soft-Lithography. Areas that should not be etched or deposited on are protected by the resist after patterning.

The ‘etch mask’ could be a software program which controls when the ion beam turns on and off as it scans the surface, or it could be a hard mask such as chrome layer that is in between an ion source and the substrate.

E-beam lithography and photolithography use a beam of electrons and light respectively to pattern the resist in certain areas and a substrate etch takes place after the resist is developed. Both methods were investigated for their ability to make the moth eye features required for the purposes of this thesis because they were available in the clean room at Southampton. This investigation will be discussed in detail in sections 4.2 and 4.3 respectively.

Nano-imprint lithography was not directly used and the work shown here was done in collaboration with NILT technologies, Denmark. Nano-imprint technology uses e-beam lithography to make a hard stamp which is then used to mold the etch mask on a substrate. This technique is explained further in Section 4.4

Focused Ion Beam Lithography operates similarly to e-beam but it uses a beam of ’heavier’ material (Gallium ions) to strike the substrate compared to the electrons used in e-beam lithography (Figure 4.1). This means that there is no need for a resist or a subsequent etch procedure to create the pattern relief as the beam etches the substrate directly. In cases when the substrate is not conductive enough (e.g. the case of patterning glass), it needs to be coated with a few nanometers of a conductive material, such as gold, in order for the beam to operate effectively.

Focused Ion Beam Lithography can also be used to create the mask by removing material from a hard resist layer deposited on the surface of the substrate in the beginning of the procedure. The substrate can later be removed in the area where the hard metal mask has been patterned via a dry or wet etch using the patterned layer as a mask. This method is less commonly used as the etching of the substrate is usually performed by the beam itself.

Soft-lithography, just as nano-imprint lithography, requires a master to pattern the soft material used in the procedure. In the case of soft-lithography, a stamp is created by the master to transfer an ’ink’ onto the wafer by bringing the stamp into contact with the substrate. The printed regions of the substrate can be used as an etch mask.

The stamp is made by cast molding. First, a hard master is created via conventional nanoengineering techniques such as photolithography or nano imprint lithography. This master is usually made of a silicon dioxide layer grown on a silicon wafer. The master is then silanized by exposure to FTDS (fluorodecyltrichlorosilane whose chemical bond structure is: $CF_3(CF_2)_6(CH_2)_2SiCl_3$) vapor. An elastomeric material usually PDMS (Polydimethylsiloxane) mixed with a curing agent is then poured over the master. Heat is applied and the polymer is hardened by cross-linking the elastomer by the hydrosilylation reaction between the vinyl ($SiCH{=}CH_2$) groups and hydrosilane (SiH) groups [96].

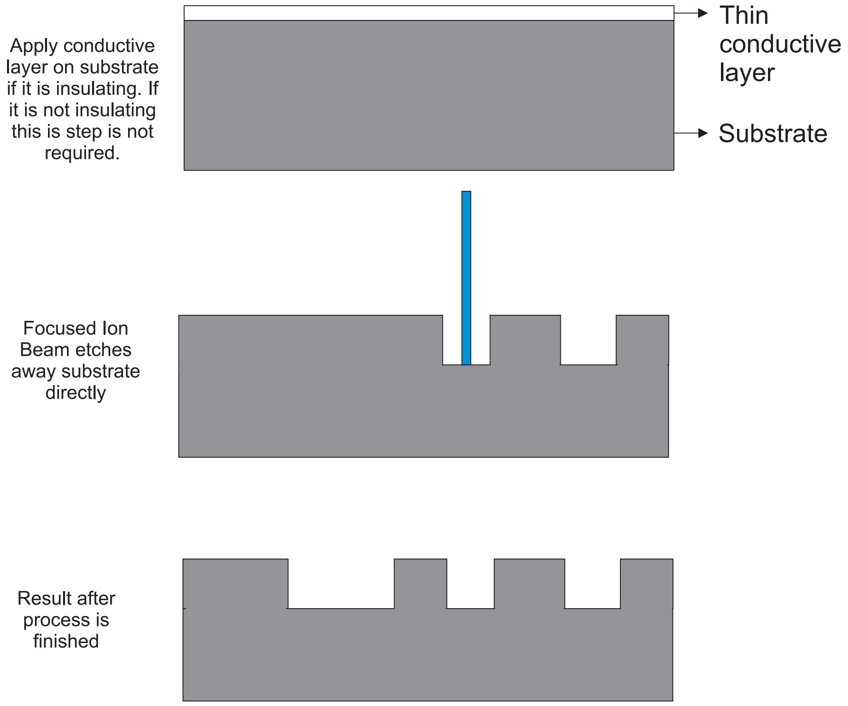

FIGURE 4.1: Process steps in creating pattern via focused ion beam lithography

Five techniques used for cast molding are: microcontact printing (μCP), replica molding (REM), microtransfer molding (μTP), micromolding in capillaries (MIMIC) and solvent-assisted micromolding (SAMIM) [96]. The main advantage of soft-lithography is that non-planar surfaces can be textured by this technique. Three dimensional microstructures and systems can also be created via soft-lithography. Stamps are cheap to create and once made can be used in mass manufacturing large substrate areas.

One of the disadvantages of this method is that deformation and distortion of the stamp takes place when transferring the pattern to the substrate which complicates the procedure because the stamps have a certain lifetime before they have to be made again. Furthermore, the elastomer has to be optimized, for features with very small sizes because there is a certain density of defects in the final patterns which needs to be characterized so that the stamp created is compatible with the tolerances specified by the fabrication requirements. Finally, the master is created by conventional top-down techniques such as e-beam lithography and photolithography which means that the technological limits of the stamp are bound by the technological limits of the methods used to make the master.

4.1.2 'Bottom-up' pattern design methods

In the “top-down” nanoengineering techniques previously presented, a design is prearranged in set locations and is scaled down to fit the size required on the wafer. The

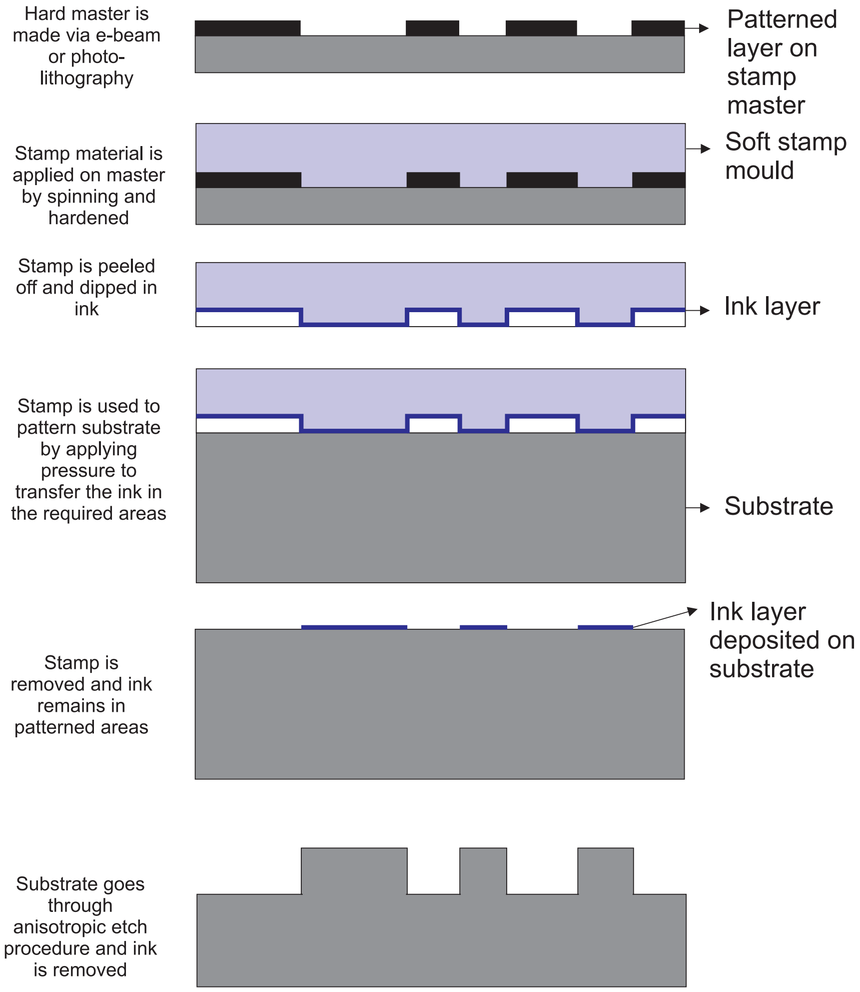

Figure 4.2: Process steps in creating pattern via soft lithography

techniques that will be presented here are referred to as ‘bottom-up’ or ‘self-assembly’ techniques. These methods are called ‘bottom-up’ because they create the design particle by particle. The design is constructed ‘automatically’ by achieving the minimum energy state of the particle ensemble after deposition takes place. Self-assembly techniques could be cheaper and faster than ‘serial’ nanoengineering techniques such as e-beam lithography when patterning large areas. This is mainly because there is no design procedure required to create the mask, the minimum features used are cheap to mass manufacture and the technique is massively parallel because the pattern is created on the whole substrate concurrently. The deposition of the nanoparticles is usually performed via a chemical procedure because the particles are handled in colloid suspensions. Nanosphere lithography [97] and DNA assembly [98] are examples of self-assembly techniques.

In nanosphere lithography (NSL), a colloid suspension of nanosphere particles (usually made of polystyrene, PMMA or silica) is processed to produce either mono-layers or multi-layers of organized sphere ensembles. This technique was pioneered by Deckman and Dusmuir [99] in 1982 and is a very versatile and materials general nanofabrication process.Nanosphere self-assembly can be achieved by multiple methods which will be outlined further in Section 5.1 but three types of forces are mainly used to assemble the spheres namely electrostatic, gravitational and capillary forces.

Partial control of the ordering of the nanospheres can be applied by creating a template on the substrate to bias the self-assembly procedure. For example Blaaderen et al. [100] have shown that it is possible to control the orientation of a 3D nanosphere lattice by using a template of holes etched into the substrate before nanosphere sedimentation. With this technique growth of nanosphere lattices with (110) and (100) plane orientations instead of the common and energetically favourable (111) lattice orientation was achieved. Two-dimensional control of the orientation of nanosphere monolayers within guided templates has also been demonstrated by Kiziroglou et al. [101] (Figure 4.3).

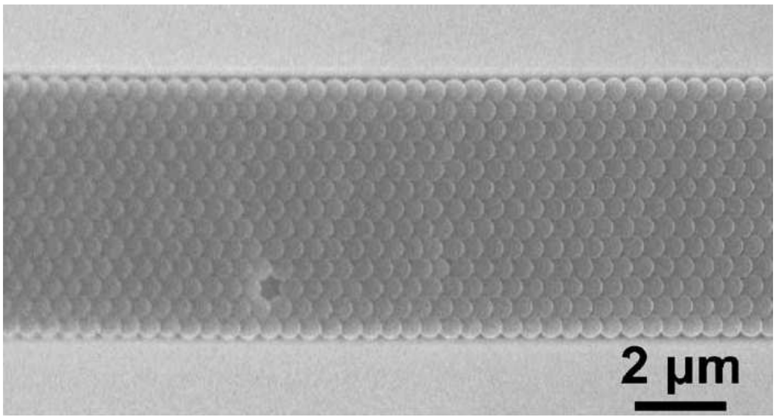

Figure 4.3: SEM image from [101] depicting 2D colloidal crystal organization via a SiO_2 patterned template created on a silicon substrate to guide the nanosphere deposition. The template width is 6μm and the SiO_2 thickness deposited is 250nm. PMMA photoresist patterned via photolithography was used as the etch mask to creating the template in the silicon dioxide layer via 20:1 Buffered HF etch. A short subsequent 20:1 Buffered HF etch was used to terminate the silicon surface with hydrogen and make it hydrophillic. The deposition of the nanospheres was achieved by drop casting a 1% water suspension of 500nm-diameter spheres.

Three general types of nanoscale motifs can be created via the nanosphere lithography process, namely opals (and inverse opals), evaporated patterned layers and etched patterned substrates (Figure 4.8). Inverse opals and opals can be created by using a close-packed arrangement of nanospheres self-assembled in multilayers [102], [103].The ability of creating inverse opals has been extensively used to study the properties of photonic crystals that can be created via this route. [104] (Figure 4.4) , [105], [106], [107], [108].

Closely spaced nanoparticles organized in hexagonal arrays can be evaporated on the substrate by using a close-packed nanosphere monolayer or bi-layer as the evaporation

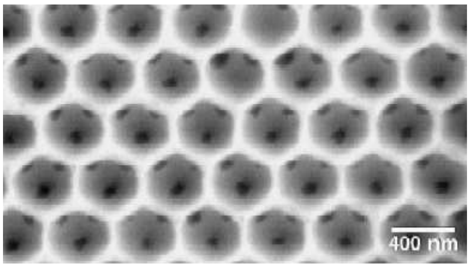

Figure 4.4: SEM image from [104] depicting a silica inverse opal created by 3D colloidal crystal organization of 400nm diameter polystyrene particles and subsequent filling with a sol-gel technique. These inverse opals are also called 3DOM structures which have been successfully created with a wide range of materials. In [104] a review of 3DOM structures made by metals, simple oxides, ternary oxides, polymers, chalcogenides, alloys and hybrid organo-silicates has been presented.

mask. [109], [110], [111]. This method is usually called the 'lift-off' technique. The process is relatively simple, first, the material is evaporated directly onto the nanosphere layer and then the nanospheres are subsequently dissolved. When the nanospheres are dissolved they remove only the material which was deposited on them directly, leaving the rest of the material that evaporated through the sphere voids onto the substrate. Changes to the shape of the evaporated particles can be induced via changing the angle of the nanosphere array relative to the beam of the evaporated material [112]. This technique has been extensively used to study the plasmonic properties of size-tuned metal nanoparticles[113], [114], [111], [115].

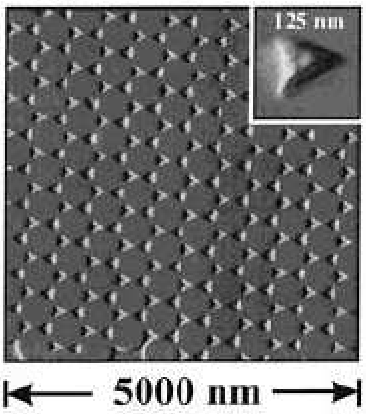

Figure 4.5: SEM image from [111] depicting a silver nanoparticles created on the surface of a silicon substrate after evaporation of a 48nm silver layer and subsequent 'lift-off' of 542nm diameter polystyrene nanospheres by sonication in methylene chloride for 3 minutes.

If the size of the nanospheres is reduced via an isotropic etch before evaporation of the material, instead of the evaporated layer being in the form of scattered nanoparticles a continuous macroporous layer is created. This macroporous layer can be used as an etch mask to create a macroporous substrate, [116] or electrodeposition can take place to form spherical cavities [117]. A monolayer of nanospheres can also be directly used as an etch mask to create a porous substrate if the selectivity of the etch between the substrate and the nanosphere material allows this [118].

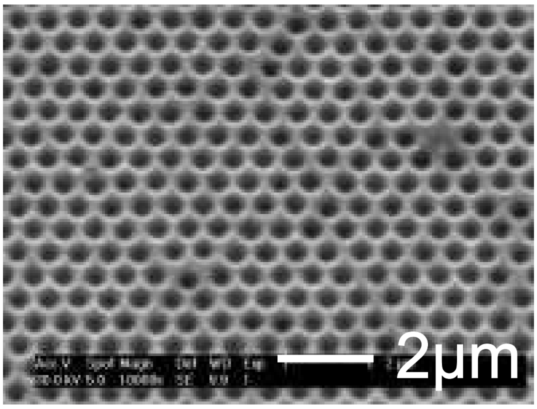

FIGURE 4.6: SEM image from [117] depicting a gold film which was prepared by initially evaporating gold through a 700nm-diameter close packed configuration of polystyrene nanospheres on a cysteamine-coated 200nm thick gold layer which was handled on a glass slide substrate. The nanospheres were then dissolved and 500nm-diameter spheres were assembled onto the voids of the previous evaporated pattern. Finally, gold was electrodeposited through the 500nm-diameter polystyrene sphere template, filling the voids between spheres. The spheres were subsequently removed creating a layer of macroporous gold which was patterned with 500nm diameter voids, on a 700nm diameter pitch.

By reducing the size of the nanospheres in the monolayer prior to etching the substrate, the nanosphere ensemble can be used directly as an etch mask to form nanopillars on the substrate [97], [119]. This method was used to create moth-eye pillar layers shown in this work and will be described in detail in Section 5. NSL can also be used to create nanopillars on the substrate indirectly via patterning a Nano-Imprint lithography stamp as shown recently by Ling et al.[120].

NSL is thus useful for creating numerous types of structures which can find use in various applications. Macroporous polysilicon created by a nanosphere etch mask has been recently suggested as a drug delivery device [121] [122]. Muscatello et al. at the Asher Group have suggested that polymerized photonic crystal assemblies can be included into contact lenses and used as devices which can monitor glucose levels in the body [123]. Zhu and co-workers have demonstrated the ability of texturing the surface of glass via NSL in order to use the corrugated layer to create ultra thin solar cells with enhanced efficiency [124]. Broadband antireflective layers created by NSL for the enhancement of monocrystalline solar cells has also been recently suggested [119]. Creation of periodic magnetic media via NSL is also possible, and can be used to create very dense magnetic memory storage [101], [125], [126], [127]. Patterning large arrays metal nanoparticles via NSL on flat substrates is very useful for biosensing applications, [128], [129], [130]. Due to the large surface area of nanosphere-templated inverse opals, it has also been

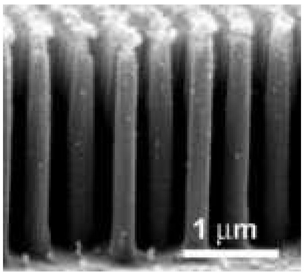

FIGURE 4.7: SEM image from [97] depicting the creation of nanopillars in silicon via nanosphere lithography. The 350μm nanosphere water suspension was mixed with 50μl of Triton X-100 diluted with methanol (1:400). The mixture was then spin coated on a silicon wafer (stage 1: 400rpm for 10seconds, stage 2: 800rpm for 2minutes, stage 3: 1400rpm for 10seconds). The spheres were then etched for 120seconds in an O2 plasma etch which reduced their diameter from 500nm to 400nm. A subsequent Bosch etch by alternating SF_6 (12sccm, 12seconds) and C_4F_8 (85sccm, 9seconds) gases was used to etch the pillars in the substrate (RF power: 600W, Platen power: 14W, Chamber pressure: 4.5mTorr, Substrate temperature: 25^o).

suggested that they could be useful in reducing solid state ionic diffusion form battery electrodes and hence improve batterty lifetime [131].

DNA nanoassembly was recently shown to create addressable structures. In the work by Park et al [98], two methods have been depicted in combining DNA tiles, the first creates curled tiles which are not created to be flat on the substrate due to the inherit curvatures of the tiles used. The second method described proved more efficient in creating addressable flatter tiles whilst adding different materials to the tiles before assembly. Selected tiles were combined with fluorescent markers for proof-of-concept of self-assembled addressability, by spelling the three letters D,N,A in the correct sequence with three 4x4 unit prototiles. Hence, it is shown that there is a very large control over the relative positions of individual particles after self-assembly. The particle arrays created are individually addressable and controllable. This method is a very cheap and powerful method of nanoassembly in the sense that only the initial conditions are specified and the natural folding of the DNA takes care of the rest of the assembly procedure. This leads to a low number of production steps, which makes it a very quick and simple method of defining patterns in large areas. However, the process is not yet able to produce high area addressability and control (only 4x4 matrices are addressable). Furthermore, the yield of complete arrays on the surface is low and the orientation and position of DNA lattices on final substrate are random. Finally, this method is size-limited by the DNA strand used to make prototiles which cannot be scaled down readily (25x25nm area).

Using the self-assembly of block copolymers to create ordered nanostructures has also been suggested in the literature [132]. Block copolymers are made up of blocks of polymerized monomers which can micro-phase separate to create nanostructured arrays. However, a great disadvantage of block co-polymers is that they don't allow control

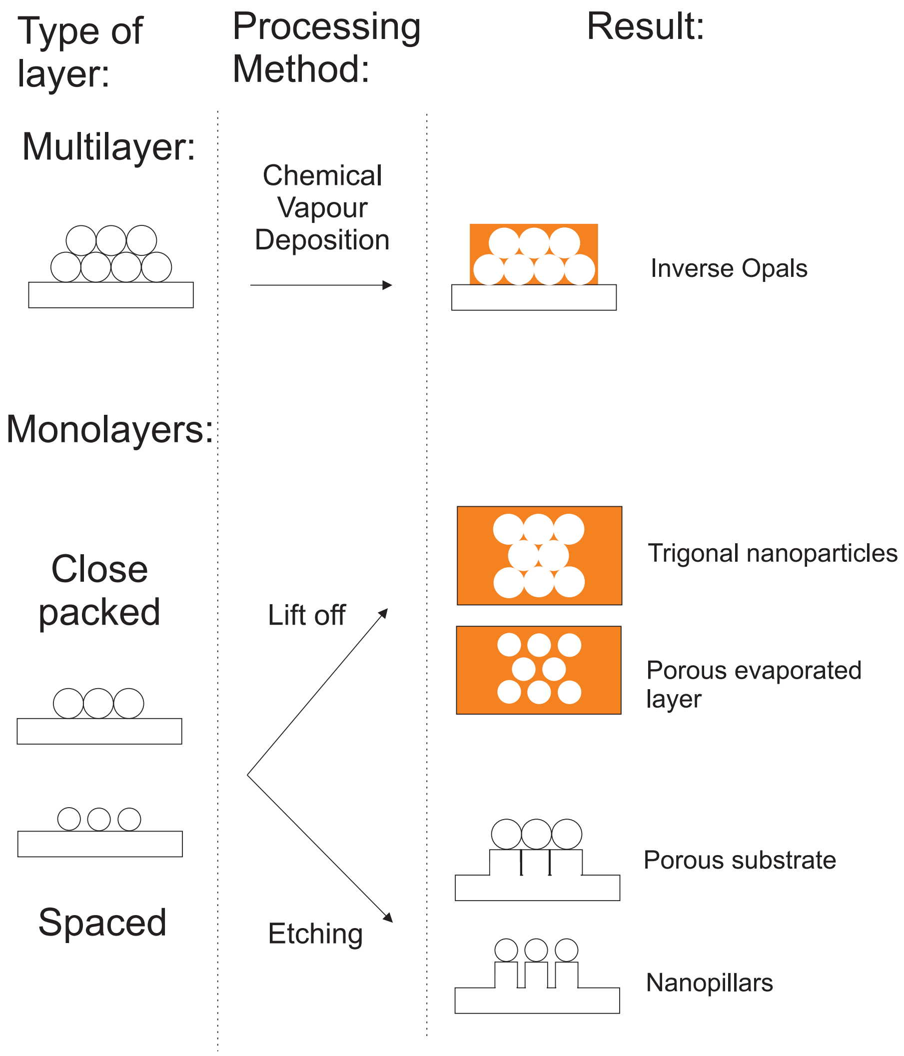

FIGURE 4.8: Different types of structures which can be created via nanosphere lithography

of the shape of the nanostructures [132]. The reason that colloidal self-assembly was selected to create some of the samples of this work was because of its inherit ability to control the formation of the patterns on the substrate in order to create biomimetic ‘tessellated’ crystals of close-packed patterns. These patterns are similar to the subwavelength feature patterns found on the eye of a moth, whose optical properties were under investigation in this work. Neither DNA self-assembly or block copolymers could offer a simpler, more adequate match to the needs of creating such samples on silicon.

4.1.3 Future directions of nanoengineering

Out of all the techniques described, the one which is most commonly used in commercial production processes is photolithography. It is expected that research funded by large semiconductor companies will push this technology to its limits until physical or practical constraints render further size reduction unfeasible. This is due to the dominant position of photolithography in current nanomanufacturing. It is cheaper for a company to buy a new component for a photolithography system than to change the whole production line to adapt to a new method which requires valuable time to set up (the process learning curve).

In general, the freedom of pattern design is higher with ‘top-down’ manufacturing procedures where any pattern can be written on the sample, but as designs become smaller to keep up with production trends, the write time for producing a full wafer increases, especially for e-beam lithography and the manufacturing capability is reaching the limit of what is possible with these technologies. ‘Bottom-up’ techniques on the other hand are massively parallel and are carried out simply by allowing natural forces to reach a steady state or minimum energy. The cost in using these techniques can be much lower than ’top-down’ techniques.

If the semiconductor industry (which is the main driver of commercial nanotechnology) decides to change its workhorse technology, it will not switch to e-beam lithography because of its very slow manufacturing yield. E-beam lithography is a serial process and mainly a prototyping tool which requires orders of magnitude more time to pattern a full silicon wafer than photolithography. There have been some procedures that seek to reduce the cost and the production time of ’serial’ top-down techniques by using a master or a stamp that can be reused via embossing the texture onto soft substrates. Two such techniques are Soft-lithography and Nano-Imprint Lithography. In the aforementioned procedures the creation of the initial stamp is the only really ‘expensive’ part of the process because it requires time consuming e-beam lithography to be manufactured. As soon as this first stage is completed, the production of samples using the master or stamp is much faster and approaches production rates which can enable mass manufacturing.

Soft-lithography is an option but it has too many limitations to date and has not been able to integrate with the requirements and procedures used by current silicon chip manufacturing. This is the main reason why for the short term, the future of nanoscale mass production lies in Nano-Imprint Lithography. As it was shown, nano-imprint lithography combines the precision of e-beam lithography with a fast manufacturing process by using either heat or UV radiation (currently also used in photolithography procedures) to liquefy a soft resist on the substrate and subsequently apply pressure to mould the resist to the required pattern.

If we look into the long term future though, the NIL procedure depends on the constraints set by e-beam lithography (because e-beam lithography is used to make the NIL master) and also has additional difficulties introduced by the limitations of the mould that is textured. Self-assembly techniques are much cheaper than NIL. In NIL a main component of the production cost comes from the high temperatures or the power of UV radiation used to liquefy the mould. On the other hand, self-assembly techniques such as Nanosphere Lithography and DNA self-assembly do not require a pattern design or any high-energy manufacturing step to form their patterns since they are defined by the procedure dynamics. Additionally the particles that are being assembled are used as the final etch mask. Hence, no intermediate steps such as designing and developing the mask are involved in the procedure. Nanosphere assembly works with colloids and can be applied rapidly via spin coating or spray painting on a large area. Eventually, the low cost of self-assembly techniques will force the mass manufacturing industry to prefer them in order to keep manufacturing costs down to a minimum. The only drawback with these techniques is that full control of the self-assembly procedure which would allow specification of any pattern is not possible, so complicated designs cannot be created. However, for the purposes of this thesis, the close-packed pattern that can be defined via nanosphere lithography can be used and this procedure was selected to manufacture some of the samples.

Hence, for this work, various techniques of nanofabrication were available either in NILT Denmark or University of Southampton at different stages of the process. E-beam, nano-imprint and nanosphere lithography were used for the samples created in this thesis.

4.2 Pattern definition by Photolithography

Photolithography defines patterns by forcing light to sensitize a photo resist in specific areas via a mask that defines dark and bright regions on the resist. There are several ways of setting up this mask layer in relationship with the substrate: contact lithography, where the mask is in contact with the substrate; proximity lithography, where the mask and resist are very close to each other; and projection lithography where an optical system exists between the mask and resist.

There are two types of mask that can be used, conventional ’shadow’ generating masks and phase-change masks. A phase-change mask is able to take advantage of destructive interference of the diffracted light by inducing a phase change of half the wavelength in the light shown through one of the slits so that a smaller spacing between features is possible. The main disadvantage of phase change masks is that they are expensive to make.

There are two kinds of photo resist available which are useful in different pattern design scenarios. One is called a positive and the other is called a negative resist. A positive resist becomes soluble when activated by the light exposure process, whereas the negative resist hardens when exposed to light. The choice between resists depends on the design required. For example, in a serial process like e-beam lithography, if the design is such that the majority of the resist needs to be removed from the wafer, then in order to minimize write time, the beam will be exposed to the parts which need to remain on the wafer as they consume less space and thus will take less time to write, so a negative resist would be used. In the opposite case a positive resist would be used. In either case, the definition of the mask would be optimized for minimum write time. In photolithography this is less of an issue because the light floods the whole wafer, but a mask still needs to be designed and if the write time for the mask needs to be minimized it will influence the decision of which resist to use in a similar fashion.

Photolithography is very fast at accomplishing large area patterning because it is a 'parallel' technique. Light is illuminated on the whole mask to form the projection of the required image on the resist for the small amount of time required to harden the resist. It is hence fast enough to be used for mass production. Historically, a relatively simple alteration used to reduce the size of the features created by photolithography is decreasing the wavelength of light used in the process. Wavelength is one of the factors that limits the size of features which can be created via photolithography as described by the Rayleigh formula (Equation 4.1) along with the Numerical Aperture of the lens and the process factor.

$$\Delta x = k_1 \lambda / NA[133] \tag{4.1}$$

k_1 = is a process factor determined by the exact details of the optical system

λ = wavelength

NA = numerical aperture

By reducing the wavelength used in the photolithographic process, the microelectronics industry has been able to keep up with the continuous need of reducing the size of transistors built for processing chips in order to make them faster. In particular, Moore's law of exponentially scaling down the size of the transistors will be available until the physical limits of the technology come into play. Moore's law is the infamous empirical observation made by Intel co-founder Gordon E. Moore, that the number of transistors which can fit in a silicon die are doubled every 18 months. This observation has since become a fundamental guideline which the microprocessor industry uses for designing new product cycles.

Photolithography has pushed the boundaries of the length of the minimum features it can inscribe from 365nm in 1996, to 45nm in 2009 by using Deep Ultra Violet Photolithography (DUV) ($\lambda = 139nm$). With an expected jump to Extreme Ultra Violet Lithography ($\lambda = 13nm$) (EUV) it seems that lithography has some lifetime yet before becoming completely obsolete and is currently successfully being preferred to other nanoengineering methods. However, the smaller the wavelength, the lower the tolerances for error in designing the optics of the system (lenses etc) and the harder the mask creation [133]. Additionally there is no optical system known to manipulate wavelengths

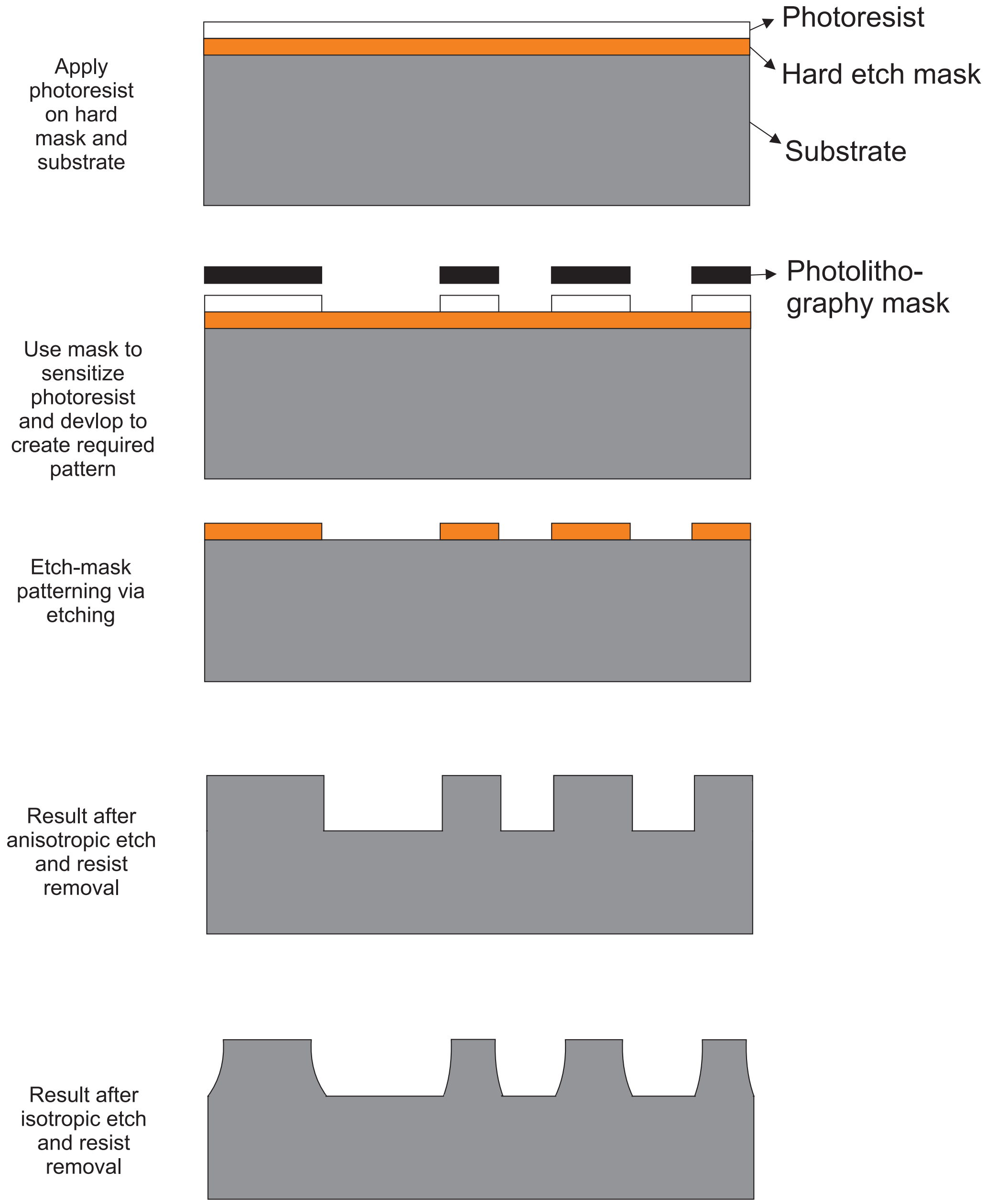

FIGURE 4.9: Process steps in creating pattern via photolithography

that are smaller than Deep UV part of the spectrum (i.e. for X-Rays and Gamma rays).

Reducing the wavelength of the photolithography process has worked so well this far because the transition costs of 'improved' versions of this technology relatively 'low' because only the light source and the optics of the system need to change, not the whole installation. The disadvantages of using photolithography for nanoengineering are that nano-scale feature sizes are not readily available yet (i.e. smaller than 45nm) and X-Ray, EUV technologies are still under development. It is also very difficult to create optical projection systems with wavelengths in the EUV and XRay spectra [134].

The photolithography facilities available in the clean room at Southampton did not allow for such small feature sizes, (minimum achievable feature size using the photolithography system was $\sim 1\mu$m) so this method was not selected for manufacturing the samples.

4.3 Pattern definition by Electron-beam Lithography

In e-beam (or electron-beam) lithography, a beam of electrons is used to sensitize a resist. A typical e-beam process is shown in Figure 4.10. The electron dose of the beam needs to be optimized for each resist material and thickness. In this work, PMMA (Poly methyl methacrylate), a commonly used resist was selected.

The operation of the e-beam machine is similar to an SEM (Scanning Electron Microscope) where an electron beam is created and focused onto the sample. However instead of using electrons to image the sample, the electron beam sensitizes the negative resist in specific areas to make the pattern. The beam is moved around by applying an electric or magnetic field and a total pattern size of 100 by 100μm can be written at once. For large patterns, it is possible of stitching the image if the stage is able to provide very accurate movement of the substrate. This option was not available on the e-beam available at the University of Southampton so a maximum writing area of 100μm x 100μm was possible. This size of sample was able to be optically characterized with the microscope but not with the white light reflectometry system because the beam size is much larger than the sample. So the facilities at the University of Southampton were not used to create samples via e-beam lithography.

The limits of e-beam technology are related to the electron scattering within the resist, this is known as the proximity effect. The proximity effect describes the high probability of the injected electron traveling laterally in the resist and sensitizing a much larger resist area than the diameter of the beam. The limit of fundamental feature size which can be resolved depends on the magnitude of this effect. This is why feature sizes are limited to 10-20nm in most cases, even though the size of the electron beam is much smaller.

The greatest advantage of e-beam lithography is that it can produce very small feature sizes of any type of pattern across the substrate because the location of the beam on the sample can be controlled very precisely via a computer file created from a CAD program. Additionally, there is no mask needed so there are no limitations associated with the mask (such as diffraction and optics, which are additional limitations in photolithography) because the exposure is defined by aiming the electron beam at the areas which are necessary and switching the beam on and off to control the electron dose.

The main limitation in applying e-beam lithography to industrial processes is that it is a 'serial' process where each feature is defined individually. Hence, it takes much more time to define a large pattern compared to 'parallel' techniques such as photolithography

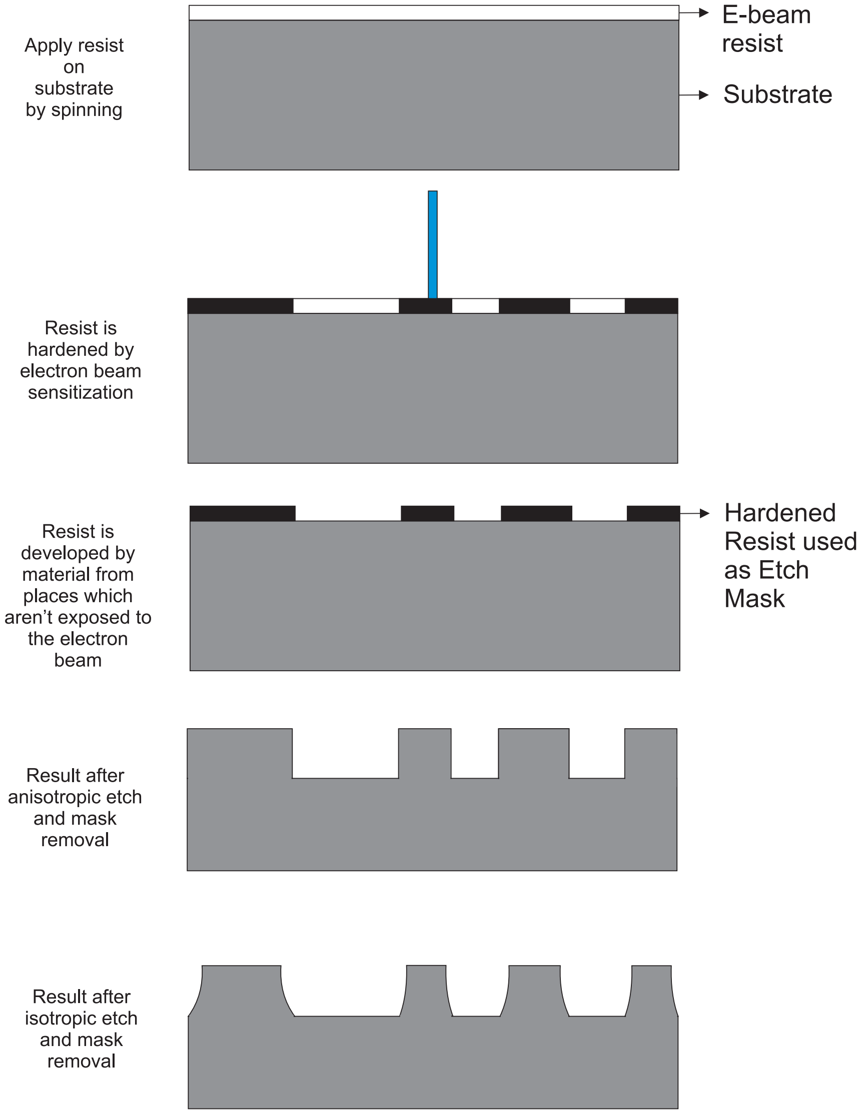

FIGURE 4.10: Process steps in creating pattern via e-beam lithography

were a whole wafer is defined at once. This slow process is a major factor which leads to very high manufacturing costs, rendering the method impractical for commercialization [135]. However, it does produce very good results and is very useful in prototyping.

The e-beam lithography system available at NILT was able to create large samples via stitching and was used to create a regular close-packed pattern sample and a sunflower pattern sample shown in this work (Section 6.6). A sunflower sample was also created by INNOS at their Eindhoven facility (Section 7.2).

4.4 Pattern definition via Nano-Imprint Lithography

Nano-imprint lithography was not available for this project locally and some samples were created with this technique at NILT Technologies, Denmark. In Nano-Imprint Lithography (NIL) there are two basic methods of defining patterns. Their difference resides in the method used to mold the soluble resist. One method uses thermal energy to harden the material and the other uses UV radiation for the same purpose. Before the NIL process begins, a master is designed and patterned by e-beam lithography, this master is then used to transfer the pattern onto the substrate. The soft resist material that is to be patterned is placed on the top surface of the substrate in liquid form. The master is then brought into contact with the material that is molded via pressure and heat to make the material form and harden. The master is removed and the excess material is then etched away from the substrate. The final etch mask pattern is thus created. The substrate material is ready to be etched so that the resist pattern is transferred to the substrate. The main advantage of using this technology compared to e-beam lithography is that essentially it can create reproducible patterns on a very large substrate in a parallel manner, which is much faster than using e-beam lithography alone. It also allows for an alternative technology to e-beam that is suitable for mass production. Very small minimum features have been achieved using this technique ($\sim$ 14nm) [136]. The main disadvantage of using NIL is that the initial stamps are created by an e-beam process which makes prototyping very time consuming.

Hubbard et al [137] have recently demonstrated a wafer-scale nano-imprinting method that uses disposable masters to reduce the cost and increase the speed of nano-imprint lithography. This allows for kilometers of disposable masters to be created very cheaply. The pattern is then applied onto the resist by bringing it into contact with the disposable master and applying minimal pressure. The final pattern is transferred to the substrate via dry etching.

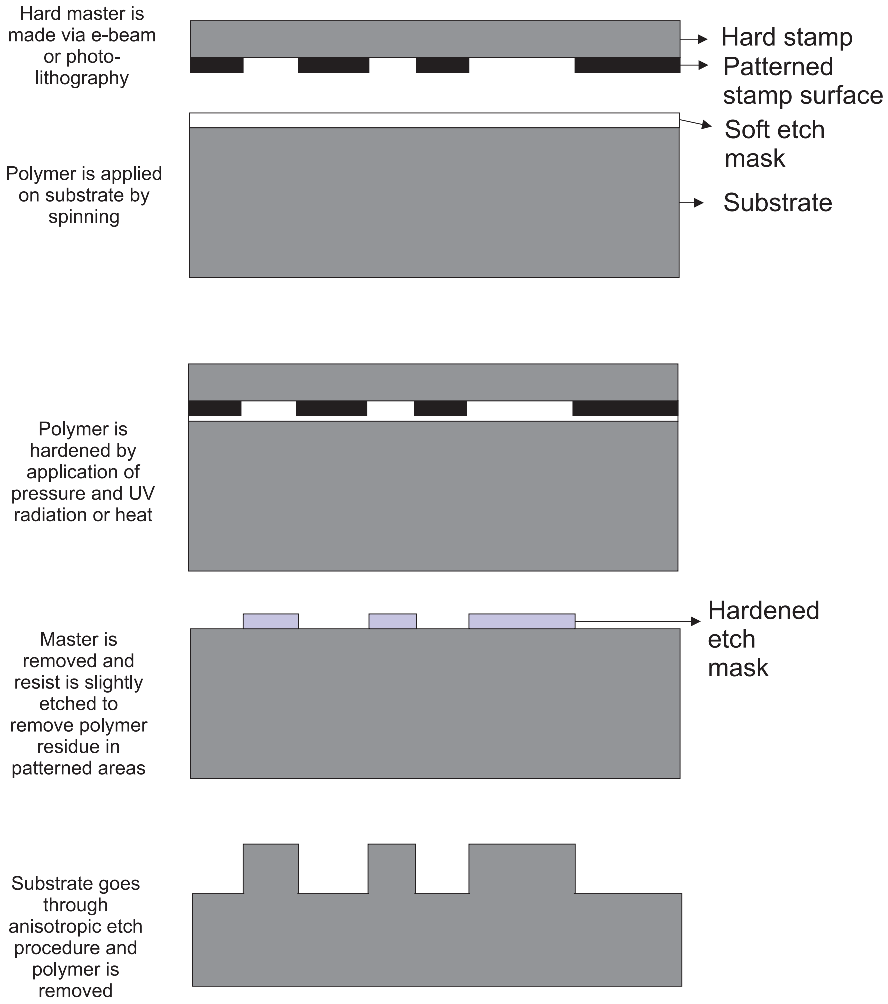

Figure 4.11: Process steps in creating pattern via nano-imprint lithography

Chapter 5

Developing and characterizing a nanosphere lithography technique for manufacturing ‘moth-eye’ layers

Creating moth-eye nanopillars on silicon in a close packed structure can be done via self-assembly with nanosphere lithography (NSL). Nanosphere self-assembly was first presented by Deckman in 1982 [99]. The two step process in creating a pattern using nanosphere lithography is shown in Figure 5.1. First, a close packed nanosphere monolayer is created on the liquid-air surface. Then the water level is reduced so the close packed monolayer attaches the the substrate. Finally, when the water solution dries completely, this monolayer can be used directly as an etch mask for the substrate, provided that the substrate can be selectively etched from the mask material. In this work, polystyrene spheres were used for the etch mask and the substrate was silicon. After the substrate etch, the spheres are removed to reveal the final pattern.

Creating features using this procedure is not as straightforward as using e-beam or photolithography where a CAD design file is passed to a machine that will carry out the procedure. The self-assembly process has a certain element of unpredictability in that results differ slightly from run to run and the manufacturing procedure involves a learning curve because its carried out manually. The equipment and procedure shown here was designed commissioned and calibrated especially for this work. In any case a regular hex pattern on the whole substrate was not available. The tessellated close-packed monolayer areas that were achieved in this process were used to make samples with biomimetic ’moth-eye’ topographies such as those found on the original eye of a moth.

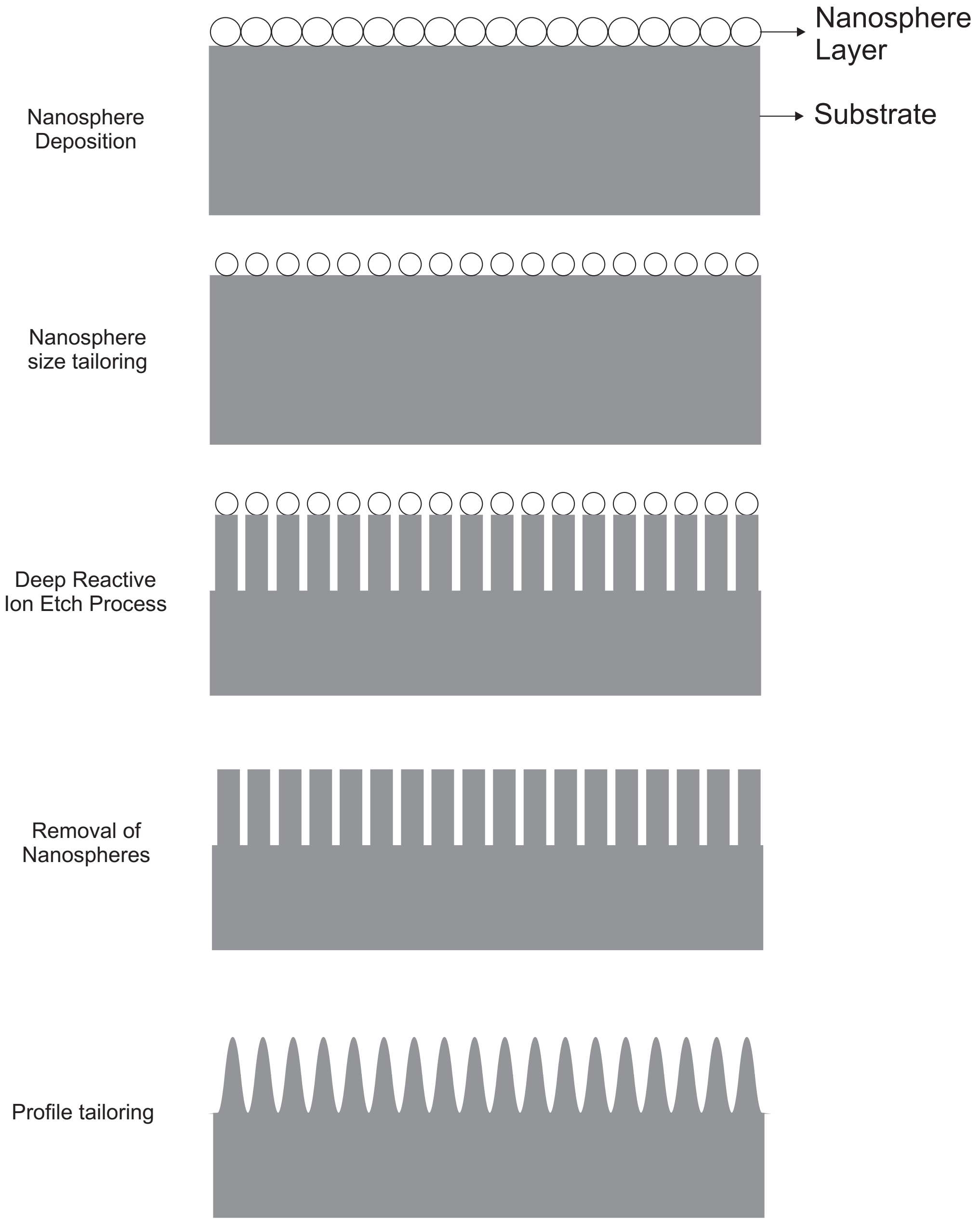

Figure 5.1: Process steps in creating moth-eye antireflection layers via NSL.

The limits of nanosphere lithography depend on the size of the constituent nanospheres used to create the pattern. The polystyrene nanospheres are commercially available and can be scaled down to 20nm (Brookhaven Ltd). The nanospheres used in this work were three suspensions of size-standardized spheres of 200nm (+/- 5nm, standard deviation 4.7nm), 380nm (+/- 6nm, standard deviation 5.3nm) and 780nm (+/- 9nm, standard deviation 4.8nm) diameter with a concentration of $1.05 g/cm^3$ in water (Brookhaven Instruments Ltd, UK).

The reason for selecting this range of sphere sizes was two fold, the first was to practice the technique of deposition on larger spheres before using smaller sizes. This is necessary because of the fact that a close packed lattice of 780nm-diameter spheres, when created successfully on the water interface, is clearly visible to the naked eye because the diffraction grating that is produced operates in the visible spectrum. As the size of the spheres becomes smaller, the diffraction grating wavelengths shift to the UV, with the 200nm spheres not diffracting any visible light, and thus the deposition process for this sphere size is done 'blindly' without any feedback on the quality of the close packed monolayer which is being deposited.

Thus the 780nm-diameter spheres were used mainly to practice and to learn the intricacies of the deposition process that affect the packing of the spheres in order to be able to create high quality monolayers. Once success had been achieved with the 780nm-diameter spheres the idea was to master deposition on the next size down (380nm diameter spheres) which was more difficult to verify and relied on having very good knowledge of the technique. After this was achieved, the process of self-assembling the 200-nm diameter spheres could be carried out without any feedback during the deposition but with high confidence that a high quality monolayer had been achieved based on the success of the previous two sphere sizes. For the 200nm-diameter spheres, the packing could only be verified after the process was complete via SEM imaging.

The second reason of selecting this range of sphere sizes was that the sphere diameter in the solution dictates the period of the final close-packed pattern, since the spheres are later reduced in size before etching the substrate with their centre positions unaltered. The 200 and 380nm-diameter spheres were within the range of periods which were simulated for close-packed nanosphere samples in Section 3.1.5.1. The reason for specifically selecting 200nm spheres was due to the fact that a 200nm period is the largest diameter which can create subwavelength antireflection layers which absorb light with wavelengths larger or equal to 400nm at oblique angles of incidence [22] (i.e. the whole visible spectrum).

A major factor that adds to the complication of the procedure is that there is not one unique self-assembly method for depositing nanospheres on a surface. To determine which procedure was the most adequate one for the requirements of this work several methods required testing.

5.1 Nanosphere monolayer creation

A great variety of methods have been suggested in the literature for self-assembling nanosphere monolayers, for example: Spin Coating [102] , Drop Casting [138], Thermoelectrically Cooled Angle Coating [139], Dielectrophoretic Deposition [140], Electrophoretic Deposition [141] Liquid Interface Assembly [127] are the most common. All of these methods begin by using a suspension of nanospheres in a liquid as the enabling medium for self-assembly. The nanospheres used in this work were suspensions of 200nm, 380nm and 780nm diameter spheres with a concentration of $1.05 g/cm^3$ in water (Brookhaven Instruments Ltd, UK).

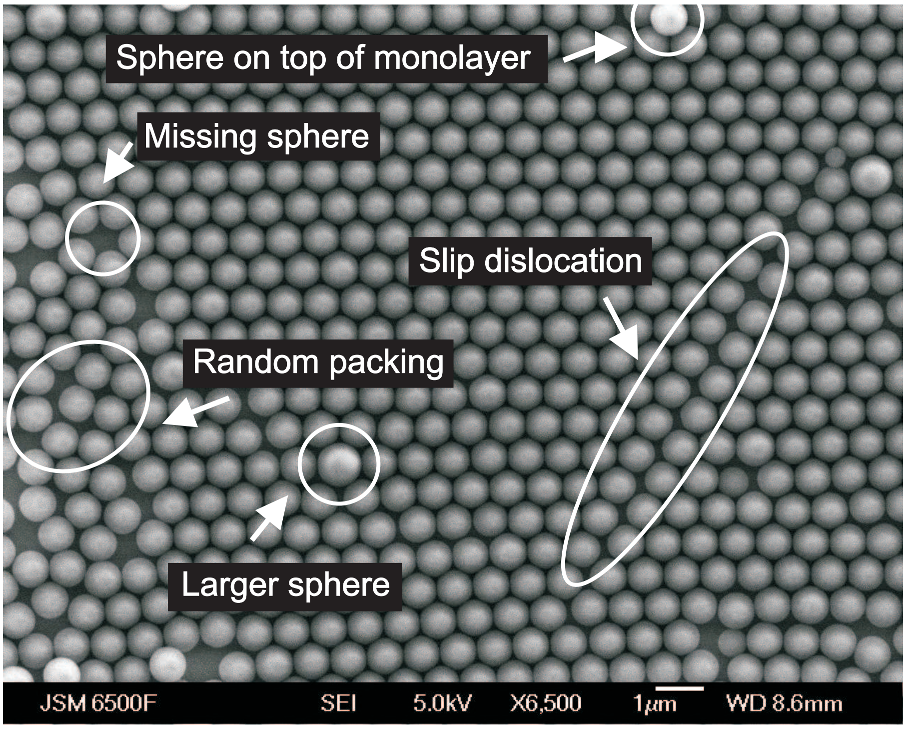

FIGURE 5.2: Depiction of the different kind of defects noticed in nanosphere monolayer self-assembly. The diameter of the nanospheres used here was 380nm and the method of deposition is described in Section 5.2.1

In the ideal case, the natural minimum energy state of a monolayer of spheres is the close-packed (hexagonal or trigonal packing) pattern. As shown by simulation models [82], if we consider the nanospheres as a network of nodes interconnected with springs, the process of self-assembly is equivalent to relaxing these springs to their states of minimum energy which results in the spheres forming a close packed monolayer.

This ideal case however seldomly is achieved by practical self-assembly procedures on the whole substrate. The monolayer usually contains a multi-crystalline structure whereby small domains of hexagonally packed spheres are formed. However, this case is precisely what is required to model the pattern shown on real moth-eye antireflective domains. Five nanosphere monolayer techniques were tested to get to the quality of monolayer shown in Figure 5.13.

Lattice defects which are usually present in the close-packed monolayer domains are slip dislocations, missing spheres, spheres which were placed on a level on top of the monolayer and random packing which is not close-packed. Examples of these are shown in Figure 5.2. A non-ideal nanosphere lattice formation can be due to various reasons. A

#	Method	Size		Quality	
		Area Coverage (%)	M.C. Domain Size (μm^2)	Defects	Fourier Analysis
1	Spin coating	32	< 100	Multilayers present	No 6-fold
2	Drop casting	94.9	$< 10^4$	Multilayers present	Multiple of 6-fold
3	Template evaporation	81.6	$< 10^5$	Multilayers present	Multiple of 6-fold
4	Teflon Bath	86.8	> 10	Triplet Spheres present	Multiple of 6-fold
5	Teflon Bath Improved	95.3	> 10	Almost defect free	Multiple of 6-fold

Table 5.1: Comparison Table between different nanosphere methods

fundamental problem that exists in nanosphere assembly is the variability of the sizes of the spheres and the standard deviation which exists on the sphere diameter. As the diameter of the nanospheres chosen to conduct the self-assembly is decreased, their standard deviation increases as a percentage of their diameter, but in any case the nanospheres have different sizes which on a local scale may not be important but the additive effect of all these differences produces strains in the spheres at different points of the lattice which lead to voids or defects. Spheres with diameter sizes that are much larger than the average sphere size in the colloid can also introduce cracks and inconsistencies in the monolayer lattice on a local scale.

Another reason for the imperfections noticed in the close packed nanosphere monolayer is the forces that exist between particles during the self-assembly formation procedure due to the interactions of different pockets of close-packed domains during the lattice formation. Hence random tessellated areas which are not close-packed are usually noticed between two such close packed domains. When two or more nanospheres collide, the impact forces need to relax either by pushing some of the nanospheres on and additional layer above the monolayer or by making extra space somewhere else in the lattice.

Four techniques namely spin coating, drop casting, liquid interface assembly and template evaporation were compared in terms of the size and quality of the monolayer formed when using each method. The results of the comparison are shown in Table 5.1. The most effective technique proved to be the Improved Liquid Interface Assembly which is explained in detail in section 5.2. More details of the other techniques can be found in Appendix A.3. Improved Liquid Interface Assembly was used to create the samples because it can create monolayers which closely match the needs in this work namely with good surface coverage, low number of defects and a tessellated close packed pattern with domain sizes around 10μm^2 in area.

In Liquid Interface Assembly, the monolayer assembly is preformed separately to the deposition of the nanospheres on the surface of the silicon substrate. Hence, it provides more control over the final quality of the monolayer which proved to be excellent according to the specifications. It also has a very good surface coverage (Appendix A.1) which is one of the main requirements in creating a moth eye pattern which could be characterized optically with the equipment available.

LIA uses a liquid surface, (in this case the surface of distilled water) on which self assembly of the nanospheres takes place. The water was contained in a hydrophobic bath made out of polytetrafluoroethylene (also known as PTFE or Teflon), on which the nanospheres are suspended and assembled in a close packed array before being deposited onto the substrate. The procedure is depicted in Figure 5.4. LIA has demonstrated the ability to deposit nanosphere monolayers on a range of surfaces including metals [127].

The fundamental reason for which the nanosphere self-assembly takes place on the water-air interface has been investigated by Nikolaides et al.[142] as being the balance of attractive capillary forces, due to the distortion of the interface by the particle, and repulsive dipolar interaction. This results in creating a close packed pattern which can later be deposited onto a submerged silicon substrate by removing the water from the bath. The procedure is depicted in Figure 5.4.

5.2 Improved Liquid Interface Assembly (iLIA)

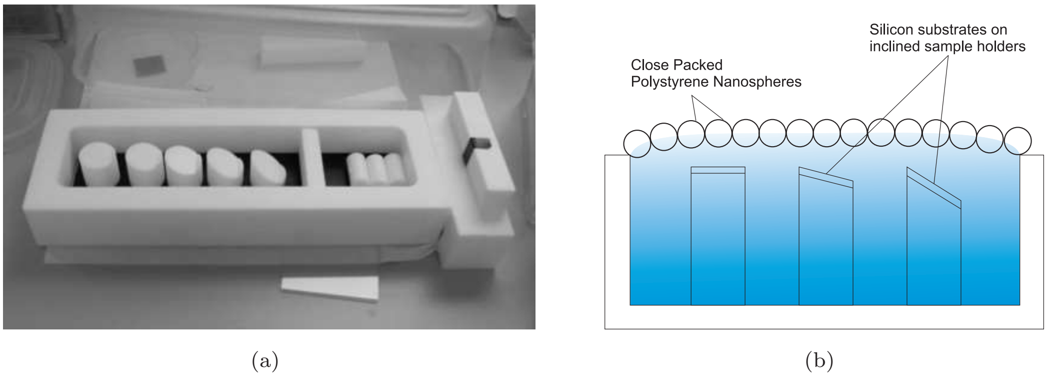

(a) (b)

Figure 5.3: (a) Photograph and (b) schematic diagram of the experimental setup used for Liquid Interface Assembly

The Liquid Interface Assembly (LIA) technique (also known as Teflon Bath technique) was first shown by Weekes [127]. The self-assembly takes place on the surface of a water bath and then the water is removed from the solution. The substrate which is submerged in the water receives the self-assembled nanosphere layer as the water level in the bath decreases.

In the Improved Liquid Interface Assembly method that was developed in this work, a similar process is used, with the exception of the sample being submerged at an angle and not completely parallel with the water surface Figure 5.5. It was found that by changing the angle of the substrate to the water surface as shown in the LIA method can be improved. The results of improving the method as a result of this work were recently published [143]. It was found that by inclining the substrate at a suitable angle, the water evaporates from one side of the substrate faster than the others, thus improving the directionality of the convection process and the meniscus achieved is similar to that used in the template evaporation method [144]. This alteration combines the fundamentals of two methods, Template Evaporation and Liquid Interface Assembly and was called Improved Liquid Interface Assembly.

Three stages can be identified in the deposition of the nanospheres. The first is the close packing of the spheres on the liquid surface the second is the deposition of the pattern on the substrate and the third is the evaporation of the water from the substrate surface(Figure 5.4).

Before the procedure takes place, the substrate has to be made hydrophilic. The substrates that were used were 2x2cm pieces of <100> crystal orientation Si wafers, (350um thick, 8-22 ohm-cm resistivity, P type (Boron), single side polish). By nature, silicon is hydrophobic and this is not optimum for nanosphere deposition [139]. There are various methods of making silicon hydrophilic, however the most simple one is the one presented by Haginoya et al. [145]. The silicon wafers were treated to 1 hour ultra-sonication in acetone and dipped in water for 24 hours to make the surface hydrophilic. The suitability for this method was tested by setting up a contact angle measurement experiment.

As is shown in Figure 5.6 (a) and (b) the surface is more hydrophilic after processing the wafer because the contact angle the water droplet creates with the surface of the silicon wafer is smaller than before. To measure the contact angle, an open source software plugin developed by Stalder et al. [146] was used in conjunction to an open source image processing software called ImageJ. In this case the contact angle was reduced from 47 to 19 degrees.

5.2.1 Carrying out the nanosphere deposition via iLIA

The procedure that was followed to assemble and deposit the monolayer on the silicon substrate is as follows:

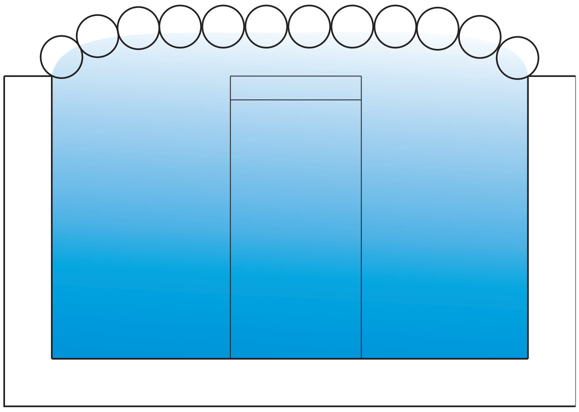

(a) Close packing the monolayer on the water-air interface

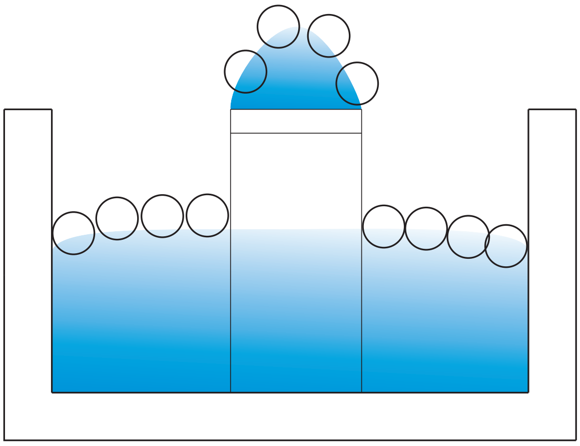

(b) Reducing the level of the water in the bath so that the nanospheres are deposited onto the silicon substrate

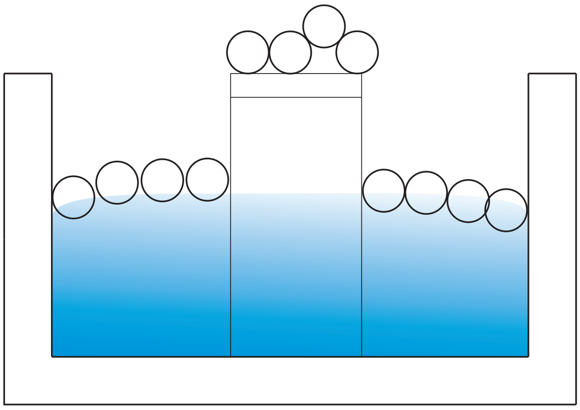

(c) Allowing water to evaporate and nanospheres to re-assemble on the surface

Figure 5.4: Schematic Diagram of Liquid Interface Assembly Method for depositing nanospheres onto a silicon substrate

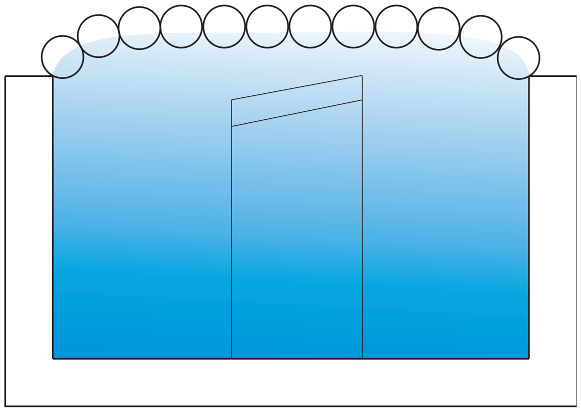

(a) Close packing the monolayer on the water-air interface

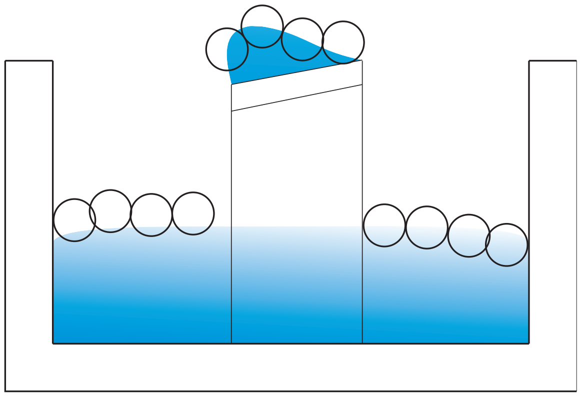

(b) Reducing the level of the water in the bath so that the nanospheres are deposited onto the silicon substrate

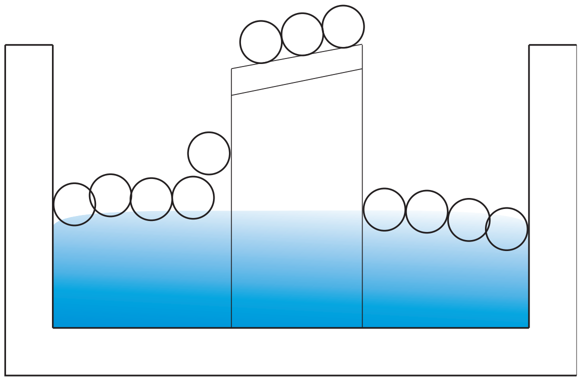

(c) Allowing water to evaporate and nanospheres to re-assemble on the surface

FIGURE 5.5: Schematic Diagram of Improved Liquid Interface Assembly Method for depositing nanospheres onto a silicon substrate

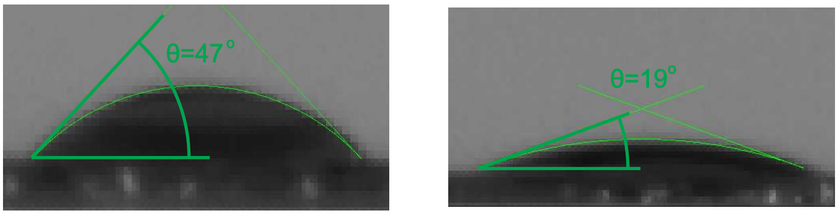

(a) Distilled water droplet shape on silicon before surface processing. Contact angle: 47.7^o

(b) Distilled water droplet shape on silicon after surface processing. Contact angle: 20.1^o

FIGURE 5.6: Making silicon surface more hydrophilic with the method shown in [145]

- The prepared hydrophilic silicon substrate (350μm thick, (100) orientation, 8-22 ohm-cm resistivity, P type (Boron), single side polish, supplier: Si-Mat, Victor-Frankl-Str. 20, D - 86916 Kaufering, Germany) is placed on the Teflon holders in the bath.

- The bath is filled with de-ionized (DI) water of at least 9MOhm conductivity.

- A glass slide is placed diagonally in the water secured at one edge of the bath. Half of the glass slide has to be left outside the water because this will guide the spheres to roll gently on the air- water interface. If placed on the surface with a pipette directly they will just plunge in the bath water.

- A pipette with a maximum 5μL capacity is used to transfer the spheres from the solution. The solution is prepared as 1:1 v/v mix of ethanol and nanosphere colloid suspension (1.05 g/mL mixture of nanospheres in DI water).

- Teflon sliders are placed on top of the bath to trap the nanosphere monolayer which is formed on the air-water interface and guide it on top of the silicon substrate.

- The water is removed from the Bath via syringe extraction until the water level is below that of the silicon substrate.

- The monolayer trapped on the silicon substrate is allowed to dry at constant humidity (40%) and at room temperature (25^o).

- After evaporation the sample is removed and the water from the rest of the bath is emptied and the apparatus cleaned. The glass slide is stored in a 1% w/v SDS (sodium dodecyl sulfate)/ DI water mixture to keep it clean.

This technique was used for all the LIA and iLIA runs. For iLIA, an optimisation with respect to the angle of the silicon substrate was conducted to generate the most optimum quality of monolayer. This will be explained in detail hereafter.

5.3 Characterizing the effect of changing the angle of deposition in the Improved LIA (iLIA) method

5.3.1 Scanning Electron Microscope Analysis

Five samples were created at different drying angles (5^o, 10^o, 20^o, 30^o, 40^o). The samples were evaporated at room temperature (25^oC) and at a constant humidity. Scanning Electron Microscope (SEM) images of the nanosphere monolayer were taken to verify the absence of long range order in the samples. Nine points across the five samples, each 5mm apart (Figure 5.7) were photographed. The Fourier Transforms of the SEM images in those regions confirm that the monolayer pattern of the samples are not aligned over the whole 2x2cm wafer area and hence the close packed monolayer is multicrystalline. The largest consistent close packed region was measured to be around 10μm^2 in size (Figure 5.7). The domains were packed very closely with surrounding domains with very few voids between them.

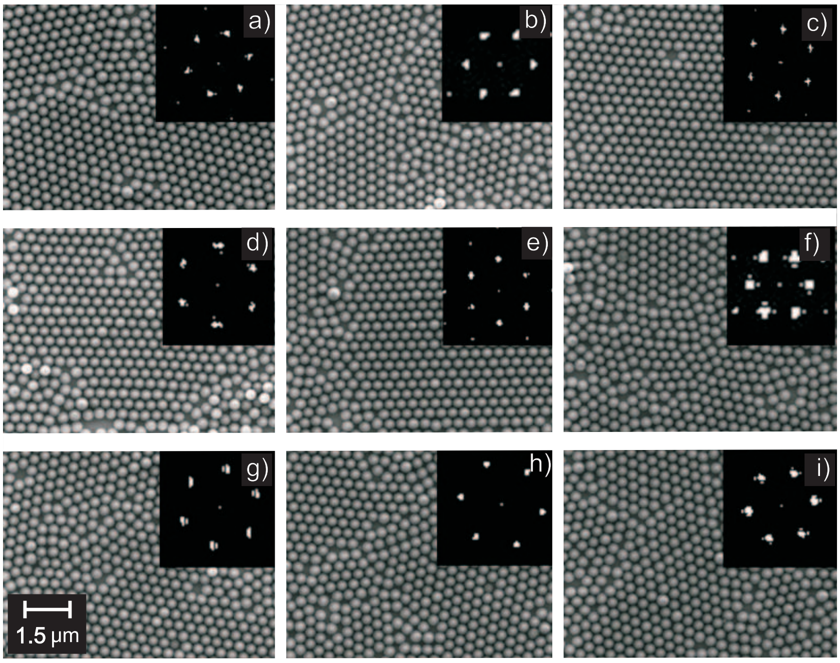

FIGURE 5.7: SEM images from 9 different parts of a 350nm-diameter (+/- 6nm, standard deviation 5.3nm) nanosphere monolayer created by self-assembly. Accompanying Fourier transform of images showing lattice crystallinity and six fold symmetry are shown on the top right of each image.

This outcome was expected due to the relatively fast evaporation rate that was selected (20^oC) which did not allow the monolayer to fully relax to a monocrystalline close packed pattern and hence domains were formed. It has been proposed that improvements could be made for increasing the monocrystallinity of the layer by selecting a slower evaporation rate (i.e. lowering the temperature) [147] and the application of a random force during evaporation [148]. However, this was not the focus of this work as multicrystalline domains were sought and the manufacturing procedure developed gives acceptable results for characterization, so no further optimization was necessary.

5.3.2 Dark Field Microscopy

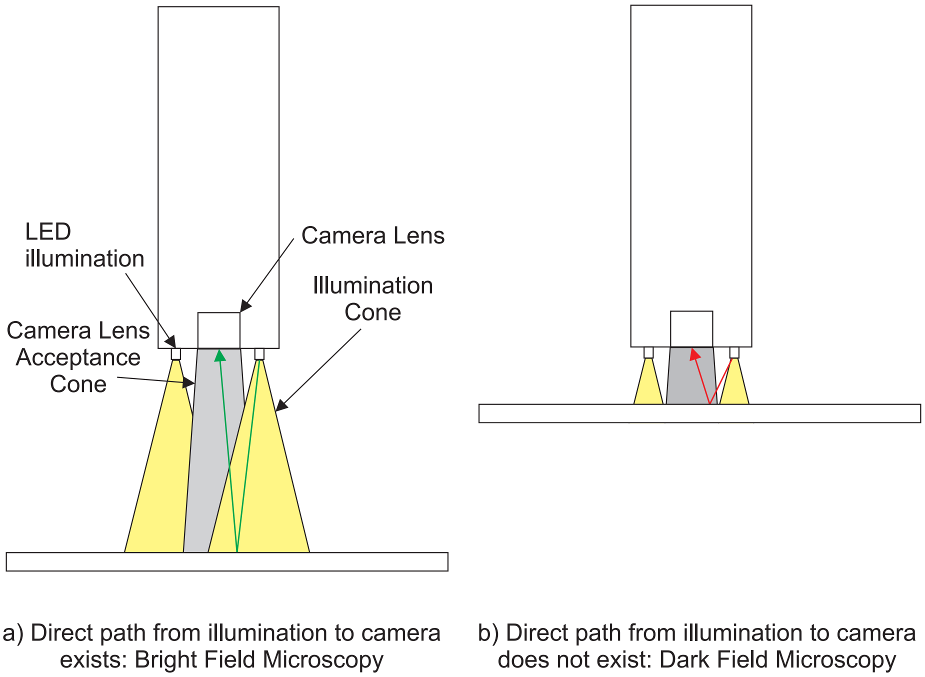

FIGURE 5.8: Achieving Dark Field Microscopy by over-focusing on a LED-illuminated Microscope

A microscope camera with LED lights around the lens, which was mounted on a precision stage was used for Dark Field Microscopy characterization. This system is part of the Wollam M-2000 spectroscopic ellipsometer and is normally used for aligning the sample on the stage but it was ideal to study the large samples in terms of their scattering defects.

The microscope was used to collect the scattered light from the sample, ignoring the directly reflected light via over-focusing the lens when bringing the stage closer to the lens (Figure 5.8 (a)). This type of viewing made the highly scattering regions of the drying-line defects very distinct from the rest of the sample (Figure 5.9).

Dark field microscopy was used because it is the most efficient way of inspecting the monolayer quality of a large area (~2x2cm) in which the nanospheres were deposited. This method was very useful in providing feedback for the success of the procedure. It is much faster than electron microscopy and it can characterize the whole monolayer which was deposited. Three types of monolayer defects can be identified by dark field microscopy namely drying-line multilayers, individual spheres and multiple sphere voids (which are missing more than 5 spheres).

These three types of defect cannot be directly filtered in the dark-field images since they are all induced by the light scattered by the spheres, however, they be identified by visible inspection of the images, when one has knowledge of the orientation of the drying direction and the size of the particles. Hence, large un-oriented closed-loop scattering defects are classified as large nanosphere voids whereas small circular scattering defects of the size of the sphere diameter are classified as individual spheres which have deposited on top of the monolayer and finally parallel contours which are vertical to the drying direction of the liquid are recognized as drying line defects and are due to the variation of the meniscus and drying rate of the solution.

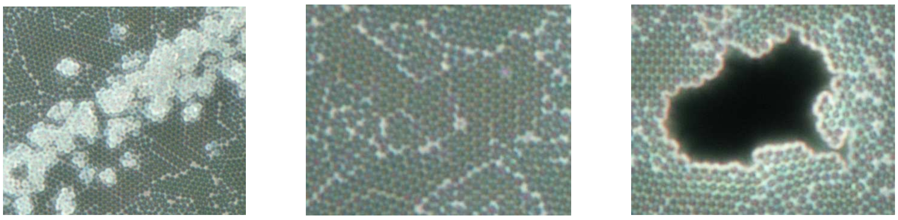

(a) (b) (c)

Figure 5.9: Comparison of three dark field images from a self-assembled 780nm-diameter nanosphere monolayer on silicon showing (a) drying-line defects and (b) no scattering defects and (c) a large nanosphere void, all taken with a Nikon LV100DA-U microscope.

Brightness thresholding of the dark field microscopy images allows for defect analysis to be carried out by clearly highlighting the scattering defects. The defects were assigned to be black in color while the complete monolayer was set to be white in order to provide maximum contrast and easiest detection. A stripe in the middle of each sample along the drying direction was sequentially photographed and the final image was stitched together to show the coverage of the defects along the drying direction (Figure 5.10). As expected, most of the defects were due to the multilayers arising from the drying lines which are quasi-parallel to each other and vertical to the drying direction of the water meniscus as it dries off the sample. The total defective region on each sample was calculated by analyzing these images shown in Figure 5.10 using image analysis software (ImageJ).

5.3.3 Integrating Sphere Measurements

Total reflectance measurements were taken to characterize the defects with an integrating sphere. The sample was illuminated by a broadband laser source (Supercontinuum laser, Fianium, UK) with a wavelength range of 450-1800nm. A spectrometer was used, (Ocean Optics USB2000) to compare the reflection from the samples in the wavelength range

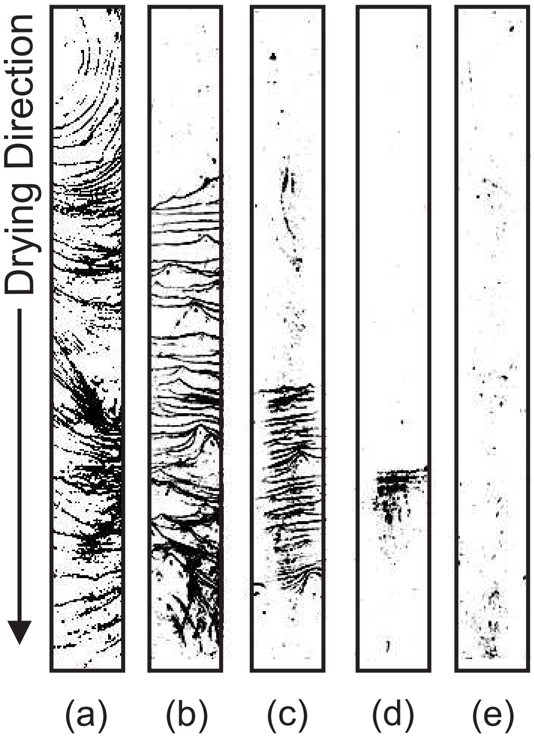

FIGURE 5.10: Intensity thresholded images stitched together to form thin strips traversing samples 1-5 along the drying directions at (a) 5^o (b) 10^o (c) 20^o (d) 30^o (e) 40^o degrees tilt respectively

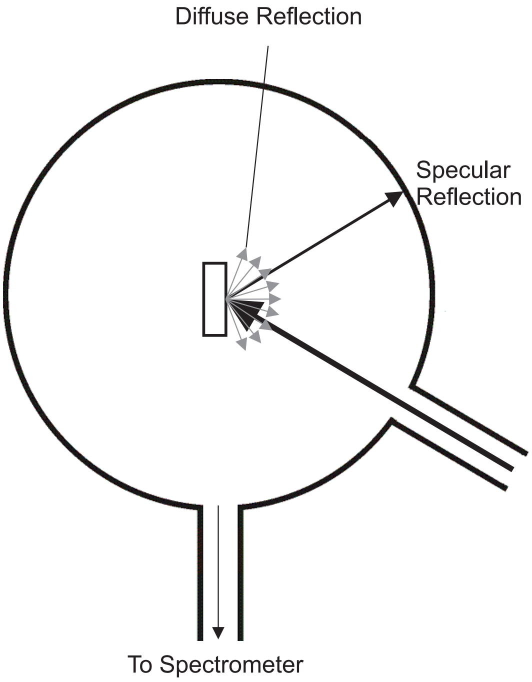

FIGURE 5.11: Collecting diffuse reflectance with integrating sphere setup.

between 725-950nm. The laser beam was 1mm in diameter and the samples were 2x2cm in area so small regions on each sample could be tested.

Sample 1 was very densely covered by drying-line defects as can be concluded by the thresholded image in Figure 5.10(a). This sample could not be effectively resolved by the apparatus, so comparative measurements of the defective and monolayer areas from this sample were not available. For the rest of the samples (2-5), total reflectance measurements were taken from 1mm^2 regions with drying-line defects, and compared to areas without these defects on the same sample. This increase in scattering was obvious by naked eye as well, since the drying line defects have a distinct bright white color.

A close-packed monolayer of particles does not expose single nanospheres and hence does not create diffuse scattering of incident light from the surface. The results of subtracting the reflectance of areas without defects, from that of areas with defects shows an average increase in reflectance which matches the single particle scattering simulations predicted by MIE scattering theory for a 780-diameter polystyrene sphere in vacuum (Figure 5.12). Hence the increase in total reflectance caused by the increased scattering from the defect particles can be used to characterize the these large 2x2cm samples in terms of monolayer quality.

The experimental measurements obtained for each sample were correlated with the expected scattered efficiency of an single polystyrene nanosphere using a scattering simulation software (MIE Plot) which uses Mie theory to predict the particle scattering. Mie theory is an analytical solution of Maxwell's equations that describes the scattering of electromagnetic radiation caused by dielectric spherical particles. Due to its complicated calculation procedure it is usually used when Rayleigh scattering is not valid, since Rayleigh scattering is simpler to solve for. Rayleigh scattering describes the elastic scattering of electromagnetic energy by the nanoparticle and is valid when the size parameter a is smaller than 1,(i.e. the spherical particle size is much smaller than the incident wavelength). The size parameter is given by [149]:

$$a = \frac{2\pi R}{\lambda} \tag{5.1}$$

Where R is the radius of the particle and λ is the wavelength of light in the surrounding medium which in our case is air.

In our case, the wavelength range of the incident light (700-950nm) is not much smaller than the particle size which is 780nm in diameter, so Mie theory was required to calculate the scattering efficiency of the particle for each wavelength in the spectrum [149]:

$$Qsca = \frac{2}{a^2}\sum_{n=1}^{\infty}(2n+1)(|a_n|^2 + |b_n|^2) \tag{5.2}$$

Where a_n and b_n the outgoing spherical wave coefficients, and a the size parameter calculated previously in Equation 5.1 .

The scattering efficiency (Qsca) calculated by Mie Plot uses an algorithm published by Bohren[150]. The parameters set for the Mie simulation sphere were 780nm for the sphere diameter and for the material refractive index polystyrene was selected. The sphere's surrounding medium was set to be vacuum and the incident light spectrum was set to 700-950nm. The results of the differential reflectance increase between the scattering and non-scattering regions from each sample for the wavelength range measured (Figure 5.12 b-e) showing a broad peak in reflectance around 750nm and match the scattering efficiency of the single nanosphere polystyrene particle predicted by MIE scattering theory (Figure 5.12 a). Hence, it is confirmed that the increase in total reflectance is caused by the scattering of the defective areas can this can be used as a measure of characterizing the samples in terms of monolayer quality.

5.3.3.1 Conclusions

The difference in reflectance between the non-scattering and scattering regions correlates to that of the scattering efficiency predicted for a single polystyrene particle (Figure5.12) and hence it can be concluded that the scattering originates from spheres which have been exposed either on a layer above the monolayer such as single nanospheres or ridges created by the drying lines.

Characterizing the scattering defects on the whole sample creates a figure of merit in comparing the quality of the self-assembled surface of the entire sample in terms of absolute defect-free monolayer size. By creating a figure of merit that would take into account both the total area and the scattering intensity of the defects, the quality of the deposition can be compared between samples. This figure of merit was created by combining the data from the dark field microscope images and the integrating-sphere measurements. The total reflectance increase of each sample was measured by multiplying the reflectance spectra of the defective region (Figure 5.12) and the total defective area measured. Table 5.2 collects these results.

After this analysis was complete, it was found that an optimization of the deposition angle was possible. It was concluded that the optimum angle at which the samples were deposited on the sample is at 30 degrees from level (sample 4). This choice was made even though the defects in sample 5 (decline of 40 degrees) are a smaller part of the total area in absolute terms(Table 5.2). The reason for this choice is that in sample 5 the defects are randomly distributed and do not follow the drying lines. The increased scattering in this case originates from large cracks in the nanosphere lattice (Figure 5.12 d,e) and not multilayers.

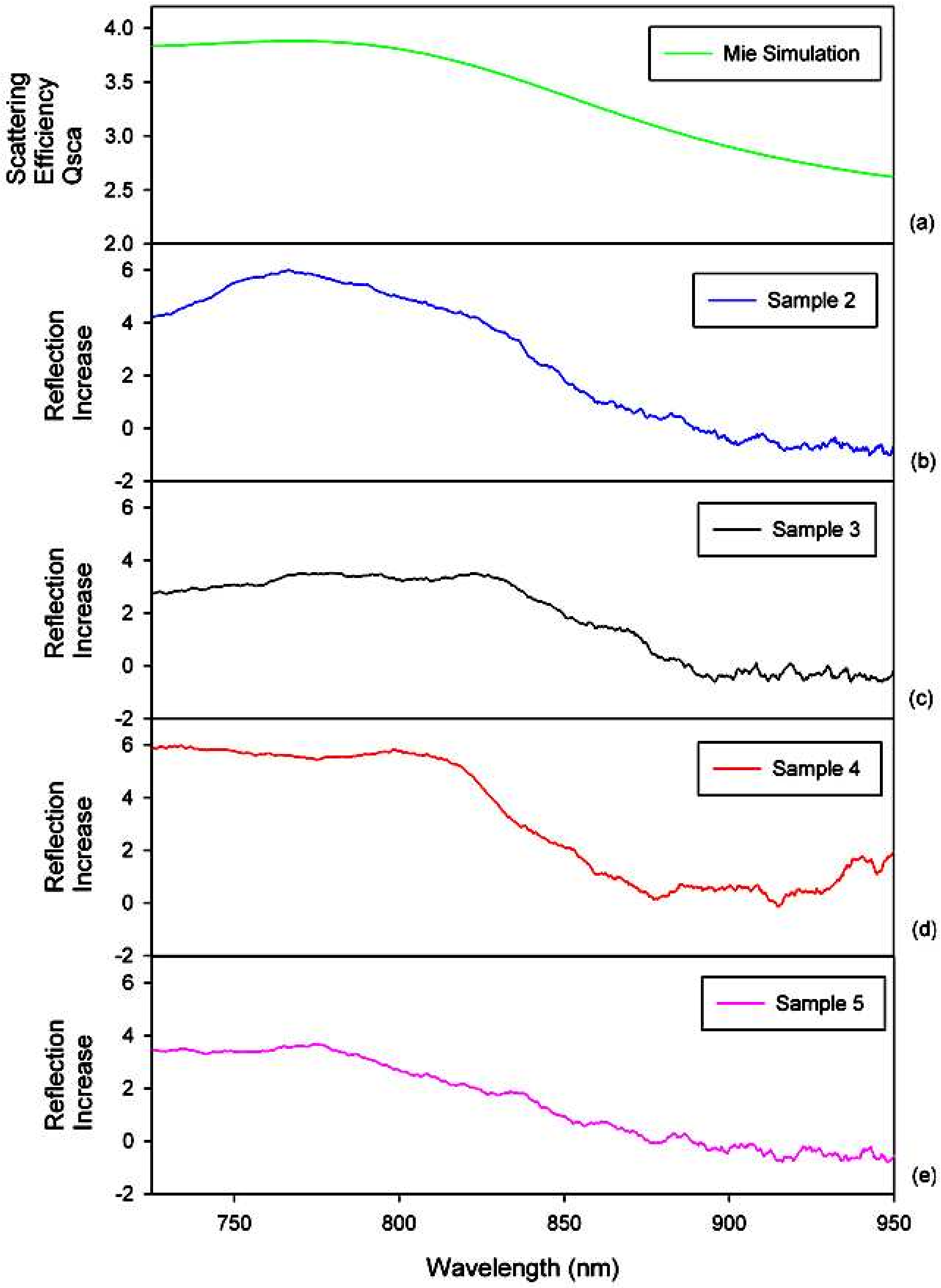

FIGURE 5.12: Increase in scattered reflectance between closely packed nanosphere region without scattering defects and region with scattering defects on samples 2-5 (Figure 5.10) which are compared to simulated result of the scattering of a 780nm polystyrene nanosphere using MIE scattering theory

Sample	Defective Area (percentage of whole area)	Increased total reflectance (in percent)	Figure of merit per sample (Defective area x reflectance increase)
2	8.9	3.29	29.2
3	4.2	2.21	9.28
4	1.1	3.41	3.75
5	0.6	1.61	0.966

Table 5.2: Analysis of defects on different samples

Hence, the sample with the largest contingent area of monolayer was formed for the sample evaporated at a decline angle of 30 degrees. We can also conclude that there is a trade-off between drying line defects and cracks in the lattice.

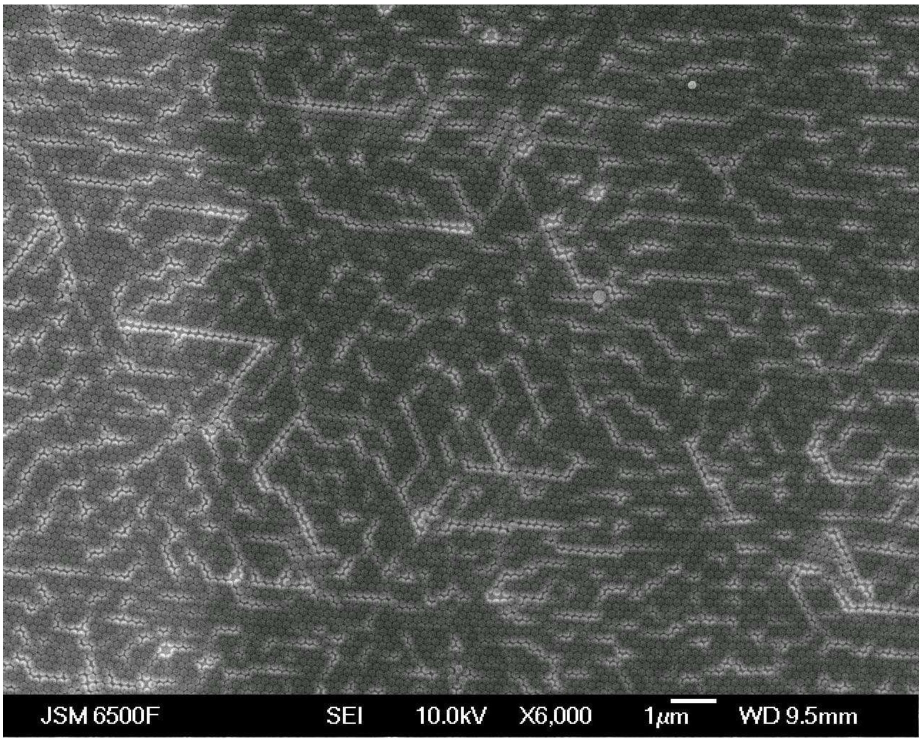

Figure 5.13: SEM image of close packed nanosphere monolayers via Liquid Interface Assembly procedure described in Section 5.2.1(Sphere diameter 200nm, Evaporation temperature 25^{o}C, Evaporation time 15mins)

There might be an angle between 30-40 degrees where the whole surface would be covered by a contingent monolayer, but this fine tuned optimization was not possible with the available apparatus and the area created in sample 4 was large enough for optical characterization (1x1cm^2). Perhaps future versions of the iLIA could use a variable angle sample holder and optimize this further but for the context of this work, this rough optimization provided us with working samples Figure 5.13.

O_2 Flow	10sccm
RF Power	100W
Platen power	14W
Pressure	4.5 mTorr

TABLE 5.3: Oxygen Plasma Etch Process parameters for creating nanopillars on silicon with a nanosphere mask. Procedure is identical for all samples made via DRIE in this thesis.

5.4 Customizing the nanosphere size

After self-assembly of the polycrystalline monolayer, the spheres were close-packed (the sphere surfaces were touching) and hence the nanosphere layer required some etching before it could be used as a etch mask (Figure 5.1) . Reduction of the sphere size was needed to create a large enough space between the spheres so that a subsequent DRIE etch would form individual pillars on the silicon substrate and not nano-'wells' between the sphere voids. Reduction of the sphere size was realized via oxygen plasma etching [151] (Plasmalab 80, Oxford Instruments, UK) . An example of a calibration run where different etch times were used for 780nm-diameter spheres is shown in Figure 5.15.

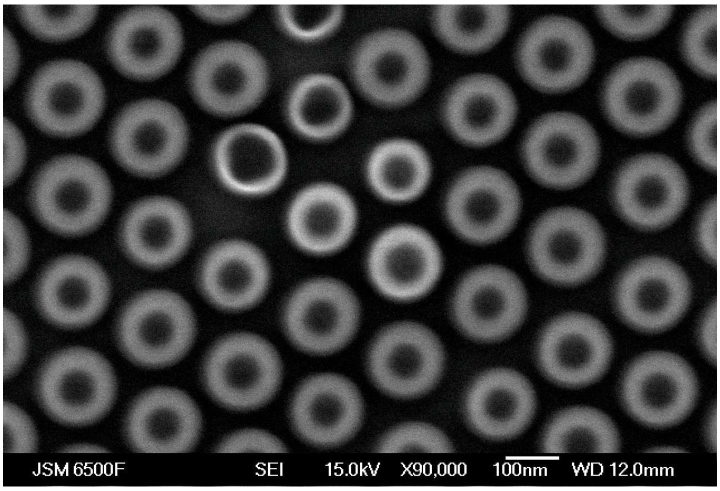

FIGURE 5.14: SEM image of 200nm-diameter self-assembled nanospheres on a silicon substrate after a 30sec O_2 Plasma Reactive Ion Etch. (Table: 5.3)

Reduction of the sphere size was required so that a subsequent DRIE etch would form individual pillars on the silicon substrate and not nano-'wells' between the sphere voids. The reduction was carried out via oxygen plasma etching (Plasmalab 80, Oxford Instruments, UK). Reduction of the sphere size was calibrated before the required diameter could be achieved [151].

In the examples shown here we have reduced the sphere diameter of the 200nm spheres to 100nm within the original close-packed lattice by using the smallest oxygen etch cycle

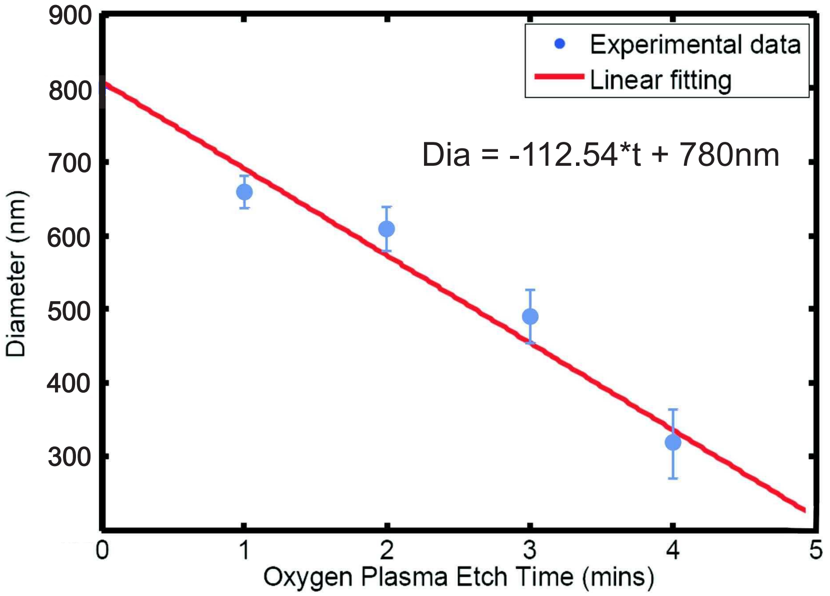

Figure 5.15: Plot of the mean diameter of the nanospheres after the oxygen plasma etching process. The solid line represents the linear fit whose parameters are shown in the equation. The error bars represent the standard deviations of the nanosphere diameters detected in the SEM images

available on the RIE machine which lasts 1minute shown in Figure 5.14 (details in Table 5.3). A similar etch was realized for the 780nm spheres which were also etched around 100nm from their initial size to 680nm.

5.5 Etching the silicon substrate

After creating the etch mask on the substrate either by nanosphere or e-beam lithography, the etching of the substrate takes place. Three methods were investigated for dry etching silicon, Reactive Ion Etching (Oxford Instruments, PlasmaLab 80 Plus), Deep Reactive Ion Etching (Surface Technology Systems, Pegasus) Cryogenic Inductive Coupled Plasma (Oxford Instruments, ICP380+). The etch gas that is used depends on the etch mask and the shape required. In this work, the etch masks that were chosen were PMMA for the e-beam lithography and polystyrene for the nanosphere lithography procedures. Dry etching of silicon with good selectivity between silicon and organic masks can be done using a combination of SF_6 and other gases in the plasma chamber.

All three procedures can use SF_6 in gas form to provide dry etching of the substrate. The schematics of the configuration used for creating the plasma in these two different procedures are shown in Figure 5.16. RIE uses a double metal plate, whereas ICP and DRIE use a coil setup to create gas plasma and accelerate the ions towards the substrate.

The coil setup increases the anisotropy of the etch because it creates a much higher plasma density. The difference between the two technologies that use a coil setup to create the plasma, ICP and DRIE, is that DRIE uses the 'Bosch' method which alternates different gases in the chamber to get a high aspect ratio of features whereas ICP uses a continuous flow of a mixture of gases.

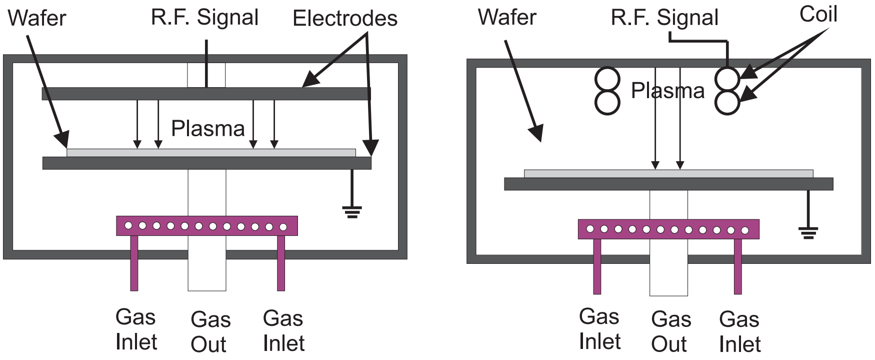

(a) Double plate plasma chamber (b) Coil plasma chamber

FIGURE 5.16: Platen and coil plasma etch chambers

DRIE is a technique normally used for creating very deep structures (>10μm). It is designed for maximum anisotropy of the etched pattern and it achieves this by alternating between passivation and etching of the substrate by alternating between C_4F_8 and SF_6 gases respectively (Bosch process). A problem with DRIE is that the procedure is carried out in steps so if the parameters are not carefully optimized, 'wavy' pillars are created (Figure A.3, Appendix A.2). The parameters that might affect the quality of the etch are the speed of degradation of the handling wafer, as well as the quality of the thermal coupling of the handling wafer and the sample. The 2x2cm^2 square samples

Substrate Temperature	25^o
C_4F_8 Cycle	Flow: 85sccm, Time: 9sec
SF_6 Cycle	Flow: 12sccm, Time: 12sec
RF Power	600W
Platen power	14W
Pressure	4.5 mTorr

Table 5.4: DRIE Process Parameters for creating nanopillars on silicon with a nanosphere mask at the clean room in Southampton.

created by nanosphere lithography were etched via DRIE. They had to be mounted onto to a 6inch-diameter silicon transfer wafer before it could be placed in the DIRE etch machine (Pegasus, STS Technologies) because the load lock was designed to only accept such large wafer sizes. It is observed that as the silicon handling wafer was degraded, its surface thermal conductance was altered which was important for the quality of the etch (Figure 5.18) and thus the transfer wafer had to be changed frequently. The thermal conductance of the adhesive used to adhere the samples to the wafer was also important as the quantity of the carbon tape used directly affected the etch results. A top view of the sample that was created after sphere reduction and DRIE is shown in Figure 5.17. The machine parameters used to create the pillars via DRIE were similar to those published by Cheung [97] and are shown in Table 5.4. The speed of this etch was found to be 48.6nm / cycle. Hence, the number of cycles required to create the depth of at least 400nm was 9, which actually produces a pillar of height of around 437.4nm. This depth was selected because it was shown by simulations to be the minimum depth at which very low reflectance is achieved for the wavelengths in the visible spectrum (400-700nm) as shown in Figure 3.7 and explained in section 3.1.5.1.

	Anisotropic Etch	Isotropic Etch
Machine	STS ASE ICP	STS RIE
Pressure(mTorr)	10	36
Power (W)	350 (Passivation) 500 (Etch)	20
Gasses, flow rate (sccm)	C_4F_8: 50, SF_6 :50	SF_6: 30, CHF_3: 10, O_2: 30

Table 5.5: Parameters for anisotropic and isotropic etching carried out at NILT.

RIE is a technique that can be used to etch the surface or clean the substrate. RIE uses a plasma generated by a 13.56MHz RF power generator to ionize the gas. Argon and Oxygen gases are used to buffer the SF6 or CHF3 reaction. The RIE machine available in the clean room was a Oxford Instruments Plasmalab 80. Parameter maps for the variables that affect the etching rates of Si/SiO_2 using this gas mix are commonplace [152] but accurate parameter effects for each machine have to be calibrated individually.

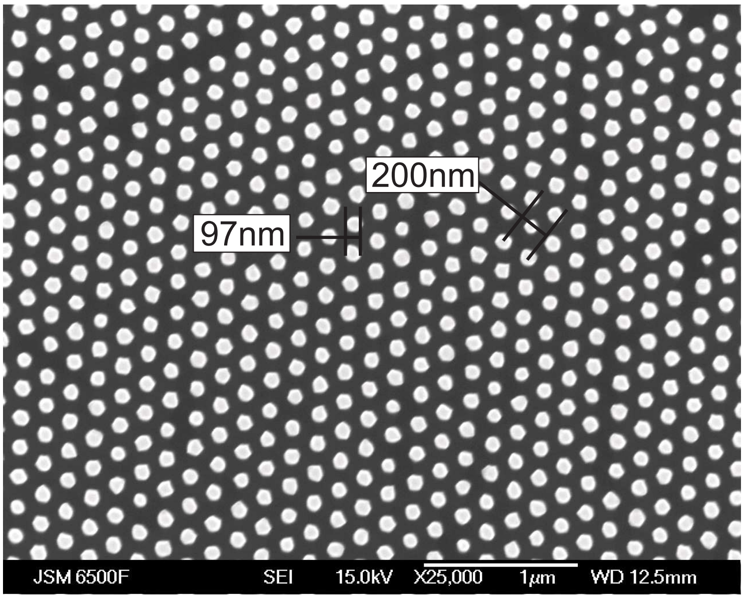

Figure 5.17: Top view of 200nm-period close-packed silicon pillars created via nanosphere lithography. The nanospheres were reduced via oxygen etch (Table 5.3 (for 30seconds)) and the vertical pillars were created via DRIE (Table 5.4 (9 cycles)) the residual nanospheres were removed by a further 15min oxygen etch (Table 5.3) which also removed the DRIE passivation layer.

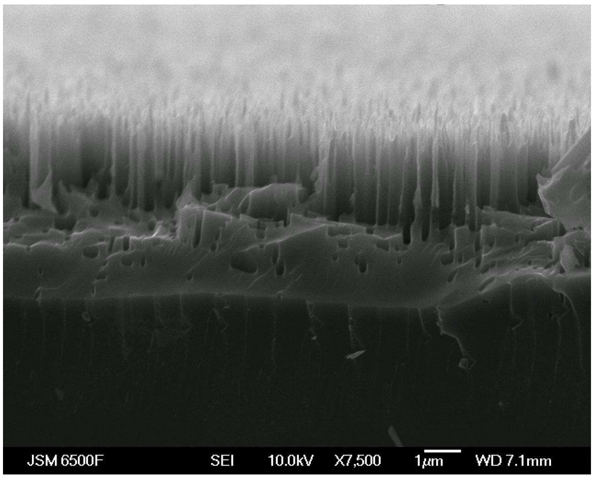

Figure 5.18: 'Grassing' damage on surface of the silicon handling wafer after creating multiple samples with recipe shown in Table 5.4 a further 15min oxygen etch (Table 5.3) was used to remove the passivation layer.

Gogolides et al. [153] have shown structures etched with a hard mask which have aspect ratios of 25:1 down to 50nm.

Theoretical studies in using SF_6 for anisotropic etching of the substrate have been carried out by Cooke et al. [154] which show that the etch parameters affect the shape of the profile created during the etch. The possible types of profiles that can emerge when etching a substrate with a nanosphere mask using simple RIE can be grouped in three categories: the dome topped pillar (Figure 5.19a), the conical pillar (Figure 5.19b), and the spike shaped pillar (Figure 5.19c). However, the temperature controlled stage used in [153] was not available in the Plasmalab 80 and also the mask they used was a ‘hard’ metal mask. Attempting a silicon etch in the RIE at 25 degrees did not give the anisotropy that was required.

ICP is a technique which can be used instead of DRIE for making shallow anisotropic samples. It uses a mixture of C_4F_8, O_2 and SF_6 gases. It was shown to produce very good anisotropic results when etching the substrate with ’soft’ etch masks such as PMMA and polystyrene. A single test sample was created via ICP at Oxford Instruments, but ICP it was not available in the clean room at the time and hence was not used.

Hence, since the RIE machine was not able to give a good enough anisotropy and cryogenic ICP was not available in the clean room. DRIE was the only method available for etching the substrate and this was used throughout the samples that were created in Southampton. For the samples made at NILT, Denmark a combination of RIE and DRIE were used to create different profile pillars, and this was carried out at their etching facilities. The variation of etching conditions carried out at NILT was able to allow a study of the effect of a combination of isotropic, anisotropic and oxidation growth/removal methods in creating various profiles. These samples will be analyzed in detail in following sections.

As previously noted, for maximum broadband antireflection, a silicon pillar would require to have a shape which creates a quintic effective refractive index variation [33]. For a material with refractive index of 3.42 in air, the pillar shape that would produce a quintic variation is shown in (Figure 3.11). To etch such a profile is very complicated as very detailed knowledge and calibration of the machine parameters is necessary. The batches that were made at NILT with different etch combinations were not successful in creating a quintic profile but yielded a range of silicon pillar profiles which were used to evaluate the change of reflectance with profile variation (Section 6.4).

5.6 Conclusions

The nanosphere lithography method developed in this section has shown to be capable of creating high quality monolayers which can be used to fabricate ‘moth-eye’ samples

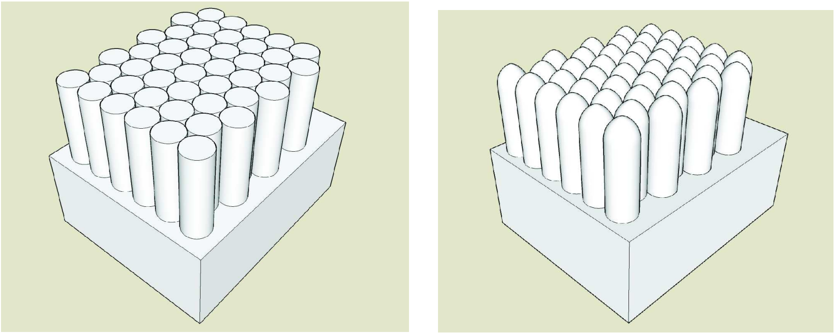

(a) Hexagonal arrangement of silicon pillars after E-beam Lithorgaphy and Deep Reactive Ion Etching.

(b) Hexagonal arrangement of silicon pillars with smoother profile after Nanosphere lithography (NSL) and Deep Reactive Ion Etching.

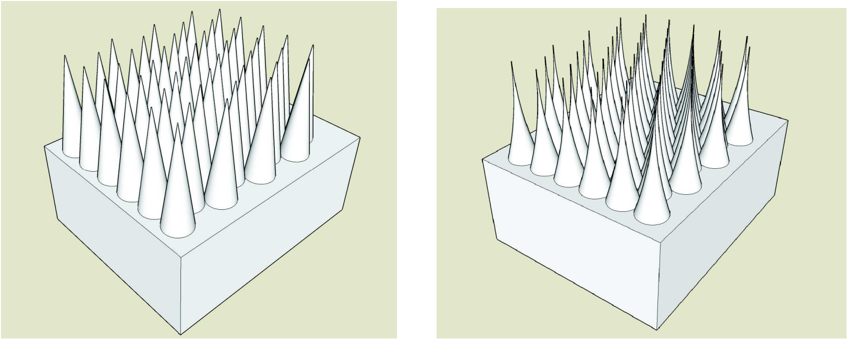

(c) Hexagonal arrangement of silicon pillars with conical profile.

(d) Hexagonal arrangement of silicon pillars with spike profile.

Figure 5.19: Nanopillar profiles after substrate Reactive Ion Etching takes place.

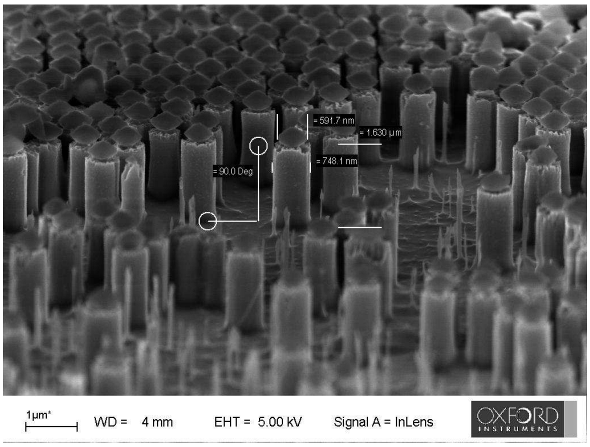

Figure 5.20: Anisotropic ICP method with nanosphere mask. The nanosphere monolayer etch mask was created at Southampton on a silicon substrate and sent to Oxford Instruments to be etched as proof-of-concept. ICP Etch parameters were not made available. Nanospheres were 780nm in diameter and were reduced in oxygen plasma (Table 5.3).

Batch No	Fabrication Method	Number of samples	Sample Size	Measurement	Variation in samples
1	NIL	1	1x1cm^2	Hemispherical Reflectance at different angles of incidence	N/A
2	NIL	5	1x1.5mm^2	Normal incidence reflectance	Design period
3	NIL	3	1x1mm^2	Normal incidence reflectance	Packing density
4	NIL	5	100x100μm^2	Normal incidence reflectance	Feature profile
5	NSL	3	2x2cm^2	Normal incidence reflectance	Feature height
6	e-beam	2	1.5mm(circle diameter)	Normal incidence reflectance	Feature topology
7	NIL	3	1x1mm^2	Diffraction isotropy variation	Feature topology
8	NIL, NSL, e-Beam	3	1x1mm^2	Diffraction isotropy variation	Feature topology

TABLE 5.6: Table of sample batches created with different nanoengineering methods. Measurements conducted on Batch 1 (Figure 6.1) are shown in Section 6.1, Measurements conducted on Batch 2 (Figure 6.9) shown in Section 6.2, Measurements conducted on Batch 3 (Figure 6.17) shown in Section 6.3, Measurements conducted on Batch 4 (Figure 6.20) shown in Section 6.4, Measurements conducted on Batch 5 (Figure 5.1) shown in Section 6.5, Measurements conducted on Batch 6 (Figure 6.23) shown in Section 6.6, Measurements conducted on Batch 7 (Figure 7.1) shown in Section 7.1, Measurements conducted on Batch 8 (Figure 7.5) shown in Section 7.2.

which are large enough to be characterized optically in terms of reflectance and diffraction both at normal and oblique incidence with the equipment available in the lab. The spacing between the close-packed spheres could be tailored by reducing their diameter via oxygen plasma etching. This is necessary to enable the further etch of substrate into pillars. The DRIE process which was carried out was able to preserve the sphere diameter and create the pillar heights required for moth-eye layers (~200-800nm). A collection of all the samples manufactured via all manufacturing methods presented in this and the previous chapter are collected in Table 5.6. These samples will be characterized in the following chapters.

Chapter 6

Reflectance characterization of sub-wavelength “moth-eye” antireflection layers

6.1 Reflectance of a close-packed sub-wavelength pattern at various angles of incidence

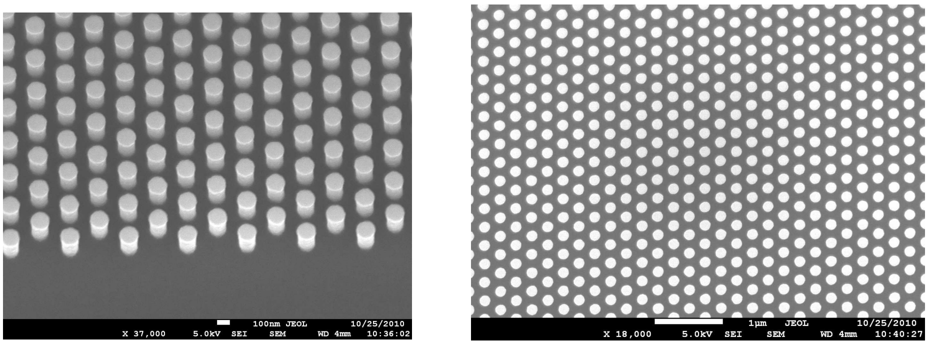

(a) SEM image of pillars at 15deg tilt

(b) Top down view of pillars

FIGURE 6.1: SEM Images of pillars constructed via Nano-Imprint Lithography on a silicon substrate. The subwavelength features were organized in a close packed pattern with a period of 270nm and a pillar diameter of 150nm. The pillar profile is vertical and the etch height of the pillars is 400nm. The conditions of the anisotropic etch are shown in Table 5.5. The total pattern size was 1cm^2 in area.

6.1.1 Design and Manufacturing

In this section the reflectance of a close-packed moth-eye antireflection layer will be measured at various angles of incidence between 0-65 degrees. The close-packed moth-eye pattern pillar sample that was manufactured was designed to have a pillar period of

280nm, a pillar height of 400nm and a pillar diameter of 140nm. The total patterned area was 1cm^2. This large area pattern was required in order to compensate for beam stretching at high angles of incidence. The laser beam diameter was 1mm, which at an angle of incidence of 65 degrees turns into an ellipse with a minor axis which is similar to the beam diameter at normal incidence (1mm) and a major axis of 2.4mm. At 80 degrees the major axis becomes 5.7mm. An SEM Image of the moth-eye surface manufactured is shown in (Figure 6.1)

6.1.2 Normal incidence measurements

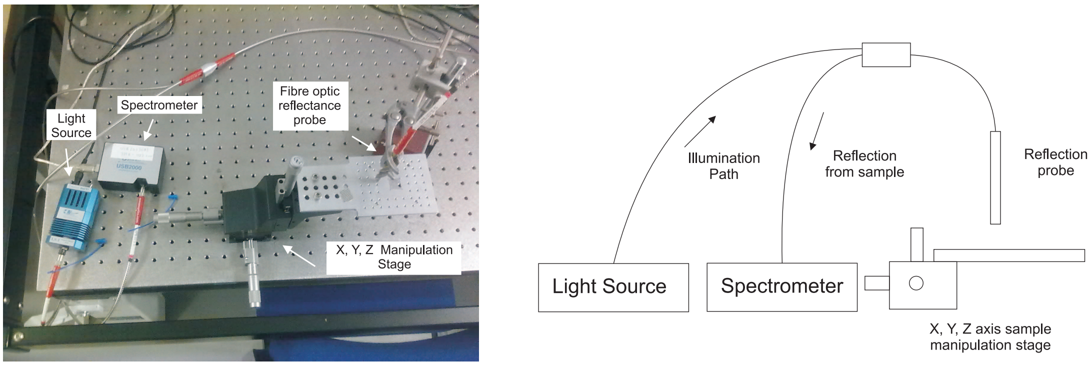

(a) Photo of setup (b) Schematic of setup

FIGURE 6.2: Picture of Normal Incidence Specular Reflectance Measurement (NISRM) Setup, depicting halogen white light source (Ocean Optics), spectrometer (Ocean Optics USB2000), 3-axis sample translation stage and reflectance probe (Ocean Optics). The light source couples light to the central the fibre in the probe bundle which illuminates the part of the sample that is measured, the reflected light comes back up through the surrounding fibres in the bundle to the spectrometer which records the measured spectra. A more detailed sketch of the reflectance probe is available in Figure 6.3

Normal incidence measurements of the pattern were carried out first. A simple reflectance measurement setup was assembled (Figure 6.2) consisting of a multiple core fibre probe in a 6-1 arrangement (6 fibres in a hex arragement with an illumination fibre in the middle, as shown in Figure 6.3a), a tungsten-halogen white light source and a spectrometer (both from Ocean Optics, Florida, USA). In this setup, the inner core of the fibre probe was used to shine the light onto the sample and the outer cores were used to collect the reflected light and direct it to the spectrometer (Figure 6.3b).

In order for the results to be reliable, the probe has to be set at the same height from each sample. To achieve this, the height was controlled by a manual micrometer stage. The maximum signal was obtained by monitoring the reflectance from the sample. When the reflectance was maximum, the height of the measured surface was at the right distance because most of the reflected light could be guided back into the fibre. This positioning procedure would also guarantee that the best signal to noise ratio was achieved from each measurement.

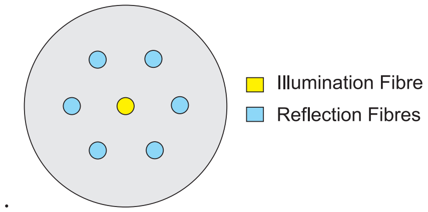

(a) Fibre arrangement on reflectance probe tip

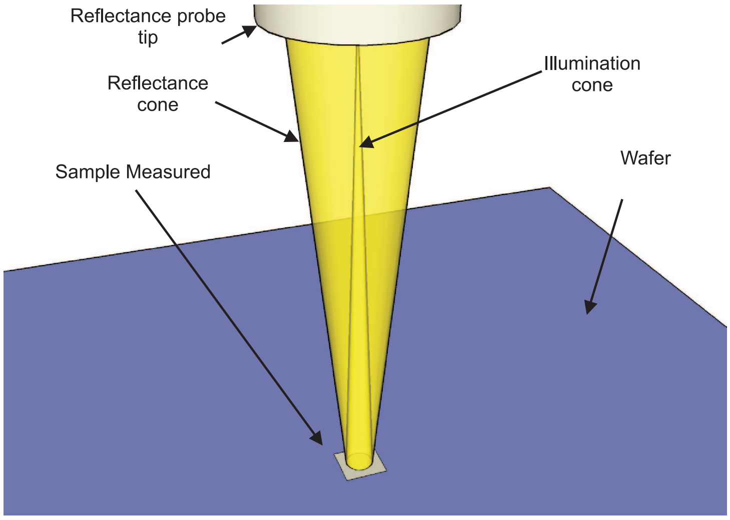

(b) 3D sketch of the NISRM operation

FIGURE 6.3: Sketch of the NISRM operation showing (a) the close packed configuration of illumination and reflection fibres on the reflectance probe tip and which fibres were used for illumination and reflectance during the experiment and (b) a sketch depicting the ray path between the reflectance probe and the sample showing the illumination cone diverging towards the sample and the reflectance being collected by the peripheral fibres.

One of the limitations of this setup is that the reflectance and illumination paths have a small distance between them (Figure 6.3a). This means that the results which are obtained are not strictly at normal incidence but at a very small angle of incidence of 7^o. Additionally, the fibre illumination spot at the maximum reflectance position is about 1mm so samples which are smaller than this cannot be accurately measured.

The measurements carried out at normal incidence were used to validate the simulation procedure, and similarly confirm that the expected results agree with theoretical predictions. The reflectance measurement that was taken with the fibre probe at normal incidence along with the simulation results is shown in (Figure 6.4).

Two simulation methods were used to verify normal incidence measurements. The first is a rigorous coupled wavelength analysis (RCWA) approach (introduced in Chapter 3). The RSoft Diffract MOD software was used to simulate the reflectance of the moth eye structure via definition of a 3D CAD model similar to that shown in previous simulations (Figure 3.1).

The other simulation method that was used was an effective medium theory (EMT) approach. This approximation was possible because the pillars have quite a vertical profile that makes the metamaterial layer equivalent to an intermediate thin film layer with an effective refractive index.

6.1.2.1 Effective medium theory simulation procedure

The effective refractive index was calculated by taking the average effective refractive indices for polarized light parallel and vertical to a rectangular grooved relief pattern as shown by Gaylord [155].

For the Electric Field vertical to the grooves the effective refractive index is calculated as:

$$\tilde{n}_{effE\perp K} = [n_1^2(1-F) + n_2^2 F]^{\frac{1}{2}} \tag{6.1}$$

Where n$_{effE\perp K}$ is the effective refractive index perpendicular to the grooves, n$_1$ and n$_2$ the refractive indecies of the substrate and the medium and F the fill factor of material with refractive index n_2.

And for the Electric Field parallel to the grooves the effective refractive index is calculated as:

$$\tilde{n}_{effE\parallel K} = [\frac{(1-F)}{n_1^2} + \frac{F}{n_2^2}]^{-\frac{1}{2}} \tag{6.2}$$

Where n$_{effE\parallel K}$ is the effective refractive index parallel to the grooves, n$_1$ and n$_2$ the refractive indecies of the substrate and the medium and F the fill factor of material with refractive index n_2.

For the average refractive index of the layer we take the RMS behavior of the parallel and vertical polarizations:

$$\tilde{n}_{eff} = [\frac{n_{eff\parallel}^2 + n_{eff\perp}^2}{2}]^{\frac{1}{2}} \tag{6.3}$$

Where $\tilde{n}_{eff}$ the average refractive index, n$_{effE\parallel K}$ is the effective refractive index parallel to the grooves and n$_{effE\perp K}$ is the effective refractive index perpendicular to the grooves.

6.1.2.2 Comparison of EMT and RCWA simulations with the experimental results

As mentioned before, the manufactured sample was designed to have a pattern period of 270nm, a pillar diameter of 150nm and a height of 400nm. The pillar period and diameter of the pillars were verified by the SEM images (Figure 6.5). The parameters that were used in the EMT simulation of the sample were the average period of the pillars in the vertical (270nm) and horizontal (470nm) directions which is 370nm and the diameter of the pillar that was simulated was 150nm. In the RCWA simulation which was carried out, the parameters that were used for the simulation were 270nm for the period, 150nm for the diameter and 400nm for the sample height.

It is shown that the RCWA simulation corresponds to the measured result quite well (Figure 6.4). The troughs around 500nm and 650nm are present in both in simulation and the experimental data.

For shorter wavelengths (450-500nm) EMT predicts the reflectance of the sample more accurately, however for the rest of the wavelengths considered, there is an extra trough in the experimental data around 630nm which was not predicted.

This discrepancy in the graph around 630nm (Figure 6.4) was because of the grating coupling mode which could not be included in the calculation *de facto* since flat surfaces do not contain such modes. To prove that this is the case, diffraction grating coupling theory will be used to calculate the resonant wavelength.

We begin by assuming that the grating coupling order is around 630nm, and work back to prove that this is the case. The diffraction coupling equation for a grating at normal incidence is shown below (Equation 6.4) [156].

$$\lambda = 2n_e\Lambda \tag{6.4}$$

Where: n_e - effective refractive index, λ - wavelength, Λ - grating period.

Out of plane coupling occurs for second order gratings [156] thus where Λ we replace $\Lambda/2$ and get Equation 6.5.

$$\lambda = n_e\Lambda \tag{6.5}$$

Hence, knowing the average period of the pillars in the x and y directions (370m) and the grating coupling wavelength, we get Equation 6.6 for the effective refractive index of the layer at that wavelength.

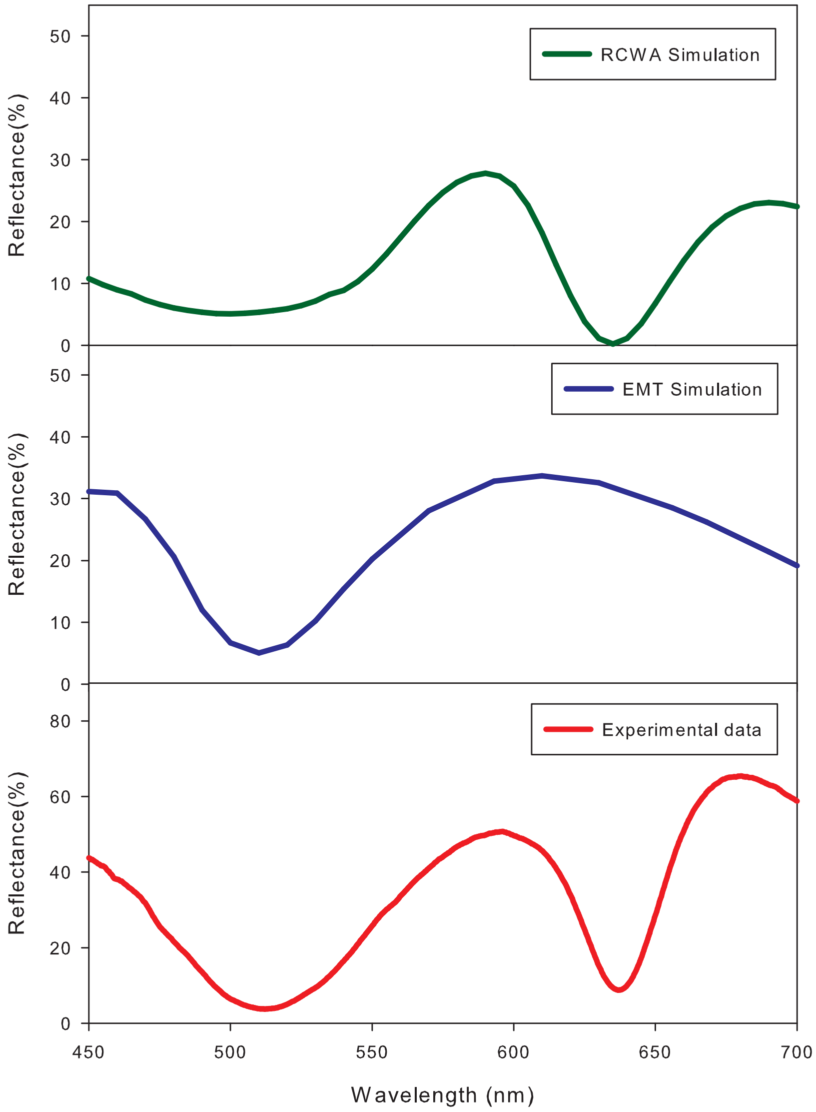

FIGURE 6.4: (a) RCWA simulation for a close packed pillar pattern with a straight cylindrical pillar profile, 270nm in period, 150nm in pillar diameter and 400nm in pillar height (b) EMT simulation for the same pattern described previously, the period used in EMT simulations is the average pillar period in the vertical (470nm) and horizontal (270nm) directions which is 370nm (Figure 6.5 (a,b)) and (c) the experimental reflectance data obtained at normal incidence, for the close packed sample that was measured which is shown in Figure 6.1.

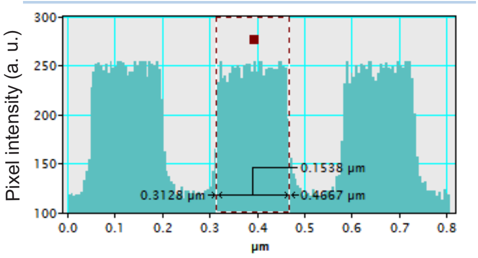

FIGURE 6.5: Pillar diameter profile extracted from contrast information in SEM image in Figure 6.1b.

$$n_e = \frac{\lambda}{\Lambda} = \frac{630nm}{370nm} = 2.25 \tag{6.6}$$

A simple method of calculating the effective refractive index is by using the pillar-to-air volume density and weighing that in terms of the refractive index of each material. The effective refractive index of the layer n_e is calculated [157] according to Equation 6.7.

$$n_e = \sqrt{D(n_{silicon}^2 - 1) + (1 - D)n_{air}^2} \tag{6.7}$$

Solving for fill factor density D and assuming $n_{air} = 1$ we get (Equation 6.8)

$$D = \frac{n_e^2 - 1}{n_{silicon}^2 - 2} = 0.145 \tag{6.8}$$

From the geometry of the close packed structure it can be shown that the density can be written as a function of the radius and period of the pillars (Equation 6.9)

$$D = \frac{\pi r^2}{\Lambda^2} \frac{2}{\sqrt{3}} \tag{6.9}$$

Solving for pillar radius we get $r = 74nm$ hence a diameter of 148nm.

From the SEM Image taken (Figure 6.1 b) an image analysis software (Digital Micrograph, Gatan) was used to measure the exact distance of the pillar diameter and period (Figure 6.5) which was 153.8nm, very close to what was predicted.

Hence, it has been shown that the dip that occurs in the reflectance spectrum around 630nm originates from the grating coupling orders in the structure and that the EMT simulation is as successful as its assumptions allow it to be, since it was not meant to take the grating coupling orders into account.

This fact was double-checked via RCWA (Rigorous Coupled Wave Analysis) simulation whereby the structure was simulated by modeling it in 3D. Indeed as can be shown in Figure 6.4 the RCWA simulation produces results that compare closely to the experimental data and include the diffraction coupling at a wavelength around 630nm.

Although the shapes of the graphs are consistent with theory the intensity levels differ in the region 10-30% in reflectance between experiment and the simulations. This is could be due to the imperfections in the nanopillar layer and possible variations in the lamp intensity over time.

6.1.3 Reflectance measurements for angles of incidence that are higher than zero

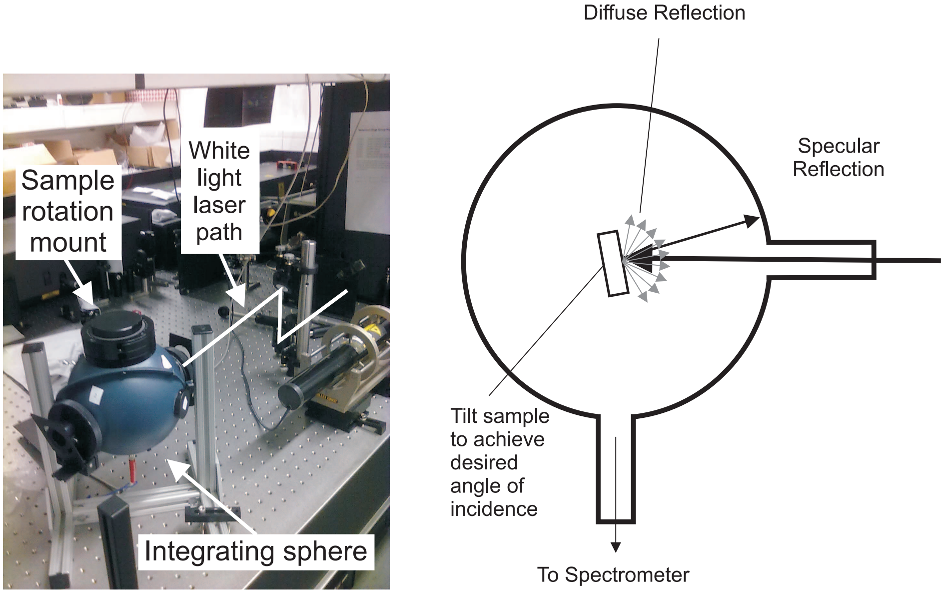

(a) Photo of setup (b) Schematic

FIGURE 6.6: (a)Integrating sphere setup coupled to white light laser. Light was directed from an enclosed laser source to a periscope and onto the target inside the integrating sphere. Laser path shown as white line on figure. (b) Target was tilted in the integrating sphere to change angles of incidence with a rotation mount and total reflectance was collected via a fibre optic cable which led to a spectrometer.

After the normal incidence results showed a confirmation of predictions according to the simulations that were carried out, measurements at higher angles of incidence were done. The reflectance setup that was used consisted of an integrating sphere setup (RT Series, Labsphere, USA) which was coupled to a white light laser source (SC450, Fianium, UK). (Figure 6.6)

To confirm that the results obtained from the integrating sphere and the fibre probe were consistent, a comparison of reflectance was made at a low angle of incidence (5 degrees). As shown in Figure 6.7 the results are consistent with each other. This fact validates the experimental data observed from the integrating sphere and verifies the validity of further results obtained at other angles.

The samples were attached to a mount that has an integrated goniometer and clip holder. This holder allows the angle of incidence of the laser on the sample to be controlled. The output was taken via a fibre optic cable that was attached to the bottom of the sphere which led to a spectrometer (B&W Tek).

The reflectance measurement was taken in single beam mode. The reference sample that was used was a silver mirror because silver has a reflectance close to 100% for wavelengths in the 450 - 700nm region.

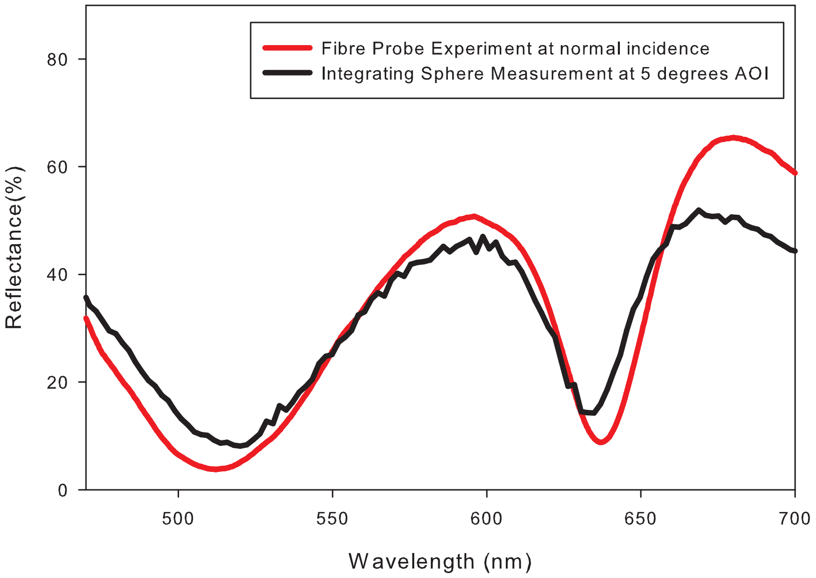

Figure 6.7: Comparison of the fibre probe experiment at normal incidence, and the result obtained from the integrating sphere at a 5 degree AOI, for the close packed subwavelength sample with a pattern period of 270nm, a pillar diameter of 150nm and a pillar height of 400nm shown in Figure 6.1

Just as for the experiments conducted at normal incidence (Section 6.1.2), RCWA and EMT simulations were carried out. 3D graphs of Reflectance vs wavelength and angle of incidence were compared between measurement and simulation. The RCWA (Figure 6.8a), EMT (Figure 6.8c), and experimental data (Figure 6.8f) agree quite well in terms of the progression of the peaks and troughs of the reflectance graphs with angle of incidence(AOI) variation.

More specifically, at zero degrees AOI, two troughs and one peak are distinguished in the experimental data (Figure 6.8f). The first trough is near 520nm at normal incidence and its progression as the AOI increases to 60 degrees splits into two troughs, both of which are blue shifted as the AOI increases. This trend is evident both in the RCWA (Figure 6.8 a) and EMT (Figure6.8c) simulations.

The second trough in the experimental data around 640nm remains near the same wavelength range 620-640nm as the angle of incidence increases (Figure 6.8e). This is represented in the RCWA, but not the EMT simulation because it is due to a diffraction coupling mode, which, as shown in Section 6.1.2.2, is not considered in the EMT simulation by definition. The peak in the experimental data around 580nm (Figure 6.8e), is blue shifted as angle of incidence is increased, following EMT simulation predictions (Figure 6.8c). The RCWA simulation shows a similar peak progression which is fragmented in two parts (Figure 6.8b). The first peak is centred around 600nm at normal incidence and decreases in intensity near 30 degrees AOI and from then onwards a second peak starts appearing between 30-65 degrees in the 500 - 560nm wavelength region which correlates with the experimental data. The reason suspected for the difference between experiment and simulations was that pillars simulated were completely vertical in profile whereas the ones manufactured were not. A clear flat-top region is not distinguishable in the SEM image (Figure 6.1a) and it is noticed that the pillars actually have a slight curvature on the top which contributes to the discrepancy between simulation and experiment.

6.1.4 Conclusions

The experimental measurements show that as angle of incidence increases (5-65 degrees), the reflectance of the pillars increases slightly in intensity (Figure 6.8e). However, the most pronounced change is that of the blue shift of the minimum reflection region in the low wavelength end of the spectrum. The trough noticed in the higher wavelengths is only slightly blue shifted. The reflectance of the structure does not significantly change between 0-30 degrees AOI, and for larger AOI a blue shift of the minimum reflectance and a broadening of the reflectance peak was noticed (Figure 6.8e).

A validation of the RCWA simulation technique for subwavelength patterns has been carried out by comparing it to EMT and the experimental results at normal incidence. The RCWA simulation helps explain the dip shown around 630nm wavelength which originates from diffractive order coupling that occurs due to the periodicity of the pillars. Hence, even though EMT does provide a good estimate the reflectance of the subwavelength structure, the RCWA technique is more accurate in predicting the reflectance of these structures and will be the method of choice for comparing the experimental results with theory in all the following experimental chapters.

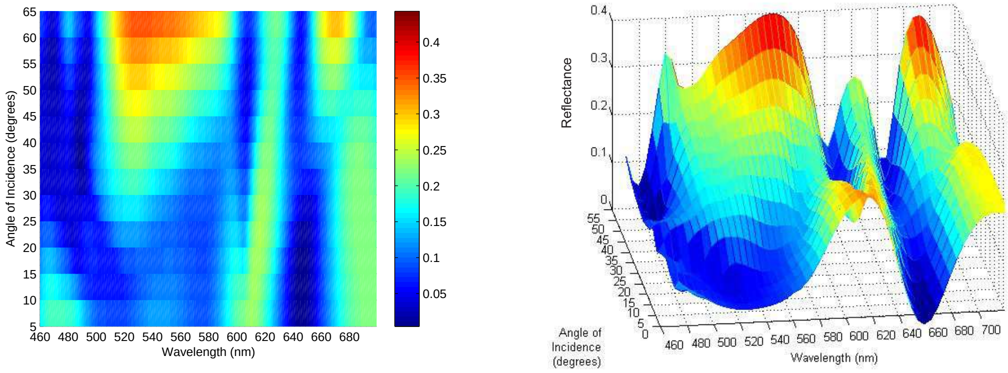

(a) RCWA simulation of Reflectance v Angle of Incidence and Wavelength - Top view

(b) RCWA simulation of Reflectance v Angle of Incidence and Wavelength - 3D view

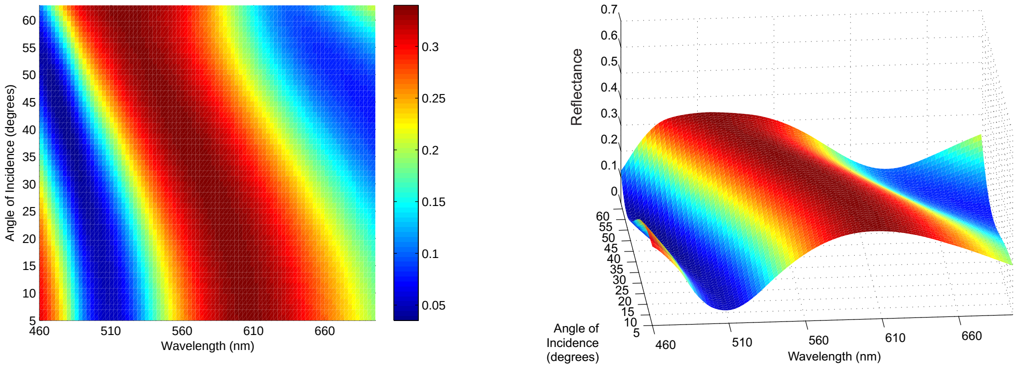

(c) EMT simulation of Reflectance v Angle of Incidence and Wavelength - Top view

(d) EMT simulation of Reflectance v Angle of Incidence and Wavelength - 3D view

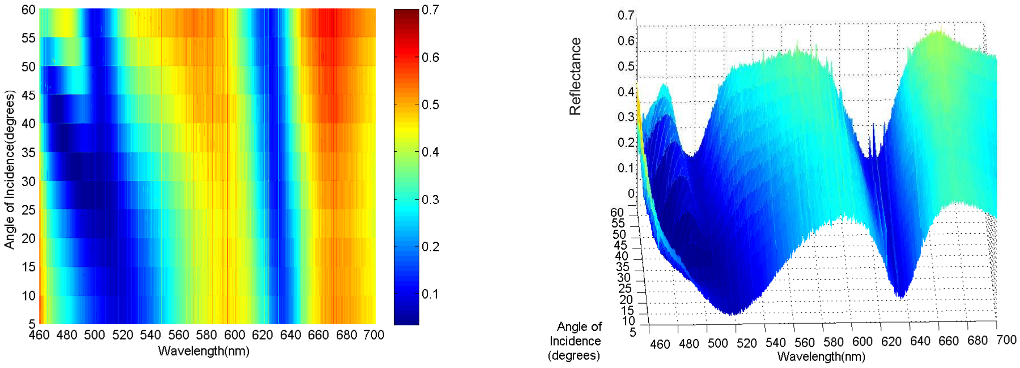

(e) Experimental data of Reflectance v Angle of Incidence and Wavelength - Top view

(f) Experimental data of Reflectance v Angle of Incidence and Wavelength - 3D view

FIGURE 6.8: Comparison of experimental and simulation data in the 450-700nm wavelength range for various angles of incidence for the close packed subwavelength sample with a pattern period of 270nm, a pillar diameter of 150nm and a pillar height of 400nm shown in Figure 6.1.

6.2 Normal incidence reflectance of close-packed sub-wavelength patterns with varying periods

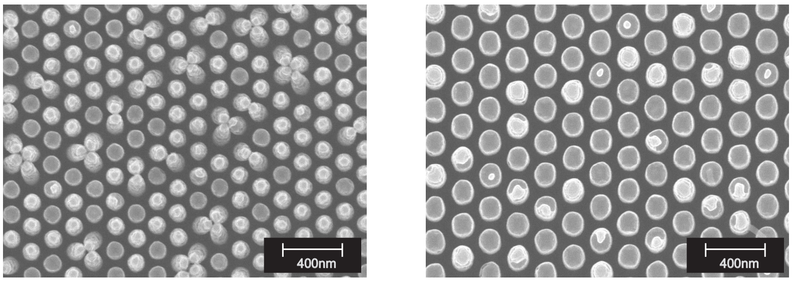

(a) Sample 1, 150nm period close-packed pillar pattern.

(b) Sample 2, 200nm period close-packed pillar pattern.

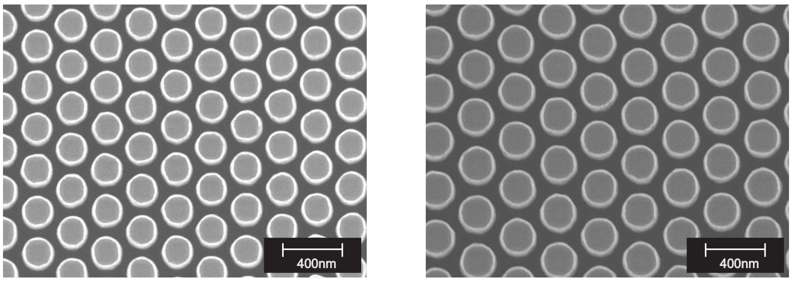

(c) Sample 3, 250nm period close-packed pillar pattern.

(d) Sample 4, 300nm period close-packed pillar pattern.

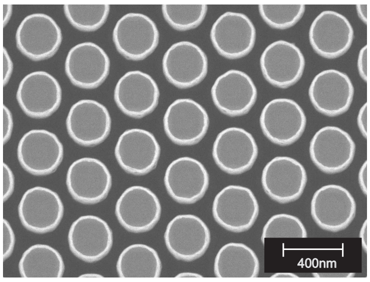

(e) Sample 5, 350nm period close-packed pillar pattern.

FIGURE 6.9: SEM Images of close-packed samples made at NILT via nano-imprint lithography with increasing pattern period. The subwavelength features were designed in a close-packed pattern with periods of 150nm, 200nm, 250nm, 300nm and 350nm and a density factor of 0.5. The pillar profile is vertical and the etch height of the pillars is 400nm. The etch conditions of the anisotropic etch which was used to create this sample are shown in Table 5.5. The residue noticed on figures (a) and (b) is part of the aluminium mask that has not been fully removed from the sample.

6.2.1 Design and Manufacturing

Five samples of close-packed nanopillar moth-eye layers with varying periods (150-350nm) were produced at via Nano-Imprint Lithography (NIL). The five design periods that were selected were 150nm, 200nm, 250nm, 300nm and 350nm. The area density factor (packing density) for the close packed pattern was selected to be 0.5. The depth of the pillars was set to be 400nm and the overall area of each sample was a parallelogram of 1x1.5mm.

In chapter 3, section 3.1.2, the pillar density was defined via a density factor, which is the fraction of the diameter over period. In this chapter, pattern density is measured via the term packing density or area density factor which is defined as the fraction of the area of the base of the pillars with respect to the total area of the unit cell (Equation 6.10).

$$\text{Area Density Factor} = \frac{\text{Pillar base area}}{\text{Total area}} = \frac{\pi * R^2/2}{P^2 * sin(60)/2} \tag{6.10}$$

Where R the radius of the pillar base and P the period of the pillars in the close-packed arrangement.

6.2.2 Experimental Procedure

FIGURE 6.10: Nikon LV100DA-U microscope apparatus in the lab

To measure the reflectance of these samples the fibre probe could not be used because the spot size (1.2mm diameter) was larger than the sample. Instead, a modified Nikon Eclipse LV100DA-U microscope was used for these measurements (Figure 6.10). It was converted to facilitate as an experimental apparatus for normal incidence reflectance measurements of very small samples by attaching a fibre probe to the second port module (Figure 6.11).

The limiting resolution of this customized solution was calculated as follows. The image of the sample projected on the second extraction port is circular and 4.91cm^2 in area.

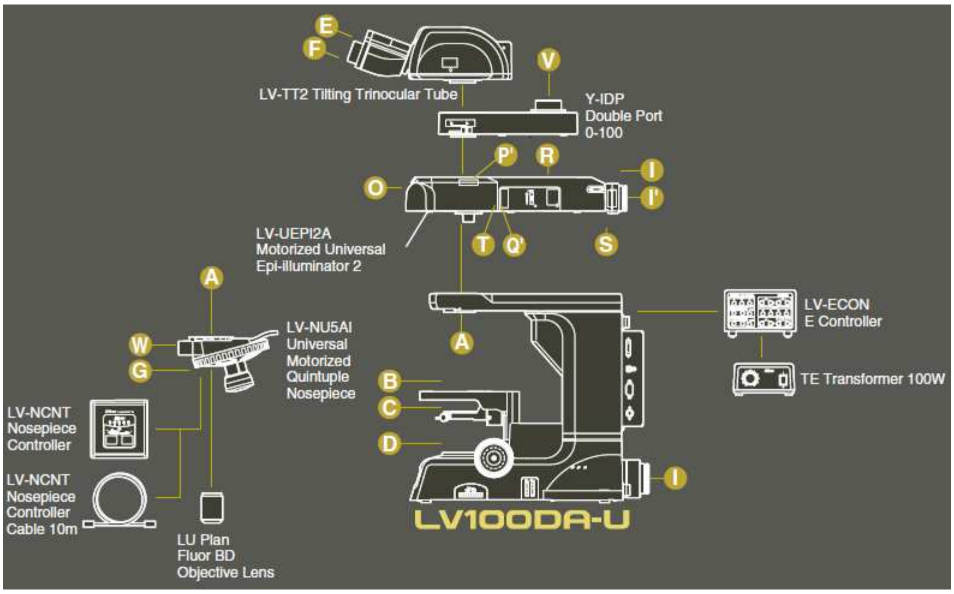

Figure 6.11: Nikon LV100DA-U microscope apparatus with optional components [Image edited from: Nikon microscope brochure]

Lens Magnification	Resolution of fibre measurement
10X	24μm
20X	12μm
50X	4.8μm
100X	2.4μm
150X	1.6μm

Table 6.1: Variation of measurement resolution with increase in lens magnification

The fibre core used on this port to collect the light that would be measured in the spectrometer is 400μm in diameter (125,700um^2 in area), so the resolution of this system is 1/3900 times that of the projected image. The true size of the area that corresponds to the projected image depends on the lens. With the smallest magnification (10X lens) the real size of the projected image corresponds to a circle 1.5mm in diameter or 1.767mm^2 in area. Hence the resolution of the system was 1.767mm^2 / 3900 = 453μm^2 which corresponds to a circle of 24μm in diameter. As the magnification increases so will the resolution, hence for the maximum magnification of 150X, the resolution was 15 times larger (i.e. a 1.6μm diameter feature). The resolutions achieved by the other available magnifications are shown in Table 6.1.

As the magnification of the lens gets larger, the acceptance angles of the lens increase. This means that the light collected and transmitted from a lens with high magnification includes angles of incidence and detection in a range that is not close to that of normal incidence. The reflectance results will therefore not be in accordance with reflectance predictions at normal incidence since a lot of angles of incidence are considered simultaneously when taking the reflectance measurement. It is expected as the magnification used to take the measurements increases, the accuracy of the results decrease for normal incidence measurements decreases.

In order to find the maximum magnification at which the measurements would give reliable results for normal incidence reflectance, a calibration of the different magnifications needed to be carried out for a sample whose normal incidence reflectance is well known and characterized. The reflectance of all the magnification lenses were tested with a thin film sample of 150nm of SiO_2 on a silicon substrate (Figure 6.12) to determine which ones could be used to obtain accurate normal incidence measurements.

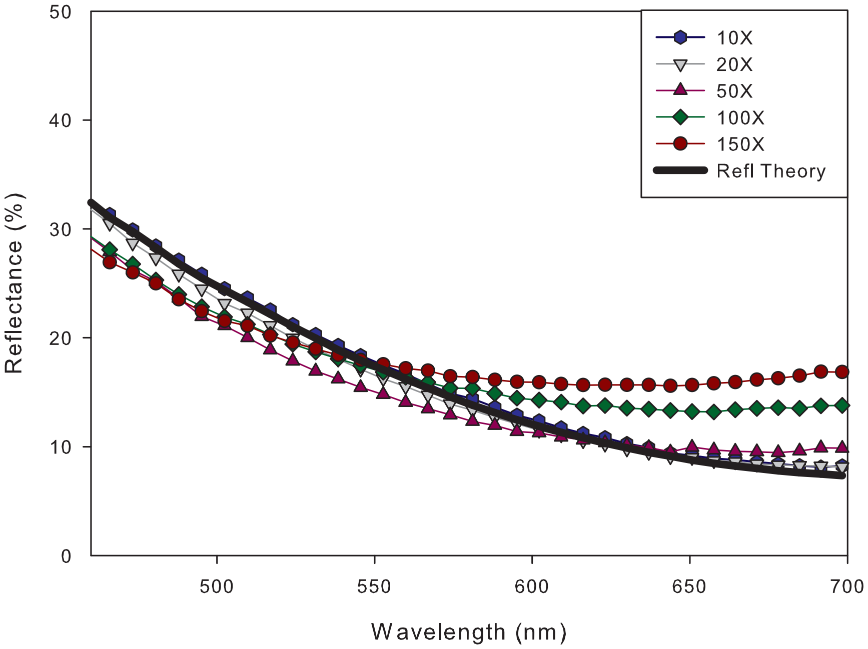

Figure 6.12: Normal incidence reflectance results for a 150nm-thick layer of SiO_2 on Si taken to measure the accuracy of the results at different magnifications

As it is shown in Figure 6.12, the lowest (10X) magnification lens gives the smallest error compared to what is expected from theory because the beam has the smallest distortion for this lens. As the lens magnification changes, the beam distortion becomes progressively worse with the 150X lens giving the largest error. The maximum magnification lens that could be used for normal reflectance measurements is the 20X lens since this magnification also shows minimal deviation from theoretical expectations, but for the most accurate results the 10X lens should be used.

The 10X lens allows for a system a resolution of a 24μm-diameter circular area. Since the smallest samples that needed to be measured (100x100μm) were larger than the limiting resolution of the system, accurate measurements were possible for all the samples that were investigated in this thesis.

After selecting the 10x lens for the measurement process, the experimental sequence that was needed for obtaining a measurement of normal reflectance using the Nikon microscope was as follows:

- First the sample is selected and brought into focus using the CCD camera and the the trinocular tube on the first output port.
- The light is then redirected to the second reflectance output port by moving the internal mirror to redirect the light.
- The height of the stage is then adapted so that the path difference between the two ports is accommodated for and the image comes in focus at the fibre optic cable on the second port.
- The measurement is then recorded from the sample.

Before any data acquisition, a reference measurement needs to be used to calibrate the measurement. In our case the reference measurement was taken from a silver mirror. The spectrometer software could take this reference measurement into account in order to produce calibrated reflectance values.

6.2.3 Results and Conclusions

The samples shown in this section were designed in order to verify the predictions of the RCWA simulations in Chapter 3 and hence were designed to be identical in profile (vertical), height (400nm) and packing density (0.5) to the ones which were simulated. It was particularly sought to confirm the phenomenon of the red shift of the reflectance minima as the period of the pattern increases.The normal incidence measurements taken by the Nikon microscope for each period are presented in Figure 6.13. The red-shift of the reflectance profile as the period of the close-packed pattern was increased was verified, just as was expected from simulations that were carried out previously (Figure 3.12 (a)).

Since the samples were designed to be identical to those considered in the RCWA simulations in Chapter 3 the comparison between experiment and simulation can be easily done by taking the appropriate data slices out of the 3D simulation graphs at the respective periods 150, 200, 250, 300 and 350nm (Figure 6.14). A comparison of the simulations to the reflectance measurements acquired by experiment is shown in Figure 6.13.

Reasons for discrepancies between the simulation and experiment include:

- It can be deduced from the SEM images that were taken (Figure 6.15), that the profile of the pillars was not entirely vertical as was intended. The pillars made by NILT were not totally flat-topped pillars but there was an added collar on the top

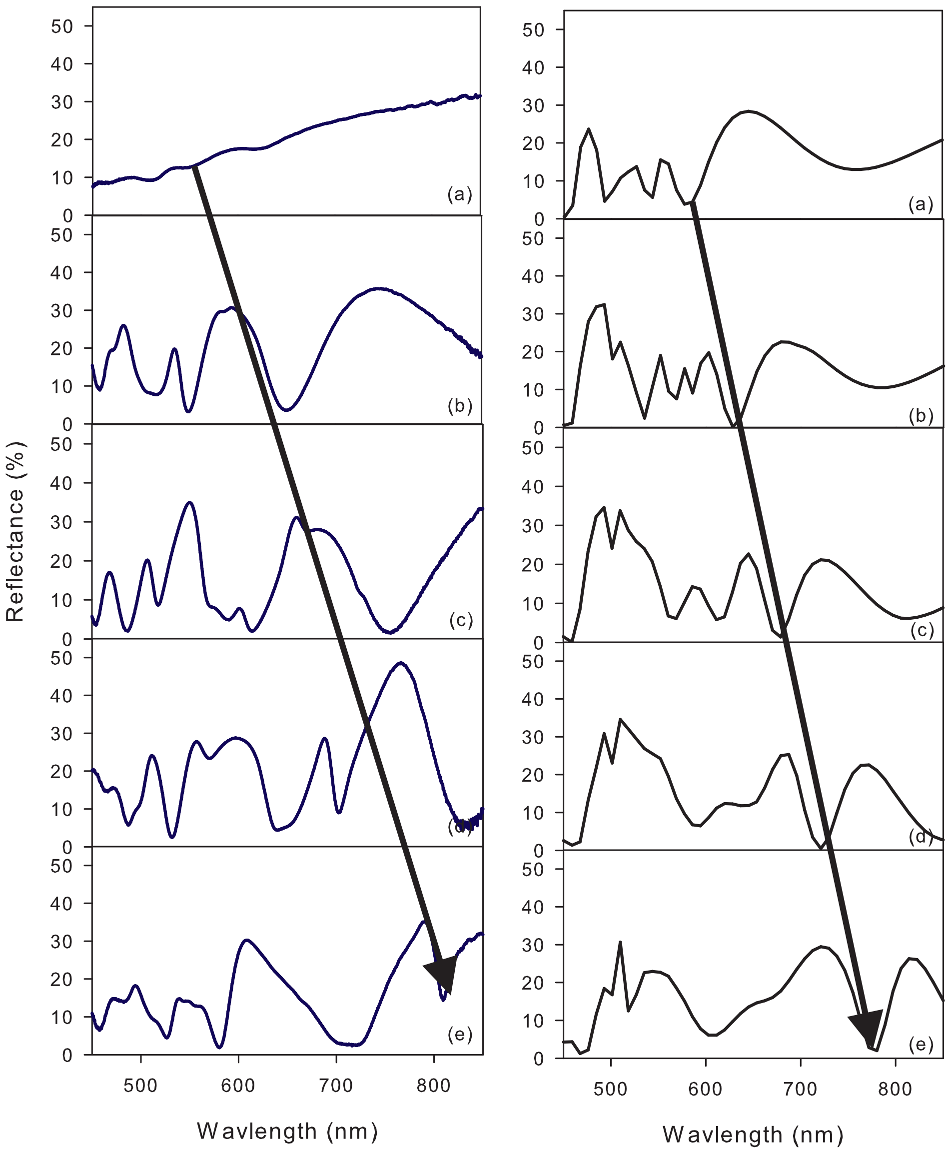

Figure 6.13: Comparison of experiment (left) to simulation (right) for samples with increasing close packed pattern periods of (a) 150nm (b) 200nm (c) 250nm (d) 300nm (e) 350nm shown in Figure 6.9. The parameters for pillar height (400nm), a density factor (0.5) and profile (vertical) were identical between simulated and manufactured samples.

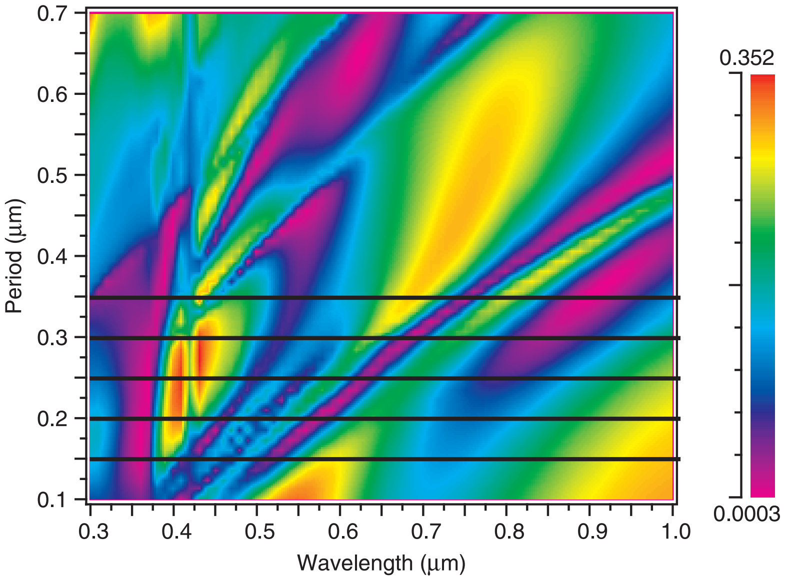

Figure 6.14: Depiction of the selection of simulation slices from a simulation carried out in section 3.1.5.4 (Figure 6.13) of reflectance of a sub-wavelength close packed pattern of silicon pillars on a silicon substrate whose close packed pattern periods vary from 100-700nm. The simulation pillar height is 400nm, their profile is vertical and their density factor is 0.5 which is identical to the characteristics of the samples which were measured in this chapter (Figure 6.9)

of the pillars which did not allow a direct comparison with the profile simulation carried out. This was confirmed by tilting the sample at a 20 degree angle and analyzing the brightness data of the SEM image with a post-processing software called DigitalMicrograph (Figure 6.15).

- The SEM images also show that there is residue from the NILT process on the top of the pillars. Additionally for the smallest fill factor, some pillars could not take the stress and have collapsed into groups of three or four. This is considered to be the main reason for which the reflectance results for this sample period are very different to the ones expected from simulation.
- Some of the samples were visibly tainted with residual material which might be left over after the NIL procedure and would affect the measurements Figure 6.16.

Concluding, even though the simulations did not match up exactly to the experimental results due to the aforementioned reasons, the trend of the reflectance graph compares well with expectations from simulations; as period of the structure is increased, the region(s) of minimum reflection shift to higher wavelengths. The samples were found to be contaminated and did not come out as flat-topped as expected from the NIL process and in the case of the 150nm period pillars they were not able to survive the etch as they collapsed into groups of three or four. These are thought to be the main reasons for which discrepancies were noticed between simulation and experiment.

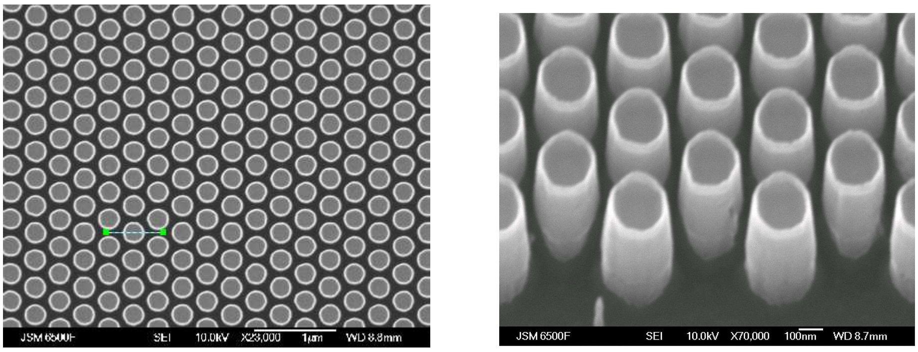

(a) SEM image of top view

(b) SEM image taken at a 20 degree angle which makes the collar on top of the pillars visible.

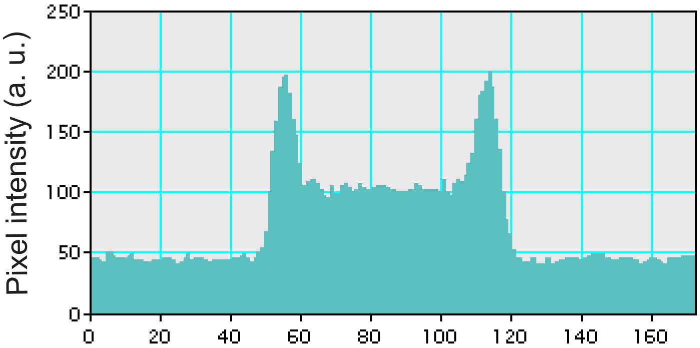

(c) Profile of height measured in image (a)

FIGURE 6.15: Images of identical pattern created via NanoImprint Lithography a) Top view SEM image of pillars b) 20 degree side view of pillars showing pillar collars, c) slice of intensity taken from SEM image. The manufacturing parameters for the sample shown in these images were: Close-packed pattern period 250nm, pillar height 400nm, packing density 0.5 and pillar shape was vertical.

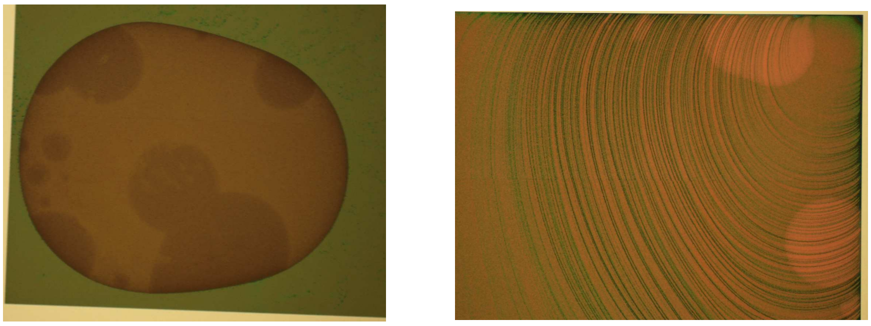

(a) Residual material left over after NIL

(b) Concentric rings associated to defects in NIL procedure

FIGURE 6.16: Optical Microscope Images of patterns created via NanoImprint Lithography for samples in (a) Figure 6.9d and (b) Figure 6.9c with 250 and 300nm close packed periods respectively. Both samples have a 400nm pillar height, 0.5 packing density and vertical pillar profile.

6.3 Normal incidence reflectance of close-packed sub- wavelength patterns with varying packing densities

6.3.1 Design and Manufacturing

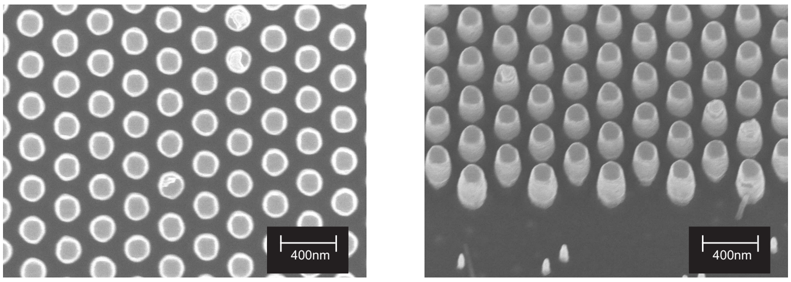

(a) Top view of Sample A (b) Tilt view of Sample A

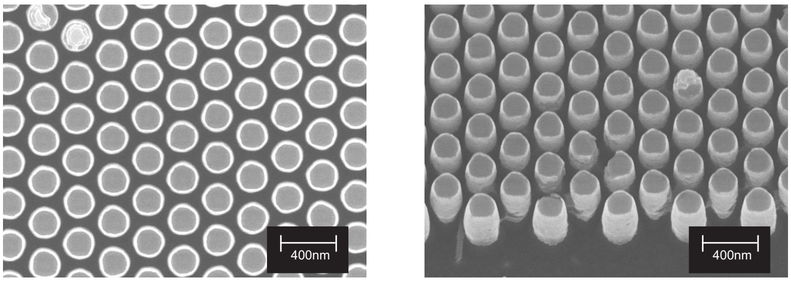

(c) Top view of Sample B (d) Tilt view of Sample B

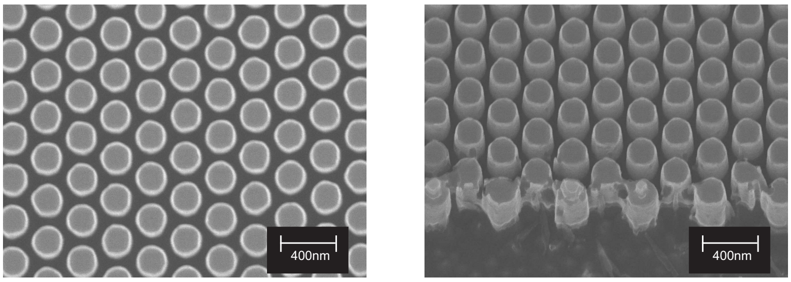

(e) Top view of Sample C (f) Tilt view of Sample C

FIGURE 6.17: SEM images of samples A,B,C created at NILT via nano-imprint lithography with an increasing packing density of 0.2, 0.35 and 0.5 respectively. The sub-wavelength features were organized in a close-packed pattern with a period of 250nm, and feature diameters of 117nm, 155nm and 185nm. The pillar profile is almost vertical and the etch height of the pillars is 400nm. The etch conditions of the anisotropic etch which was used to create this sample are shown in Table 5.5. The residue noticed on figures (a), (b), (c) and (d) is part of the aluminium mask that was not fully removed from the sample during the mask removal.

In this section the packing density of three samples was varied between 0.2 (sample A), 0.35 (sample B) and 0.5 (sample C). The three samples, A, B and C had pillar diameters 117nm, 155nm and 185nm respectively. The period of all the samples kept at 250nm, the depth of the samples was set at 400nm and the topology was set to be a close-packed pattern. The patterns were made on silicon wafers via NIL (Figure 6.17).

6.3.2 Experimental Procedure

The experiments were carried out using the Nikon microscope setup (explained in Section 6.2.2), because the sample sizes (1x1mm squares) were smaller than the 1.2mm-diameter beam used in the fibre probe setup. The reflectance measurements are shown in Figure 6.18.

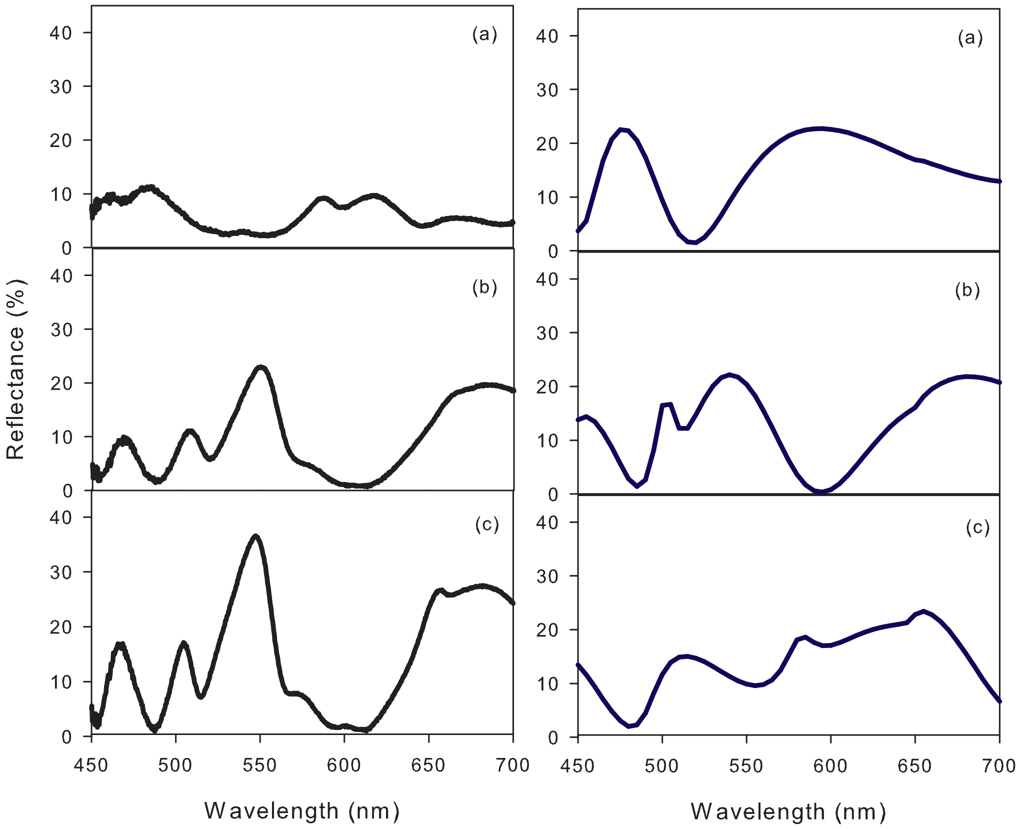

FIGURE 6.18: Normal incidence reflectance (left) of the manufactured samples shown in Figures 6.17(a, c and e) respectively and simulations (d-f) for samples with packing densities of (a) 0.2 (b) 0.34 and (c) 0.5 The experimental results (left) for samples B and C are almost identical which verifies that there was a problem with etching sample C on the whole area. Please refer to the simulation of Sample B to compare the reflectance results of the actual manufactured result for Sample C to simulation.

6.3.3 Results and Conclusions

It is obvious from the SEM images (Figure 6.17c) and the optical measurements (Figure 6.18c) of Sample C that the manufacturing process was not successful, as they match those of Sample B. The pillar diameter of sample C was measured to be 156.8nm (Figure 6.19c) very close to the diameter required for Sample B 153.4nm and not 185nm which was what was required to achieve a packing density of 0.5 for a period of 250nm. The diameter achieved was similar to the pillar diameter required to achieve a packing density of 0.35 for sample B (155nm). The reason for the unsuccessful etch was that the etch stamp could not be manufactured down to the resolution required for the spacing between features to be only 62.5nm.

The two first simulations of the structures which were designed for Samples A and B (Figure 6.18d,e) show a correlation with the experimental results (Figure 6.18a,b). For the first sample, the exact shape of the measured reflectance (Figure 6.18a) might be poor compared to simulation (Figure 6.18d), but the positions of the peaks and troughs of the simulation do correlate with the characteristic troughs and peaks in the experimental result. For the second sample, the positions of the peaks and troughs and the shape of the measured reflectance (Figure 6.18b) correlate very well with the simulated reflectance (Figure 6.18e), whereas the experimental results of the third sample (Figure 6.18c) aren't at all similar to the expected simulation of reflectance for that sample (Figure 6.18f), but are very similar to the experimental and simulation results for the reflectance of the second sample (Figure 6.18e). As previously mentioned, this was because the third sample (Figure 6.19c) was not created according to design but erroneously resulted in having a diameter which was almost identical to the second sample (Figure 6.19b).

Concluding, based on the samples that were made with 0.2 and 0.35 packing densities (samples A and B), as packing density increases, the main reflection dip observed in the reflectance curves moves to higher wavelengths (specifically from 550nm to around 600nm). SEM image analysis shows that the manufacturing of the sample with packing density of 0.5 (Sample C) was unsuccessful because after the etching procedure, the pillar diameter turned out to be similar to that of the sample with 0.35 packing density.

The optical measurements were verified by RCWA simulations quite well. Sample A did not match the simulation as well as sample B. Possible reasons for this include the larger amount of defects noticed on the tops of the pillars when examining the sample via SEM. The peaks seem to be at the right positions, but the reflectance intensity is lower than expected.

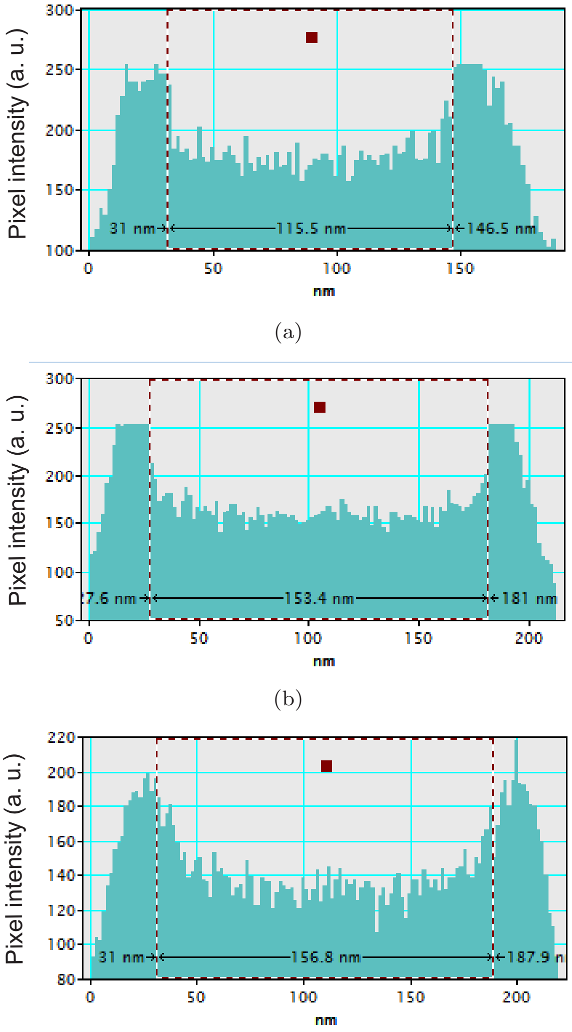

(a)

(b)

(c)

Figure 6.19: SEM image intensity analysis of one pillar diameter for samples with packing densities of (a) 0.2, (b) 0.35 and (c) 0.5 shown in Figure 6.17 a, c, e, respectively.

6.4 Normal incidence close-packed sub-wavelength patterns with varying profiles

6.4.1 Design and Manufacturing

To investigate the change of the reflectance of the metamaterial layer when varying the pillar profile, a close-packed mask pattern was defined via NIL and etched via different etching procedures. The period of the close-packed pattern was chosen to be 250nm, the packing density was 0.5, the pillar depth chosen was 400nm and the total size of the samples were 100x100μm^2. The reason for creating considerably smaller samples for the pillar profile investigation compared to the ones made in the previous sections was to reduce the production cost because a lot of sample testing and optimization was necessary.

As described in Section 5.5, the profile of the pillars can be varied by etching the substrate via different isotropic and anisotropic dry etch process conditions. The profile shapes that were achieved are shown in the SEM images of the samples in Figure 6.20. Varying the time of the etch did not change the pillar profile considerably.

The etch techniques that were used to shape the profile of the pillars after the initial 400nm deep anisotropic etch were: Oxidation, Isotropic dry etching and a combination of Isotropic and Oxidation etching procedures. The specific conditions that were used are shown in Figure 6.20.

6.4.2 Experimental Procedure

The sizes of these samples (100x100μm^2) were much smaller than the beam diameter of the fibre probe setup (1.2mm diameter) and thus reliable fibre probe results would not be possible. The normal incidence reflectance of all the samples was tested with the customized Nikon microscope setup that is detailed in Section 6.2.2. The results taken from the samples created with the different etch methods are displayed in Figure 6.21.

6.4.3 Results and Conclusions

A direct comparison of the manufactured samples was not done because matching the simulation pillar profile to that which was manufactured proved very difficult to do reliably. However a trend could be established since RCWA simulations of varying the feature profile from cylindrical to conical have been carried out in Section 3.1.5.3. It was shown that as the tip diameter reaches zero, (i.e. the cylindrical feature becomes a conical feature) the reflectance is reduced considerably. A collection of simulations

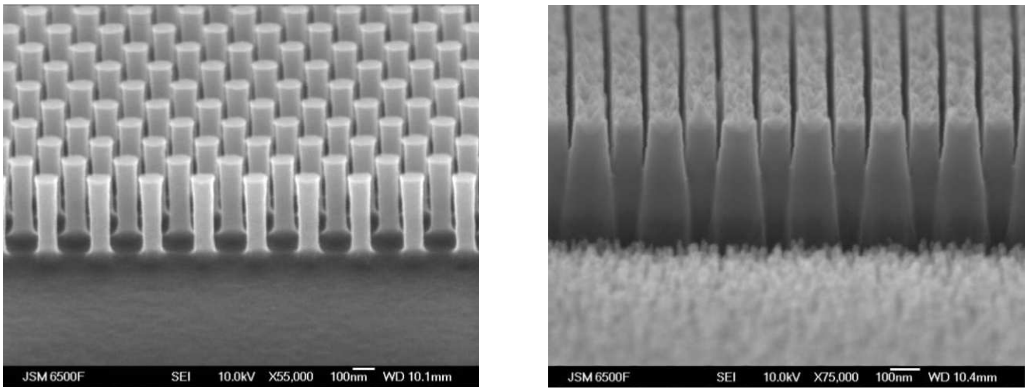

(a) Sample 1: Anisotropic etch followed by oxidation for 10mins and oxidation strip

(b) Sample 2: Anisotropic etch followed by Isotropic etch for 3mins

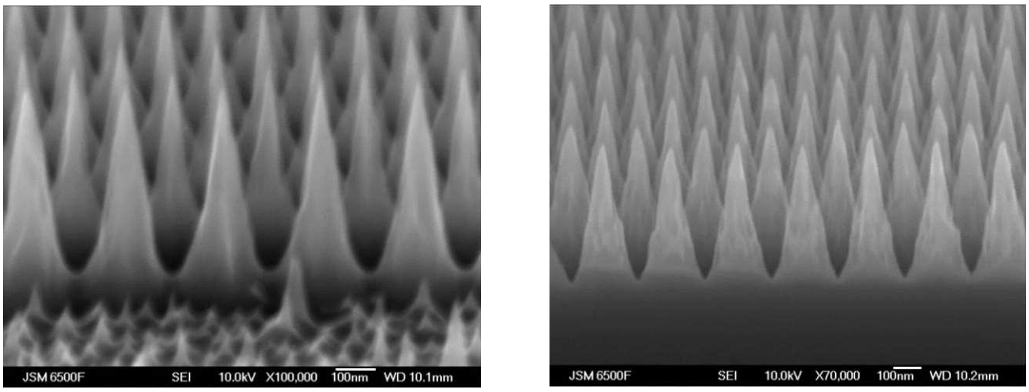

(c) Sample 3: Anisotropic etch followed by Isotropic etch for 12mins, Oxidation for 5mins and oxidation strip

(d) Sample 4: Anisotropic etch followed by Isotropic etch for 20mins

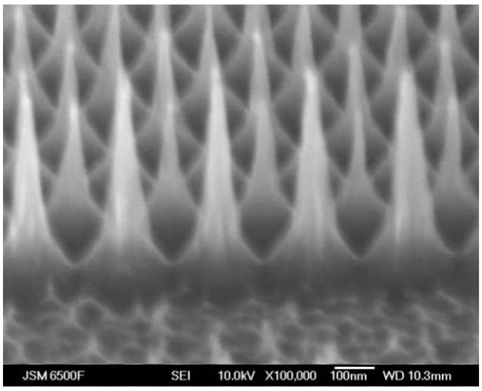

(e) Sample 5: Anisotropic etch followed by Oxidation for 10mins, Oxidation strip and Isotropic etch for 12mins

FIGURE 6.20: SEM Images of different etch profiles that were made via Nano-Imprint Lithography on silicon substrates via various combinations of etching procedures.The period of the close-packed pattern was chosen to be 250nm, the pillar diameter was 130nm, the pillar height chosen was 400nm. The parameters of the initial anisotropic etch which was used to create cylindrical features is shown in Table 5.5 as are the parameters of the isotropic etch. Where oxidation was performed at 1000^o via thermal oxidation which was later stripped by dipping the wafer it in HF. The specific times and combinations of each etch are mentioned in the subfigure legends for each sample.

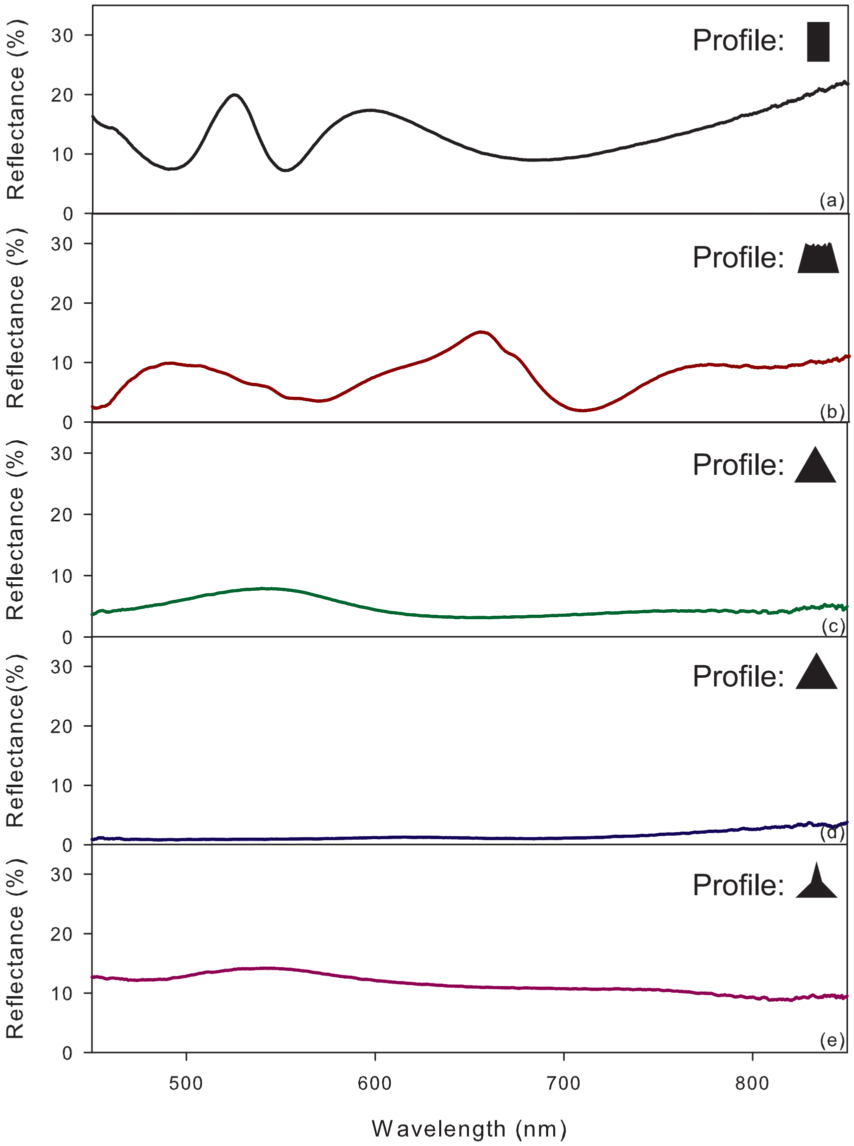

FIGURE 6.21: Reflectance of samples with different pillar profiles at normal incidence. Graphs correspond to the reflectance of (a) Sample 1 (b) Sample 2 (c) Sample 3 (d) Sample 4 (e) Sample 5 shown in Figure 6.20 a-e respectively.

depicting this for 200nm diameter pillars is shown in Figure 6.22. According to simulations, a change in profile affects the reflectance of the metamaterial layer substantially more than the depth or packing density.

Single-layer EMT simulation of the antireflection layers was not carried out because they would not be valid since the pillars are not simply vertical but change in profile, and hence do not behave as thin film layers with an effective refractive index.

The trend, however, that was obtained when comparing the different profiles that were

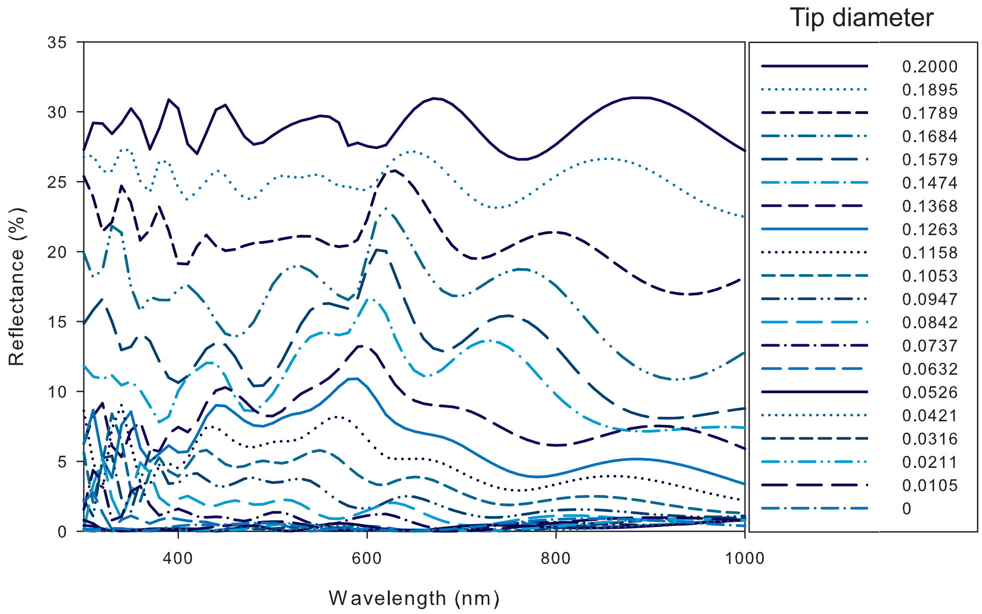

Figure 6.22: RCWA Simulations in RSoft DiffractMOD showing the reduction in reflectance from a silicon substrate when varying the tip diameter of cylindrical sub-wavelength silicon pillars on the surface from 0.2-0μm. All pillars have a base diameter of 0.2μm, a height of 0.4μm and the close packed pattern simulated has a period of 0.2μm (i.e. a fill factor of 1).

created, was similar to what was shown in RCWA simulations where a dramatic reduction in the reflectance was noticed as one moves from a cylindrical to a conical pillar feature. The optimum 'quintic' profile shown in the literature [33] as the most antireflective profile could not be replicated because the number of samples that were manufactured did not allow for a full mapping of the parameters of the etching procedure and for specific tailoring of the pillar shape.

The sample that had a profile which was closest to a quintic variation (Figure 6.20 e), is the 'double peak triangle'. This sample shows a reduction in performance compared to a simple trigonal profile which just comes to prove how sensitive the reflectance of the surface is to the profile of the pillar.

It was verified from the trend of the results, that even slight changes in profile alter the antireflection properties of the layer in a very pronounced manner. Pillar profile is therefore one of the most important design parameters that has to be taken into account when designing an antireflective metamaterial moth-eye layer. More conical profiles provide a very broadband antireflection. For the samples created, a very low reflectance (<5%) was achieved for the 450-850nm wavelength spectrum. It is thought that a quintic profile would be able to achieve an even lower reflectance but the sample that was meant to be a good approximation to a quintic profile came out as a double triangle pillar (Figure 6.20 e) and thus this could not be verified.

6.5 Normal incidence reflectance of close-packed sub-wavelength patterns with varying pillar heights

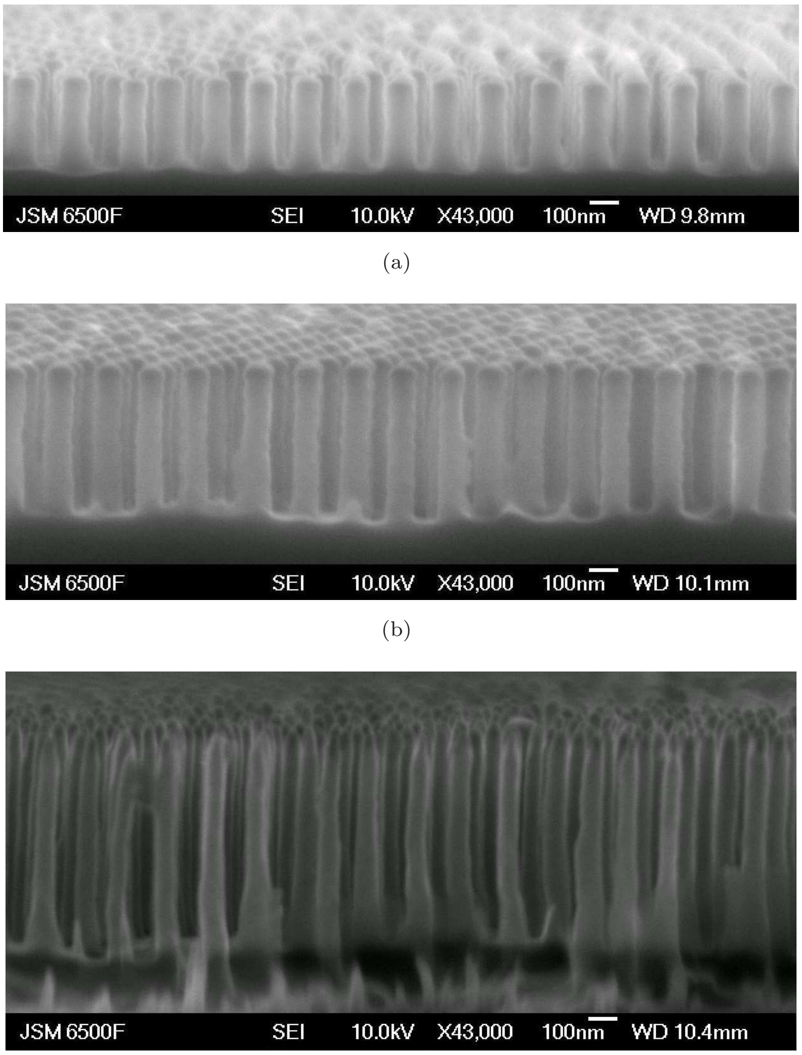

(a)

(b)

(c)

Figure 6.23: SEM image of (a) 300nm, (b) 530nm and (c) 730nm high pillars created by Nanosphere Lithography and DRIE etching.The topology of the subwavelength features was tessellated close-packed. The period of the sample was 200nm and the pillar diameter was 100nm. The spheres were reduced in size with the oxygen etch described in Table 5.3. The substrate etch procedure used for samples (a), (b) and (c) was DRIE and the etch conditions used for these samples are described in Table 5.4. The etch was run for 8, 12, and 15 cycles respectively.

6.5.1 Design and Manufacturing

In order to measure the change of the reflectance of the antireflection layer when varying pillar depth, three close-packed antireflection samples with a pillar period of 200nm and a pillar diameter 100nm were created via nanosphere lithography and etched via DRIE for an increasing number of cycles.

To achieve the required feature period, 200nm-diameter nanospheres were used as the etch mask. The Deep Reactive Ion Etching (DRIE) (Surface Technology Systems, Newport, UK) was done via a process similar to the one described by Cheung et al[97].

DRIE uses an alternation of SF_6 and C_4F_8 gases in cycles so that the surface is etched and passivated in steps. Three samples of different depth have been produced by etching via DRIE for 8, 12 and 15 cycles, which resulted in pillars with 300nm, 530nm and 730nm height respectively, as shown in Figure 6.23.

It is important to note that the pillars retained their original diameter of 100nm at the end of the DRIE procedure as can be shown from a top view SEM in Figure 6.24.

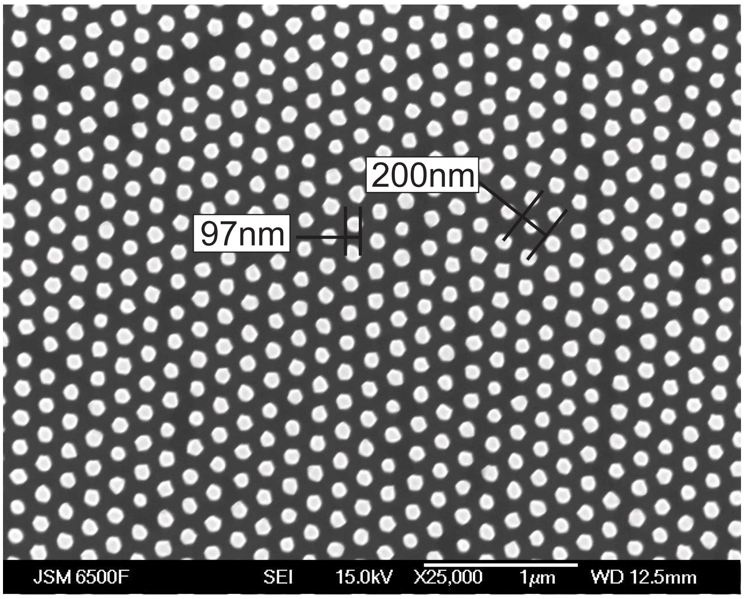

Figure 6.24: Top view of silicon pillars shown in Figure 6.23a after DRIE etch and nanosphere mask removal.

6.5.2 Experimental Procedure

The Nikon microscope was not required for these measurements because the samples created were very large in area ($2x2cm^2$) compared to the samples created via e-beam lithography in the previous section ($100x100\mu m^2$). The setup that was used to attain the normal incidence reflectance was the double core fibre probe.

6.5.3 Results

The trend obtained from the experimental results is shown in Figure 6.25. As the depth of the etch increases the overall reflectance decreases with the drop being more pronounced in the wavelength region of 400-500nm.

By using a Rigorous Coupled Wave Analysis (RCWA) simulation software (RSoft, Ossining, NY, USA) the specular reflectance at normal incidence could be simulated whilst taking into account pillar profile (Figure 6.25). Three hexagonal-packed structures with pillar heights of 300nm, 530nm and 730nm were then simulated.

The profile of the simulations conducted for first two samples was set to be vertical because the slight edge smoothing observed on the pillar tips in the SEM images of these two samples (Figure 6.23(a),(b)) is minimal and does not appear to affect the reflectance much. For the third sample, a vertical edged profile would not suffice and the profile was specified in two parts, the bottom half of the pillar was vertical-edged and the top half was a sinusoidal peak Figure 6.26. This structure more accurately represents the profile seen in Figure 6.23 (c) and the simulation was much more representative of the measurements and verified the experimental observation.

The trend shown by simulations closely correlates to that observed in the normal incidence reflectance experiments carried out (Figure 6.25). As depth increases the reflectance decreases but does not have such a strong impact on the reflectance of the whole visible spectrum (400-700nm) as does pillar profile (Section 6.4). It does however have a great impact on a small part of the visible wavelength range (400-500nm).

6.5.4 Conclusions

From the results collected, it is confirmed that the longer the DRIE etch, the deeper the pillars get without significant loss in diameter thickness as shown in Figure 6.24. The samples that had taller pillars created a more broadband reduction in reflectance than did samples with shorter pillars as expected from simulations in Section 3.1.5.1.

The most promising sample was the sample that had undergone the longest etch (15 cycle DRIE). It was compared to the reflectance of polished silicon (Figure 6.27) and very noticeable reduction exists in the region 400-500nm with the mean reflectance of the sample being lower than 5% in that range and rising steadily with wavelength thereafter.

Simulating the behavior of these pillars with EMT is difficult for various reasons associated with the manufacturing procedure:

- Using nanosphere lithography for mask patterning combined with the DRIE etching method to create the pattern on the substrate results in slight inconsistencies

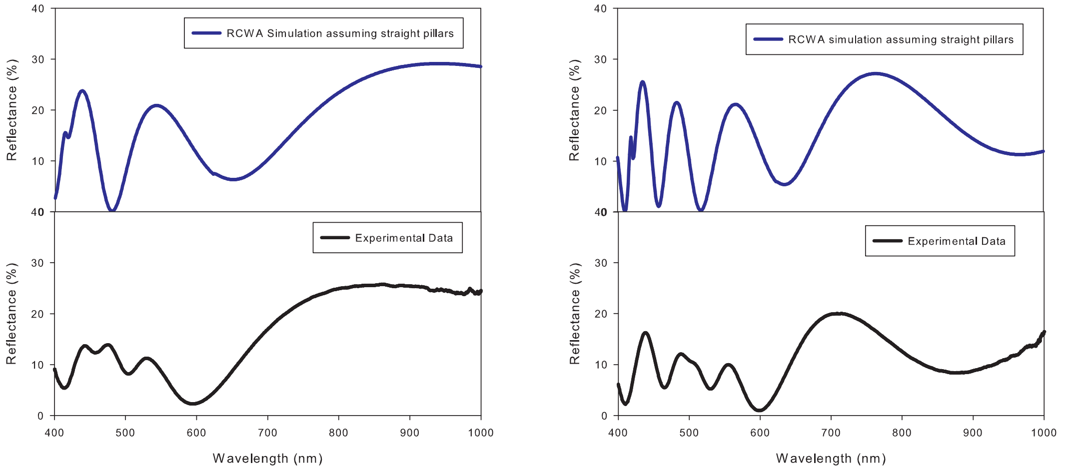

(a) Reflectance v. wavelength for 8cycle Bosch etch

(b) Reflectance v. wavelength for 12cycle Bosch etch

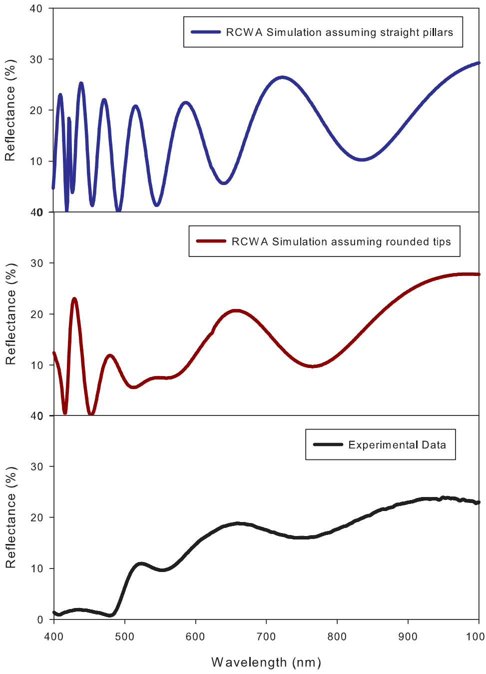

(c) Reflectance v. wavelength for 15cycle Bosch etch

Figure 6.25: Simulation and measurement of normal incidence reflectance for samples with heights of (a) 300nm, (b) 530nm and (c) 730nm shown in Figure 6.23. For (a) and (b) a cylindrical flat-top pillar RCWA simulation of the manufactured samples was carried out with a close packed pattern period of 200nm, a pillar diameter of 100nm, a vertical pillar profile and a pillar height of 300 and 530nm respectively. For (c) both a flat-top and curved-top pillar RCWA simulation were carried out with a period of 200nm, a pillar diameter of 100nm and a height of 730nm as shown in Figure 6.26. For the curved top pillar, a sinusoidal profile with a tip height of 182.5nm was used, with the total height of the pillar still kept at 730nm.

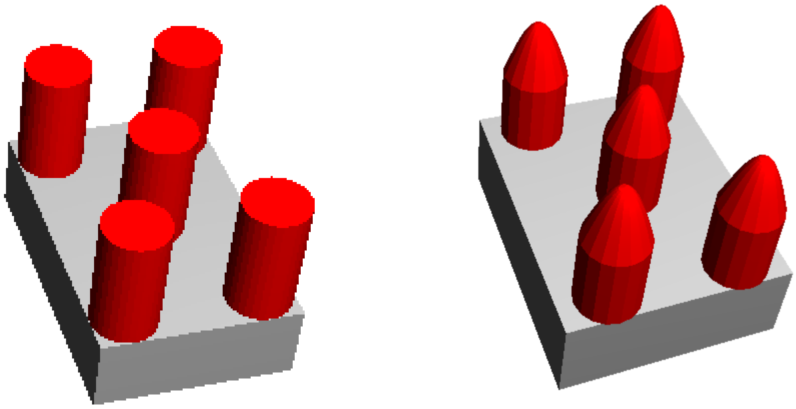

(a) Cylindrical pillar (b) Sinusoidal dome tipped pillar

Figure 6.26: Two types of RCWA simulation models used to represent the close-packed pillar structure, the cylindrical and dome tipped pillars

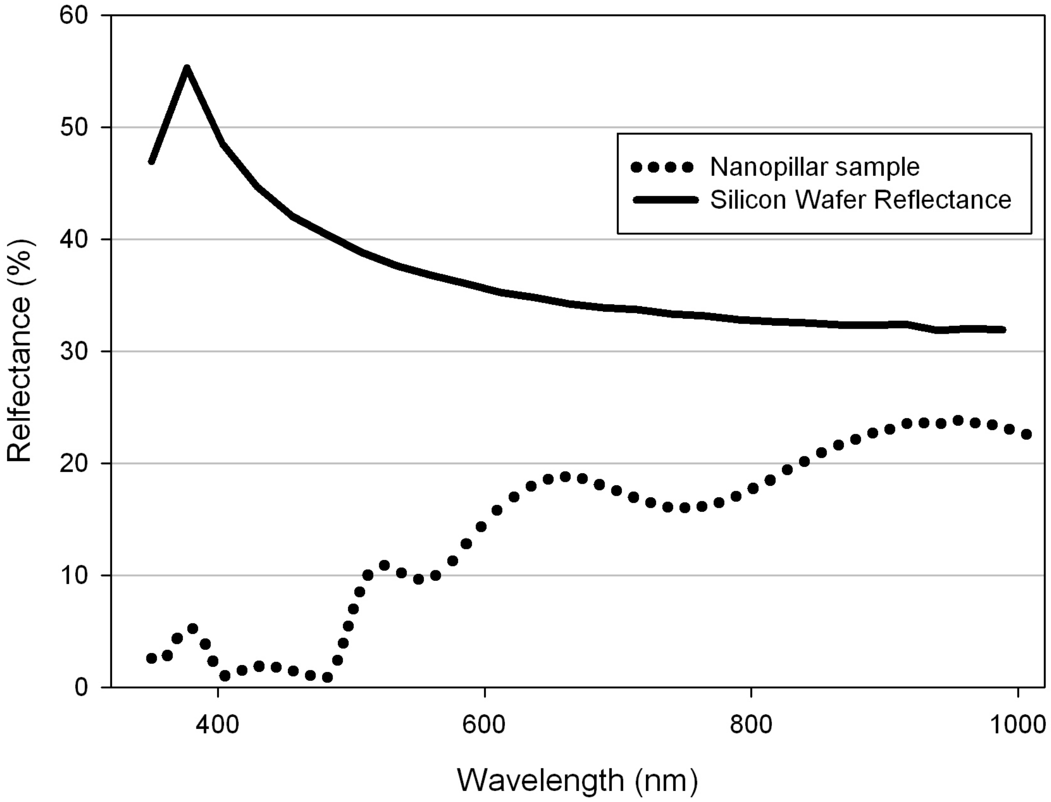

Figure 6.27: Specular reflectance at normal incidence for the tallest sample created via NSL(shown in Figure 6.23c) and compared to the reflectance of polished silicon wafer.

in packing density and height across the sample which makes it behave differently than a medium with a single effective refractive index.

- The pillars in some cases are actually tapered as a result of the DRIE etching such as in Figure 6.23 (c) which also makes the sample behave differently to a thin film with one effective refractive index.

A close correlation with experimental results was achieved with RCWA simulation. There are some sources of discrepancy between simulation and experiment. It is suggested that more accurate simulation of the experimental results would be possible if the slight differences in period, size, height and shape of each pillar in the structure are taken into account because the sample is not completely consistent in pillar size due to inherent limitations of the NSL process. There was no method of exactly representing this with the simulation software that was available because it assumes perfect hexagonal symmetry with all pillars being identical in height, diameter and shape. Additionally the slight rounding of the pillars does pose problems in verifying the reflectance results with simulation because this profile differs from the vertical profile that was assumed in simulation, especially for deeply etched samples. This fact however was taken into account with a sinusoidal tip approximation which proved quite successful in explaining the results obtained for the 15-cycle Bosch-etched sample.

In conclusion, as the height of the pillars was increased, a trend of reflectance reduction was noticed, albeit smaller than that of changing pillar profile. The reduction was more pronounced at lower wavelengths and this was thought to be due to the slight rounding of the pillar tips that was noticed after the etch procedure. Simulations correlate well with experiments especially when a closer approximation of the manufactured profile was carried out.

6.6 Normal incidence reflectance of a sub-wavelength moth-eye patterns with close-packed and sunflower pillar topographies

6.6.1 Design and Manufacturing

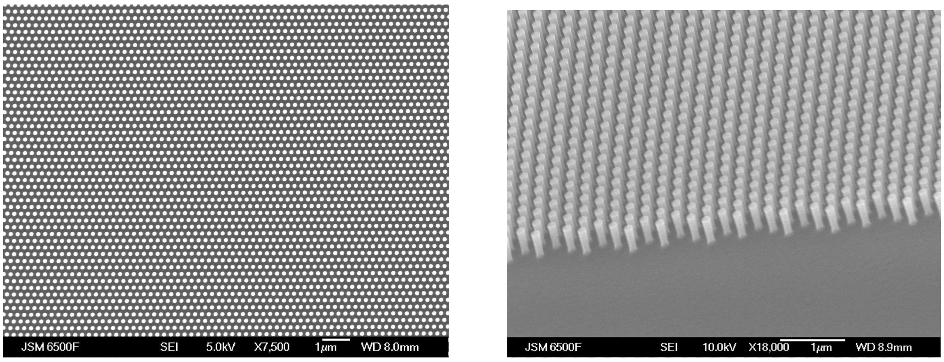

(a)

(b)

FIGURE 6.28: Close-packed vertical pillar patterns inscribed by E-beam lithography on a silicon substrate viewed at (a) 0^o tilt (b) 40^o tilt. The period of the close-packed design was set to be 250nm with a pillar diameter of 130nm. The pillar profile is vertical and the etch height of the pillars is 400nm. The etch conditions of the anisotropic etch which was used to create this sample are shown in Table 5.5

In this section the packing topology of the moth-eye layer was varied to determine if it plays a role in normal incidence reflection. A close-packed and sunflower sample were prepared by E-beam lithography (Figure 6.28). The period of the design was set to be 250nm with a pillar diameter of 130nm. The depth of the pillars was 400nm. Both samples were made to have identical pillar packing densities so a fair comparison could be carried out.

The close-packed pillars that resulted were completely vertical with flat tops, as shown in Figure 6.28. Successful manufacturing was very helpful in validating the simulation procedure because a direct comparison could now be made with both RCWA and EMT techniques.

The sunflower pattern which was created via e-beam lithography was designed via a custom C program. The file was then transformed to a format which could be used on the e-beam machine to define a lithography process mask (Figure 3.27a). The sunflower pattern (Figure 6.29) was created on the same silicon wafer as the close-packed pattern for consistency. Hence, the result obtained for the sunflower topology in terms of pillar quality was identical to that of the flat topped pillars, (i.e. extremely vertical pillar profiles).

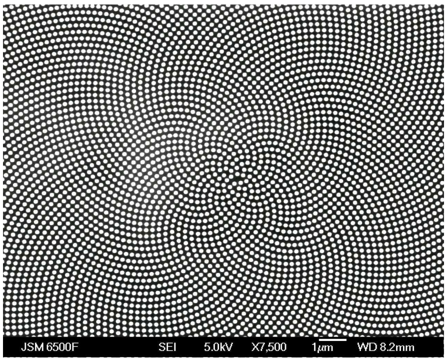

FIGURE 6.29: Sunflower pillar pattern inscribed by e-beam lithography on a silicon substrate. The modal period of the sunflower design was set to be 250nm with a pillar diameter of 130nm. The pillar profile is vertical and the etch height of the pillars is 400nm. The etch conditions of the anisotropic etch which was used to create this sample are shown in Table 5.5

Thus both the close-packed and sunflower sample experienced the exact same manufacturing conditions, so it was possible to carry out a fair comparison between them in specular reflectance.

6.6.2 Experimental Procedure

Specular reflectance measurements at normal incidence have been carried out for the samples shown in Figure 6.28 and Figure 6.29. The apparatus that was used was the fibre probe setup (Figure 6.3) because the samples created were larger than the probe beam diameter and did not require the microscope to be evaluated. Because of the flat-top vertical profile of the pillars created, the reflectance of the close-packed pattern could be accurately interpreted using both Effective Medium Theory (EMT) and Rigorous Coupled Wave Analysis (RCWA).

6.6.3 Results

For the close-packed sample, the specular reflectance of the pillars was calculated via EMT and RCWA and it was compared to the experimental results (Figure 6.30). RCWA is a better match to the data than EMT. The extra dip in the reflectance graph noticed around 630nm in the RCWA simulation compared to the EMT calculation agrees with experimental observation, and is due to diffraction order coupling as was the case for the samples in Section 6.1.2.2. The 159nm diameter extracted from the SEM micrographs (Figure 6.31) agrees with the 158nm diameter predicted by the diffraction coupling mode which was calculated with the procedure shown in Section 6.1.2.2.

The specular reflectance results of the sunflower, as for the close packed pattern, agreed with effective medium theory Figure 6.32. As was also noticed with the close packed pattern, there is an extra dip in reflection around 630 nm which was due to the diffraction grating coupling that occurs at that wavelength (Figure 6.32). RCWA simulation could not be used to confirm this for the sunflower pattern due to the large size of the model required which was impractical to simulate, but by comparing this reflectance spectrum with that of the close-packed pattern it is observed that the extra dip is at identical wavelengths (Figure 6.33).

It can thus be concluded that because the modal period of the points on the sunflower pattern was designed to be equal to the period of the pillars in the close packed sample, this extra dip in the reflectance spectrum which occurs at the same wavelength is also due to diffraction coupling.

6.6.4 Conclusions

The specular reflectance measurements of the sunflower and close-packed pattern were almost identical (Figure 6.33) because both topologies were designed to have similar packing densities and profiles. It is shown that changing the topology of the pillar pattern of a sub-wavelength moth-eye layer whilst retaining similar packing density does not affect specular reflectance.

The experimental results for both samples closely correlate to EMT and RCWA simulations. The reason for the very good correlation is suspected to be the very good manufacturing quality of the vertical pillar profile. The RCWA model was very accurate because the pillar profile assumed in the simulation was vertical which was very close to the pillar shape observed. The EMT simulation of the reflectance of the close-packed topology closely matched the experimental result because the flat vertical profiles of the pillars caused the layer to behave as thin film layer with only one intermediate refractive index which was what was assumed in the simulation. Small differences between simulation and measurement are thought to be because of the fact that the fibre probe measurements are at a small angle of around 7 degrees from normal incidence.

It was postulated that due to the distribution of spacings in the sunflower pattern, a broader antireflection response would be possible compared to the hex packing whose feature spacing is set. However, it seems that because the period variance is very small around the modal period (Figure 3.27c) the reflectance is essentially not affected. The backscattering azimuth angle dependent measurements for these two patterns however, are very different in contrast to their normal incidence reflectance results, and this will be analysed in Section 7.2.

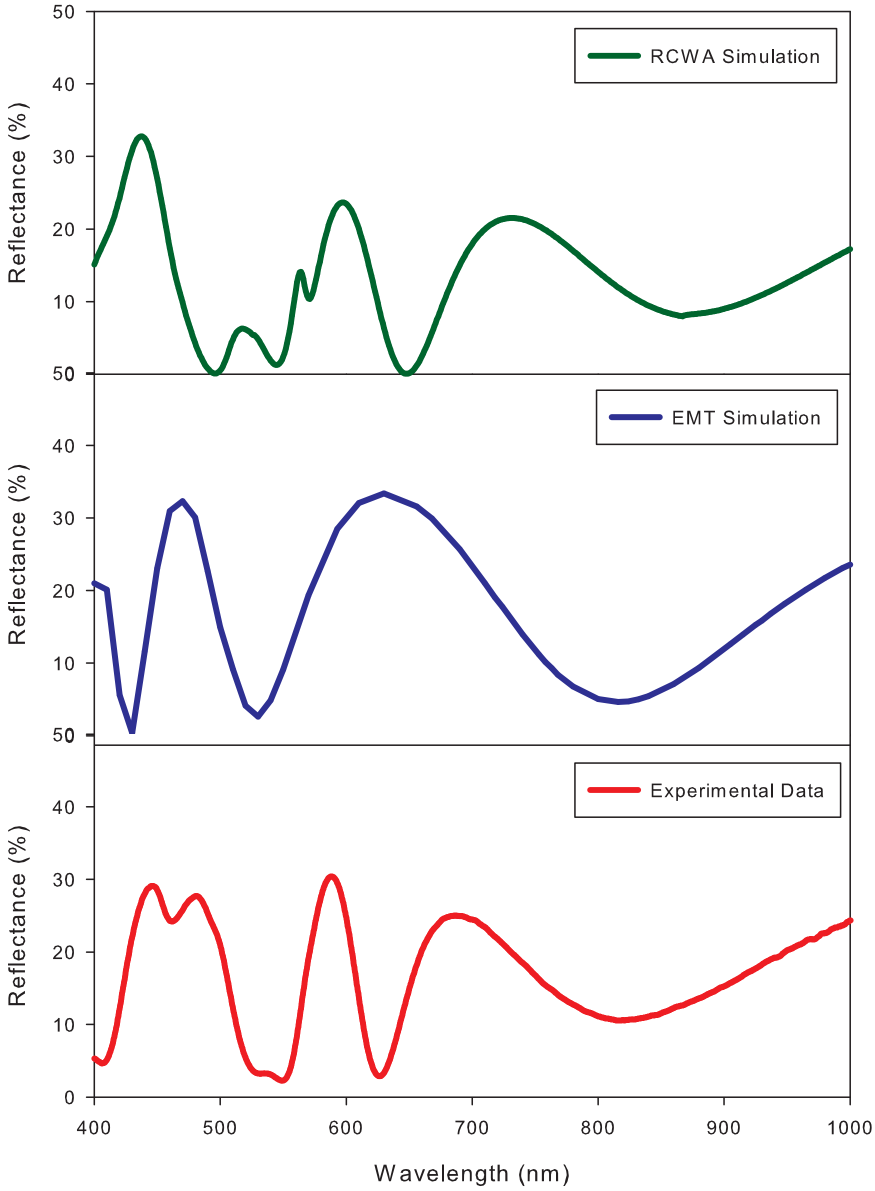

FIGURE 6.30: (a) RCWA simulation for reflectance v wavelength for a close packed pillar pattern with a straight cylindrical pillar profile, 250nm in period, 130nm in pillar diameter and 400nm in pillar height (b) EMT simulation for the same pattern described previously, the period used in EMT simulations is the average pillar period in the vertical and horizontal directions which is 341.5nm and (c) the experimental reflectance data obtained at normal incidence, for the close packed sample that was measured which is shown in Figure 6.28.

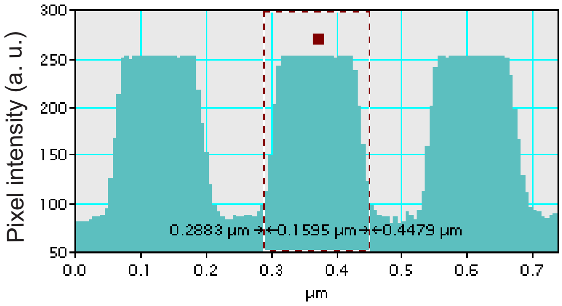

FIGURE 6.31: Pillar diameter profile extracted from contrast information in SEM image shown in Figure 6.28a.

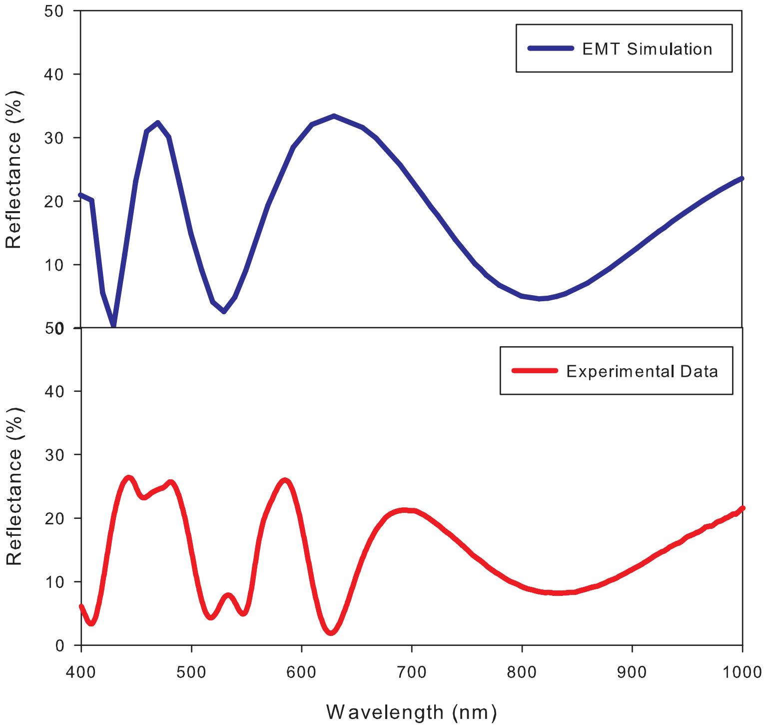

FIGURE 6.32: (a) EMT simulation for reflectance v wavelength for a sunflower pattern with a straight cylindrical pillar profile, the period used in EMT simulations is the average pillar period in the vertical and horizontal directions which is 341.5nm, identical to the close-packed pattern and (b) the experimental reflectance data obtained at normal incidence, for the sunflower sample shown in Figure 6.29.

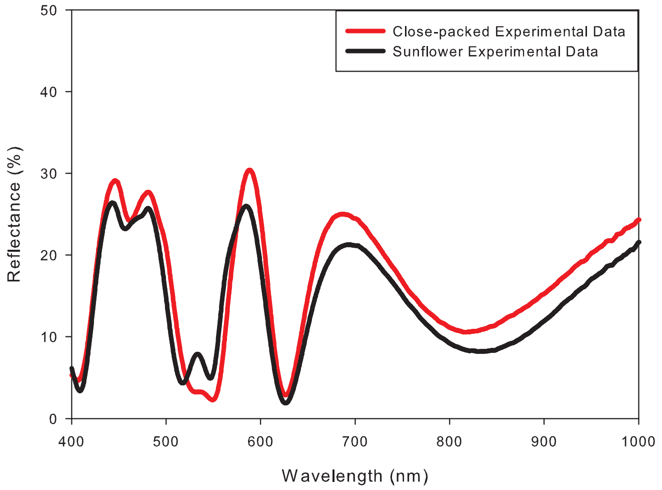

Figure 6.33: Comparing Reflectance v Wavelength for sunflower and close-packed patterns shown in Figures 6.29 and 6.28 respectively.

6.7 Conclusions

In this chapter a systematic study of the trends observed in the reflectance spectra of the experimental results collected from manufactured samples was carried out. Simulations of each sample were performed to validate the experimental observations and confirm that the simulated results agree to the measured reflectance spectra. The trends detected in the measured reflectance peaks and troughs agree with simulation.

An indirect comparison can be made between the results shown in this chapter and the simulations previously carried out in Chapter 3. However, comparison between these results and most of the simulations in Chapter 3 can only be done on a qualitative basis as most of the pillars measured in this chapter had a cylindrical profile and hence cannot be directly compared. For a direct comparison one should refer to the simulations carried out previously in each section of this chapter which are a closer representation of the manufactured sample.

In Section 6.2 it was shown that by increasing the pillar period, a red-shift of the minimum reflectance wavelength is observed. This agrees to the trend previously noticed in Figure 3.5. A red-shift of the minimum reflectance was observed when increasing the fill factor (Section 6.3), which agrees with previous simulations (Figure 3.6). Pillar profile (Section 6.4) has the most dramatic effect out of all the design parameters. It was noticed that as the pillar profile becomes more conical, the reflection is greatly decreased for the whole spectrum which was considered (450-850nm). This agrees with the trend observed when varying the pillar profile from cylindrical to conical in previous simulations (Figure 3.10).

Varying the height of the pillars (Section 6.5) broadens the reduction in reflection achieved for wavelengths at the low end of the visible spectrum more than the rest of the wavelengths. However, it was shown that this was due to the fact the pillars had also changed slightly in profile. The trend doesn't agree well with previous simulations in Chapter 3 (Figure 3.7) which show that reflection is reduced in a more pronounced manner as height is increased. This is due to the fact that the previous simulations had considered a sinusoidal pillar profile whereas the pillars created here were mostly vertical in profile. When simulating the structures via RCWA with a pillar profile that more closely matches the one observed in the SEM images a strong correlation to measured results was achieved.

By varying the pillar topology whilst keeping a consistent pillar profile produced no change in the reflected signal (Section 6.6). The effect of changing the topology could not be simulated as the requirements for this type of simulation on a large non-periodic pattern such as the sunflower were impractical to carry out with the resources available. As it will be shown in later chapters, the azimuthal isotropy of the backscattered diffraction originating from these surfaces is highly dependant on pillar topology.

Chapter 7

Diffraction characterization of ‘moth-eye’ antireflection layers with different topologies

Developing a method of achieving isotropic planar diffraction behaviour, but with a cheap and fast self-assembly technique, would be very useful for use in commercial optical applications that require high optical symmetry, such as low-index contrast photonic crystals [90] or extracting more light from LED’s [158]. Single-orientation, close-packed structures have been previously studied for antireflection applications [31], as have been self-assembled tessellated close-packed surfaces [119], [85]. The optical characterization of these surfaces however, has mostly been limited to normal incidence reflectance measurements of the samples whereas the effect of the pattern tessellation on the diffraction orders that emerge from the lattice at high angles of incidence is usually ignored.

7.1 Optimizing isotropic diffraction using a biomimetic-inspired moth-eye topology of increasing complexity

The hypothesis that was postulated when simulating the biomimetic pattern symmetry in Section 3.2.5.4, was that when the number of orientations of the hexagonal close packed pattern increases, the sample’s azimuthal diffraction isotropy is also increased. It is also expected that the power of the diffracted light each of the azimuthal directions decreases as the orientations of the underlying pattern increase. This would confirm the stealth functionality of these patterns which are found on the real moth-eye.

In this section, a systematic study of increasing the orientations of a close packed pattern from 1-9 (Figure 7.1), whist maintaining an even coverage of all orientations on the surface was carried out to investigate this hypothesis.

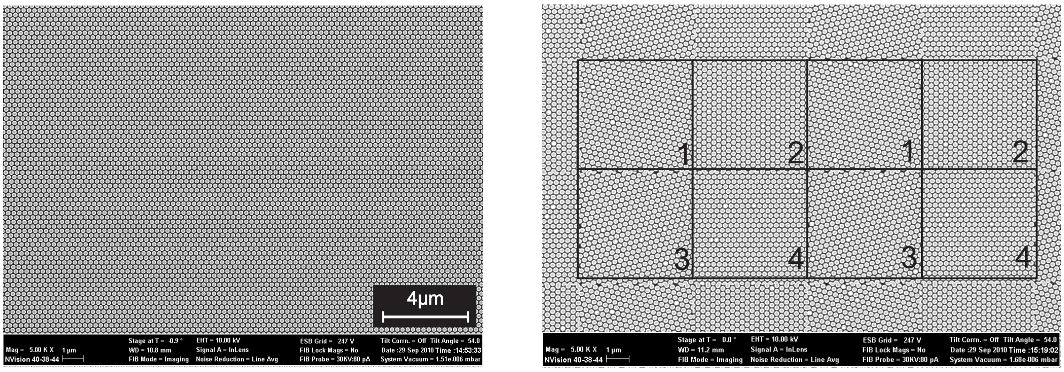

(a) Mono-orientated sample

(b) Four orientations of close-packed sample

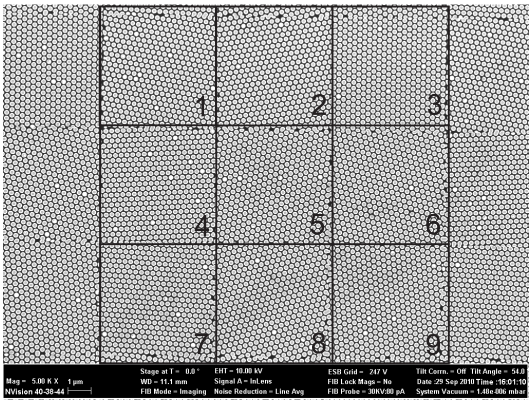

(c) Nine orientations of close-packed sample

FIGURE 7.1: SEM Images of topologies that were manufactured with (a)1,(b)4 and (c)9 orientations of the close-packed pattern. The close packed base pattern has a period of 250nm and the pillars were 130nm in diameter. For sample (b) the orientation angles of the close-packed pattern used in the sub-cells numbered 1-4 were at an offset of 0,15,30 and 45 degrees respectively compared to sample (a). For sample (c) the nine orientation angles of the close-packed pattern used in sub-cells 1-9 were at an offset of 6.7, 13.4, 20.1, 26.8, 33.5, 40.2, 46.9 and 53.6 degrees respectively compared to sample (a). The individual domain sizes were designed to be in 5μm-side squares. The pillar profile is vertical and the etch height of the pillars is 400nm. The parameters of the anisotropic etch that was used to create the pillars are shown in Table 5.5

7.1.1 Design and Manufacturing

The samples were manufactured via NIL at NILT Technologies, Denmark (Figure 7.1). The underlying close-packed pattern was 250nm in period and the pillars were 130nm in diameter. The depth of the pillars was selected to be 400nm. The etch selected was anisotropic so a vertical pillar profile was created. The size of each sample was 1mm^2.

Three moth-eye antireflection samples were created on silicon with 1, 4 and 9 non-repeating orientations of the close-packed pattern evenly distributed on the surface plane in a square grid. The square grid has a spacing of 5μm between grid lines, the diameter of the light source used is 1mm which can accommodate 31400 orientations of the close-packed pattern. The samples were defined by tiling a unit cell over the area required.

The unit cells for the 4 and 9 orientations are different in area but have similar domain sizes (5x5μm). The unit cells of the patterns are shown in Figure 7.2.

7.1.2 Fourier analysis

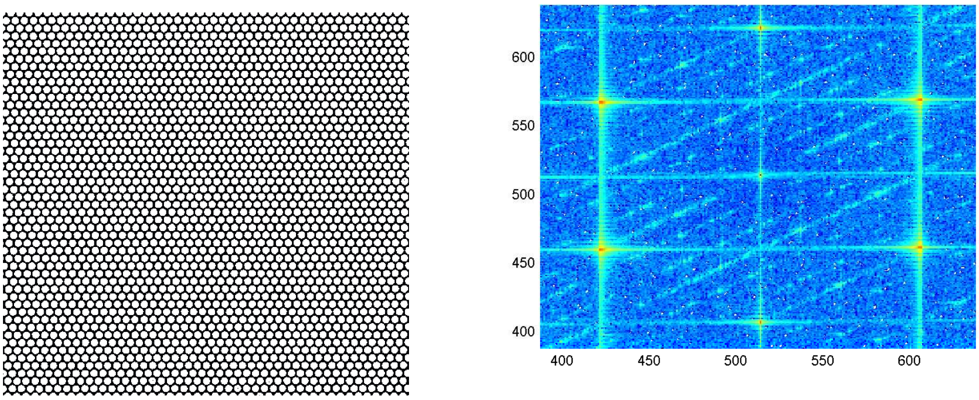

(a) Mono-orientated sample

(b) Fourier transform of sample with 1 close packed orientation depicting 6-fold symmetry

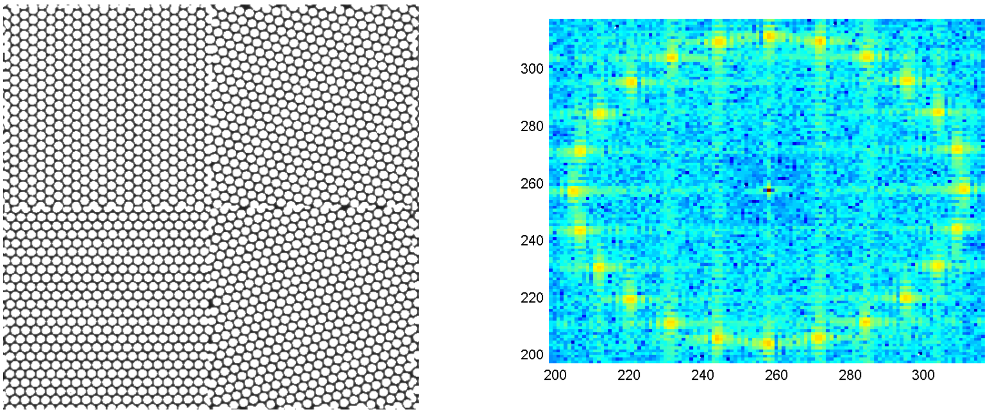

(c) Four orientations of close-packed sample

(d) Fourier transform of sample with 4 close packed orientations depicting 24-fold symmetry

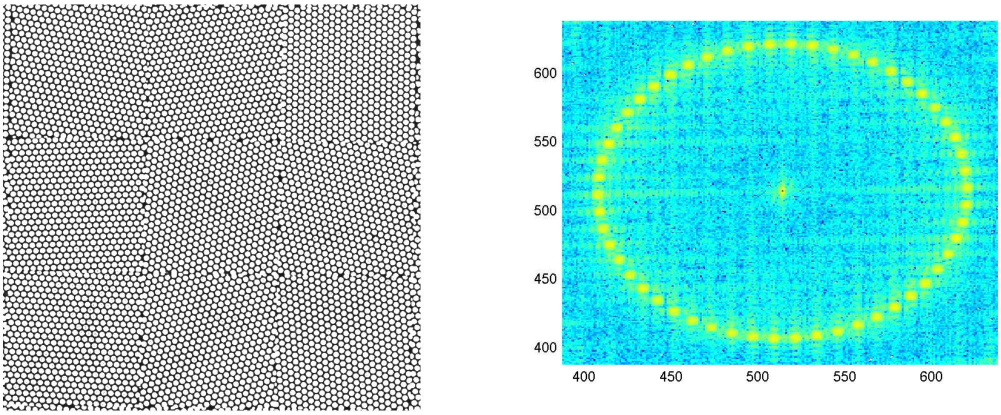

(e) Nine orientations of close-packed sample

(f) Fourier transform of sample with 9 close packed orientations depicting 54-fold symmetry

FIGURE 7.2: Unit cells of moth-eye topologies and their respective Fourier transforms

The diffractive properties of biomimetic structures that possess order which is confined to their nearest neighbours correlates with the Fourier Transform of their image, as is the case with patterns that retain order throughout the whole surface they cover [159]. A unique property that was noticed for a tessellated close-packed surface is that the diffractive symmetry of the pattern is tunable and proportional to the number of orientations considered in the pattern. This means that the rotational symmetry of the pattern increases linearly, as more orientations of the base pattern are included.

By taking Fourier transforms of the pattern unit cells, a prediction of the number of diffraction orders can be achieved (Figure 7.2). It can be observed that as the number of orientations is increased, the diffraction symmetry predicted by their Fourier Transforms also follows a linear increase (in multiples of the basic symmetry of the underlying pattern). The underlying pattern that is considered is a close-packed pattern and thus when considering 1 orientation of this pattern the Fourier transform depicts 6-fold symmetry (Figure 7.2b). For the sample with 4 orientations of the close packed pattern, 24-fold symmetry is attained (Figure 7.2d) and when 9 orientations of the close packed pattern are considered, 54-fold symmetry is observed (Figure 7.2f). The results from these Fourier Transforms, which came out as expected from previous simulations in Chapter 3.2.5.4, confirm the successful manufacturing of the samples.

7.1.3 Experimental Procedure

In order to observe diffraction effects, wavelengths under 450nm had to be used. A bespoke experimental setup for this investigation was required because the only light source that would produce a spectrum below 400nm (down to 300nm) and have an intense enough light to produce diffraction was the quantum efficiency system available in the lab(PVE300, Bentham).

The experimental apparatus that was built inside the quantum efficiency system consisted of two concentric rotation stages which were mounted on top of each other in such a way that one rotation stage had an arm attached to it on which the sample holder was placed and the other was used to control the angular position of the fibre optic detector as shown in Figure 7.3a. The sample holder was assembled by using two translation stages and a rotation stage with an x-y positioning plate attached to it. This way the sample can be placed in the middle of the vertical rotation axis. The rotation axis was aligned to the beam which was directed onto the sample by a mirror (Figure 7.3).

7.1.4 Results

The results of monitoring the diffracted wavelength of 395.12nm whilst rotating the samples in a full circle in azimuth verified our hypothesis (Figure 7.4). The angle of

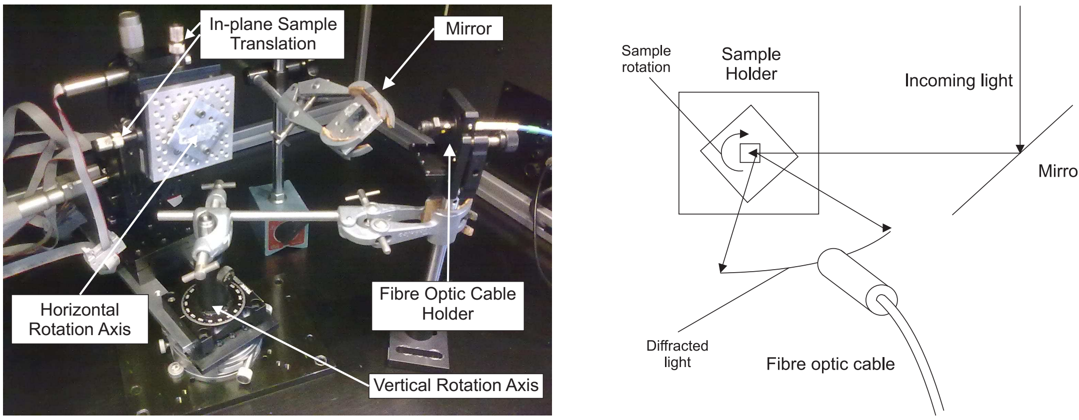

(a) Photograph of system

(b) Schematic of system showing axis of rotation and path of light

FIGURE 7.3: Customized azimuth reflectometry built inside a quantum efficiency system (PVE300, Bentham)

incidence selected was 85 degrees and the angle of detection was 70 degrees from surface normal.

As shown in Figure 7.4 (a, c, e) evenly spaced diffraction powers were detected for the 1, 4 and 9 orientation samples. As patterns with increasing azimuthal diffraction symmetry were considered, the number of diffraction peaks was increased from 6 - 54 (Figure 7.4 (b, d, f)), while the average power of each of the peaks reduced monotonically.

7.1.5 Conclusions

It can thus be concluded that the random domain orientations of the close packed pattern noticed on the real moth eye, contribute to the animal's stealth capabilities by reducing the power of azimuthal diffraction orders, whilst spreading the power into more azimuthal directions. This was verified by systematically increasing the number of orientations on a 1mm^2-size sample while keeping the total surface area of each orientation on the interface equal. Similarly it is concluded that it is possible to engineer a bespoke optimized stealth antireflection surface by using an appropriate number of orientations in order to tune the intensity of the diffraction orders.

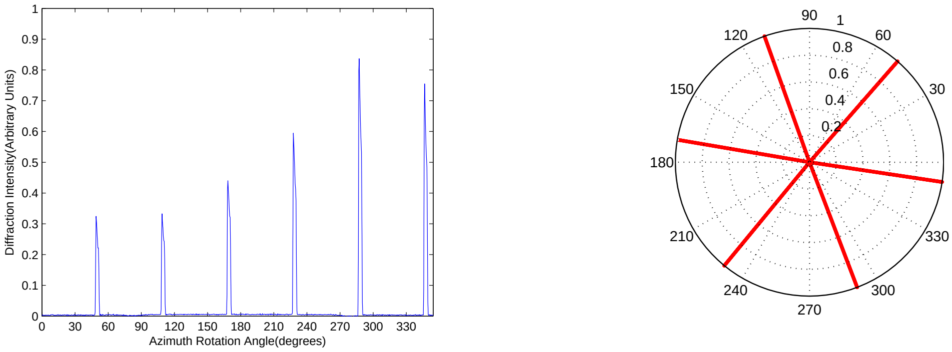

(a) Intensity of diffraction wavelength vs azimuth rotation for mono-oriented close-packed sample

(b) Polar plot of azimuth diffraction directions for mono-oriented close packed sample

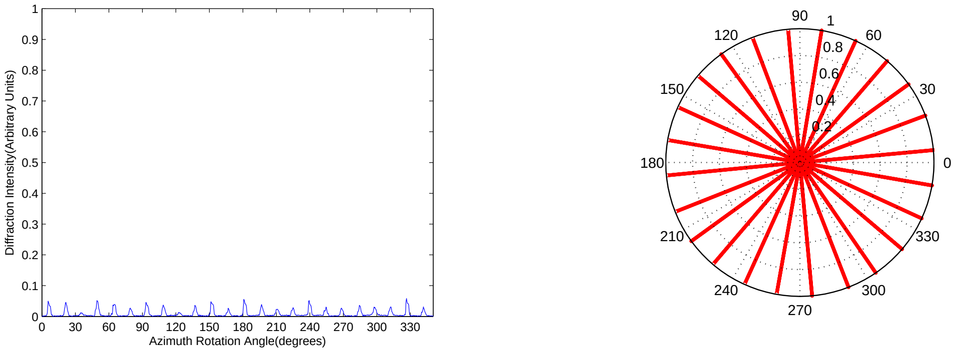

(c) Intensity of diffraction wavelength vs azimuth rotation for sample with 4 close-packed pattern orientations

(d) Polar plot of azimuth diffraction directions for sample with 4 close-packed pattern orientations

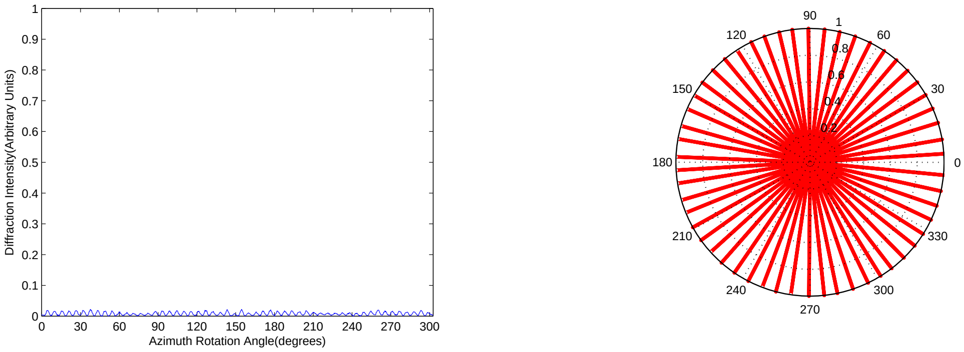

(e) Intensity of diffraction wavelength vs azimuth rotation for sample with 9 close-packed pattern orientations

(f) Polar plot of azimuth diffraction directions for sample with 9 close-packed pattern orientations

FIGURE 7.4: Linear plots diffraction intensity vs azimuth rotation and respective polar plots of diffraction direction vs azimuth rotation for the 1,4 and 9-orientation close-packed samples shown in Figure 7.1 a,b and c respectively.

7.2 Comparison of diffraction between close-packed, sunflower and moth-eye biomimetic topologies

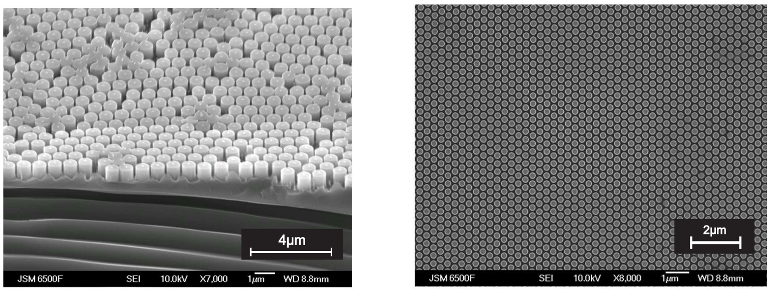

(a) Tessellated close-packed pattern (b) Close-packed pattern

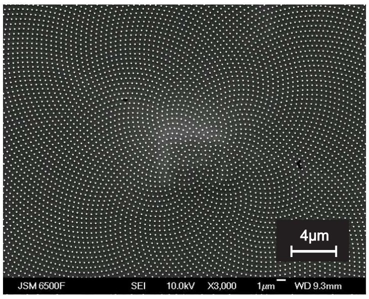

(c) Sunflower pattern

FIGURE 7.5: (a) A biomimetic tessellated close-packed pattern was compared to (b) a simple close-packed pattern and (c) a biomimetic sunflower pattern. The pillar profile is vertical in all samples but the rest of the design parameters were different. The tessellated close-packed pattern had a feature period of 780nm a feature diameter of 680nm and a feature height of 780nm. The sample was created in the clean room at the University of Southampton and the parameters of the anisotropic etch used for this pattern are shown in Table 5.4 . The simple close-packed pattern had a feature period of 350nm a feature diameter of 175nm and a feature height of 400nm. The sample was created at NILT. The parameters of the anisotropic etch used for this pattern are shown in Table 5.5. The sunflower pattern was created at INNOS had a period of 560nm a diameter of 168nm and a height of 700nm. The parameters of the anisotropic etch used for this pattern are shown in Table 5.5

In this chapter, the diffraction of moth-eye metamaterial layers with biomimetic pattern topologies will be investigated. Namely the close-packed, the sunflower and the tessellated close-packed topologies will be compared. Emphasis will be put on the characterization of the diffraction properties of the tessellated close-packed topology that was self-assembled via nanosphere lithography.

7.2.1 Design and Manufacturing

The samples that were created were not consistent because they were not created at the same time and they were all made for different purposes. However, a qualitative comparison is only required in this chapter. It is sought to prove that a self-assembled nanosphere sample is a cost effective way of creating isotropic diffraction which could possibly be used in stealth antireflective surfaces.

The close packed sample used was that shown in Figure 6.9 (e) and had a period of 350nm a packing density of 0.5 and a depth of 400nm. The nanosphere sample that was created had a period of 780nm and a pillar diameter of 680nm. The depth of the pillars was 780nm. The sunflower sample had a characteristic period of 560nm a depth of 700nm and a packing density of 0.3.

Large area tessellated close-packed structures with patterns that are oriented in lots of different orientations were able to be produced in large areas (~2cm^2) via nanosphere lithography. The angular offset and area distribution of the orientations of the close-packed pattern in the tessellated domains cannot be fully controlled because they depend on the specific molecular dynamics of each self-assembly run.

The nanosphere monolayer mask was self-assembled via a method called improved liquid surface assembly which was optimized for this work (Section 5). It operates by depositing a nanosphere colloid on the surface of ultra pure deionized water stored in a Teflon container. Using the Teflon bath, carboxylate-modified 780nm-diameter sized polystyrene nanospheres (Duke Scientific) were deposited in tessellated close-pack patterns onto 2x2cm silicon sample areas. The nanosphere deposition technique was based on a method described in the literature [127] and was improved and optimized [143] so that a monolayer of nanospheres in tessellated close packed structures was assembled in large areas (>1cm^2) on the silicon substrate.

The nanospheres were then etched in the radial direction using oxygen plasma etch recipe in the Reactive Ion Etcher (Oxford Instruments, Plasmalab80) whilst maintaining their initial positions. The subsequent anisotropic etching of the substrate was realized via DRIE, (Deep Reactive Ion Etching) as shown in [97]. This anisotropic etch procedure is selective to the substrate and etches away the exposed silicon material creating silicon rods with a diameter equal to that of the spheres in the nanosphere mask. The spheres are then dissolved in a subsequent long oxygen etch via O_2 plasma etching (Figure 7.5a).

The other two samples created, namely the sunflower and close-packed pattern, were defined by e-beam lithography (Figure 2 b, c) in a PMMA resist. The samples then underwent a subsequent mask developing and an anisotropic etching procedure to create a cylindrical pillar profile of pattern features, similar to that created by nanosphere lithography.

7.2.2 Fourier analysis

At first glance, the Fourier transform of the self-assembled tessellated close-packed sample that was created(Figure 7.5b) is closer to that of the highly isotropic [160] sunflower pattern.As shown by simulation in Section 3.2.5.4 by increasing the number of orientations of the close-packed pattern in the structure between 1-4, the number of peaks noticed in the Fourier Transform increase from 6 to 24.

It was also previously shown in the same section that in order for an orientation to contribute in increasing the overall optical diffraction symmetry of the pattern, the angular offset between all the pattern orientations and the reference orientation has to be unique and smaller than the angle of repeating symmetry of the underlying pattern. In this case the close-packed pattern is six-fold symmetric and the repeating angle is 60 degrees (Figure 7.6).

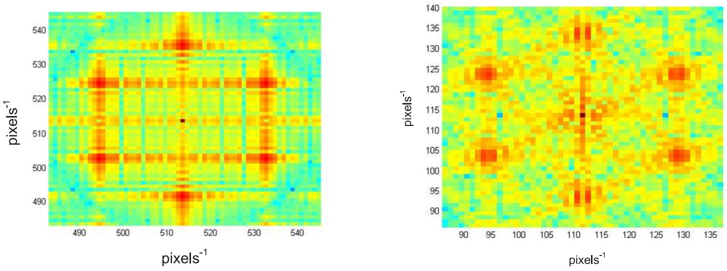

(a)

(b)

Figure 7.6: Matching Fourier transforms for a pattern containing (a) one orientation (Figure 3.29a) and (b) two orientations (Figure 3.29a,f) of the close packed pattern offset by 60 degrees

It was projected therefore that the diffraction pattern will keep increasing linearly in symmetry the more such unique orientations of the base pattern we take into account. The pattern that was manufactured with nanosphere lithography does possess an very high amount of orientations and is expected to have a very isotropic diffraction pattern.

When comparing the Fourier Transforms of different magnifications of the nanosphere-manufactured self-assembled pattern we notice that as magnification increases from 1000x to 6500x the Fourier transform of the pattern changes from resembling that of a very isotropic ring, to one having pronounced six-fold symmetry (Figure 7.7). This shows that the symmetry of the diffraction pattern can only be achieved when considering an area as large or larger than the area that is needed to include lots of different orientations of the close-packed pattern. It was considered in the SEM image of Figure 7.7(a) was large enough because the Fourier Transform of that area (∼80x80μm) shows a complete ring. The white light laser beam that is going to be used to probe the sample (SC450, Fianium, UK) has a diameter of 1mm^2 and hence detecting the isotropy of the sample was not considered to be a problem.

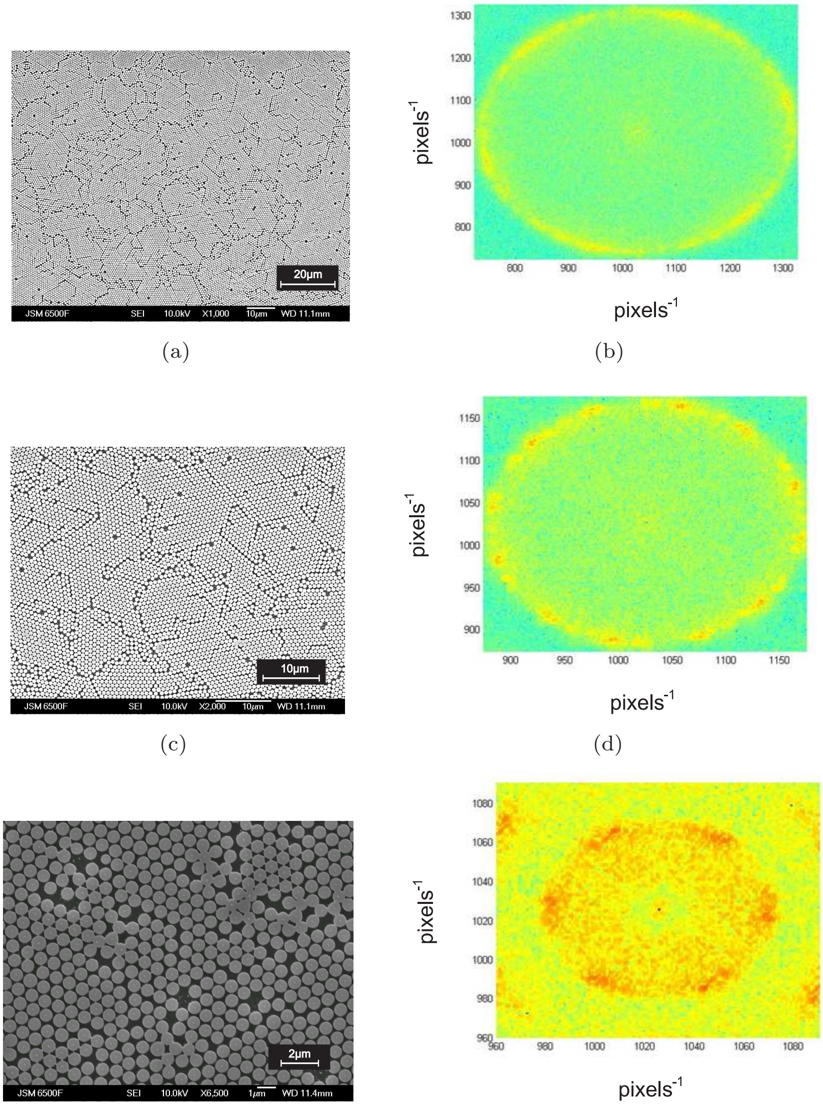

(a) (b)

(c) (d)

(e) (f)

FIGURE 7.7: SEM images of the tessellated close-packed sample at increasing magnifications (a,c,e) and their corresponding Fourier transforms (b,d,f). These SEM images are all from the same sample shown in Figure 7.5a

The optical symmetry that was predicted by taking Fourier Transforms of the SEM images from the other two samples constructed was similar to expectations. The close pack pattern has a strong six-fold symmetry (Figure 7.8b) as depicted in its Fourier Transform, whereas the sunflower pattern depicts a complete ring in its SEM image Fourier Transform (Figure 7.8c) corresponding to a very isotropic diffraction pattern which is similar to the one that is predicted for the close-packed sample (Figure 7.8a).

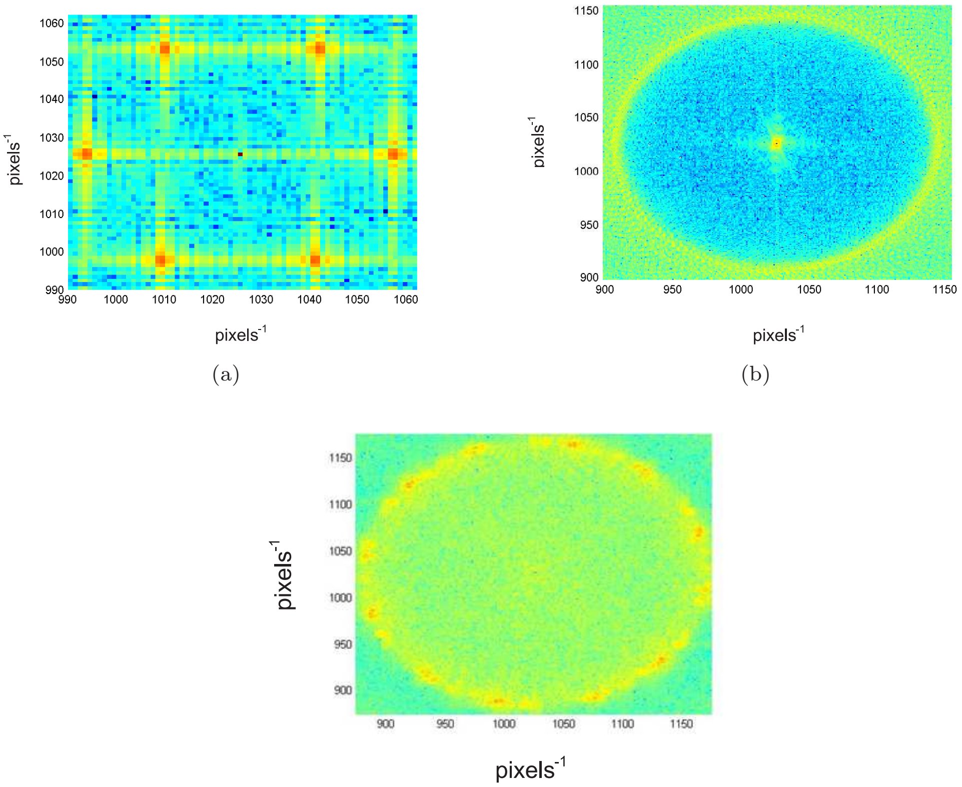

(a) (b) (c)

FIGURE 7.8: Fourier transforms of SEM images in Figure 7.5

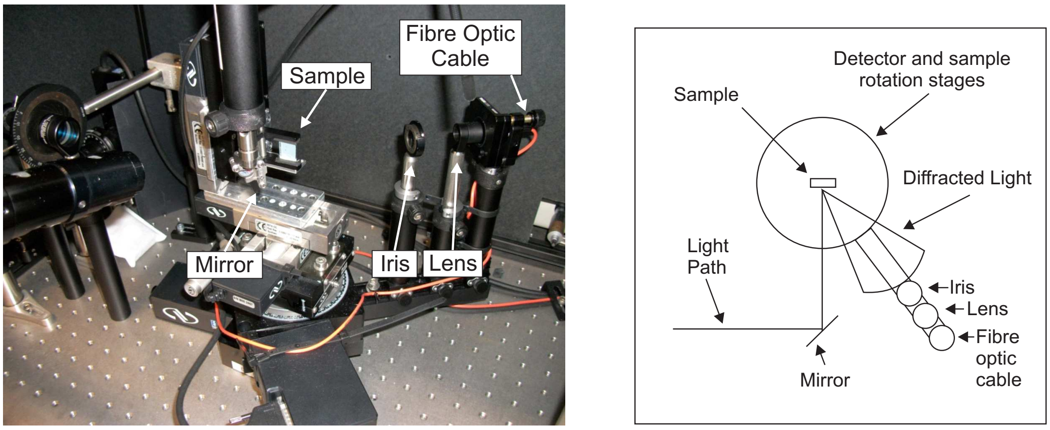

(a) Photograph (b) Top View diagram

FIGURE 7.9: Custom built automated reflectometry apparatus

7.2.3 Experimental Procedure

A custom reflectometry apparatus was built for the experiment (Figure 7.9). The light source used was white light laser (SC450, Fianium, UK) and the spectrum acquisition was done through a fibre optic cable attached to a detector arm, which led to a spectrometer (B&W Tek). In total 7 motors controlled via a PC with LabView software were used to make a robust and automated measurement rig. Three computer controlled motors were used to be able to give the sample rotation, height and lateral adjustment. A tilt stage with 2 axes of freedom was used to provide 3D tilt for the sample when aligning the setup. Two computer controlled rotation stages were used to rotate the fibre optic cable around the sample at any detection angle. Finally a computer controlled stage was added to allow the sample to rotate in azimuth.

The patterns that were used in this comparative analysis have diffraction grating periods of, 350nm for the monocrystalline close packed pattern, 780nm for the tessellated close packed sample and 560nm for the sunflower sample. The values were verified by inferring the grating period from an angular scan of the diffraction spectrum for all three samples and fitting the diffraction equation to the experimental results. (Figure 7.10-7.12)

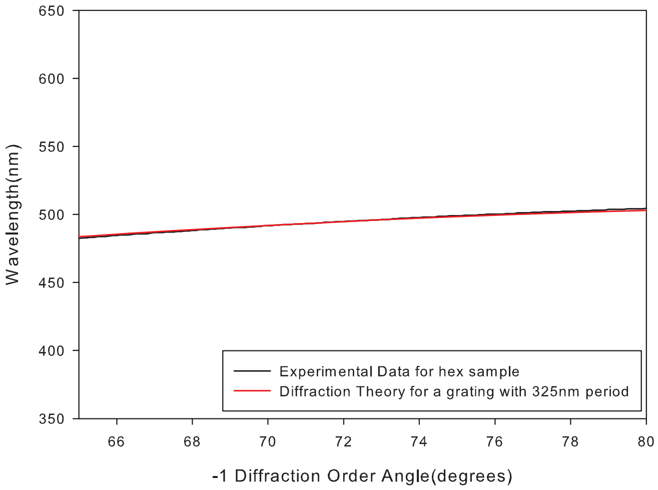

Figure 7.10: Diffraction order wavelength v angle of diffraction for close packed sample shown in Figure 7.5b.

The range of angles of incidence that can be used to create diffraction of the -1 order in the visible spectrum (400-700nm) for samples with the aforementioned periods can be found using the equation of diffraction maxima [161]:

$$sin\theta_m - sin\theta_0 = m\lambda/d \tag{7.1}$$

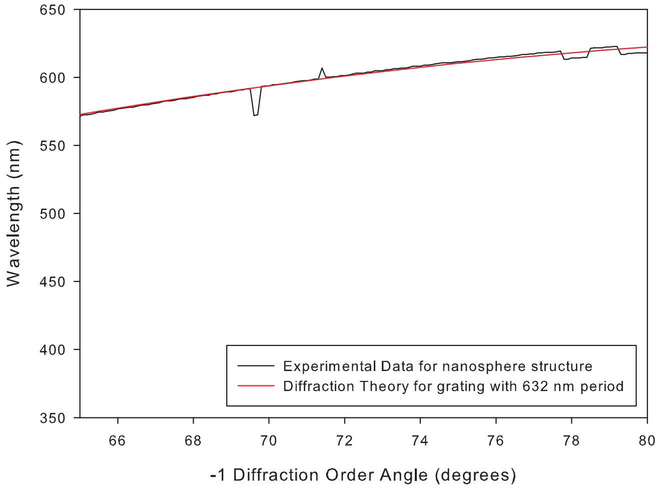

FIGURE 7.11: Diffraction order wavelength v angle of diffraction for nanosphere sample shown in Figure 7.5a.

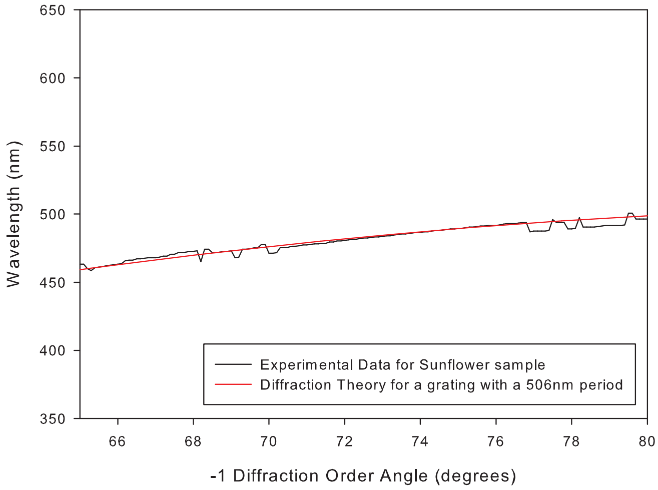

FIGURE 7.12: Diffraction order wavelength v angle of diffraction for sunflower sample shown in Figure 7.5c.

Where θ_m the angle of the diffracted order maxima, θ_0 the angle of the incident beam, λ the incident wavelength, m the diffraction order and d the grating period.

It was expected that diffraction would be observed for the close-packed sample at an angle of incidence close to 60 degrees, whereas the sunflower and tessellated close-packed samples have large enough periods to diffract at normal incidence.

Hence, when measured, the nanosphere and sunflower samples were placed and rotated in azimuth at normal incidence and the close packed sample was rotated in azimuth at an angle of incidence of 60 degrees. The detector was placed at an appropriate position to monitor the intensity of the diffracted wavelength as the sample is rotated in azimuth and the results were recorded (Figure 7.13). For all the samples the monitored diffraction wavelength was 423nm.

7.2.4 Results

As shown in the azimuth scan of the -1 diffraction order for the close-packed pattern (Figure 7.13 a), the number of diffraction peaks detected were six, as was expected from the Fourier transform. The sample created via nanosphere lithography on the other hand has a large number of diffraction peaks, even though the underlying pattern in the tessellated domains is the same (Figure 7.13b). In comparison, the azimuthal diffraction of the sunflower pattern is also isotropic but more homogeneous with respect to the power produced at each azimuth diffraction angle(Figure 7.13 c).

In all plots a threshold of 4000 counts in intensity was set to distinguish the diffraction peaks from the background noise level ($\sim$1000 counts) and this method was also used in order to produce their respective boolean polar plots Figure 7.13 (b,d,f). The polar plots in Figure 7.13b, d depict the difference between the optical symmetry of these patterns in a qualitative comparison, ignoring diffraction power. It is shown that the isotropic nature of the nanosphere sample is very similar to the sunflower sample (Figure 7.13f) and does not at all resemble at all that of the close packed structure.

By combining the data of the azimuth and elevation angle scans, a holistic view of the diffraction can be produced. Three dimensional graphs were constructed to represent the complete set of measurements taken from each sample. The data represented on these graphs is a combined collection of diffraction wavelength, azimuth, elevation and relative light intensity (Figures 7.14 - 7.16).

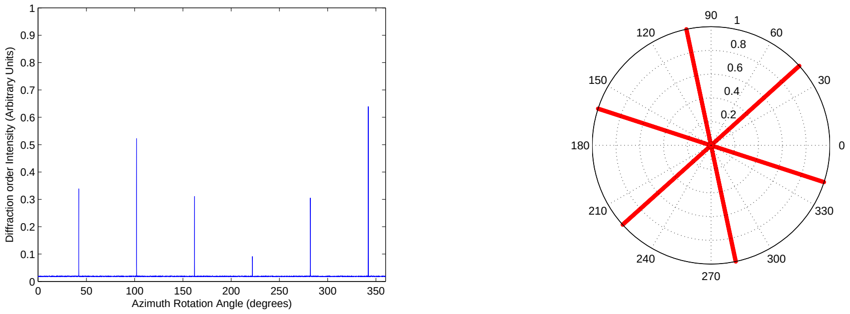

(a) Diffraction order intensity v azimuth angle for close packed sample

(b) Polar plot of azimuth diffraction directions for close packed sample

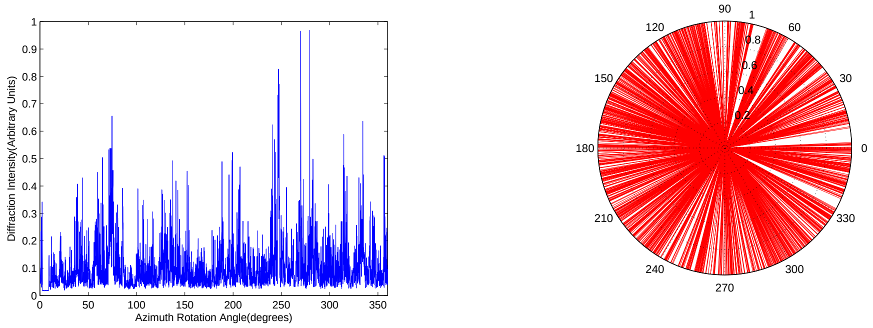

(c) Diffraction order intensity v azimuth angle for nanosphere sample

(d) Polar plot of azimuth diffraction directions for nanosphere sample

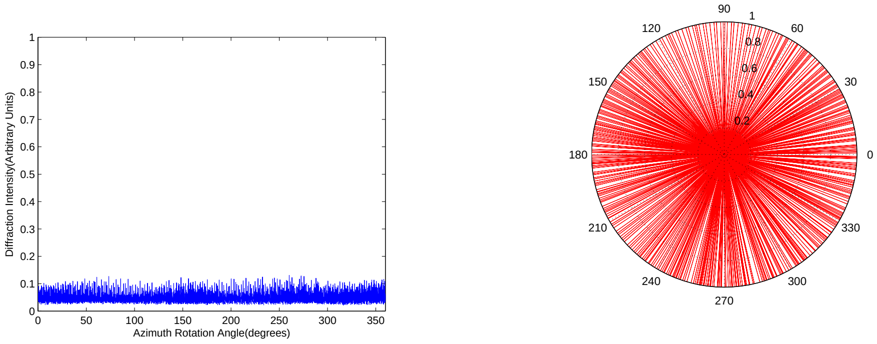

(e) Diffraction order intensity v azimuth angle for sunflower sample

(f) Polar plot of azimuth diffraction directions for sunflower sample

FIGURE 7.13: Linear plots of diffraction intensity vs azimuth rotation and their respective polar plots of diffraction direction vs azimuth rotation for close-packed, nanosphere and sunflower samples shown in Figure 7.5 a,b and c respectively

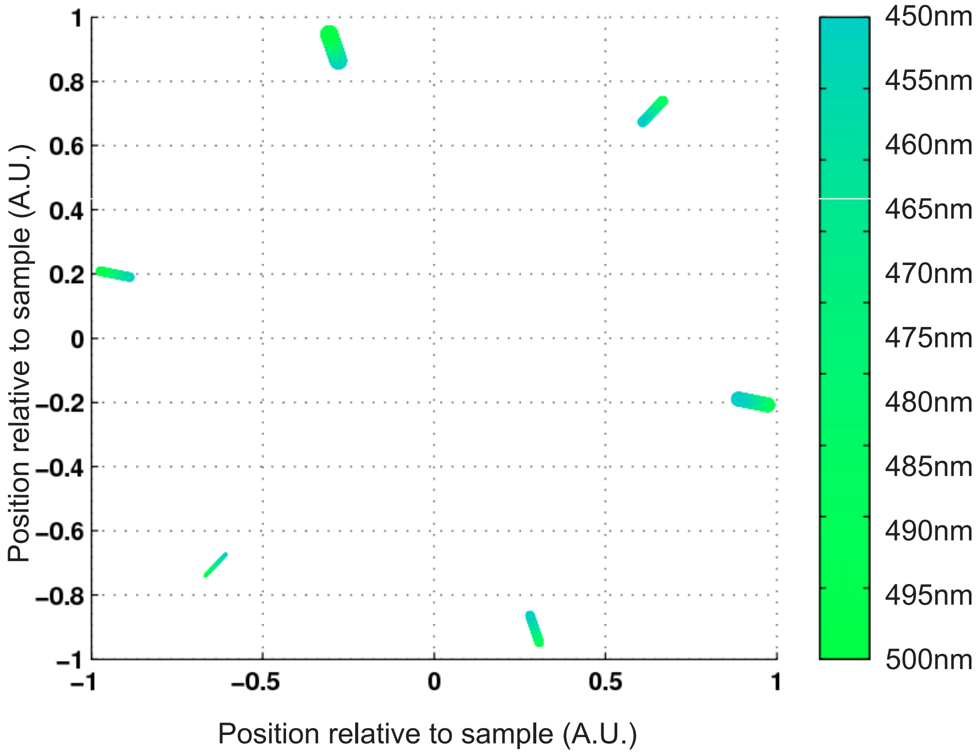

(a) Top down view

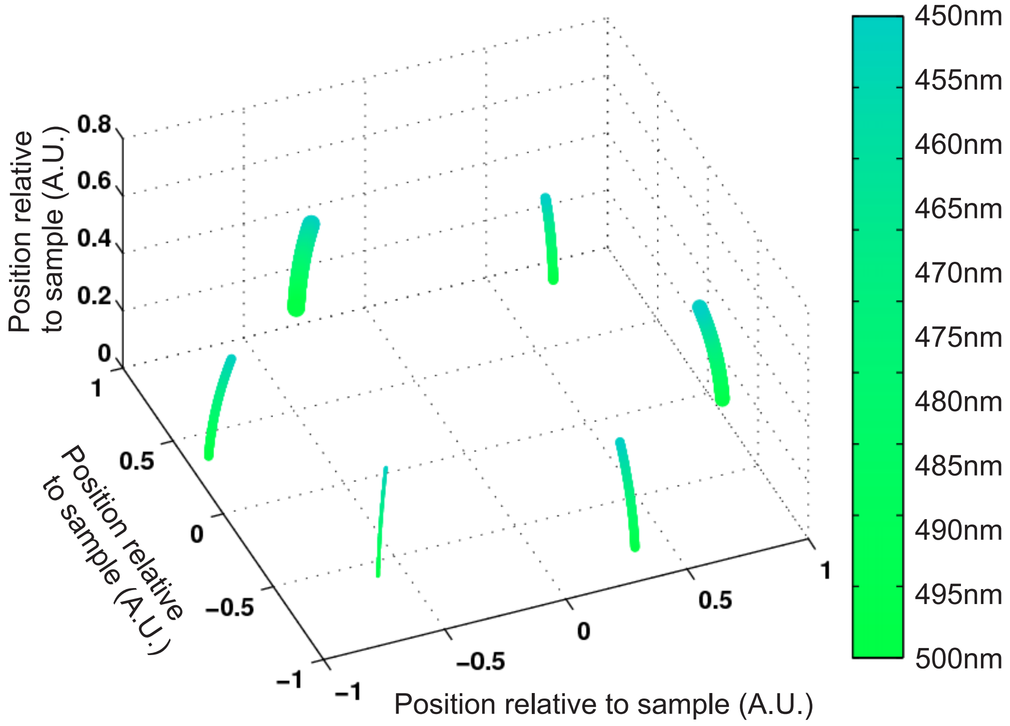

(b) 3D View

FIGURE 7.14: Hex Diffraction Dome.

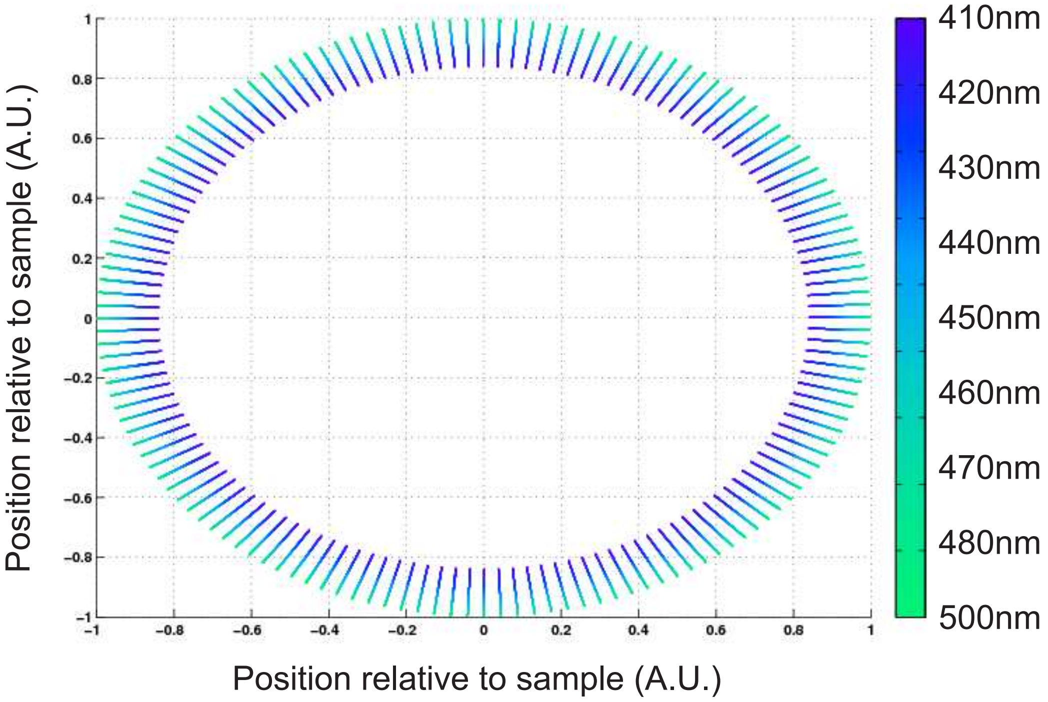

(a) Top down view

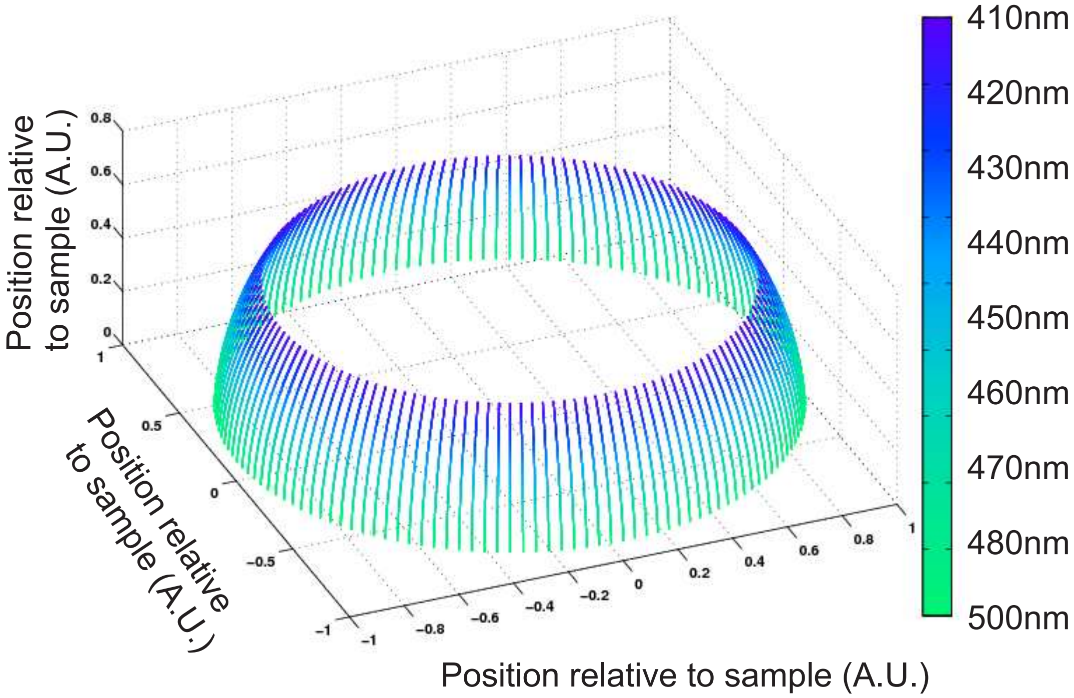

(b) 3D View

FIGURE 7.15: Sunflower Diffraction Dome.

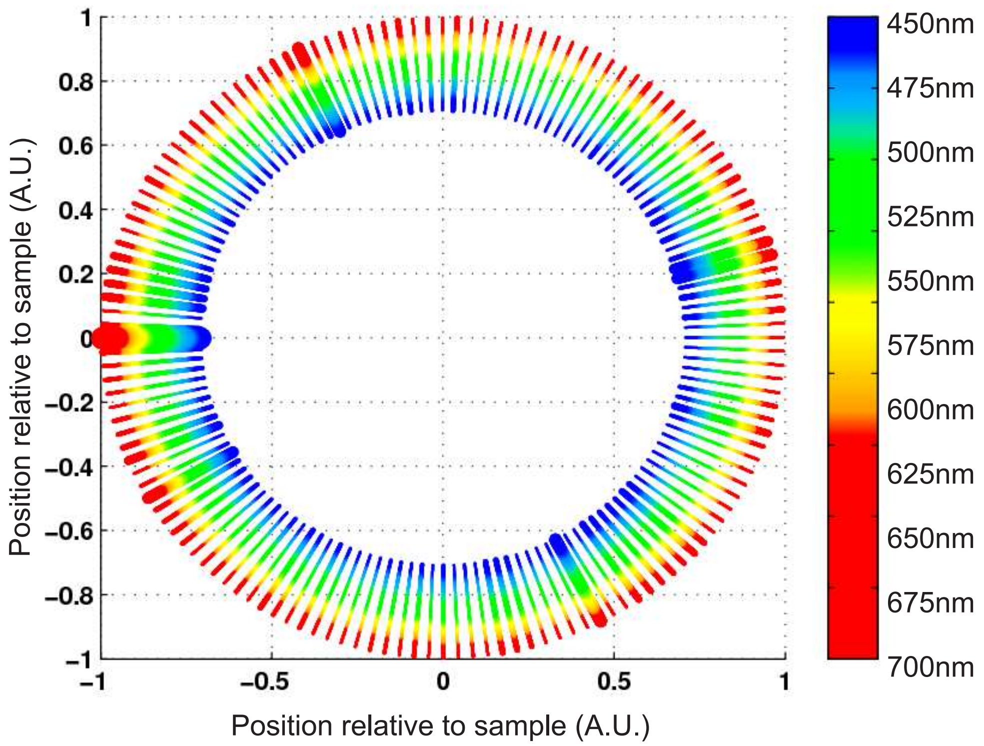

(a) Top down view

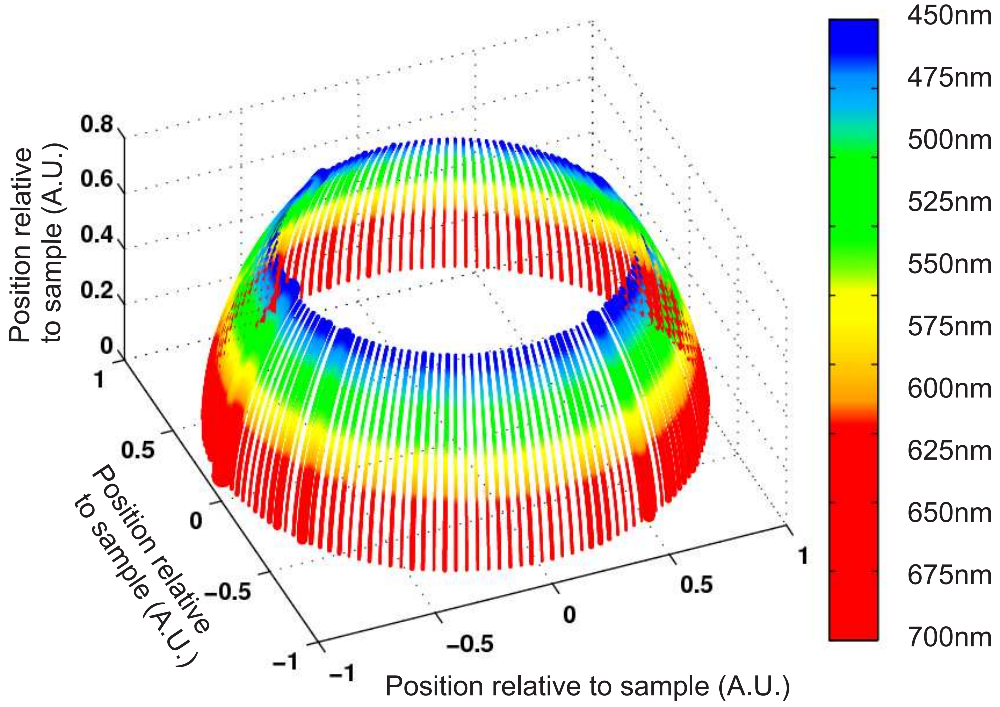

(b) 3D View

Figure 7.16: Nanosphere Diffraction Dome.

7.2.5 Conclusions

The sunflower, tessellated close-packed and close-packed samples that were measured were not directly comparable because the surface density, pillar profile and pillar period of the samples were all different. Thus, although the variation of diffraction power for various angles of azimuth was measured and shown, it could not be used as a basis to compare the performance of the three samples. The analysis carried out in this chapter was done on a qualitative basis in order to compare the sunflower and hexagonal samples to a self-assembled biomimetic sample made via nanosphere lithography.

It has been verified via Fourier transform analysis and experimental measurement that tessellated close-packed moth-eye inspired topologies with high optical symmetry can be created by nanosphere lithography. It can be concluded that highly multi-oriented tessellated close-packed topologies exhibit enhanced optical diffraction symmetry compared to a single-orientation close-packed pattern and resemble the optical symmetry achieved by topologies that are highly symmetrical, such as the sunflower pattern. Hence, proof-of-concept for creating antireflection surfaces with isotropic diffraction via a cheap nanosphere lithography manufacturing procedure has been exhibited.

It is suggested that in order to achieve complete diffraction isotropy via use of the tessellated close-packed biomimetic concept, both for diffraction symmetry and power, a more homogeneous distribution of the various orientations of the close-packed domains is required. This is not something which could be achieved in the time and scope of this thesis. However, possible methods of achieving this result via nanosphere lithography have been suggested in Section 8.3.

Chapter 8

Discussion and Conclusions

In this thesis an investigation of the diffraction and reflection of sub-wavelength 'moth-eye' antireflection surfaces has taken place by simulation and experiment. Nano-scale antireflection surfaces were created by texturing the surface of silicon wafers via e-beam, nano-imprint and nanosphere lithography.

Investigations of the change of reflectance with variation of the angle of incidence, and for different feature period, shape, height and topography were carried out. The trends extracted form the experimental results were found to agree with RCWA and EMT simulations which were conducted. Discrepancies between the values derived from experiment and expected by simulation were due to various reasons, the most important being the inability to exactly replicate the constructed pillar profile in simulation. A small difference in profile proved to produce a large change in the reflectance result as was shown when simulating different pillar profiles. Another issue detected was that the manufacturing quality of the samples at times was perceived to contain a reasonable amount of defects and inconsistencies which also affected the experimental results. For those samples which manufacturing quality was high, the simulations closely matched the measured data (Section 6.6).

An investigation of the diffractive properties of biomimetic 'moth-eye' structures has also been carried out for different pillar topographies. A new concept inspired by the topology of the features on the eye of a moth was proposed for increasing azimuthal diffraction symmetry by employing multiple orientations of a low symmetry pattern. Fourier transforms of the topology images were used to measure the diffraction isotropy of each pattern. Samples with a gradual increase of available orientations of a six-fold symmetric pattern were created to test the hypothesis. It was confirmed that a design containing multiple orientations of a pattern with low optical symmetry can artificially increase the diffraction symmetry of the whole surface by scattering the diffracted power in more directions that before. The azimuthal isotropy of the diffraction that was measured by experiment correlated very well with the Fourier transforms of the topology images. As the symmetry of the pillar topology increased, the number of azimuthal diffraction directions was also increased, thus reducing the power of the diffracted beam equally in all directions.

Hence, an innovative stealth antireflection surface containing a large number of orientations of a pattern with low symmetry was suggested. A low-cost nanosphere lithography manufacturing procedure was developed and suggested as a method of manufacturing a multi-oriented domain surface for a pattern with six-fold symmetry. This surface showed considerable increase of diffraction isotropy compared to the measurements achieved for the previous samples, which only contained a few unique orientations of the close-packed pattern. The isotropy measured was comparable to that of the sunflower pattern which was also measured for comparison. Ways of improving the homogeneity of the azimuthal power distribution in each diffraction order will be outlined in Section 8.3.

To summarize the results of the experiments conducted in this thesis, a suggested combination of design parameters which can be used for creating moth-eye antireflection layers for different applications is collected in the following sections.

8.1 Suggested methods of designing moth-eye antireflection layers for applications in the visible spectrum

Moth-eye antireflection surfaces have proven to have a great design flexibility. Various design parameters can be varied and depending on the application requirements, these can be optimized for improved performance. Below, some genres of antireflection applications will be presented along with the required parameters to design a subwavelength antireflection solution for each one.

8.1.1 Tuning minimum reflection

If the antireflective application only requires a ‘narrow’ wavelength band as for optical components used for laser applications, the profile design need not be complicated, a cylindrical pillar profile will suffice. Changing the period can change the minimum reflectance region of the metamaterial layer in a controllable way such that it can be predicted. It was shown by simulation (Section 3.1.5.1) and experiment (Section 6.2) that the period can then be tuned to the wavelength that needs to be minimized in reflection.

8.1.2 Tuning maximum antireflection bandwidth

Increasing pillar depth and pattern fill factor have shown to widen the antireflection bandwidth but the most dramatic effect was attained by tuning the pillar shape.

A set of simulations comparing different pillar shapes shows that by slowly converting a pillar shape from cylindrical to conical, the reflectance reduces dramatically reaching very low levels for a conical pillar shape (lower than 5% reflectance for the whole bandwidth 400-1000nm: Section 3.1.5.3).

Hence, if the application is broadband in nature (solar/visible spectrum applications) the profile of the pillars should be tapered so that the largest possible band can be absorbed. It has been already shown by Southwell [33] that a quintic variation in refractive index would produce maximum antireflection for surface relief structures, but it was found that this profile is very hard to produce with standard etching procedures. However, the conical pillar shape that was created was found to create very low reflectance (<5%) for a very large bandwidth (400-1000nm).

8.1.3 Managing diffraction orders to obtain a completely stealth antireflection surface

Military and other stealth applications require that the lowest possible detection levels are achieved for any wavelength, angle of incidence and angle of detection. If a close-packed topology is designed, even with the most optimized design parameters of achieving broadband antireflection, diffraction orders may still arise for high angles of incidence and glancing angles of detection. To minimize detection of high power diffraction orders, the power of these diffraction orders can be spread over the whole azimuth range rather than having the diffracted power concentrated in a small number of diffraction angles. This can be done by tessellating the surface and re-organizing the topology of the pattern in domains in which different orientations of the periodic pattern are placed. This way the power of the diffracted orders decreases while the number of orders increases making detection of any specific order very difficult.

8.1.4 Managing diffraction orders to relax manufacturing requirements of antireflection layers

All commercial manufacturing procedures have limitations in the scale of the features they can produce. If the feature sizes available are not completely sub-wavelength to the incident light, diffraction orders will start appearing at high angles of incidence.

If this becomes an issue, it cannot be completely avoided, but trapping the diffraction orders via total internal reflection may be possible. This can be done by engineering the capping layer such that the diffracted angle of the smallest wavelength in the range of interest is larger than the angle of total internal reflection.

8.1.5 Widespread application - cheap methods of manufacture

Creating sub-wavelength structures rapidly on a large scale may prove very expensive with most current nanomanufacturing methods hence producing these features with nanosphere lithography was suggested as a way of reducing the cost and making the process more compatible with mass-manufacturing.

It was found that tessellated close-packed structures can be readily constructed via nanosphere lithography both on a sub-wavelength (Section 6.5) and also on a par-wavelength size scale (Section 7.2.1) to that of the visible spectrum. Creating large areas of tessellated close-packed structures at room temperature with water suspensions of cheap polystyrene particles which produce a very isotropic diffraction patterns in the visible spectrum is simple and much faster than conventional ‘top-down’ nanomanufacturing methods(Figure 7.7).

However, although this method has large scale manufacture potential and was shown in this thesis to be able to create structures that are useful for antireflection and isotropic diffraction applications, a specific process that can take advantage of the procedure on a commercial basis has not been demonstrated yet.

8.2 Conclusions for tessellated moth-eye surfaces

Tessellating an ordered moth-eye surface into domains and rotating the orientation of the pattern within them seems to be nature’s way of increasing the complexity of the backscattered response from these surfaces, especially when referring to real moth eyes which inspired this work. A possible explanation of why night flying moths have developed this property for the cornea of their eye could be speculated. It could be that by natural selection, prey that did not have these structures in their eyes would reflect more light and could be spotted by their predators easier. It could also be that the process that these protuberances grow on the eye of the moth, do not allow for ordered structuring and that this randomness is just a by-product of the way that these structures are formed biologically as there is no alternative ordered mechanism to construct them. Hence, concluding whether these natural traits were intentional or not, remains to be debated.

The biomimetic pattern created in this work which was inspired by the real moth eyes was found to possess very high rotational symmetry, much greater than highly engineered quasi-crystal patterns and comparable to extremely isotropic patterns such as the sunflower pattern. Hence the tessellated close-packed pattern could be used as an alternative to sunflower patterns in applications including photonic crystals, LED's and antireflection layers because as it was shown, it can be created on substrates readily and cheaply by nanosphere lithography. However for this to happen, a commercial process which can control the nanosphere deposition process in terms of the amount of orientations and their distribution has to be developed. This kind of self-assembly, albeit possible, has not been demonstrated with any known techniques and hence requires to be researched further.

8.3 Future work suggested

8.3.1 Elimination of diffraction originating from the regular parallel domain edges by using non parallelogram-shaped domains

The domains created in section 7.1 were square in shape and hence the discontinuities between the domains were at a fixed distance across the whole sample. This regularity in the structure produces some extra diffraction around the zero reflected order. To reduce this effect the domains could be arranged in a non regular fashion via the Vonoroi method or by randomizing the square grid. An analysis of potential methods that could be used have been presented in Appendix A.4 - A.6 .

The main hurdle that needs to be overcome before using this procedure would be that one would need to control the area of the domains so that the total individual areas acquired by each orientation of the sub-wavelength pattern be of equal size across the whole tessellated surface. This is required in order to provide homogeneous azimuthal diffraction similar to that produced by the sunflower pattern. This is straightforward to do when the domains are square and of equal size but not so obvious when the domain sizes and shapes vary.

8.3.2 Controlling the tessellated pattern created via nanosphere deposition

The aforementioned problem is also the main drawback in using nanosphere lithography to create tessellated subwavelength patterns. Making moth-eye biomimetic patterns via nanosphere lithography does not provide robust control over the pattern that is created in terms of the distribution and the variety of unique close-packed pattern orientations. Nanosphere lithography can facilitate a large random number of orientations of the underlying pattern but the overall distribution of any one of these orientations on the surface is not controllable. Various ways of attempting to control this have been proposed in the literature by using directed self-assembly techniques [101].

Future work could attempt to improve the deposition method used here by employing a combination of self-assembly and directed self-assembly techniques. This fusion of techniques could improve the distribution of underlying pattern orientations whilst keeping the total domain sizes for each orientation as similar as possible. If this can be achieved, it is expected to optimize the isotropic diffraction of nanosphere self-assembled biomimetic samples not only in direction but also in power. It is foreseeable that this kind of structure would create very similar results to those attained with the sunflower pattern and at a fraction of the manufacturing cost.

8.3.3 Application of subwavelength pillar antireflection layers via nanosphere lithography on other substrates

Nanosphere lithography can be applied on a large range of different substrates with similar ease. A particularly interesting substrate to optimize sub-wavelength antireflection for would be glass because is used for a lot of different optical applications.

Additionally, other widespread applications can be envisaged using sub-wavelength antireflection layers, such as on LCD screens used in laptops and mobile phones in order to reduce glare in bright sunlight which would similarly increase colour contrast in normal indoor conditions. Ting et al. [162] have recently demonstrated glass substrates with 0.58% reflection in the visible range via 'moth-eye' subwavelength texturing whereas Song and collaborators [163] have presented dual-side glass subwavelength texturing with 99.58% transmittance over the visible range.

8.3.4 Improving the profile of the pillars

The majority of the pillars created for this thesis were made to be cylindrical in profile for two reasons. Firstly, the EMT thin film simulations had to be matched to the RCWA simulations. Hence, by creating a cylindrical structure which is equivalent to a layer with one effective refractive index it was possible to validate the experimental results with two simulation methods and consequently validating both methods to each other. Secondly, by using cylindrical pillars rather than tapered ones, the diffraction properties of the layers could be detected easier, since the power of their backscattered diffraction order is significantly larger when the profile is cylindrical. A cylindrical pillar profile however, is not optimum for creating an antireflection layer with the best possible performance.

To achieve the best possible performance of the metamaterial antireflective surface by using sub-wavelength pillars, the variation of effective refractive index within the metamaterial layer has to be quintic in nature as discussed in section 3.1.5.3 and hence a very specific profile to be made which requires deep knowledge and control of the etching procedure involved. A limited customization of nanopillar profile via combination of different etch methods which was carried out (Chapter 6.4),produced conical and flat top slanted pillars which proved to substantially increase the performance of the antireflective layer. Etch methods can be further explored in depth in order to create the optimum pillar shape to induce a quintic variation of refractive index and thus achieve the best possible performance for the antireflection layer.

8.3.5 Integrating devices into subwavelength pillar antireflection layers

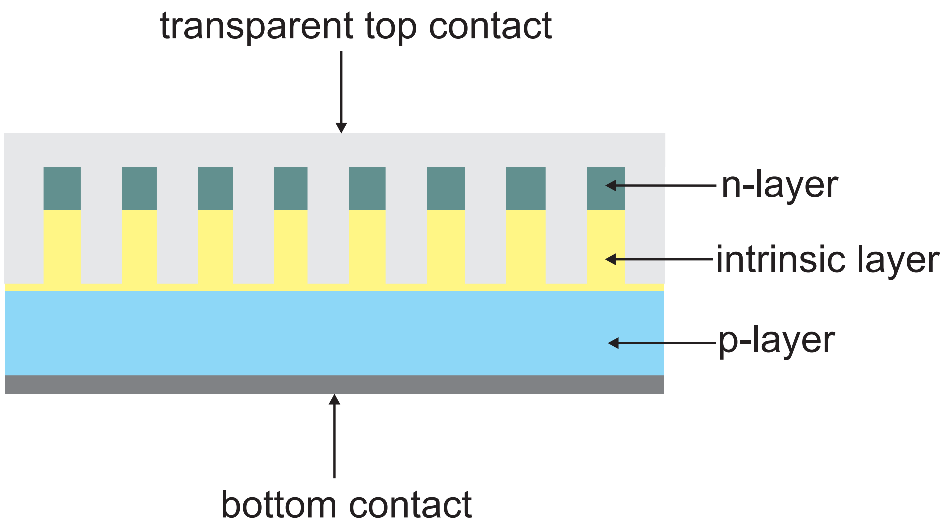

Figure 8.1: Device design proposed for a solar cell/photodetector with improved efficiency and reduced thickness compared to the classical flat layer architecture.

Devices such as photodetectors and solar cells could benefit greatly from being integrated into subwavelength pillar antireflection solutions. For solar cells specifically, constructing the active layer within the pillar structure which is used for antireflection, reduces the distance the electron-hole pairs would have to travel before being absorbed by the contacts and in turn reduces the chance of recombination of the charge carriers in the bulk. This improves device efficiency substantially which allows the cell to use less material to achieve similar efficiencies to flat architectures using the same materials (Figure 8.1). A schematic of the proposed device is shown in Figure 8.1. If this design is applied to photodetectors, it would also increase their sensitivity as more carriers would be collected at low light levels due to the more efficient design.

The research group led by Prof. Atwater has been heavily involved in producing such kind of solar cell architectures. Recently, they have demonstrated a device which in addition to using a nanowire architecture employs plasmonic light trapping techniques to achieve an efficiency of 7.9%. This device uses a volume of silicon equivalent to a very thin 4μm thick wafer [164].

Recently, an alternative idea to texturing the active layer of the cell was proposed by Zhu and collaborators at Stanford [124]. A glass substrate was pre-textured via SiO_2

nanoparticle NSL to create a close-packed corrugated surface on which an ultra-thin (280nm) amorphous silicon solar cell was grown. This is a more practical approach, however, this design lacks the benefit of laterally restricting the path required for the charge carriers to reach the contacts, since the active regions of the device are still deposited as continuous layers. Nevertheless, Zhu et al. [124] report a 5.9% power efficiency for the device they demonstrated.

Appendix A

Appendix

A.1 Nanosphere coverage results

The SEM (Scanning Electron Microscope) images taken from the nanosphere samples were analyzed with an image analysis software called ImageJ. The image threshold was set so that all the gaps in the nanospheres were covered in each image. This is because all the SEM images are different in contrast and brightness which could not be avoided. Then the particle analysis tool calculated the area percentage of the gaps between the spheres, and this is how the results for the nanosphere surface coverage were obtained in table 5.1.

Of course since nanosphere lithography is not entirely consistent over the whole sample several SEM images were taken and analyzed from different areas of the sample and these were averaged to give an overall coverage result.

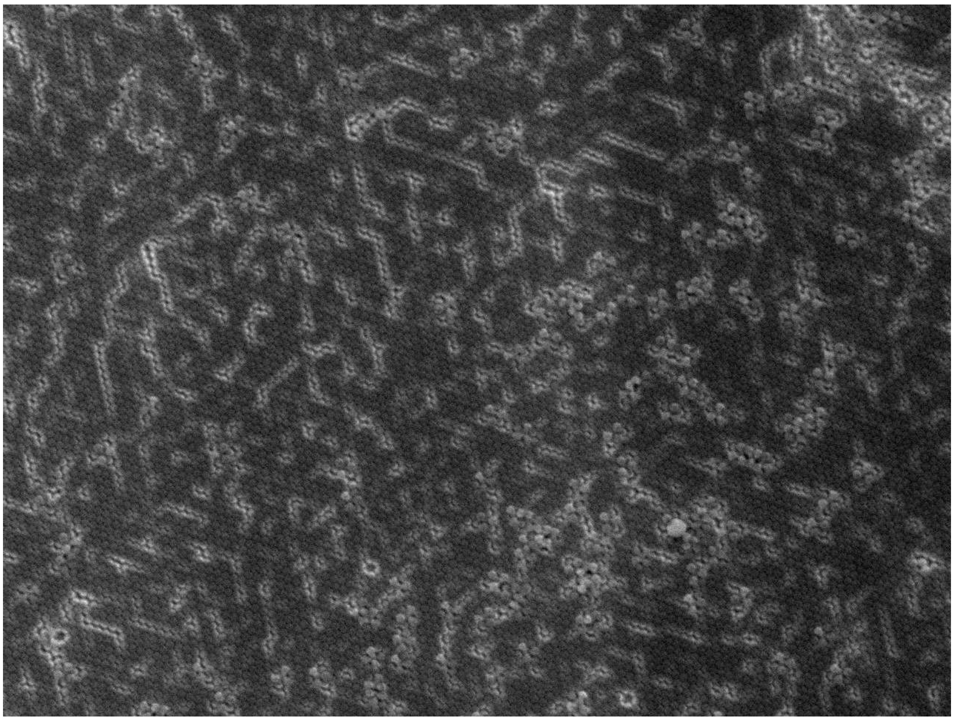

(a) SEM Image of Liquid Surface suspension Method

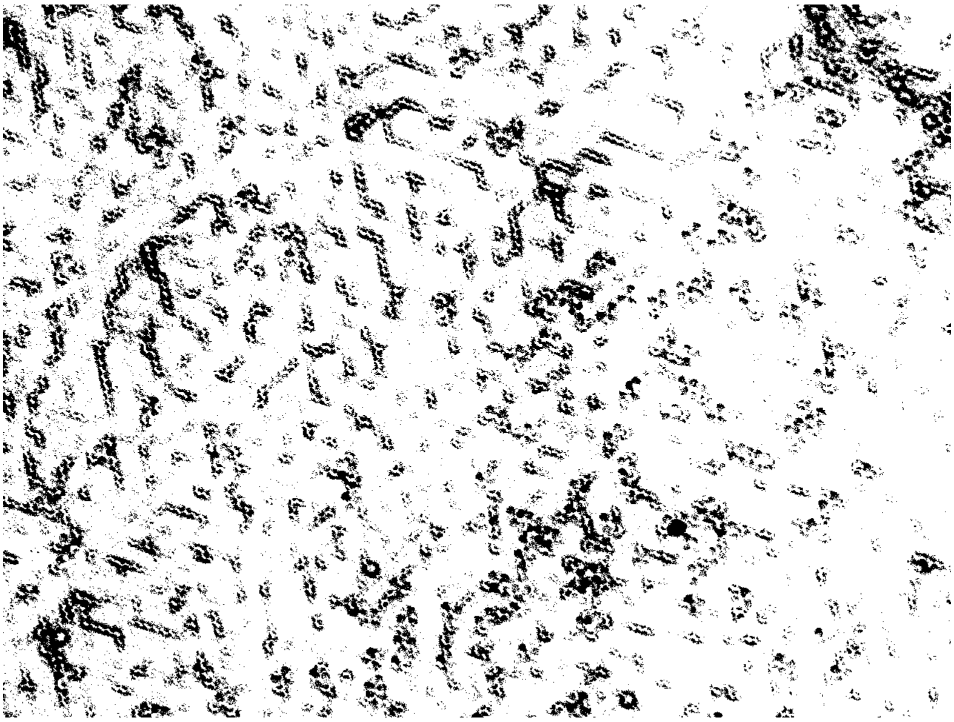

(b) After setting image threshold

FIGURE A.1: Liquid Surface Suspension Method SEM image results (a) before and (b) after image threshold setting. The nanospheres have a diameter of 200nm were assembled via the procedure described in Section 5.2.1

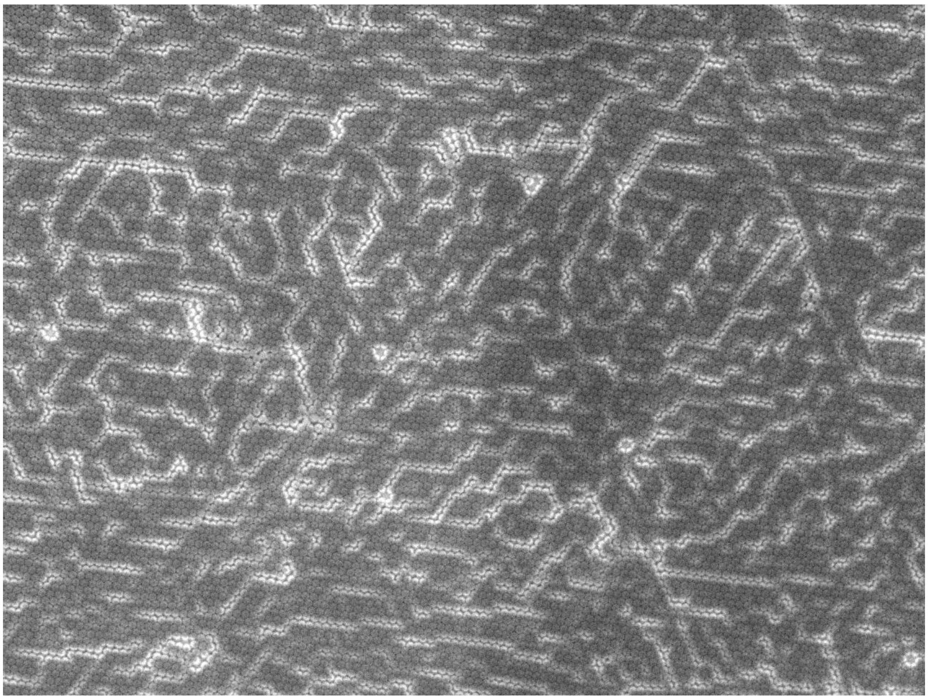

(a) SEM Image of Improved Liquid Surface suspension Method

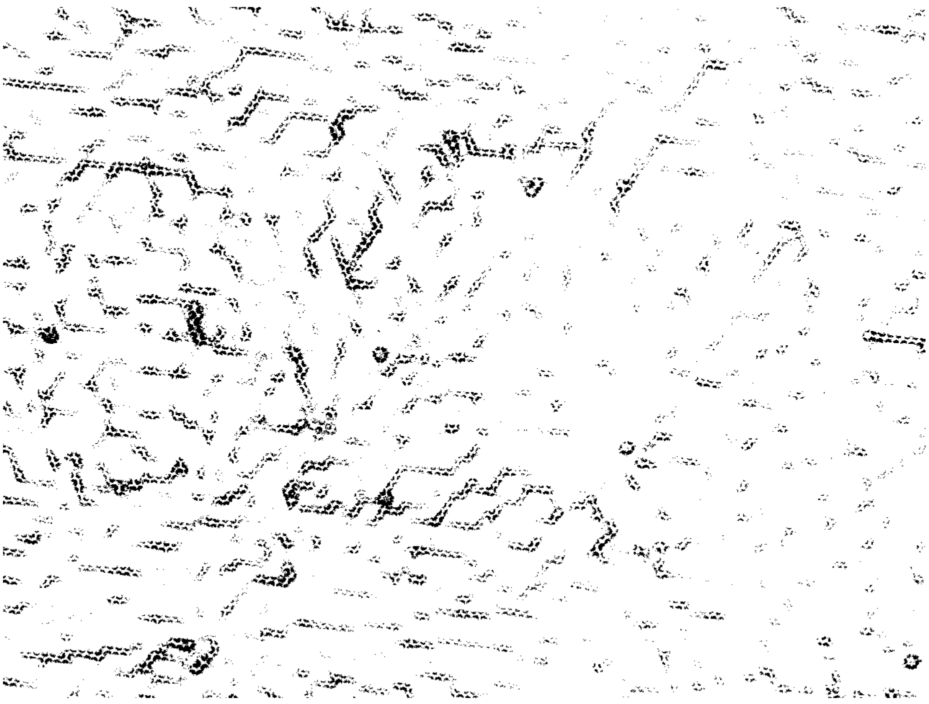

(b) After setting image threshold

FIGURE A.2: Improved Liquid Surface Suspension Method SEM image results (a) before and (b) after image threshold setting. The nanospheres have a diameter of 200nm were assembled via the procedure described in Section 5.2.1

A.2 DRIE Samples

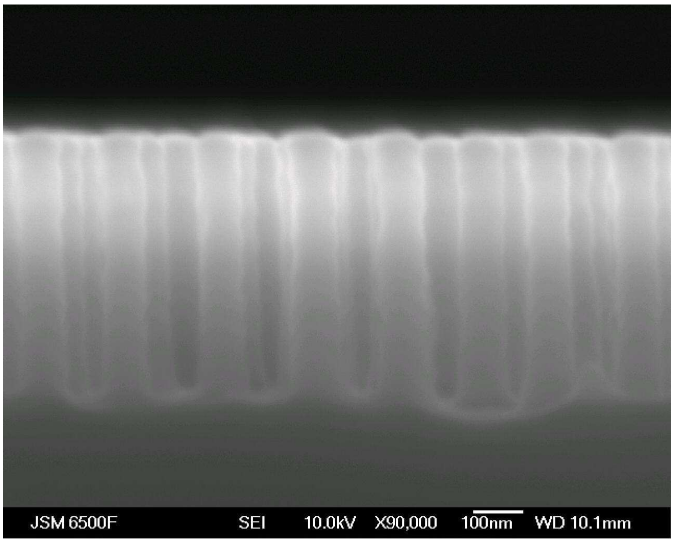

(a) Sample with acceptable vertical edges.

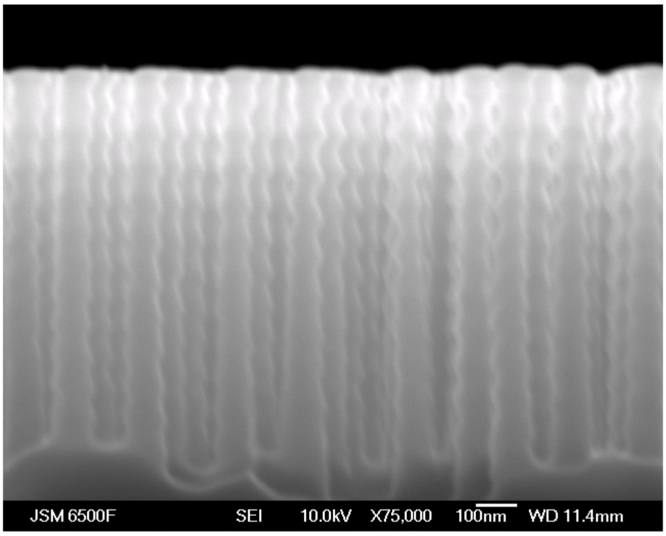

(b) Sample with distinct non vertical edges.

FIGURE A.3: Example of Bosch Etch inconsistency in making cylindrical pillars when the carrier wafer becomes degraded. The etch mask consisted of 200nm diameter spheres which were self-assembled via the technique described in Section 5.2.1. The etch parameters are described in Table 5.4

The SEM images of the example shown in Figure A.3 depict the ’wavey’ pillars that are created from cycling the different gases in the Bosch process on a substrate that is not properly thermally coupled to the handling wafer.

A.3 Description of Other Nanosphere Monolayer deposition techniques that were investigated

A.3.1 Spin Coating

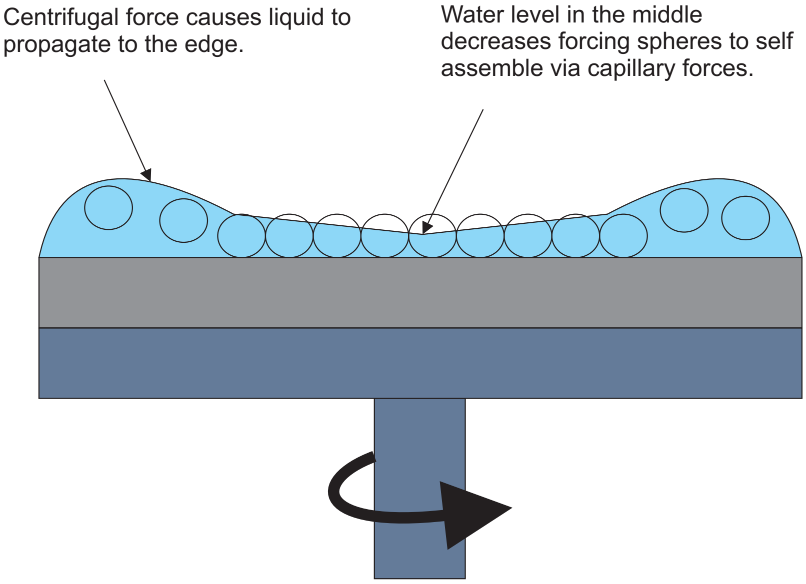

Figure A.4: Schematic of the spin coating technique for depositing nanospheres on a surface. A colloid is placed on a wafer spinning on a coater chuck spreading the colloid out on the whole surface. The spin speed determines the layer thickness.

In spin coating deposition a liquid is dropped on the substrate while or before it is spun. The dynamics of to a fluid when it is spun on a substrate are described by fluid dynamics equations. [165].

The number of spin stages that have been presented in literature can either be 2 or 3. The first stage of the spin is done at small speed. This is called the spreading speed and the purpose of this stage is so the colloid or liquid can cover the substrate in an even fashion. The next step is the spinning speed where the height of the liquid/colloid is reduced to the required level. Finally, there is an optional very fast spin stage where residual liquid is spun off.

It was found that the colloid would self assemble better if the spin stages were only two. The excess liquid would be allowed to evaporate naturally from the substrate.

Spin coating is a technique that can be shown to be very useful if it can be used efficiently. It is very fast and can be integrated in a commercial production line. However in our results only a thin radial ring of nanosphere monolayers was created on the samples with no deposition in the center and multilayers formed at the sides.

A.3.2 Drop Casting

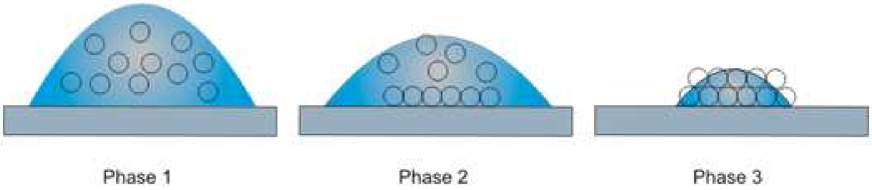

FIGURE A.5: Schematic of the drop casting technique for depositing nanospheres on a surface. A colloid is placed in the middle of the surface that is coated and the solvent is left to evaporate.

In drop casting deposition a colloid drop is left to evaporate on a surface naturally. The drop does not cover the whole surface and is bounded by surface tension on the gas-air-liquid interface. Different percentages of ethanol and water, different temperatures. However, this technique did not produce required results either as it mostly created close packed multilayers.

A.3.3 Template Evaporation

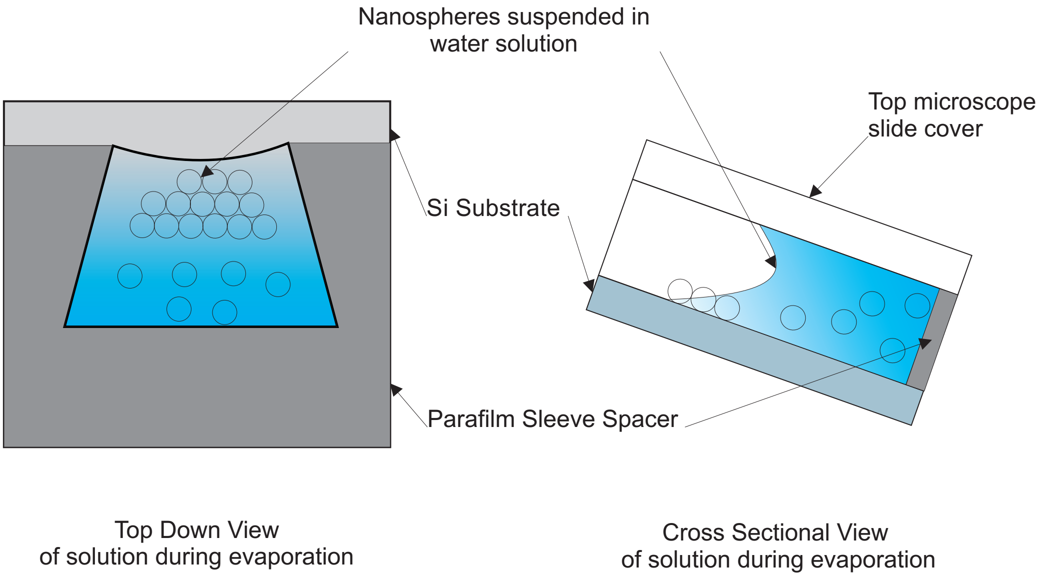

FIGURE A.6: Schematic of the drop casting technique for depositing nanospheres on a surface. A glass slide is placed on top of the surface and sealed with parafilm. The nanosphere colloid is placed in the pocket between the wafer and the slide and is set to an angle and left to evaporate.

Template evaporation is a technique by which a liquid is confined by a thin template and is left to evaporate from a certain direction at an angle. The mechanism by which the close packing takes place is explained by [144] and [166].

A.4 Plane tessellation via method of square-grid randomization

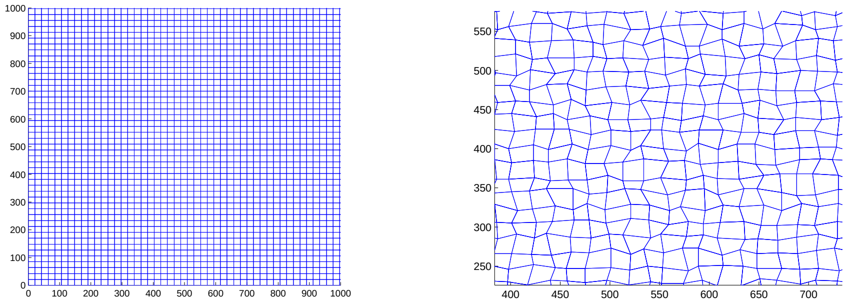

(a) Square lattice domain surface.

(b) Semi-Random domain surface based on a square lattice.

Figure A.7: Design of semi-random polygons using square grid randomization.

This method is based on randomizing the positions of the vertices of a square grid (Figure A.7(a)). The vertices of each square on the grid are allowed to randomly be re-positioned in a bounded region about their initial location creating a distorted tessellated version of the square grid (Figure A.7(b)).

A.4.1 Setting the square grid

The allowed area around each point of the square grid is defined by the design area specifications. Specifically, this area is bounded by the required maximum and minimum area set at the beginning of the algorithm (Figure A.8 b).

An example of the deduction of this area is given here. Assuming we require to make domains with areas from $100nm^2$ to $10000nm^2$ The variables used here are:

D - original square grid spacing
d - half distance of the side of the free movement area
a - side of minimum square

With this method we set the minimum and maximum areas to be square (as shown in Figure A.8 a). Thus the side of that square can be found by taking the square root of the minimum and maximum areas respectively. The minimum side will be a $= \sqrt{400} = 20$, and the maximum side will be b $= \sqrt{10000} = 100$. The half distance of the side in the free movement area is then given by rearranging the relationship $b = a + 4d$, and hence $d = (b - a)/4 = 100 - 20/4 = 20$ (Figure A.8 c).

Now, following simple geometry we can deduce the pitch of the underlying square grid D (Figure A.8 b) needed to cover the area we want to tessellate (which is also limited to be square) as,

$$D = a + 2 * d = 20 + 2 * 20 = 60nm \tag{A.1}$$

To tile an area of, for example, $4\mu m^2$ or 4,000,000nm^2, the side of the square that would cover that area is $\sqrt{4,000,000} = 2000nm$

We can divide this length with the pitch of the square grid:

$$n = 2000/60 = 33.33333^{-} \tag{A.2}$$

Since we cannot select a non integer number we round up to the next integer. In this way we make the area tiled marginally bigger, and that is enough to cover the required space set in the beginning. Thus the initial square grid is a 34x34 lattice with a point distance equal to $D = 60nm$.

A.4.2 Repositioning the vertices of the square grid

After setting the square grid and the allowed area for each point (Figure A.8 a) we randomize the location of these points within their allowed area of existence. The allowed movement area is quantized in 10 x and 10 y displacements centered at the square grid points. The source of these offsets is a non-sequential stream of numbers. In this algorithm the stream is set to be the decimal places of the number π: 3.{141592653589793....}. The result is shown in (Figure A.7(b)).

A.4.3 Conclusions

The main reason for selecting this method would be because of its ease of use and integration with a CAD design program. A tessellated surface was created in a C program and later imported into a CAD program called LEdit (Tanner EDA, California,USA). Within LEdit the periodic pattern can be placed in different orientations within each domain to complete the design.

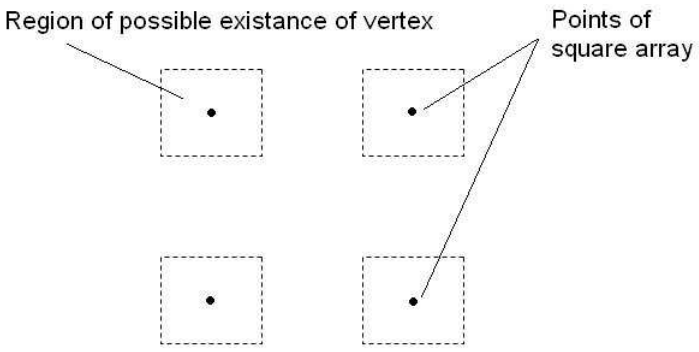

(a) Unit cell of square point matrix with regions of possible existence of vertices.

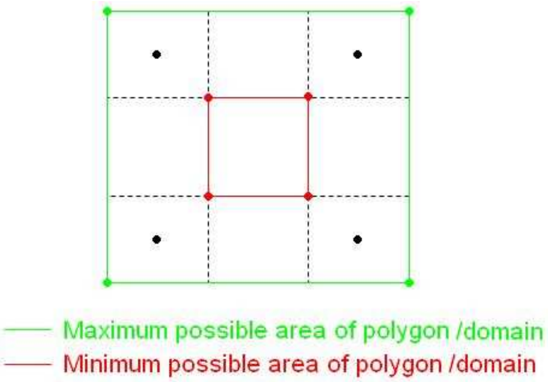

(b) Unit cell of square point matrix depicting minimum and maximum area.

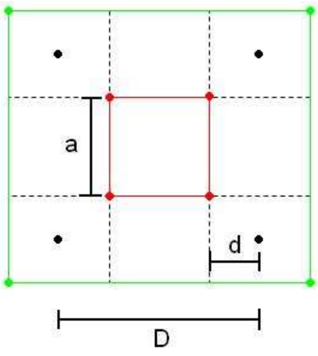

(c) Length variables used.

Figure A.8: Design of semi-random polygons.

A.5 Plane tessellation via Voronoi domains

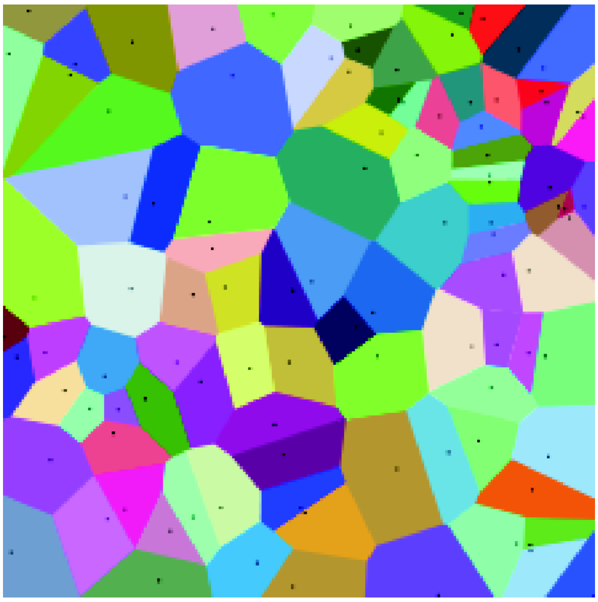

Figure A.9: Example of Voronoi Tessellations. [167]

The Voronoi diagram or the Dirichlet tessellation is a method of tessellating a surface by placing a number of random points on a surface and creating domains based on the nearest neighbors of each point. The basic methodology starts with calculating the closest neighbors of each point on the surface (Figure A.10(a)). Once this is done, bisecting lines are created for each of these neighbors (Figure A.10(b)). The region enclosed by these bisecting lines forms a domain around the central point(Figure A.10c).

The creation of these domains via a totally random processes such as using a Poisson distribution of points, is not ideal for our purposes. Controlling the size of these domains is crucial because the total area of one orientation of the periodic pattern over the whole surface has to be similar to combine the effect of all these orientations individually.

This is the reason for which a filtering method has been realized whereby the domains are first created randomly as shown in Figure A.11 and then points are removed based on a minimum inter-particle distance rule. The result is a more uniform cell size, as shown in Figure A.12. By controlling the minimum domain size for the Voronoi plot as shown before, a lower boundary for our area which has a minimum shape of a hexagonal cell with area:

$$A = h^2/(2 * sin(60)) \tag{A.3}$$

Where A the minimum area of the domain, and h is the half of the minimum distance.

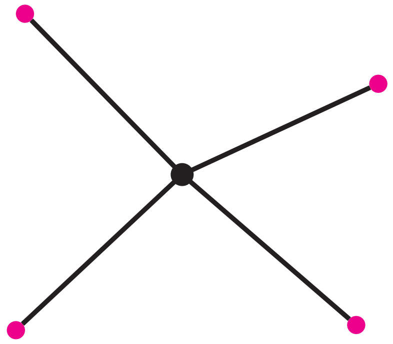

(a) Calculation of nearest neighbors

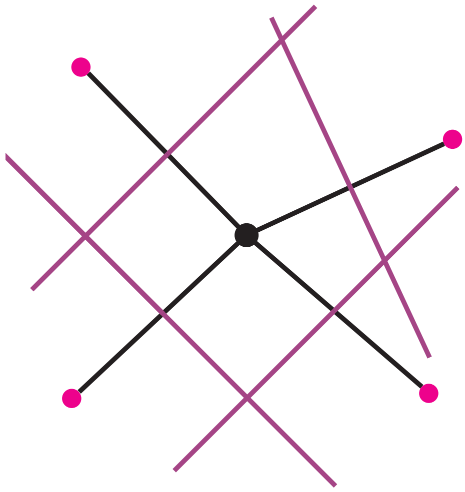

(b) Plotting bisecting lines

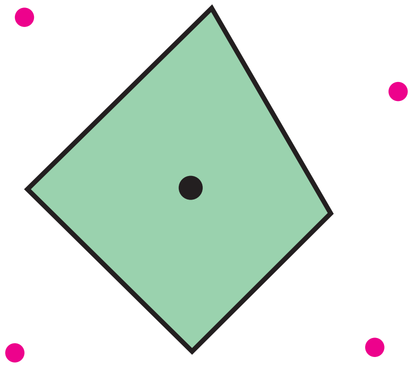

(c) Collecting intersections between lines and creating Voronoi domain

Figure A.10: Process of Voronoi domain creation

Equation A.3 can be proven by the rules of the previously stated method of creating a Voronoi diagram and the added rule that the minimum distance that two points can be now placed on the surface has been limited to a certain value. Since the smallest equidistant packing of points on a surface is a close-packed arrangement[82], the minimum Voronoi cell that is created by adding such an rule would be a hexagon. By taking the bisecting lines of these points of this minimum hexagon with the aforementioned area is formed.

The maximum domain cannot be deterministically defined because the points are put on the surface in a random fashion. The maximum domain size therefore depends on the number of points, the size of the surface but also the nature of the random algorithm or distribution that is used to place the points on the surface.

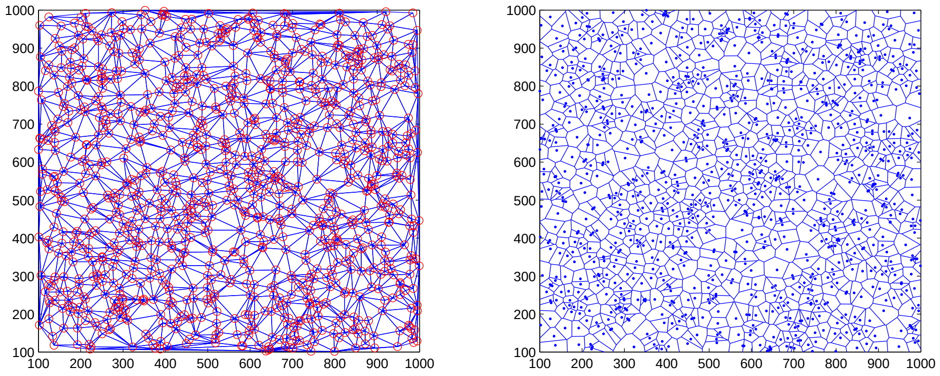

Figure A.11: Interparticle distance depicted via Delaunay triangulation (left) and respective Voronoi diagram (right) before filtering for minimum particle length.

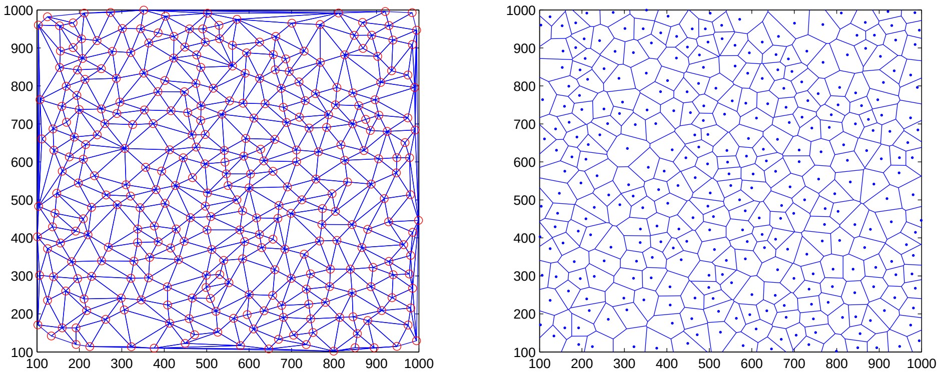

Figure A.12: Delaunay triangulation of optimized points (with a minimum interparticle distance of 30) (left) and respective Voronoi diagram (right).

A.5.1 Conclusions

The Voronoi tessellations are simple to create using a computer algorithm, but the method is not easily controllable as far as domain size and selectivity of the domains are concerned. The selectivity of the domains refers to the pattern orientation distribution on the surface. There is much less control over the creation of the domains and where they will end up after creation. Thus a lot of similar orientations of the pattern may end up into adjacent domains. All factors considered though, it is a very good method of achieving.

A.6 Assessing Pattern Algorithms

Only two restrictions are necessary in making these patterns. The resulting surface must be split in domains that are equal as much as possible in area, but with edges of consecutive patterns that are maximally random as possible (i.e. the edges of consecutive domains have to be as non-parallel as possible to avoid grating effects). In order to verify this for the domains that result from the algorithms, we have to develop a method to compare the success of each algorithm or technique.

For the first part of our specification we can set an easy variable to look at. The area of all the domains in the pattern will be measured and then plotted in a histogram. The spread of this histogram will allow us to compare methods. The technique that producing the smallest spread will be considered the most ideal.

For the other part of our specification, we need to assess to what extent the sides of each domain are non-parallel to the rest. This can be done by counting the angle of each side in all domains with respect to a common reference line, and plot the spread of angles in a histogram. In this case the technique producing the largest spread of domain angles will be considered the most ideal.

Area histograms in Figures A.14 (a) and A.15 (a) are normalized to expected domain size, which coincides with the peak of the distribution. In the Voronoi distribution this value is found by calculating the number of points and dividing it with the total area covered. For the semi-random lattice method this is found by using the underlying unit square in the grid as the expected area.

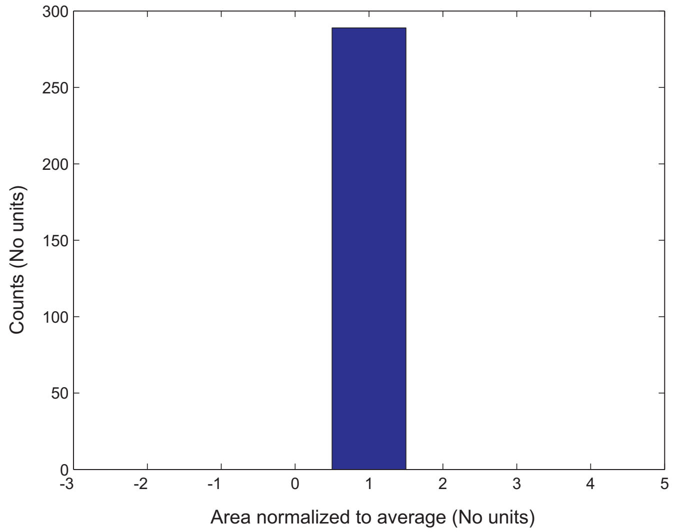

(a) Histogram of domain areas after counting 289 square areas in the grid, normalized to expected value

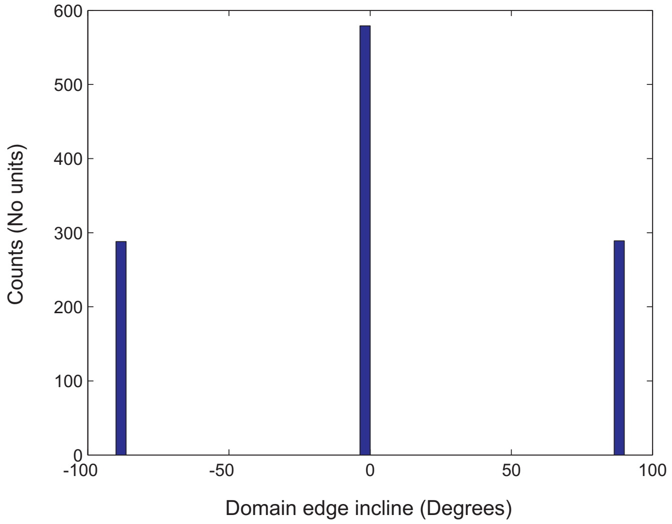

(b) Histogram of domain side angle distribution after counting 289 square grid lattice polygons

FIGURE A.13: Statistical Data for Square Grid.

For a simple square grid domain the expected results for the area of the tiles all have the same area and hence the domain area histogram would only have one column (Figure A.13a). The angle distribution histogram is also as expected with results for the domain sides only for 0, 90 and -90 degrees. 90 and -90 angle distributions are exactly half of the 0 degree distribution (Figure A.13b).

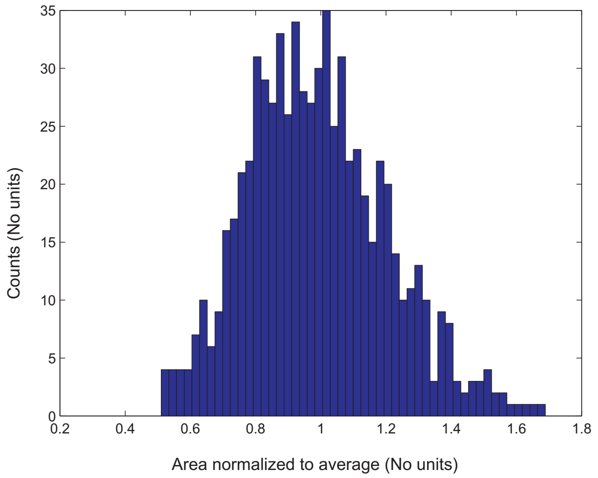

(a) Histogram of domain areas after counting 703 semi-random lattice polygons normalized to expected value.

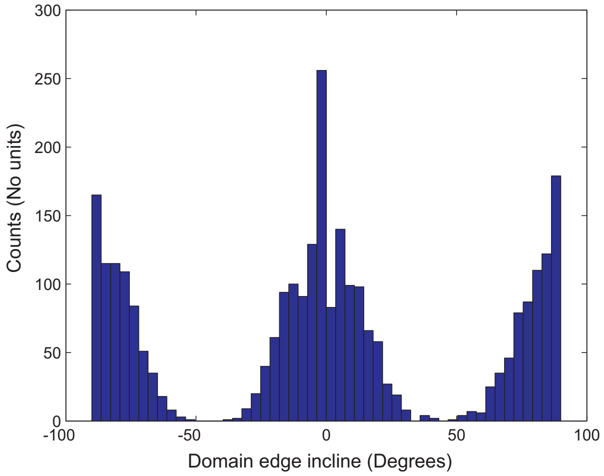

(b) Histogram of domain side angles after counting 703 semi-random lattice polygons

Figure A.14: Statistical Data for Semi-Random Polygons.

For the semi-random polygons we see a small and controlled spread for the areas. It resembles a bounded gaussian profile because not all the areas between domains are exactly equal and the spread is created by the controlled repositioning of the square lattice points (Figure A.14a). The resemblance to the square grid is more pronounced when observing the angle distribution, whose maxima coincide with that of the square grid (Figure A.13 b). There is a small spread of angles around the main 3 angles observed in the quare grid 0, 90 and -90 (Figure A.14 b) because the points are allowed to move controllably around those of the square grid.

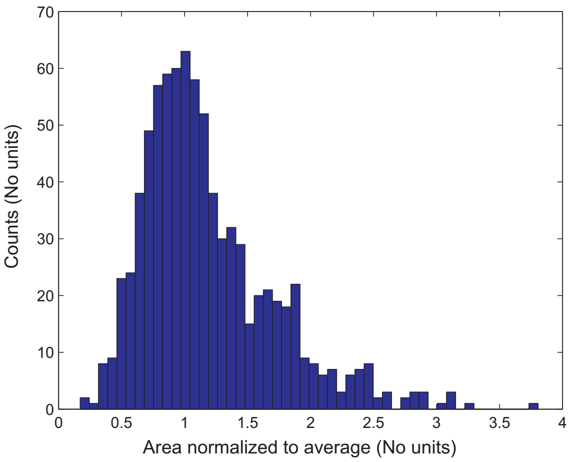

(a) Histogram of domain areas after counting 820 Voronoi polygons normalized to expected value

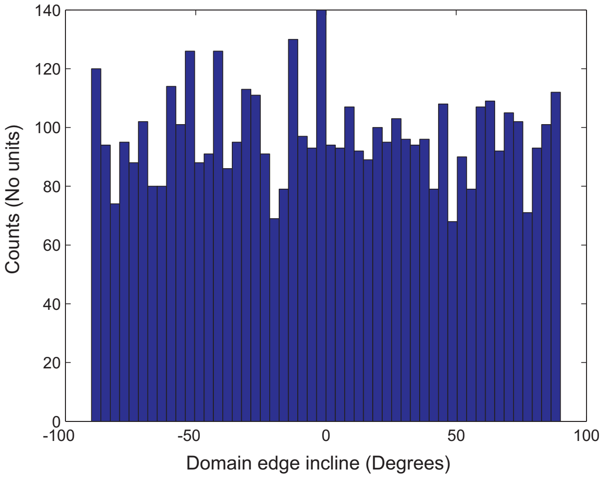

(b) Histogram of domain side angle after counting 820 Voronoi polygons

Figure A.15: Statistical Data for Voronoi Polygons.

For the Voronoi polygons we see a totally gaussian behaviour Figure A.15(a) with a much higher upper bound for the maximum domain created. The total spread of areas is much larger than the semi-random lattice method. The shape of the curve more closely resembles a gaussian because of the way that the domains are created, which is more random than the semi-random square-grid based technique (Figure A.14a). Also, the number of sides in each domain is not restricted to 4 but depends on the amount of closest neighbors each domain growth point has. This allows for a more random distribution of sides as can be shown in the angle histogram which is much flatter than the previous method shown.

The strong points of this method are that the distribution of domain side angles is almost totally random. However, the spread of angles is much larger than the previous method. This method essentially does not have a limit for the maximum domain size.

A.6.1 Conclusions

None of the techniques used to tessellate the surface satisfies the two specifications set exactly, even though the altered Voronoi method comes very close. Ideally, we require a method that will tessellate the surface into domains with an even spread of surface areas around a modal value, and also the angles of the sides of these domains have to be as varied as possible.

Tessellating the plane via Voronoi polygons largely satisfies the need for a flat angle distribution, but the semi-random square-grid produces a tighter and more symmetric distribution of polygon areas around the expected value. The ideal solution would be a trade-off between the two methods used.

In order to compensate for the drawbacks of both techniques a new technique has been conceived and is currently under development. If there is time, this will be included in the design patterns. The ultimate goal is to create a tight spread of areas without using a square grid base, and a large distribution of angles without starting from a totally random Voronoi surface.

Bibliography

[1] M. Loster. Global solar irradiance data. Study published online: http://www.ez2c.de/ml/solar_land_area (Accessed: 12/12/2007).

[2] Center for energy and processes. Ecole des mines de paris / armines / cnrs. http://sunstrides.org/?q=content/research (Accessed: 15/12/2007).

[3] BP Statistical Review of World Energy, 2010.

[4] IEA. International energy agency key world statistics 2009. http://www.iea.org/textbase/nppdf/free/2009/key stats 2009.pdf (Accessed: 16/12/2009).

[5] Bp grid parity article. http://www.bp.com/genericarticle.do? categoryId=9013609&contentId=7005395 (Accessed: 12/12/2007).

[6] L. Wissing. National survey report of pv power applications in germany. International Energy Agency Co-operative Programme on Photovoltaic Power Systems, 2006.

[7] IEA PV Power Update August 2010. http://www.iea-pvps.org/fileadmin/dam/public/report/statistics/tr 2009 neu.pdf (Accessed: 12/9/2009).

[8] EurObservER barometer 2009. http://www.eurobserv-er.org/pdf/baro196.pdf (Accessed: 10/6/2009).

[9] Bloomberg. New energy finance. http://www.nature.com/news/2009/090805/full/460677c.html (Accessed: 12/09/2009).

[10] J. Zhao, A. Wang, P. Altermatt, S. Wenham, and M. Green. 24% efficient perl silicon solar cell: Recent improvements in high efficiency silicon cell research. *Solar Energy Materials and Solar Cells*, 41-42:87–99, 1996.

[11] M. A. Green. *Third Generation Photovoltaics Advanced Solar Energy Conversion.* Springer, 2003.

[12] T. Yanagisawa. Long-term degradation tests of amorphous silicon solar cells: correlation between light and current-induced degradation characteristics. *Microelectronics Reliability*, 35:183–187, 1995.

[13] NREL. The air mass 1.5 solar spectrum. Data acquired from: http://rredc.nrel.gov/solar/models/spectral/spectrl2/ (Accessed: 10/7/2007), 2009.

[14] S.M.Sze. *Semiconductor devices*. John Wiley, 2002.

[15] S. Deb and H. Saha. Secondary ionisation and its possible bearing on the performance of a solar cell. *Solid-State Electronics*, 15:1389–1391, 1972.

[16] C. F. Klingshirm. *Semiconductor Optics*. Springer-Verlag, 1995.

[17] R. Ross and A. Nozik. Efficiency of hot-carrier solar energy converters. *Journal of Applied Physics*, 53:3813–3818, 1982.

[18] Infinite Optics. Single layer antireflection coatings. Online published data: http://www.infiniteoptics.com/IOIcolor_AR&UV.pdf (Accessed: 19/01/2010).

[19] E. Terayama. Antireflection film, U.S Patent No: 7,773,301 B2, 2010.

[20] K. Muratomi. Multi-layered antireflection film preventing reflection at two wavelength regions, US Patent No 4,997,241, 1991.

[21] S. A. Boden and D. M. Bagnall. Sunrise to sunset optimization of thin film antireflective coatings for encapsulated, planar silicon solar cells. *Progress in Photovoltaics: Research and Applications*, 17(4):241–252, 2009.

[22] S.J. Wilson and M.C. Hutley. The optical properties of 'moth-eye' antireflection surfaces. *Optica Acta*, 29:993–1009, 1982.

[23] J. Haynos, J. Allison, R. Arndt, and A. Meulenberg. The comsat nonreflective silicon solar cell: A second generation improved cell. *International Conference on Photovoltaic Power Generation*, page 487, 1974.

[24] M.A. Green, A. Wang, and S.R. Wenham. Very high efficiency silicon solar cells-science and technology. *IEEE Transactions on Electron Devices*, 46(10):1940–1947, 1999.

[25] Asahi Glass. A textured surface film traps light, enables highly efficient solar cell. Online published data: http://www.agc.co.jp/english/rd/topics_04.html (Accessed: 21/01/2010).

[26] L. Abenante. Optical path length factor at near-bandgap wavelengths in si solar cells. *IEEE Transactions on Electron Devices*, 53:3047–3053, 2006.

[27] G.A. Rao and S.P. Mahulikar. Integrated review of stealth technology and its role in airpower. *Aeronautical Journal*, 106:629–641, 2002.

[28] W.F. Bahret. The beginnings of stealth technology. *IEEE Transactions on Aerospace and Electronic Systems*, 29(4):1377–1385, 1993.

[29] C.G. Bernard. Structural and functional adaptation in a visual system. *Endeavour*, 26:79–84, 1967.

[30] P.B. Caplam and M. C. Hutley. Reduction of the lends reflection by the moth-eye principle. *Nature*, 244:281–282, 1973.

[31] S.A. Boden and D.M. Bagnall. Tunable reflection minima of nanostructured antireflective surfaces. *Applied Physics Letters*, 93:133108, 2008.

[32] W. H. Southwell. Gradient-index antireflection coatings. *Optics Letters*, 8:584586, 1983.

[33] W. H. Southwell. Pyramid-array surface-relief structures producing antireflection index matching on optical surfaces. *Journal of the Optical Society of America A*, 8:549–553, 1991.

[34] D Macdonald, A. Cuevas, M. J. Kerr, C. Samundsett, D. Ruby, S. Winderbaum, and A. Leo. Texturing industrial multicrystalline silicon solar cells. *Solar Energy*, 76(1-3):277–283, 2004.

[35] J. Zhao, A. Wang, M. A. Green, and F. Ferrazza. 19.8% efficient 'honeycomb' textured multicrystalline and 24.4% monocrystalline silicon solar cells. *Applied Physics Letters*, 73(14):1991–1994, 1998.

[36] D.L. King and M.E. Buck. Experimental optimization of an anisotropic etching process for random texturization of silicon solar cells. In *The Conference Record of the Twenty-Second IEEE Photovoltaic Specialists Conference - 1991*, volume 1, pages 303–308. IEEE, 1991.

[37] P. Campbell and M. A. Green. Light trapping properties of pyramidally textured surfaces. *Journal of Applied Physics*, 62(1):243–250, 1987.

[38] R. Brendel, H. Artmann, S. Oelting, W. Frey, J.H. Werner, and H.J. Queisser. Monocrystalline si waffles for thin solar cells fabricated by the novel perforated-silicon process. *Applied Physics A: Materials Science and Processing*, 67(2):151–154, 1998.

[39] R. Brendel, R. Auer, and H. Artmann. Textured monocrystalline thin-film si cells from the porous silicon (psi) process. *Progress in Photovoltaics: Research and Applications*, 9(3):217–221, 2001.

[40] C-H Sun, W-L Min, N. C. Linn, P. Jiang, and B. Jiang. Templated fabrication of large area subwavelength antireflection gratings on silicon. *Applied Physics Letters*, 91(23):231105, 2007.

[41] P. Papet, O. Nichiporuk, A. Kaminski, Y. Rozier, J. Kraiem, J. Lelievre, A. Chaumartin, A. Fave, and M Lemiti. Pyramidal texturing of silicon solar cell with tmah chemical anisotropic etching. *Solar Energy Materials and Solar Cells*, 90(15):2319–2328, 2006.

[42] J. An, S. Yang, Z. Liu, R. Cui, T. Sun, T. Chen, J. Wang, X. Xu, J. Wang, J. Huang, X. Li, C. Wu, and J. Du. The influence of nh4f on silicon etching in hf/hno3/h2o system. In *Proceedings of ISES World Congress*, 2007.

[43] M.J. Stocks, A.J. Carr, and A.W. Blakers. Texturing of polycrystalline silicon solar cells. In *Proceedings of 1994 IEEE 1st World Conference on Photovoltaic Energy Conversion - WCPEC (A Joint Conference of PVSC, PVSEC and PSEC)*, pages 1551–1554. IEEE, 1994.

[44] Y. Nishimoto. Investigation of acidic texturization for multicrystalline silicon solar cells. *Journal of The Electrochemical Society*, 146(2):457–461, 1999.

[45] K. Tsujino, M. Matsumura, and Y. Nishimoto. Texturization of multicrystalline silicon wafers for solar cells by chemical treatment using metallic catalyst. *Solar Energy Materials and Solar Cells*, 90(1):100–110, 2006.

[46] S. Koynov, M. S. Brandt, and M. Stutzmann. Black nonreflecting silicon surfaces for solar cells. *Applied Physics Letters*, 88(20):203107, 2006.

[47] M. Abbott and J. Cotter. Optical and electrical properties of laser texturing for high-efficiency solar cells. *Progress in Photovoltaics: Research and Applications*, 14(3):225–235, 2006.

[48] J. C. Zolper, S. Narayanan, S. R. Wenham, and M. A. Green. 16.7silicon solar cell. *Applied Physics Letters*, 55(22):2363–2365, 1989.

[49] H. Bender, J. Szlufcik, H. Nussbaumer, G. Palmers, O. Evrard, J. Nijs, R. Mertens, E. Bucher, and G. Willeke. Polycrystalline silicon solar cells with a mechanically formed texturization. *Applied Physics Letters*, 62(23):2941–2944, 1993.

[50] H. Nakaya, M. Nishida, Y. Takeda, S. Moriuchi, T. Tonegawa, T. Machida, and T. Nunoi. Polycrystalline silicon solar cells with v-grooved surface. *Solar Energy Materials and Solar Cells*, 34(1-4):219–225, 1994.

[51] D. S. Ruby, S. H. Zaidi, S. Narayanan, Benjamin Mark Damiani, and Ajeet Rohatgi. Rie-texturing of multicrystalline silicon solar cells. In *12th International Photovoltaic Science and Engineering Conference*, Jeju Island, Korea, 2001.

[52] W. Nositschka, C. Beneking, O. Voigt, and H. Kurz. Texturisation of multicrystalline silicon wafers for solar cells by reactive ion etching through colloidal masks. *Solar Energy Materials and Solar Cells*, 76(2):155–166, March 2003.

[53] Y. Inomata. Surface texturing of large area multicrystalline silicon solar cells using reactive ion etching method. *Solar Energy Materials and Solar Cells*, 48(1-4):237–242, 1997.

[54] V. G. Veselago. The electrodynamics of substances with simulataneously negative values of ϵ and μ. *Soviet Physics Uspekhi*, 10(4):509–514, 1968.

[55] J. Pendry, A. Holden, W. Stewart, and I. Youngs. Extremely low frequency plasmons in metallic mesostructures. *Physical Review Letters*, 76(25):4773–4776, 1996.

[56] J.B. Pendry, A.J. Holden, D.J. Robbins, and W.J. Stewart. Magnetism from conductors and enhanced nonlinear phenomena. *IEEE Transactions on Microwave Theory and Techniques*, 47(11):2075–2084, 1999.

[57] D. Smith, Willie Padilla, D. Vier, S. Nemat-Nasser, and S. Schultz. Composite medium with simultaneously negative permeability and permittivity. *Physical Review Letters*, 84(18):4184–4187, 2000.

[58] R. A. Shelby, D. R. Smith, and S. Schultz. Experimental verification of a negative index of refraction. *Science (New York, N.Y.)*, 292(5514):77–79, 2001.

[59] J. Pendry. Negative refraction makes a perfect lens. *Physical Review Letters*, 85(18):3966–3969, 2000.

[60] J. B. Pendry and S. A. Ramakrishna. Focusing light using negative refraction. *Journal of Physics: Condensed Matter*, 15(37):6345–6364, 2003.

[61] J. Monzon, A. Barriuso, and L. Sanchezsoto. Perfect antireflection via negative refraction. *Physics Letters A*, 349(1-4):281–284, 2006.

[62] J. A. Dobrowolski, Y. Guo, T. Tiwald, P. Ma, and D. Poitras. Toward perfect antireflection coatings. 3. experimental results obtained with the use of reststrahlen materials. *Applied Optics*, 45(7):1555–1562, 2006.

[63] D. Poitras and J. A. Dobrowolski. Toward perfect antireflection coatings. 2. theory. *Applied Optics*, 43(6):1286, 2004.

[64] J. A. Dobrowolski, Daniel Poitras, Penghui Ma, Himanshu Vakil, and Michael Acree. Toward perfect antireflection coatings: Numerical investigation. *Applied Optics*, 41(16):3075–3083, 2002.

[65] R. Capt. Sabatini. Tactical laser systems performance analysis in various weather conditions. In *RTO SET Symposium on "E-O propagation, signature and system performance under adverse meteorological conditions considering out of area operations"*, pages 29–1,29–13, 1998.

[66] S. A. Boden and D. M. Bagnall. Optimization of moth-eye antireflection schemes for silicon solar cells. *Progress in Photovoltaics: Research and Applications*, 18:195–203, 2010.

[67] E. G. Loewen and E. Popov. *Diffraction gratings and applications.* Marcel Dekker Inc, 1997.

[68] M. Neviere and E. Popov. Grating electomagnetic theory 'user guide'. *Journal of Imaging Science and Technology*, 41:315–323, 1997.

[69] M. Neviere and E. Popov. *Light Propagation in Periodic Media.* Marcel Dekker Inc, 2003.

[70] J. M. Jarem and P. P. Banerjee. *Computational Methods for Electromagnetic and Optical Systems.* Marcel Dekker, 2000.

[71] Inc RSoft Design Group. *Diffract MOD 3.0 User Guide.* 2007.

[72] M.G. Moharam, D.A. Pommet, E.B. Grann, and T.K. Gaylord. Stable implementation of the rigorous coupled-wave analysis for surface relief gratings: enhanced transmittance matrix approach. *Journal of the Optical Society of America A*, 12:1077–1086, 1995.

[73] M. G. Moharam, E. B. Grann, D. A. Pommet, and T. K. Gaylord. Formulation for stable and efficient implementation of rigorous coupled-wave analysis of binary gratings. *Journal of the Optical Society of America A*, 12(5):1068–1076, 1995.

[74] M. A. Green and M. J. Keevers. Optical properties of intrinsic silicon at 300 k. *Progress in Photovoltaics: Research and Applications*, 3(3):189–192, 1995.

[75] M. Born and Emil W. *Principles of Optics.* Cambridge, 1999.

[76] H. Nagel, A. G. Aberle, and R. Hezel. Optimized antireflection coatings for planar silicon solar cells using remote pecvd silicon nitride and porous silicon dioxide. *Progress in Photovoltaics: Research and Applications*, 32:245–260, 1999.

[77] M. Senechal. Tilings, diffraction, and quasicrystals. *The Mathematica Journal*, 4(2):10–15, 1994.

[78] J.M. Cowley. *Diffraction Physics.* North Holland, 3rd edition, 1995.

[79] M.D. Abramoff, P.J. Magelhaes, and S.J. Ram. Image Processing with ImageJ. *Biophotonics International*, 11(7):36–42, 2004.

[80] S. W. Smith. *The Scientist and Engineer's Guide to Digital Signal Processing.* California Technical Publishing, 1997.

[81] R-J. Hauy. *Traite de cristallogrphie.* Bachelier et Huzard, 1822.

[82] F. Jarai-Szabo, S. Astilean, and Z. Neda. Understanding self-assembled nanosphere patterns. *Chemical Physics Letters*, 408:241–246, 2005.

[83] C-H Sun, P. Jiang, and B. Jiang. Broadband moth-eye antireflection coatings on silicon. *Applied Physics Letters*, 92:061112, 2008.

[84] Y. Kanamori, M. Sasaki, and K. Hane. Broadband antireflection gratings fabricated upon silicon substrates. *Optics Letters*, 24(20):1422–1424, 1999.

[85] Q. Chen, G. Hubbard, P. A. Shields, C. Liu, D. W. E. Allsopp, W. N. Wang, and S. Abbott. Broadband moth-eye antireflection coatings fabricated by low-cost nanoimprinting. *Applied Physics Letters*, 94(26):263118, 2009.

[86] D. Shechtman and I. Blech. Metallic phase with long-range orientational order and no translational symmetry. *Physical Review Letters*, 53:1951–1953, 1984.

[87] M. Senechal. *Crystalline Symmetries: An informal Mathematical Introduction.* Adam Hilger, 1990.

[88] H. Wang. Proving theorems by pattern recognitionII. *Bell System Technical Journal*, 40(1):1–41, 1961.

[89] R. Berger. The undecidability of the domino problem. *Memoirs of the American Mathematical Society*, 66:1–72, 1966.

[90] M. E. Pollard and G. J. Parker. Low-contrast bandgaps of a planar parabolic spiral lattice. *Optics Letters*, 34:2805–2807, 2009.

[91] M.E. Zoorob, M.D. Charlton, G.J. Parker, J.J. Baumberg, and M.C. Netti. Complete photonic bandgaps in 12-fold symmetric quasicrystals. *Nature*, 404(6779):740–743, 2000.

[92] M Senechal. *Quasicrystals and Geometry.* Cambridge University Press, 1996.

[93] G. J. Parker, M. D. B. Charlton, M. E. Zoorob, J. J. Baumberg, M. C. Netti, and T. Lee. Highly engineered mesoporous structures for optical processing. *Philosophical Transactions: Mathematical, Physical and Engineering Sciences*, 364:189–199, 2006.

[94] H. Vogel. A better way to construct the sunflower head. *Mathematical Biosciences*, 44:179–189, 1979.

[95] J. Asmussen and B. Wright. Highly-oriented diamond substrates. http://kmf.pa.msu.edu/Research/resrch06.asp (Accessed: 3/5/2008).

[96] Y. Xia and G. M. Whitesides. Soft lithography. *Annual Review of Materials Science*, 28(1):153–184, 1998.

[97] C. L. Cheung, R. J. Nikolic, C. E. Reinhardt, and T. F. Wang. Fabrication of nanopillars by nanosphere lithography. *Nanotechnology*, 17:13391343, 2006.

[98] S-H. Park, C. Pistol, S.-J. Ahn, J. H. Reif, A. Lebeck, C. Dwyer, and T.H. LaBean. Finite-size, fully-addressable dna tile lattices formed by hierarchical assembly procedures. *Angewandte Chemie International Edition*, 45:735–739, 2006.

[99] H.W. Deckman and J.H. Dunsmuir. Natural lithography. *Applied Physics Letters*, 41:377–380, 1982.

[100] A. van Blaaderen, R. Ruel, and P. Wiltzius. Template-directed colloidal crystallization. *Nature*, 385(6614):321–324, 1997.

[101] M. E. Kiziroglou, X. Li, D. C. Gonzalez, C. H. de Groot, A. A. Zhukov, P. A. J. de Groot, and P. N. Bartlett. Orientation and symmetry control of inverse sphere magnetic nanoarrays by guided self-assembly. *Journal of Applied Physics*, 100:113720, 2006.

[102] J. C. Hulteen and R. P. Van Duyne. Nanosphere lithography: A materials general fabrication process for periodic particle array surfaces. *Journal of Vaccum Science and Technology A*, 13:1553–1558, 1995.

[103] L Pallavidino, D Razo, F Geobaldo, A Balestreri, D Bajoni, M Galli, L Andreani, C Ricciardi, E Celasco, and M Quaglio. Synthesis, characterization and modelling of silicon based opals. *Journal of Non-Crystalline Solids*, 352(9-20):1425–1429, June 2006.

[104] A. Stein and R. C. Schroden. Colloidal crystal templating of three-dimensionally ordered macroporous solids: materials for photonics and beyond. *Current Opinion in Solid State and Materials Science*, 5(6):553–564, 2001.

[105] T Prasad, R Rengarajan, D Mittleman, and V Colvin. Advanced photonic crystal architectures from colloidal self-assembly techniques. *Optical Materials*, 27(7):1250–1254, 2005.

[106] G. A. Ozin and S. M. Yang. The Race for the Photonic Chip: Colloidal Crystal Assembly in Silicon Wafers. *Advanced Functional Materials*, 11(2):95–104, 2001.

[107] S. Arpiainen, F. Jonsson, J. R. Dekker, G. Kocher, W. Khunsin, C M. S. Torres, and J. Ahopelto. Site-Selective Self-Assembly of Colloidal Photonic Crystals. *Advanced Functional Materials*, 19(8):1247–1253, 2009.

[108] Z. Zheng, X. Liu, Y. Luo, B. Cheng, D. Zhang, Q. Meng, and Y. Wang. Pressure controlled self-assembly of high quality three-dimensional colloidal photonic crystals. *Applied Physics Letters*, 90(5):051910, 2007.

[109] G. H. Chan, J. Zhao, E. M. Hicks, G. C. Schatz, and R. P. Van Duyne. Plasmonic properties of copper nanoparticles fabricated by nanosphere lithography. *Nano Letters*, 7(7):1947–1952, 2007.

[110] T. R. Jensen, M. D. Malinsky, C. L. Haynes, and R. P. Van Duyne. Nanosphere lithography: Tunable localized surface plasmon resonance spectra of silver nanoparticles. *The Journal of Physical Chemistry B*, 104(45):10549–10556, 2000.

[111] C. L. Haynes and R. P. Van Duyne. Nanosphere Lithography: A Versatile Nanofabrication Tool for Studies of Size-Dependent Nanoparticle Optics. *The Journal of Physical Chemistry B*, 105(24):5599–5611, 2001.

[112] C. L. Haynes, A. D. McFarland, M. T. Smith, J. C. Hulteen, and R. P. Van Duyne. Angle-Resolved Nanosphere Lithography: Manipulation of Nanoparticle Size, Shape, and Interparticle Spacing. *The Journal of Physical Chemistry B*, 106(8):1898–1902, 2002.

[113] J. C. Hulteen, D. A. Treichel, M. T. Smith, M. L. Duval, T. R. Jensen, and R. P. Van Duyne. Nanosphere lithography: Size-tunable silver nanoparticle and surface cluster arrays. *Journal of Physical Chemistry B*, 103:3854–3863, 1999.

[114] K. H. Baek, J. H. Kim, K. B. Lee, H. S. Ahnn, and C. S. Yoon. Surface Plasmon Resonance Tuning of Silver Nanoparticle Array Produced by Nanosphere Lithography Through Ion Etching and Thermal Annealing. *Journal of Nanoscience and Nanotechnology*, 10(5):3118–3122, 2010.

[115] A. J Haes, J. Zhao, S. Zou, C. S. Own, L. D. Marks, G. C. Schatz, and R. P. Van Duyne. Solution-Phase, Triangular Ag Nanotriangles Fabricated by Nanosphere Lithography. *Journal of Physical Chemistry B*, 109:11158–11162, 2005.

[116] Y. Zhang, X. Wang, Y. Wang, H. Liu, and J. Yang. Ordered nanostructures array fabricated by nanosphere lithography. *Journal of Alloys and Compounds*, 452:473–477, 2008.

[117] M.E. Abdelsalam, P.N. Bartlett, J.J. Baumberg, and S. Coyle. Preparation of Arrays of Isolated Spherical Cavities by Self-Assembly of Polystyrene Spheres on Self-Assembled Pre-patterned Macroporous Films. *Advanced Materials*, 16(1):90–93, 2004.

[118] X. Zhang, A. V. Whitney, J. Zhao, E. M. Hicks, and Richard P. Van Duyne. Advances in Contemporary Nanosphere Lithographic Techniques. *Journal of Nanoscience and Nanotechnology*, 6(7):1920–1934, 2006.

[119] H. Xu, N. Lu, D. Qi, L. Gao, J. Hao, Y. Wang, and L. Chi. Broadband antireflective si nanopillar arrays produced by nanosphere lithography. *Microelectronic Engineering*, 86(4-6):850–852, 2009.

[120] X. Y. Ling, C. Acikgoz, I. Y. Phang, M. A. Hempenius, D. N. Reinhoudt, G. J. Vancso, and J. Huskens. 3D ordered nanostructures fabricated by nanosphere lithography using an organometallic etch mask. *Nanoscale*, 2(8):1455–1460, 2010.

[121] C. F. Chau and T. Melvin. The fabrication of macroporous polysilicon by nanosphere lithography. *Journal of Micromechanics and Microengineering*, 18(6):064012, 2008.

[122] C Zhou and D Gall. Surface patterning by nanosphere lithography for layer growth with ordered pores. *Thin Solid Films*, 516(2-4):433–437, 2007.

[123] M. M. W. Muscatello, L. E. Stunja, and S. A. Asher. Polymerized crystalline colloidal array sensing of high glucose concentrations. *Analytical Chemistry*, 81(12):4978–4986, 2009.

[124] J Zhu, C-M Hsu, Z Yu, S Fan, and Y Cui. Nanodome solar cells with efficient light management and self-cleaning. *Nano letters*, 10(6):1979–1984, 2010.

[125] M. Albrecht, G. Hu, I. L. Guhr, T. C. Ulbrich, J. Boneberg, P. Leiderer, and G. Schatz. Magnetic multilayers on nanospheres. *Nature materials*, 4(3):203–206, 2005.

[126] S. P. Li, W. S. Lew, Y. B. Xu, A. Hirohata, A. Samad, F. Baker, and J. A. C. Bland. Magnetic nanoscale dots on colloid crystal surfaces. *Applied Physics Letters*, 76(6):748–751, 2000.

[127] S. M. Weekes, F. Y. Ogrin, W. A. Murray, and P. S. Keatley. Macroscopic arrays of magnetic nanostructures from self-assembled nanosphere templates. *Langmuir*, 23:1057–1060, 2007.

[128] J. N. Anker, W. P. Hall, O. Lyandres, N. C. Shah, J. Zhao, and R. P. Van Duyne. Biosensing with plasmonic nanosensors. *Nature materials*, 7(6):442–453, 2008.

[129] A. J. Haes, S. Zou, G. C. Schatz, and R. P. Van Duyne. Nanoscale Optical Biosensor: Short Range Distance Dependence of the Localized Surface Plasmon Resonance of Noble Metal Nanoparticles. *The Journal of Physical Chemistry B*, 108(22):6961–6968, 2004.

[130] S. Xu, G. Tu, B. Peng, and X. Han. Self-assembling gold nanoparticles on thiol-functionalized poly(styrene-co-acrylic acid) nanospheres for fabrication of a mediatorless biosensor. *Analytica chimica acta*, 570(2):151–157, 2006.

[131] J. W. Long, B. Dunn, D. R. Rolison, and H. S. White. Three-Dimensional Battery Architectures. *Chemical Reviews*, 104(10):4463–4492, 2004.

[132] J. Cheng, W. Jung, and C. Ross. Magnetic nanostructures from block copolymer lithography: Hysteresis, thermal stability, and magnetoresistance. *Physical Review B*, 70(6):064417, 2004.

[133] M. Totzeck, W. Ulrich, A. Gohnermeier, and W. Kaiser. Semiconductor fabrication: Pushing deep ultraviolet lithography to its limits. *Nature Photonics*, 1:629–631, 2007.

[134] L.R Harriot. Limits of lithography. *Proceedings of IEEE*, 89(4):366–374, 2001.

[135] E.-B. Kley and B. Schnabel. E-beam lithography: a suitable technology for fabrication of high-accuracy 2d and 3d surface profiles. *Proceedings of SPIE*, 2640:71–80, 1995.

[136] M. D. Austin, H. Ge, W. Wu, M. Li, Z. Yu, D. Wasserman, S. A. Lyon, and S. Y. Chou. Fabrication of 5nm linewidth and 14nm pitch features by nanoimprint lithography. *Applied Physics Letters*, 84(26):5299–5301, 2004.

[137] G. Hubbard, S.J. Abbott, Q. Chen, D.W.E. Allsopp, W.N. Wang, C.R. Bowen, R. Stevens, A. Šatka, D. Haško, and F. Uherek. Wafer-scale transfer of nanoimprinted patterns into silicon substrates. *Physica E: Low-dimensional Systems and Nanostructures*, 41(6):1118–1121, 2009.

[138] Y. K. Koh, L. K. Teh, and C. C. Wong. Defects in self assembled colloidal crystals. *Dspace Online Repository at Massachusetts Institute of Technology (MIT)*, 2004.

[139] R. Micheletto, H. Fukuda, and M. Ohtsu. A simple method for the production of a two-dimensional, ordered array of small latex particles. *Langmuir*, 11:3333–3336, 1995.

[140] S. O. Lumsdon, E. W. Kaler, J. P. Williams, and O. D. Velev. Dielectrophoretic assembly of oriented and switchable two-dimensional photonic crystals. *Applied Physics Letters*, 82:949–951, 2003.

[141] M. Holgado, F. Garcia-Santamaria, A. Blanco, M. Ibisate, A. Cintas, H. Miguez, C. J . Serna, C. Molpeceres, J. Requena, A. Mifsud, F. Meseguer, and C. Lopez. Electrophoretic deposition to control artificial opal growth. *Langmuir*, 15:4701–4704, 1999.

[142] M. G. Nikolaides, A. R. Bausch, M. F. Hsu, A. D. Dinsmore, M. P. Brenner, and D. A. Weitz. Electric-field-induced capillary attraction between like-charged particles at liquid interfaces. *Nature*, 420:299–301, 2002.

[143] P. I. Stavroulakis, N. Christou, and D. Bagnall. Improved deposition of large scale ordered nanosphere monolayers via liquid surface self-assembly. *Materials Science and Engineering: B*, 165:186–189, 2009.

[144] N.D. Denkov, O.D. Velev, P.A. Kralchevsky abd I.B. Ivanov, H. Yoshimura, and K.Nagayama. Mechanism of formation of two-dimensional crystals from latex particles on substrates. *Langmuir*, 8:3183–3190, 1992.

[145] C. Haginoya, M. Ishibashi, and K. Koike. Nanostructure array fabrication with a size-controllable natural lithography. *Applied Physics Letters*, 71:2934–2936, 1997.

[146] A.F. Stalder, G. Kulik, D. Sage, L. Barbieri, and P. Hoffmann. A snake-based approach to accurate determination of both contact points and contact angles. *Colloids And Surfaces A: Physicochemical And Engineering Aspects*, 286:92–103, 2006.

[147] V. I. Roldughin. Self-assembly of nanoparticles at interfaces. *Russian Chemical Reviews*, 73:115–145, 2004.

[148] F. Jarai-Szabo, Z. Neda, C Farcau A Astilean, and A Kuttesch. Shake-induced order in nanosphere systems. *European Physical Journal E*, 23:153–159, 2007.

[149] K.N. Liou. *An Introduction to Atmospheric Radiation.* Academic Press, 2002.

[150] C.F. Bohren and D. Huffman. *Absorption and scattering of light by small particles.* John Wiley, New York, 1983.

[151] P.I. Stavroulakis. Using self-assembly nanofabrication methods to increase the efficiency of solar cells by enabling mass production of anti-reflective 'moth-eye' structures. Part IV Individual Research Project, University of Southampton, 2007.

[152] R. Hsiao and J. Carr. Si/sio2 etching in high density sf6/chf3/o2 plasma. *Materials Science and Engineering B*, 52(1):63–77, 1998.

[153] E. Gogolides, S. Grigoropoulos, and A. G. Nassiopoulos. Highly anisotropic room-temperature sub-half-micron si reactive ion etching using fluorine only containing gases. *Microelectronic Engineering*, 27:449–452, 1995.

[154] M. J. Cooke and J. Pelletier. Self-biasing effects on plasma etching characteristics of si and sio2. *Applied Physics Letters*, 53(1):19, 1988.

[155] T. K Gaylord, W E Baird, and M G Moharam. Zero-reflectivity high spatial-frequency rectangular-groove dielectric surface-relief gratings. *Applied Optics*, 25:4562–4567, 1986.

[156] R. Syms and J. Cozens. *Optical guided waves and devices, p376.* McGraw-Hill Book Company, 1992.

[157] M.G. Moharam and T.K. Gaylord. Rigorous coupled-wave analysis of metallic surface-relief gratings. *Journal of the Optical Society of America*, 3:1780–1787, 1986.

[158] S. Fan, P. Villeneuve, J. Joannopoulos, and E. Schubert. High extraction efficiency of spontaneous emission from slabs of photonic crystals. *Physical Review Letters*, 78(17):3294–3297, 1997.

[159] R. O. Prum. Anatomically diverse butterfly scales all produce structural colours by coherent scattering. *Journal of Experimental Biology*, 209(4):748–765, 2006.

[160] M. Mihailescu, A. Preda, D. Cojoc, E. Scarlat, and L. Preda. Diffraction patterns from a phyllotaxis-type arrangement. *Optics and Lasers in Engineering*, 46(11):802–809, 2008.

[161] M. Born and E. Wolf. *Principles of Optics*. Cambridge University Press, 7th edition, 2002.

[162] C-J Ting, C-F Chen, and C.P. Chou. Subwavelength structures for broadband antireflection application. *Optics Communications*, 282(3):434–438, 2009.

[163] Y M Song, H J Choi, J S Yu, and Y T Lee. Design of highly transparent glasses with broadband antireflective subwavelength structures. *Optics Express*, 18(12):13063–13071, 2010.

[164] M C. Putnam, S W. Boettcher, M D. Kelzenberg, D B. Turner-Evans, J M. Spurgeon, E L. Warren, R M. Briggs, N S. Lewis, and H A. Atwater. Si microwire-array solar cells. *Energy and Environmental Science*, 3(8):1037–1041, 2010.

[165] Y. L. Wu. *Control over colloidal crystallization by shear and electric fields*. PhD thesis, Universitat Utrecht, 2007.

[166] A.S. Dimitrov and K. Nagayama. Continuous convective assembling of fine particles into two-dimensional arrays on solid surfaces. *Langmuir*, 12:1303–1311, 1996.

[167] Wikipedia. Voronoi diagram. http://en.wikipedia.org/wiki/Voronoi (Accessed: 12/12/2007).

[168] P. Ashburn and G. Parker. Elec 3024 materials and processing of devices course lecture notes. University of Southampton, 2006.

[169] J. S. Biteen, N. S. Lewis, H. A. Atwater, H. Mertens, and A. Polman. Spectral tuning of plasmon-enhanced silicon quantum dot luminescence. *Applied Physics Letters*, 88:131109, 2006.

[170] S.A. Boden. Antireflection and light trapping for photovoltaics. *Nine Month Progress Report*, 2005.

[171] S. A. Boden. *Biomimetic Nanostructured Surfaces for Antireflection in Photovoltaics*. PhD thesis, Electronics and Computer Science, University of Southampton, 2009.

[172] S.A. Boden and D.M. Bagnall. Nanoimprinting for antireflective moth-eye surfaces. *PVSAT-4 Proc.*, page 141, 2008.

[173] S.A. Boden and D.M. Bagnall. Bio-mimetic subwavelength surface for near-zero reflection sunrise to sunset. In *4th World Conference on Photovoltaic Energy Conversion*, 2006.

[174] G. Cao and C. J. Brinker. *Annual Review of Nano Research, Volume 1.* World Scientific Publishing Co. Pte. Ltd., 2006.

[175] S.L. Cheng, S.W. Lu, C.H. Li, Y.C. Chang, C.K. Huang, and H. Chen. Fabrication of periodic nickel silicide nanodot arrays using nanosphere lithography. *Thin Solid Films*, 494:307–310, 2006.

[176] K. E. Davis, W. B. Russel, and W. J. Glantschnig. Settling suspensions of colloidal silica: observations and x-ray measurements. *Journal of the Chemical Society, Faraday Transactions*, 87:411–424, 1991.

[177] A. L. Fahrenbruch and R. H. Bube. *Fundamentals of solar cells : photovoltaic solar energy conversion*. New York : Academic Press, 1983.

[178] R. F. Figueroa. Control of sidewall slope in silicon vias using sf6/o2 plasma etching in a conventional reactive ion etching tool. *Journal of Vaccum Science and Technology B*, 23:2226–2231, 2005.

[179] F. Garcia-Santamaria, V. Salguerino-Maceira, C. Lopez, and L. M. Liz-Marzan. Synthetic opals based on silica-coated gold nanoparticles. *Langmuir*, 18:4519–4522, 2002.

[180] N. Green and H. Morgan. Elec6100 course lecture notes for lab on a chip. University of Southampton, 2006.

[181] C.H. De Groot. Elec 6095 nanodevices course lecture notes. University of Southampton, 2007.

[182] Z. Gu, A. Fujishima, and O. Sato. Fabrication of high-quality opal films with controllable thickness. *New York*, 14:760–765, 2002.

[183] Z. Gu, S. Kubo, W. Qian, Y. Einaga, D. A. Tryk, A. Fujishima, and O. Sato. Varying the optical stop band of a three-dimensional photonic crystal by refractive index control. *Langmuir*, 17:6751–6753, 2001.

[184] E. Hecht. *Optics*. Addison-Wesley, 2002.

[185] Y-K. Hong, H. Kim, G. Lee, W. Kim, J. Park, J. Cheon, and J-Y. Koo. Controlled two dimensional distribution of nanoparticles by spin-coating method. *Applied Physics Letters*, 80:844–846, 2002.

[186] X. Hongbo, L. Nan, Q. Dianpeng, G. Liguo, H. Juanyuan, W. Yandong, and C. Lifeng. Broadband antireflective si nanopillar arrays produced by nanosphere lithography. *Microelectronic Engineering*, 86:850–852, 2009.

[187] P. Jiang, J. F. Bertone, K. S. Hwang, and V. L. Colvin. Single-crystal colloidal multilayers of controlled thickness. *Chemistry of Materials*, 11:2132–2140, 1999.

[188] P. Jiang and M. J. McFarland. Large scale fabrication of wafer-size colloidal crystals, macroporous polymers and nanocomposites by spin-coating. *Journal of the American Chemical Society*, 126:13778–13786, 2004.

[189] T. Kanai, T. Sawada, and A. Toyotama. Air-pulse-drive fabrication of photonic crystal films of colloids with high spectral quality. *Advanced Functional Materials*, 15:25–29, 2005.

[190] H. Keppner, J. Meier, P. Torres, D. Fischer, and A. Shah. Microcrystalline silicon and micromorph tandem solar cells. *Applied Physics A*, 69:169–177, 1999.

[191] A. Kosiorek, W. Kandulski, P. Chudzinski, K. Kempa, and M. Giersig. Shadow nanosphere lithography: Simulation and experiment. *Nano Letters*, 4:1359–1363, 2004.

[192] U. Leonhardt. Invisibility cup. *Nature Photonics*, 1:207–208, 2007.

[193] Z Liu, J Ya, Y Xin, J Ma, and C Zhou. Assembly of polystyrene colloidal crystal templates by a dip-drawing method. *Journal of Crystal Growth*, 297:223–227, 2006.

[194] R. Mayoral, J. Requena, J. S. Moya, C. Lopez, A. Cintas, H. Miguez, F. Meseguer, L. Vazquez, M. Holgado, and A. Blanco. 3d long-range ordering in ein sio2 submicrometer-sphere sintered superstructure. *Advanced Materials*, 9:257–260, 1997.

[195] H. Miguez, F. Meseguer, C. Lopez, A. Blanco, J. S. Moya, J. Requena, A. Mifsud, and V. Fornes. Control of the photonic crystal properties of fcc-packed submicrometer sio2 spheres by sintering. *Advanced Materials*, 10:480–483, 1998.

[196] A. Mihi, M. Ocaña, and H. Míguez. Oriented colloidal-crystal thin films by spin-coating microspheres dispersed in volatile media. *Advanced Materials*, 18:2244–2249, 2006.

[197] T. Ogi, L. B. Modesto-Lopez, F. Iskandar, and K. Okuyama. Fabrication of large area monolayer of silica particles on a sapphire substrate by a spin coating method. *Colloids and Surfaces A: Physicochemical and Engineering Aspects*, 297:71–78, 2007.

[198] H. Onyuksel, O Koo, A. Krishnadas, V. Sethi, and I Rubstein. Nanotechnology in drug delivery. In *NSTI Nanotechnology Conference and Trade Show*, 2005.

[199] G. J. Parker, M.D.B. Charlton, M.E. Zoorob, J.J. Baumberg, M.C. Netti, and T. Lee. Highly engineered mesoporous structures for optical processing. *Royal Society*, 364:189–199, 2005.

[200] F. L. Pedrotti, L. M. Pedrotti, and L. S. Pedrotti. *Introduction to Optics*. Pearson Prentice Hall, 2007.

[201] P. Pieranski. Colloidal crystals. *Contemporary Physics*, 24:25–73, 1983.

[202] R.O. Prum and R.H. Torres. A fourier tool for the analysis of coherent light scattering by bio-optical nanostructures. *Integrative and Comparative Biology*, 43:591–602, 2003.

[203] Y. Roichman and D. G. Grier. Holographic assembly of quasicrystalline photonic heterostructures. *Optics Express*, 13:5434–5439, 2005.

[204] C.A. Ross. Patterned magnetic recording media. *Annual Review of Materials Research*, 31(1):203–235, 2001.

[205] M. Sasaki and K. Hane. Ultrasonically facilitated two-dimensional crystallization of colloid particles. *Journal of Applied Physics*, 80:5427–5431, 1996.

[206] T. Sawada, Y. Suzuki, A. Toyotama, and N. Iyi. Quick fabrication of gigantic single-crystalline colloidal crystals for photonic crystal applications. *Japanese Journal of Applied Physics*, 40:1226–1228, 2001.

[207] A.V. Shah, J. Meier, E. Vallat-Sauvain, N. Wyrsch, U Kroll, C. Droz, and U. Graf. Material and solar cell research in microcrystalline silicon. *Solar Energy Materials and Solar Cells*, 78:469–491, 2003.

[208] M. Manso Silvan, M. Arroyo Hernandez, V. Torres Costa, R. J. Martin Palma, and J. M. Martinez Duart. Structured porous silicon sub-micrometer wells grown by colloidal lithography. *Europhysics Letters*, 76:690–695, 2006.

[209] D. L. Staebler and C. R. Wronski. Reversible conductivity changes in discharge-produced amorphous si. *Applied Physics Letters*, 31:292–294, 1977.

[210] P.I. Stavroulakis. Manufacturing of domain-separated anti-reflective moth-eye structures using nanosphere lithography. MSc Project, 2007.

[211] P.I. Stavroulakis. Polarisation studies of anti-reflective 'moth-eye' metamaterials. Part III Project, University of Southampton, 2006.

[212] T.L. Temple, G.D.K. Mahanama, H.S. Reehal, and D.M. Bagnall. Influence of localized surface plasmon excitation in silver nanoparticles on the performance of silicon solar cells. *Solar Energy Materials and Solar Cells*, 93(11):1978–1985, November 2009.

[213] O. D. Velev and A. M. Lenhoff. Colloidal crystals as templates for porous materials. *Current Opinion in Colloid and Interface Science*, 5:56–63, 2000.

[214] S. Veprek and V. Marecek. The preparation of thin layers of ge and si by chemical hydrogen plasma transport. *Solid-State Electronics*, 11:683–684, 1968.

[215] M.P.C. Watts, M. Zoorob, T. Lee, and J. McKenzie. The value, solutions, and costs of patterning led's. *Proceedings of SPIE*, 6462:64620N–1, 2007.

[216] J. E. G. J. Wijnhoven, S. J. M. Zevenhuizen, M. A. Hendriks, D. Vanmaekelbergh, J. J. Kelly, and W. L. Vos. Electrochemical assembly of ordered macropores in gold. *Advanced Materials*, 12:888–890, 2000.

[217] J. Yang, A. Banerjee, and S. Guha. Triple-junction amorphous silicon alloy solar cell with 14.6and 13 *Applied Physics Letters*, 70:2975–2977, 1997.

[218] R. Waser, editor. *Nanoelectronics and Information Technology.* Wiley, 2005.